Experimentelle Physik

Measurement of the Cross Section of π^0, η and ω Meson Production in Ultrarelativistic Proton-Proton Collisions

Inaugural-Dissertation
zur Erlangung des Doktorgrades
der Naturwissenschaften im Fachbereich Physik
der Mathematisch-Naturwissenschaftlichen Fakultät
der Westfälischen Wilhelms-Universität Münster

vorgelegt von:
Jens Robert Lühder
aus Bochum

- Münster 2023 -

Dekan:	Prof. Dr. Michael Rohlfing
Erster Gutachter:	Apl. Prof. Dr. Christian Klein-Bösing
Zweiter Gutachter:	Prof. Dr. Anton Andronic

Tag der mündlichen Prüfung:	_____
Tag der Promotion:	_____

Contents

1 Einleitung

Teilchenbeschleuniger sind ein wichtiges Instrument, um unser Verständnis der grundlegenden Fragen auf dem Gebiet der Elementarteilchenphysik zu verbessern. Der weltweit leistungsstärkste Teilchenbeschleuniger ist der Large Hadron Collider (LHC), der sich bei der Europäischen Organisation für Kernforschung (CERN) in Genf befindet. Ein großer Erfolg der am CERN arbeitenden Wissenschaftler war die Entdeckung des Higgs-Bosons als letzter Baustein des Standardmodells im Juli 2012 [1]. Während der LHC in der Lage ist, zwei Protonen (pp), zwei schwere Ionen (A–A) oder eine Kombination davon (p–A) zu kollidieren, konzentriert sich diese Arbeit auf pp-Kollisionen bei einer Schwerpunktsenergie von $\sqrt{s} = 13$ TeV. Die dabei entstehenden Teilchen werden mit dem A Large Ion Collider Experiment (ALICE) gemessen. ALICE ist der Erforschung des Quark-Gluon-Plasmas (QGP) gewidmet, eines Materiezustands, in dem Quarks als quasi freie Teilchen beschreibbar sind. Dieser Zustand war bis etwa 10 µs [2] nach dem Urknall vorhanden und ensteht voraussichtlich bei hochenergetischen Kollisionen von schweren Ionen.

In dieser Arbeit wird der Wirkungsquerschnitt der π^0-, η- und ω-Meson Produktion gemessen. Die Messung des Wirkungsquerschnitts der π^0- und η-Meson Produktion erfolgt über den Nachweis des Zerfalls dieser Mesonen in zwei Photonen ($\gamma\gamma$). Der Wirkungsquerschnitt der ω-Meson Produktion wird anhand dessen Zerfalls in drei Pionen ($\pi^+\pi^-\pi^0$) gemessen. Während π^+ und π^- direkt mit Hilfe der Spurdetektoren von ALICE gemessen werden können, müssen π^0- und η-Mesonen rekonstruiert werden. Zum einen können die beiden Photonen aus dem π^0- und η-Zerfall direkt mit einem der Kalorimeter in ALICE gemessen werden: EMCal, DCal oder PHOS. Andererseits können sich Photonen innerhalb des Detektormaterials in e^+e^--Paare umwandeln. Die resultierenden e^+ und e^- können dann, analog zu den π^+ und π^-, mit den Spurdetektoren gemessen werden. Die Messmethode, die sich diese Photonenumwandlung zunutze macht, heißt Photon Conversion Method (PCM). Es ist außerdem möglich, ein Zerfallsphoton mit Hilfe eines Kalorimeters und das zweite Zerfallsphoton mit Hilfe von PCM zu messen. Während die dedizierten Messungen des Wirkungsquerschnitts der π^0- und η-Meson Produktion in dieser Arbeit den PHOS-Detektor und dessen Kombination mit PCM nutzen, werden bei der Messung der π^0-Mesonen für die ω-Rekonstruktion alle genannten Methoden eingesetzt.

Die Messungen der Wirkungsquerschnitte der neutralen Meson Produktionen in pp-Kollisionen spielen durch ihren Vergleich zu Schwerionenkollisionen eine bedeutende Rolle für das Verständnis verschiedener Eigenschaften des QGP und der Teilchenproduktion im Allgemeinen. Die Messung des Wirkungsquerschnitts neutraler Mesonen wird benötigt, um das Verständnis der Quanten Chromodynamik (QCD) und ihre Implementierung in QCD-basierten Ereignisgeneratoren wie PYTHIA zu testen. Dabei werden die Fragmentationsfunktion und die Partonverteilungsfunktion durch Parametrisierungen gemessener Mesonenspektren bei verschiedenen Kollisionsenergien eingeschränkt. Außerdem wird die Teilchenproduktion im Bereich kleiner Transversalimpulse durch phänomenologische Modelle beschrieben, die durch Mesonenmessungen verifiziert werden müssen.

Hinzu kommt, dass Photonen in verschiedenen Phasen der Kollision erzeugt werden und nicht stark wechselwirken. Daher sind sie ideale Teilchen, um das QGP zu untersuchen. Um jedoch den Anteil der direkten Photonen an allen erzeugten Photonen zu bestimmen, sind präzise Messungen der Spektren von neutralen Mesonen erforderlich. Die drei größten Beiträge von Zerfallsphotonen zur Gesamtmenge aller Zerfallsphotonen kommen aus dem Zerfall von π^0-, η- und ω-Mesonen. Da erwartet wird, dass das QGP die Hadronenproduktion in Schwerionenkollisionen im Vergleich zu pp-Kollisionen unterdrückt [3], kann die Teilchenproduktion in pp-Kollisionen außerdem zur Untersuchung des QGP verwendet werden. Darüber hinaus sind experimentelle Daten zur Produktion von Vektormesonen, wie dem ω-Meson, bei LHC-Energien rar [4]. Die Messung des ω-Meson Wirkungsquerschnitts in dieser Arbeit wird über den bislang größten Impulsbereich durchgeführt und liefert wichtige Präzisionsdaten für zukünftige theoretische Rechnungen im Bereich der Vektor-Mesonen-Fragmentierung.

In dieser Arbeit werden die grundlegenden theoretischen Konzepte für Teilchenproduktionen und deren Messung im Kapitel 3 erläutert. Diesen Erläuterungen folgt eine Beschreibung des experimentellen Aufbaus des ALICE-Experiments in Kapitel 4. Nach einem kurzen Überblick über die im Rahmen dieser Arbeit durchgeführte „Service Task“ in Kapitel 5 werden der verwendete Datensatz und die Auswahl der Ereignisse in Kapitel 6 erläutert. Schließlich werden die Messungen von geladenen Pionen und Photonen in Kapitel 7 und 8 beschrieben. Die Messung des Wirkungsquerschnitts der π^0- und η-Meson Produktion wird in Kapitel 9 beschrieben, während die Messung des Wirkungsquerschnitts der ω-Meson Produktion in Kapitel 10 beschrieben wird.

2 Introduction

Particle colliders are an important tool to enhance our understanding of fundamental physics. The most powerful particle accelerator is the Large Hadron Collider (LHC), located at the European Organization for Nuclear Research (CERN) in Geneva. A major achievement by the scientists working at CERN was the discovery of the Higgs Boson in July 2012 [1]. While the LHC is able to collide two protons (pp), two heavy-ions (A–A) or a combination of those (p–A), this thesis is focussing on pp collisions at a center-of-mass energy of $\sqrt{s} = 13$ TeV, measured with A Large Ion Collider Experiment (ALICE). ALICE is dedicated to the exploration of the Quark-Gluon Plasma (QGP), a state of matter in which quarks can be seen as quasi-free particles. This state was present until 10 µs [2] after the Big Bang and is expected to be created at heavy-ion collisions.

In this thesis, the measurement of the cross section of π^0, η and ω meson production is presented. The measurement of the cross section of π^0 and η mesons is making use of their decay into two photons ($\gamma\gamma$). The ω meson cross section measurement is using its decay into three pions ($\pi^+\pi^-\pi^0$). While π^+ and π^- can be measured directly, using the tracking detectors of ALICE, π^0 and η mesons have to be reconstructed from their decay products. On the one hand, the two photons of the π^0 and η decay can directly be measured with one of the calorimeters available in ALICE: EMCal, DCal or PHOS. On the other hand, photons can convert into e^+e^--pairs within the inner detector material. The resulting e^+ and e^- can then be tracked analogous to the π^+ and π^-. The measurement method that utilizes this photon conversion is called Photon Conversion Method (PCM). Furthermore, it is possible to measure one decay photon with the help of a calorimeter and the second decay photon utilizing PCM. While the dedicated measurements of the cross section of π^0 and η meson production in this thesis are making use of the PHOS detector and its combination with PCM, the measurement of the π^0 mesons used for the ω reconstruction is utilizing all methods mentioned.

Measurements of the cross sections of neutral meson productions in pp collisions are valuable probes for various properties of the QGP, through their comparison to heavy-ion collisions, and particle production in general. The measurement of the cross section of neutral mesons

is needed to test the understanding of Quantum Chromodynamics (QCD) and its implementation in QCD-based event generators like PYTHIA. The fragmentation function and parton distribution function is constrained by parametrizing measured data at different collision energies. Furthermore, the low-momentum regime is described by phenomenological models, which can be verified by meson measurements.

In addition to that, photons are produced during different stages of the collision and do not interact strongly. Hence, they are ideal particles to probe the QGP. However, to acquire the fraction of direct photons from all generated photons, precise measurements of neutral meson spectra are needed. The three largest contributions of decay photons to the total amount of decay photons are given by the π^0, η and ω mesons. As the QGP is expected to suppress hadron production in heavy-ion collisions compared to pp collisions [3], particle productions in pp collisions can furthermore be used to probe the QGP. In addition to that, experimental data of vector meson production, like the ω meson, at LHC energies is scarce [4]. The measurement of the ω meson cross section in this thesis is performed over an unprecedented momentum range and provides important precision data for future theoretical calculations in vector meson fragmentation.

This thesis will explain the basic theoretical concepts for particle productions and their measurement in chapter 3. These explanations are followed up by a description of the experimental setup of the ALICE detector in chapter 4. After a quick overview of the Service Task, that has been performed during this work, in chapter 5, the used data sets and the choice of selected events are explained in chapter 6. Finally, the measurements of charged pions and photons are described in chapter 7 and 8, while the measurements of π^0 and η meson production cross sections are described in chapter 9. The ω meson production cross section measurement is described in chapter 10.

3 Theory

3.1 Standard Model (SM) and Quantum Chromodynamics (QCD)

The Standard Model (SM) [5][6] is the theory in particle physics to describe the fundamental constituents and how they interact with each other. It is a Quantum Field Theory (QFT) combining Quantum Chromodynamics (QCD) and electroweak interactions. While QCD is describing interactions via the strong force, the electroweak interaction is a unification of electromagnetic interactions described by Quantum Electrodynamics (QED) and weak interactions. Gravity is not part of the SM, but being the weakest of all forces by several orders of magnitude, it can be neglected in context of particle physics. Major parts of the SM were developed by Sheldon Glashow, Abdus Salam and Steven Weinberg, who were awarded the Nobel Prize in Physics in 1979 "for their contributions to the theory of the unified weak and electromagnetic interaction between elementary particles, including, inter alia, the prediction of the weak neutral current" [7].

Fundamental interactions are realized by gauge bosons for strong, electromagnetic and weak interactions as well as the Higgs boson. The strong force is, like the name suggests, the strongest force. It is mediated by 8 gluons which couple to the charge of the strong force, the so-called color charge or color. There are three different colors and three corresponding anti-colors. Each gluon possesses a color and an anticolor. The electromagnetic force is mediated by photons which couple to the electromagnetic charge, or just charge, while photons do not carry a charge themselves. The weak force is mediated by the charged W^+ and W^- or the neutral Z^0 and couples to the weak charge. Gluons, photons, W^+, W^- and Z^0 have spin of 1, while the Higgs boson has a spin of 0. The latter is the excitation of the Higgs field, which

Force	Coupling to	Gauge boson
Strong	Color charge	8 gluons (g)
Electromagnetic	Electromagnetic charge	Photons (γ)
Weak	Weak charge	W^+, W^-, Z^0

Table 3.1: Fundamental forces in the SM.

Fermions	Generations 1	2	3	Strong	Electromagnetic	Weak
Quarks	u	c	t	✓	✓	✓
	d	s	b	✓	✓	✓
Leptons	e	μ	τ		✓	✓
	ν_e	ν_μ	ν_τ			✓

Table 3.2: Quarks and Leptons in the SM and their interaction with fundamental forces.

interacts with all particles except photons and gluons and gives them a mass. In the SM, all known matter consists of combinations of certain spin 1/2 fermions, called quarks and leptons. There are 6 different quarks and 6 different leptons divided into three families or generations with increasing masses. The 6 quark types, also called flavors, are up (u), down (d), charm (c), strange (s), top (t) and bottom (b). They carry a color, an electromagnetic and a weak charge. The u and d quark have the lowest masses and are therefore part of the first generation. Analogously the heavier c and s quarks are part of the second generation while the heaviest t and b quarks are part of the third generation. A change of flavor from the first to the second generation is suppressed by an order of magnitude, while a change of flavor from the first to the third generation family is further suppressed by an additional order of magnitude. The relative amplitudes for all possible transitions are described by the Cabibbo-Kobayashi-Maskawa (CKM) matrix [5]. One lepton is the charged electron (e) but there also exist two electron-like particles: The muon (μ) and the tauon (τ). Besides their difference in mass, their interaction with the fundamental forces is exactly the same. In addition to these, there exist three leptons called neutrinos, which only couple to the weak force. As concluded from the width of the Z^0 resonance, there cannot be a fourth light neutrino [8]. The three neutrinos are called electron-neutrino (ν_e), muon-neutrino (ν_μ) and tau-neutrino (ν_τ). The light e and ν_e are part of the first generation, while the heavier μ and ν_μ are part of the second generation and the heaviest τ and ν_τ are part of the third generation. There exists an antiparticle for each of the described 12 fermions, possessing the same mass as the corresponding particle but having opposite charge-like quantum numbers (color, weak and electromagnetic). Furthermore, particles and antiparticle can annihilate each other. In this work, quantities will be given in terms of electron volts (eV) and the speed of light c. One eV is the kinetic energy an electron acquires by traversing through an electric field with a potential difference of 1 V. One eV is equivalent to $1.602176634 \cdot 10^{-19}$ J, while the speed of light is given by 299792458 m/s [9].

Quantum Chromodynamics (QCD is a gauge field theory, which describes interactions of the strong force with colored quarks and gluons [10]. With the Einstein summation convention, the Lagrangian can be written as:

$$\mathcal{L} = \sum_q \bar{\Psi}_{q,a}(i\gamma^\mu \partial_\mu \delta_{ab} - g_s \gamma^\mu t^C_{ab} \mathcal{A}^C_\mu - m_q \delta_{ab})\Psi_{q,b} - \frac{1}{4} F^A_{\mu\nu} F^{A\mu\nu} \tag{3.1}$$

The two fundamental parameters of QCD are the quark mass m_q and its coupling constant g_s or $\alpha_s = \frac{g_s^2}{4\pi}$, which have to be determined by experiments. Coupling constants describe the strength of forces. $\bar{\Psi}_{q,a}$ and $\Psi_{q,a}$ are the quark-field spinors with flavors q and color a. γ^μ are the Dirac γ-matrices while $\mathcal{A}^C_\mu$ describes the gluon fields of the 8 different gluons. t^C_{ab} corresponds to the eight 3×3 generator matrices of the SU(3) group. $F^A_{\mu\nu}$ is the field tensor. With the structure constants f_{ABC} of the SU(3), $F^A_{\mu\nu}$ is defined as:

$$F^A_{\mu\nu} = \partial_\mu \mathcal{A}^A_\nu - \partial_\nu \mathcal{A}^A_\mu - g_s f_{ABC} \mathcal{A}^B_\mu \mathcal{A}^C_\nu \tag{3.2}$$

For massless particles, the Lagrangian is invariant under the exchange of left- and right-handed component of the quark spinors, which is called chiral symmetry. However, as quarks possess masses, this symmetry is explicitly broken for quarks. For massless particles, The

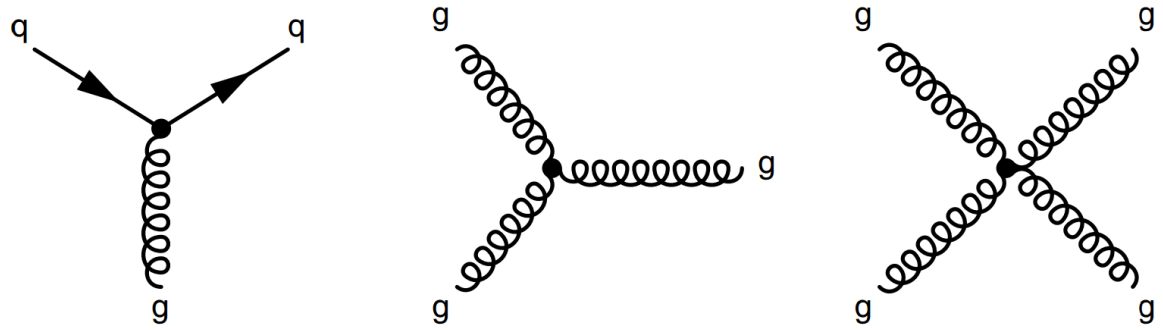

Figure 3.1: Vertices of QCD. Quarks are represented by solid lines with an arrow. Gluons are represented by curled lines [6]. Left: Coupling of gluon on quark. Middle and right: Gluon-gluon coupling.

coupling of quarks and gluons due to their color can be seen in Fig. 3.1. As gluons possess colors, they can interact with themselves. While the coupling of quarks and gluons in QCD is comparable to the coupling of charged leptons and photons in QED, gluon-gluon interaction is specific to QCD. The coupling constant in strong interactions α_s is a running variable, highly dependent on the momentum transfer Q^2. For $Q^2 \gg \Lambda^2 \approx 0.06\,\mathrm{GeV}^2/c^2$ [5], α_s can be written in first order as [11]

$$\alpha_s = \frac{4\pi}{\beta_0 \cdot \ln(Q^2/\Lambda^2)} \tag{3.3}$$

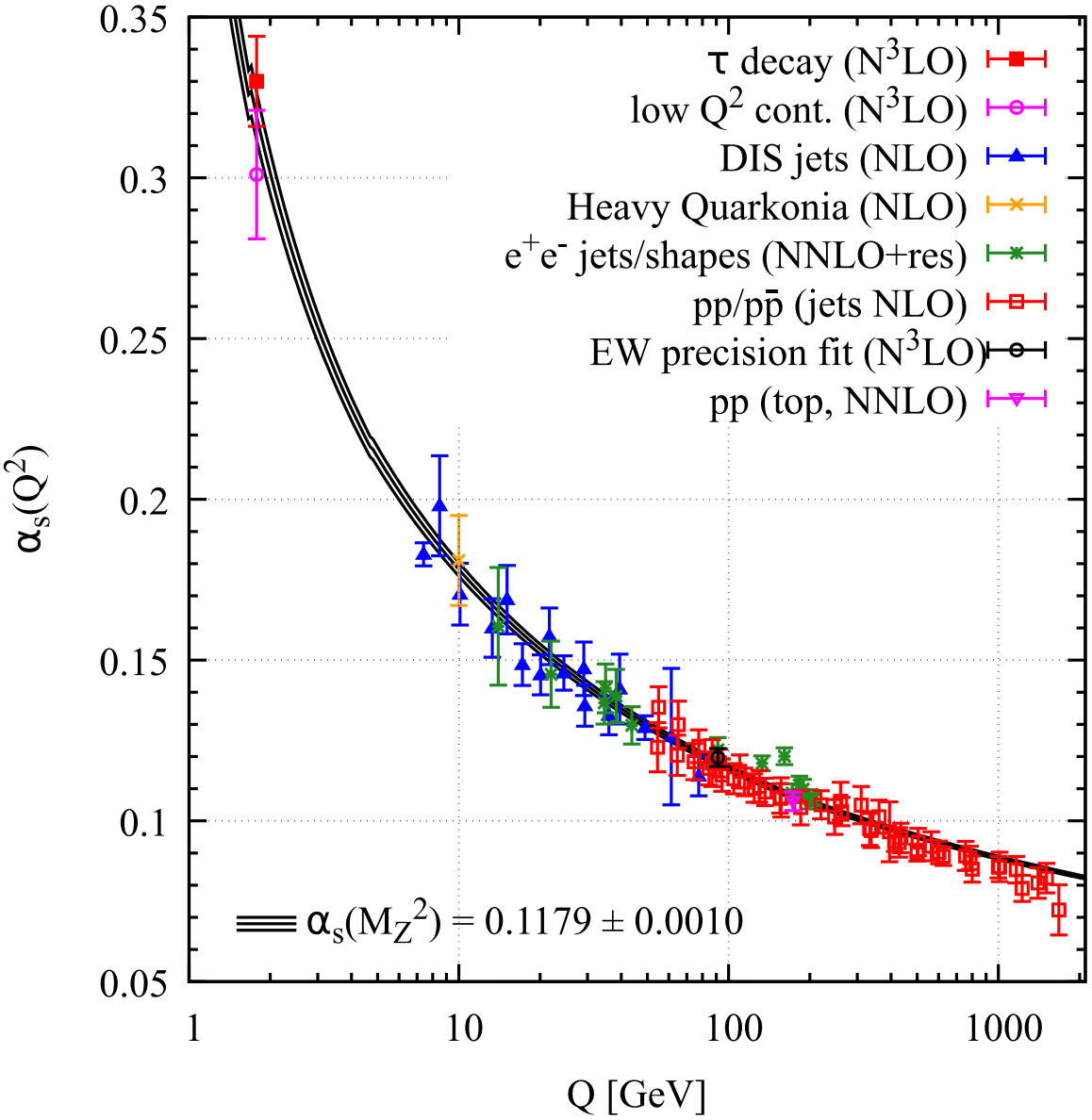

Figure 3.2: α_s as function of momentum transfer Q^2 [10]. The acronyms in brackets represent various orders of QCD perturbation theory. NLO: Next-to-leading order, NNLO: Next-to-next-to-leading order, NNLO+res: NNLO matched to a resummed calculation, N^{3}LO: next-to-NNLO

with

$$\beta_0 = 11 - \frac{1}{2} n_f. \tag{3.4}$$

Here, n_f is the number of flavors, while $\Lambda \approx 250\,\mathrm{MeV}/c$ [5] is called scaling parameter of QCD. Λ describes at which energy scale pertubative QCD (pQCD) can be applied. pQCD can be calculated analogous to QED. However, as α_s is still quite large in typical high-energy processes, higher order corrections are necessary [6].

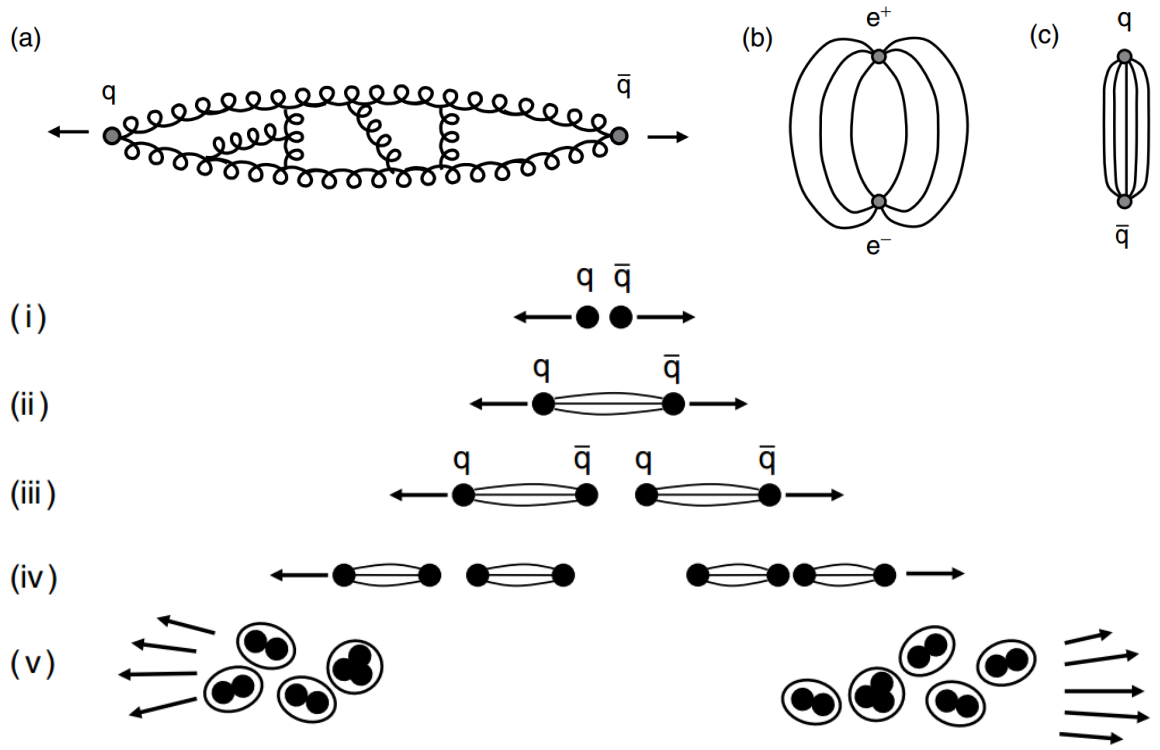

Figure 3.3: **Top:** a) Gluon-gluon interaction with exchange of virtual gluons. b) Field of QED. c) Field of QCD **Bottom:** Steps of the hadronisation process. [6]

Fig. 3.2 shows the dependence of the coupling constant α_s on the momentum transfer Q^2 for measurements of different experiments. Below this energy scale QCD has to be treated non-perturbatively. $\alpha_s(Q^2)$ is often given at the mass of the Z boson $\alpha_s(M_Z^2)$. The world average of this value has been determined to be $\alpha_s(M_Z^2) \approx 0.1187 \pm 0.0018$ [10]. As one can observe in Fig. 3.2, $\alpha_s(Q^2)$ becomes large for small values of Q^2. In this case, quarks and gluons cannot exist freely and are bound in hadrons. The boundary of quarks and gluons in colorless hadrons is called color confinement or just confinement. The interaction of gluons between each other is illustrated in Fig. 3.1. A notable exception with respect to confinement is the top quark, whose rapid decay into other quarks does not allow for a hadronisation process. If two quarks are pulled apart, virtual gluons are exchanged as shown in Fig. 3.3 (a). In contrast to QED (Fig. 3.3 (b)), the gluon interaction squeezes the color field into a tube as shown in Fig. 3.3 (c). With the distance r between two quarks, the quark-antiquark potential $V(r)$ can be described by [5]:

$$V(r) = -\frac{4}{3}\frac{\alpha_s}{r} + \kappa r \tag{3.5}$$

κ can be experimentally determined and its magnitude is $\kappa \approx 1\,\mathrm{GeV/fm}$. Due to the linear part κr in the potential, the energy between two quarks would increase to infinity if separating

them. Hence, when the energy between two quarks is large enough, new quarks will be created to confine the separating quarks in colorless hadrons. As pQCD cannot be applied in this regime, a different approach has to be considered.

Lattice QCD (LQCD) is a lattice gauge theory and a tool to perform calculations for non perturbative QCD on a discrete lattice of space-time points. LQCD calculations were able to estimate the proton mass with a precision of a few percents [6]. The calculations are computationally intensive and limited by the availability of computational resources and the efficiency of algorithms [10].

For large values of Q^2, α_s becomes small. In this case, quarks can be considered quasi-free particles, which are not bound in the radius of the proton and pQCD can be applied. As α_s decreases asymptotically, the behavior at large Q^2 is called asymptotic freedom.

3.2 Hadrons

As discussed in Sec. 3.1, quarks and gluons are bound in colorless states, so-called hadrons. Any combination of quarks and gluons, that form a colorless (white) state are able to create hadrons. The two most common types of hadrons are baryons, consisting of three quarks of different colors (qqq) and mesons, consisting of a quark and an antiquark ($q\bar{q}$) with a color and a corresponding anticolor. These quarks determine the properties of the hadron and are called valence quarks. In addition to the valence quarks, virtual pairs of quarks and anti quarks ($q\bar{q}$), called seaquarks, are created and annihilated constantly inside of hadrons. While baryons and mesons are the most common colorless states, further combinations that form bound colorless states are possible, the so-called exotic hadrons. One prominent example for an exotic hadron is the pentaquark. It is the combination of four quarks and an antiquark ($qqqq\bar{q}$) and has already been observed by LHCb [12]. Also, hybrids of quarks and gluons or states only consisting of gluons are possible.

This work focuses on the measurement of mesons, whose properties will be discussed in more detail in this section. Besides their quark content and mass, mesons can be described by their specific quantum numbers. The first quantum number is the electric charge. Electric charges are given in units of the elementary charge e. u, c and t quarks do have a charge of $2/3$, while d, s and b quarks have a charge of $-1/3$. The second quantum number is the total spin s, while every quark has a spin of $1/2$. The spins of the valence quarks in mesons can be arranged parallel ($S = 1$) or antiparallel ($S = 0$). Another quantum number is the isospin I, which distinguishes between the u and d. The z-component of the isospin I_z, often written as I_3, of u quarks is $I_z = 1/2$ and of d quarks is $I_z = -1/2$. The total isospin of mesons is

calculated analogous to the total spin. Instead of an isospin, heavier particles possess an own quantum number for their flavor. Strange quarks possess strangeness $S = -1$, charm quarks possess charm $C' = +1$, bottom quarks possess bottomness $B' = -1$ and top quarks possess topness $T = +1$. For antiparticles these quantum numbers and the electric charge have to be multiplied by -1. The baryon number B is given by

$$B = \frac{1}{3}(n_q - n_{\bar{q}}) \tag{3.6}$$

Here, n_q is the number of quarks and $n_{\bar{q}}$ is the number of antiquarks. For mesons, the baryon number is 0. With these quantum numbers the total electric charge Q can be calculated with help of the Gell-Mann-Nishijima formula [10]:

$$Q = I_z + \frac{B + S + C' + B' + T}{2} \tag{3.7}$$

Furthermore the hypercharge Y can be written as [10]:

$$Y = B + S - \frac{C' - B' + T}{3} \tag{3.8}$$

With the orbital angular momentum of the constituent quarks L, the total angular momentum J can be a natural number in the interval

$$|L - S| \leq J \leq |L + S|. \tag{3.9}$$

The parity P can be calculated by $P = (-1)^{L+1}$, while the charge conjugation or C-parity C is defined as $C = (-1)^{L+1}$. It shall be noted, that the C-parity is only defined for mesons which consist of a quark and antiquark of the same flavor. If a meson consists of a quark and antiquark of the same flavor or is a combination of u and d quarks or antiquarks, the C-parity can be generalized to the G-parity $G = (-1)^{I+L+S}$.
With the given quantum numbers, mesons can be grouped into multiplets via J^{PC}. In case of $L = 0$, mesons can be divided into pseudoscalars (0^{-+}) and vectors (1^{--}). Mesons with $L = 1$ can be separated into scalars (0^{++}), axial vectors (1^{++} and 1^{+-}) and tensors (2^{++}). The u, d and s quark can be grouped in an octet and a singlet, following an SU(3) symmetry. In this case, 9 different combinations are possible. Adding the c quark in the consideration extends the SU(3) to an SU(4), which is broken, as the c quark has a significantly higher mass. In this case, the 16 available mesons can be grouped into a 15-plet and a singlet [10]. Isoscalar states with the same J^{PC} mix, while the mixing between the light quarks with the b and c quark can be assumed negligible [10].

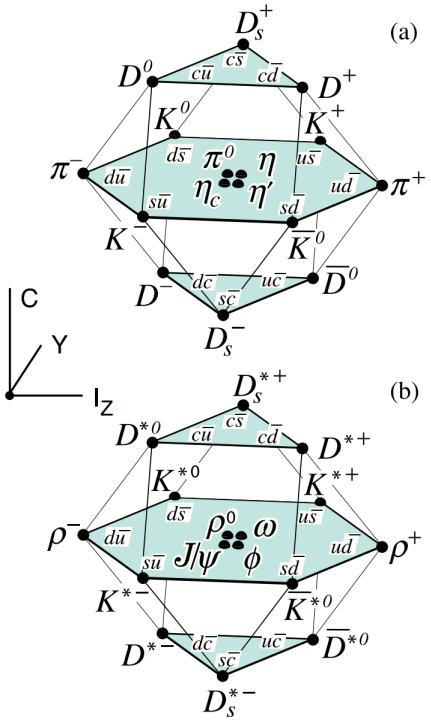

Figure 3.4: 16-plets for mesons only containing u, d, s and c quarks. a) For pseudoscalars. b) For vector mesons [10].

Three different mesons are reconstructed in this work. The π^0 meson, the η meson and the ω meson. In addition to that, the charged pions π^+ and π^- are measured to reconstruct the ω meson. The basic properties of these mesons can be found in Tab. 3.3. While the pions and the η meson only contain u and d quarks, the wave function of the ω meson contains s quarks as well. The ω meson is defined by mixing the wave functions of the SU(3) Ψ_8 and Ψ_1 with the vector meson mixing angle $\theta_v = 36.4°$:

$$\omega = \Psi_8 \cos\theta_v + \Psi_1 \sin\theta_v \tag{3.10}$$

The wave functions Ψ_8 and Ψ_1 are given by:

$$\Psi_1 = \frac{1}{\sqrt{3}}(u\bar{u} + d\bar{d} + s\bar{s}) \tag{3.11}$$

$$\Psi_8 = \frac{1}{\sqrt{6}}(u\bar{u} + d\bar{d} - 2s\bar{s}) \tag{3.12}$$

Meson	Quark content	Rest mass in MeV	I^G (J^{PC})	Mean Lifetime in s	Leading decay modes	Branching Ratio BR in %
π^0	$\frac{1}{\sqrt{2}}(u\bar{u} - d\bar{d})$	134.9768 ± 0.0005	$1^-(0^{-+})$	$8.52 \cdot 10^{-17}$ $\pm 0.18 \cdot 10^{-17}$	2γ	98.823 ± 0.034
π^+	$u\bar{d}$	139.57039 ± 0.00018	$1^-(0^-)$	$2.6033 \cdot 10^{-8}$ $\pm 0.0005 \cdot 10^{-8}$	$\mu^+\nu_\mu$	99.98770 ± 0.00004
η	$\frac{1}{\sqrt{3}}(u\bar{u} + d\bar{d} - 2s\bar{s})$	547.862 ± 0.017	$0^+(0^{-+})$	$5.5 \cdot 10^{-19}$[5]	2γ	39.41 ± 0.20
					$3\pi^0$	32.68 ± 0.23
					$\pi^+\pi^-\pi^0$	22.92 ± 0.28
ω	$\frac{1}{\sqrt{2}}(u\bar{u} + d\bar{d})$	782.65 ± 0.12	$0^-(1^{--})$	$7.8 \cdot 10^{-23}$[5]	$\pi^+\pi^-\pi^0$	89.3 ± 0.6
					$\pi^0\gamma$	8.40 ± 0.22

Table 3.3: Basic properties of mesons used in this work [10]. The π^- modes are charge conjugates of the shown π^+ modes.

Due to the mixing angle, the s is nearly completely cancelled out and the ω meson can be written as:

$$\omega = \frac{1}{\sqrt{2}}(u\bar{u} + d\bar{d}) \tag{3.13}$$

Analogously, the ϕ meson, defined by $\phi = \Psi_8 \cos\theta_v - \Psi_1 \sin\theta_v$, is nearly pure $s\bar{s}$.

3.3 Interaction of Radiation with Matter

The next sections briefly describe the interactions, upon which the measurements used in this work rely.

3.3.1 Interaction of Charged Particles with Matter

The total energy loss of charged particles $-\frac{\mathrm{d}E}{\mathrm{d}x}\Big|_{\text{Total}}$ can be written as a sum of separate energy loss effects $-\frac{\mathrm{d}E}{\mathrm{d}x}$ [14].

$$-\frac{\mathrm{d}E}{\mathrm{d}x}\Big|_{\text{Total}} = -\frac{\mathrm{d}E}{\mathrm{d}x}\Big|_{\text{Ionization}} - \frac{\mathrm{d}E}{\mathrm{d}x}\Big|_{\text{Pair Production}} - \frac{\mathrm{d}E}{\mathrm{d}x}\Big|_{\text{Bremsstrahlung}} - \frac{\mathrm{d}E}{\mathrm{d}x}\Big|_{\text{Photonuclear}} \tag{3.14}$$

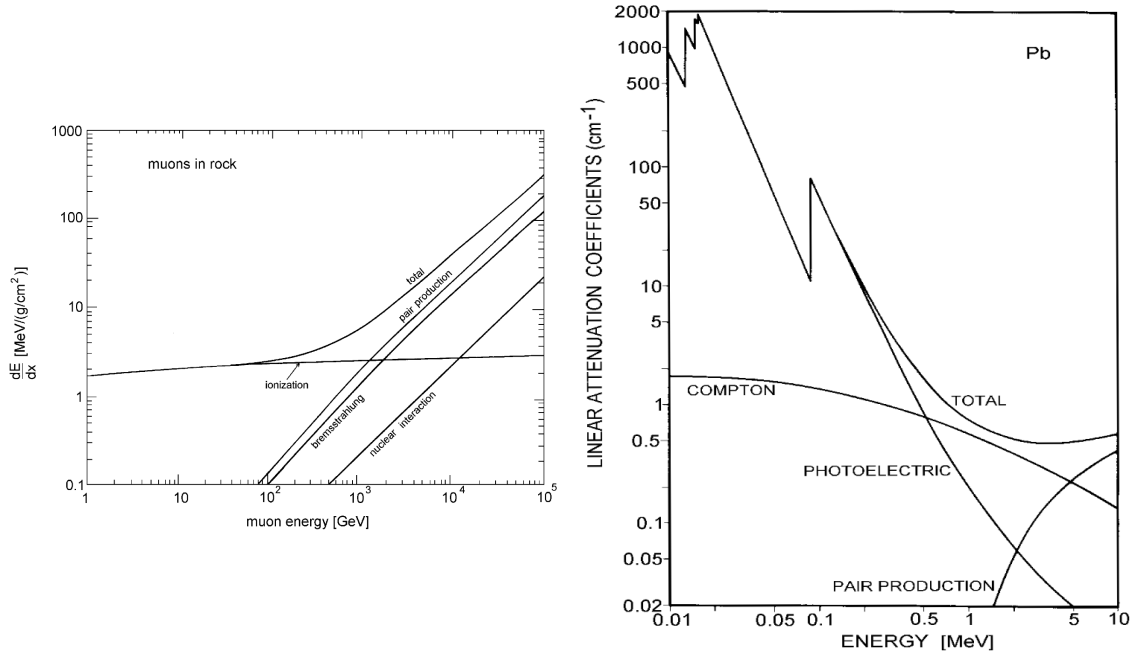

Figure 3.5: **Left**: Contributions to the energy loss of muons. **Right**: Contributions of mass attenuation coefficient in Pb. [13]

An example of the contributions of the different energy loss effects can be seen in Fig. 3.5 (left). It can be seen that for low to intermediate energies, the energy loss is dominated by ionization, which is described by $-\frac{\mathrm{d}E}{\mathrm{d}x}\Big|_{\text{Ionization}}$. For particles which are heavy in comparison to electrons, this energy loss can be calculated with the Bethe-Bloch formula.

$$-\frac{\mathrm{d}E}{\mathrm{d}x}\Big|_{\text{Ionization}} = 4\pi N_A r_e^2 m_e c^2 z^2 \frac{Z}{A}\frac{1}{\beta^2}\left[\ln\left(\frac{2m_e c^2\gamma^2\beta^2}{I}\right) - \beta^2 - \frac{\delta}{2}\right] \tag{3.15}$$

Here, z is the charge in units of the elementary charge e, Z is the atomic number of the absorber, A is the atomic mass of the absorber, m_e is the mass of an electron, r_e^2 is the classical electron radius, N_A is the Avogadro constant, I is the characteristic ionization constant approximated by $I = 16Z^{0.9}\,\mathrm{eV}$ for $Z > 1$ and $\beta = \frac{v}{c}$ is the ratio of the particle's velocity and the speed of light. δ is a parameter which represents the shielding of the field of the transverse electric field of the incident particle by the charge density of the electrons of the absorber atoms. The equation cannot be used for slow particles, whose velocity is in the order of the velocity of the absorber electrons or even smaller. Here, the energy loss is proportional to β.

For electrons, the Bethe-Bloch formula has to be adjusted. It can be approximated by [14]:

$$-\frac{\mathrm{d}E}{\mathrm{d}x}\Big|_{\text{Ionization}} = 4\pi N_A r_e^2 m_e c^2 \frac{Z}{A}\frac{1}{\beta^2}\left[\ln\left(\frac{\gamma m_e c^2}{2I}\right) - \beta^2 - \frac{\delta^*}{2}\right] \tag{3.16}$$

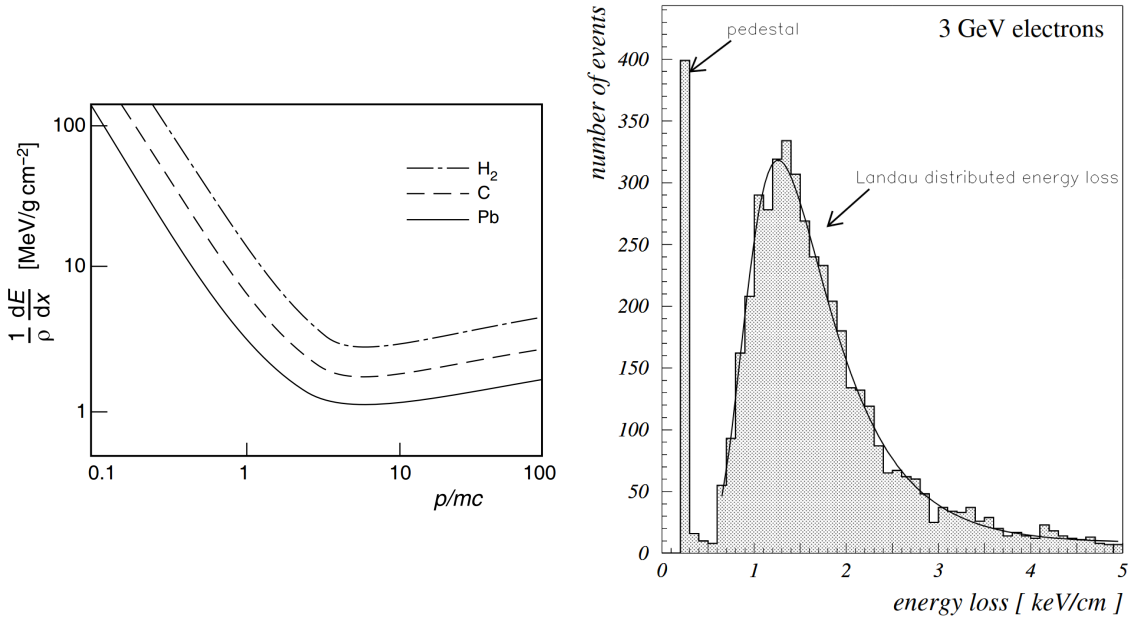

Figure 3.6: **Left**: Schematic illustration of the averaged energy loss of charged particles, due to ionization for different absorber materials [5]. **Right**: Energy loss distribution of 3 GeV electrons in a 5 cm thick, Ar/CH_4 filled, MWPC [13].

Where δ^* for electrons has different values than δ. The exact formula for electrons is given by [14]:

$$-\left.\frac{\mathrm{d}E}{\mathrm{d}x}\right|_{\text{Ionization}} = 4\pi N_A r_e^2 m_e c^2 \frac{Z}{A}\frac{1}{\beta^2} \cdot \left[\ln\left(\frac{\gamma m_e c^2 \beta\sqrt{\gamma-1}}{\sqrt{2}I}\right) - \frac{1}{2}(1-\beta^2) - \frac{2\gamma-1}{2\gamma^2}\ln 2 + \frac{1}{16}\left(\frac{\gamma-1}{\gamma}\right)^2\right] \tag{3.17}$$

Furthermore, the energy loss for positrons is given by [14]:

$$-\left.\frac{\mathrm{d}E}{\mathrm{d}x}\right|_{\text{Ionization}} = 4\pi N_A r_e^2 m_e c^2 \frac{Z}{A}\frac{1}{\beta^2} \cdot \left[\ln\left(\frac{\gamma m_e c^2 \beta\sqrt{\gamma-1}}{\sqrt{2}I}\right) - \frac{\beta^2}{24}\left(23 + \frac{14}{\gamma+1} + \frac{10}{(\gamma+1)^2} + \frac{4}{(\gamma+1)^3}\right)\right] \tag{3.18}$$

A schematic illustration of the average energy loss of charged particles due to ionization can be seen in Fig. 3.6 (left).

The Bethe-Bloch formula describes the average energy loss for different energies. The fluctuations of the energy loss of charged particles can be described by a Landau distribution. It is a probability function and can be approximated by [13]:

$$\Omega(\lambda) = \frac{1}{\sqrt{2\pi}}\exp\left\{-\frac{1}{2}(\lambda + e^{-\lambda})\right\} \tag{3.19}$$

Here, λ is the normalized deviation from the most probable energy loss. Fig. 3.6 (right) shows an example of the energy loss distribution for electrons in a MultiWire Proportional Chamber (MWPC). The energy loss falls inversely proportional to the energy transfer squared, resulting in a long tail, called Landau tail. If the absorber thickness increases, the Landau distribution becomes more symmetric [13] and can be approximated by a Gaussian distribution [14]. More symmetric distributions can also be reached via truncation to thin absorbers.

Fast particles can interact radiatively with the Coulomb field of the absorber material and lose energy. While decelerating, parts of their kinetic energy is emitted by photons. This radiation is called Bremsstrahlung and is represented by $-\frac{\mathrm{d}E}{\mathrm{d}x}\Big|_{\text{Bremsstrahlung}}$ in Eq. 3.14. For high energies, it can be described by [14]:

$$-\frac{\mathrm{d}E}{\mathrm{d}x}\Big|_{\text{Bremsstrahlung}} = 4\alpha N_A \frac{Z^2}{A} z^2 \left(\frac{1}{4\pi\epsilon_0}\frac{e^2}{mc^2}\right)^2 E \ln\frac{183}{Z^{\frac{1}{3}}} \tag{3.20}$$

Where ϵ_0 is the vacuum permittivity, $\alpha = \frac{1}{4\pi\epsilon_0}\frac{e^2}{\hbar c} \approx 1/137$ is the fine-structure constant and m is the mass of the incident particle. This energy loss is anti-proportional to the square of the incident particle mass. Hence, the influence of Bremsstrahlung is of special importance for light particles. For electrons, the energy loss due to Bremsstrahlung can be written as [14]:

$$-\frac{\mathrm{d}E}{\mathrm{d}x}\Big|_{\text{Bremsstrahlung}} = 4\alpha N_A \frac{Z^2}{A} r_e^2 E \ln\frac{183}{Z_3^1} = \frac{E}{X_0} \tag{3.21}$$

X_0 is defined as the radiation length. It is the length, after which the average energy of a traversing particle has been decreased by the factor e. In contrast to $-\frac{\mathrm{d}E}{\mathrm{d}x}\Big|_{\text{Ionization}}$, $-\frac{\mathrm{d}E}{\mathrm{d}x}\Big|_{\text{Bremsstrahlung}}$ is proportional to the energy of the incident particle. The critical energy E_c, where the energy loss due to ionization is the same as the energy loss due to Bremsstrahlung for liquid or solid absorbers can be approximated by [13]:

$$E_c = \frac{610}{Z + 1.24}\,\text{MeV} \tag{3.22}$$

For gases the critical energy is approximated by:

$$E_c = \frac{710}{Z + 0.92}\,\text{MeV} \tag{3.23}$$

At high energies, charged particles are able to create electron-positron pairs in the Coulomb field of absorbers by exchange of virtual photons. The energy loss due to trident production (like $\mu + \text{nucleus} = \mu + e^+ + e^- + \text{nucleus}$) is proportional to E and given by [14]:

$$-\frac{\mathrm{d}E}{\mathrm{d}x}\bigg|_{\text{Pair Production}} = b_{\text{Pair Production}}(Z, A, E) \cdot E \tag{3.24}$$

$b_{\text{Pair Production}}(Z, A, E)$ is a function with only slight dependence on E.

The last missing term in Eq. 3.14 is $-\frac{\mathrm{d}E}{\mathrm{d}x}\Big|_{\text{Photonuclear}}$. It describes the energy loss of inelastic interactions with the nuclei of the absorber material, due to exchange of virtual photons. This energy loss is also proportional to E and given by [14]:

$$-\frac{\mathrm{d}E}{\mathrm{d}x}\bigg|_{\text{Photonuclear}} = b_{\text{Photonuclear}}(Z, A, E) \cdot E \tag{3.25}$$

While the energy loss of transition radiation is negligible [14], it can be helpful for particle identification and shall therefore be explicitly mentioned. If charged particles traverse through materials with different dielectric permittivities, photons can be emitted. This can for example occur when a charged particle crosses the interface from vacuum or air to a dielectric medium. While approaching the medium, it induces a mirror charge and creates a dipol. The field strength of the dipol changes, while the charged particle is moving and is zero when the charged particle enters the medium. Due to the change of the field strength, electromagnetic radiation is emitted.

3.3.2 Interaction of Photons with Matter

The detection of photons requires them to create charged particles in interaction with the detector, which will then give a signal in the detector [14]. The three important effects for particle identification are the photoelectric effect, the pair production and the Compton scattering. In contrast to interactions with charged particles, photons are completely absorbed (photoelectric effect, pair production) or scattered in large angles, which are statistical processes. The intensity I of a photon beam decreases exponentially in matter, described by the formula [14]:

$$I = I_0 e^{-\mu x} \tag{3.26}$$

Here, I_0 is the initial intensity, x is the penetration depth and μ is the mass attenuation coefficient, which is typically given in g/cm^2. With σ_i beeing the cross section of a specific

energy loss process i, the total cross section σ_{Total} for a photon to interact can be written as the sum:

$$\sigma_{\text{Total}} = \sum_{i=1}^{3} \sigma_i = \sigma_{\text{Photoelectric Effect}} + \sigma_{\text{Compton Effect}} + \sigma_{\text{Pair Production}} \tag{3.27}$$

The mass attenuation is connected to the cross section by [14]:

$$\mu = \frac{N_A}{A} \sigma_{\text{Total}} \tag{3.28}$$

An illustration of the extent of different cross section contributions can be seen in Fig. 3.5 (right). It can be seen that the photoelectric effect dominates the mass attenuation coefficient at low photon energies. With increasing energies the influence of the Compton effect increases and eventually becomes the most important effect. At high energies the total cross section is dominated by the pair production.

The photoelectric effect describes the process, where a bound electron can absorb a photon to be emitted. For non-relativistic energies, the cross section for the photoelectric effect is given by the Born-approximation [14]:

$$\sigma_{\text{Photoelectric Effect}} = \left(\frac{32}{\epsilon^7}\right)^{\frac{1}{2}} \alpha^4 Z^5 \sigma^e_{\text{Th}} \tag{3.29}$$

Here, $\epsilon = \frac{E_\gamma}{m_e c^2}$ is the reduced photon energy and σ^e_{Th} is the Thomson cross section for elastic scattering. Near to absorption edges, Eq. 3.29 has to be adjusted by a function $f(E_\gamma, E_\gamma^{edge})$. For relativistic energies, the cross section for the photoelectric effect is given by [14]:

$$\sigma_{\text{Photoelectric Effect}} = 4\pi r_e^2 Z^5 \alpha^4 \frac{1}{\epsilon} \tag{3.30}$$

The Compton effect describes the elastic scattering of a photon at a quasi-free atomic electron. When neglecting the binding energies of bound electrons, the cross section per electron is given by the Klein-Nishina formula [14]:

$$\begin{aligned} \sigma^{\text{Electron}}_{\text{Compton Effect}} = {} & 2\pi r_e \left[\left(\frac{1+\epsilon}{\epsilon^2}\right)\left(\frac{2(1+\epsilon)}{1+2\epsilon} - \frac{1}{\epsilon}\ln(1+2\epsilon)\right)\right] \\ & + 2\pi r_e \left[\frac{1}{2\epsilon}\ln(1+2\epsilon) - \frac{1+3\epsilon}{(1+2\epsilon)^2}\right] \text{cm}^2/\text{Electron} \end{aligned} \tag{3.31}$$

Compton scattering at atoms is enhanced by the factor Z and given by [14]:

$$\sigma^{\text{Atomic}}_{\text{Compton Effect}} = Z \sigma^{\text{Electron}}_{\text{Compton Effect}} \tag{3.32}$$

The cross section can be approximated at high energies by [13]:

$$\sigma_{\text{Compton Effect}} \propto \frac{\ln \epsilon}{\epsilon} \tag{3.33}$$

The ratio of scattered photon energy ($E_\gamma^{'}$) to the incident photon energy E_γ can be derived by:

$$\frac{E_\gamma^{'}}{E_\gamma} = \frac{1}{1 + \epsilon(1 - \cos\theta_\gamma)} \tag{3.34}$$

Here, θ_γ is the angle between the photon before and after the scattering.

Pair production describes the creation of a particle and an antiparticle by a neutral boson. However, for this work pair production describes the creation of an electron and a positron by a photon. Photons require a minimum energy to be able to create an electron-positron pair. In the Coulomb field of a nucleus with mass m_{Nucleus}, the photon energy has to be at least [13]:

$$E_\gamma \geq 2m_e c^2 + \frac{2m_e^2 c^2}{m_{\text{Nucleus}}} \approx 2m_e c^2 \tag{3.35}$$

If the pair production occurs in the Coulomb field of an electron the minimum energy of a photon has to be at least [13]:

$$E_\gamma \geq 4m_e c^2 \tag{3.36}$$

At photon energies significantly bigger than 20 MeV, the cross section for pair production is given by [13]:

$$\sigma_{\text{Pair Production}} = 4\alpha r_e^2 Z^2 \left(\frac{7}{9}\ln\left(\frac{183}{Z^{1/3}} - \frac{1}{54}\right)\right) \approx \frac{7}{9}\frac{A}{N_A}\frac{1}{X_0} \tag{3.37}$$

Pair production is very important for this analysis as the creation of an electron-positron pair in the inner material of the ALICE detector is one reconstruction method for photons, called Photon Conversion Method (PCM).

3.4 Particle Production in Hadron Collisions

Hadron-colliders can accelerate hadrons to energies much larger than their rest mass. Hadrons with $pc \gg mc^2$ are called ultrarelativistic and the state of the system right before the collision

is called initial state. It is helpful to use observables, which are as independent as possible on the differences in momentum distributions of colliding hadrons in the initial state and at best invariant to Lorentz transformation. Each particle is described by a four-momentum-vector P, where the counting of the components of the vector is starting at zero. The zeroth component is the energy of the particle E/c. Natural units are often used in particle physics and this convention is also used in the following equations. The zeroth component will then be written as E. The first to the third component are defined as the momentum of the particle $\vec{p} = (p_\mathrm{x}, p_\mathrm{y}, p_\mathrm{z})$. The energy-momentum four-momentum-vector P is then defined as $P = (E, p_\mathrm{x}, p_\mathrm{y}, p_\mathrm{z}) = (E, \vec{p})$. Squaring of P is defined to be $P^2 = E^2 - \vec{p}^2$, which is equal to the square of the rest mass m. As this equation is Lorentz invariant, the rest mass m is also called invariant mass m_Inv.

It is possible to separate momenta of all particles in components longitudinal and transverse to the beam axis. When aligning the beam axis with the z-axis, the absolute values of the longitudinal momentum p_L and the transverse momentum p_T are given by

$$p_\mathrm{L} = p_z \tag{3.38}$$

and

$$p_\mathrm{T} = \sqrt{p_x^2 + p_y^2}. \tag{3.39}$$

Analogous to the transverse momentum p_T, a transverse mass m_T, which is invariant to Lorentz-transformations in beam direction, can be defined as

$$m_\mathrm{T}^2 = m^2 + p_\mathrm{T}^2 = m^2 + p_\mathrm{x}^2 + p_\mathrm{y}^2 = E^2 - p_\mathrm{z}^2 = E^2 - p_\mathrm{L}^2. \tag{3.40}$$

The available energy in a collision system is given in the center of mass frame. When $\vec{p}_1$ and $\vec{p}_2$ are the momenta of the colliding hadrons with corresponding energies E_1 and E_2 and the corresponding four-momentum-vectors P_1 and P_2, the center of mass frame is defined by $\vec{p}_1 = -\vec{p}_2$ and $E_1 = E_2 = E$. The Lorentz-invariant quantity to describe the available energy in a collision system is given by the square root of the Lorentz-invariant Mandelstam variable $s = (P_1 + P_2)^2$ with $\sqrt{s} = P_1 + P_2 = 2E$. However, the center of mass frame used in the LHC is the pp system, which is not the center of mass frame of colliding partons [6]. Hence, the two final state particles are boosted along the direction of the beam axis. Instead of angles, the rapidity y is used. It is defined as

$$y = \frac{1}{2} \ln\left(\frac{E + p_z}{E - p_z}\right) = \frac{1}{2} \ln\left(\frac{E + p_\mathrm{L}}{E - p_\mathrm{L}}\right). \tag{3.41}$$

Differences of rapidities Δy are invariant under longitudinal boosts. If masses of particles or jets are small compared to their energy, p_{L} can be approximated by $p_{\mathrm{L}} \approx E \cdot \cos(\theta)$. Here, θ is the polar angle between the beam axis and the particle or jet axis. In this case, the rapidity can be approximated by

$$y \approx \frac{1}{2} \ln\left(\frac{1+\cos(\theta)}{1-\cos(\theta)}\right) = \frac{1}{2} \ln\left(\cot^2(\frac{\theta}{2})\right). \tag{3.42}$$

This leads to the pseudorapidity η, defined as

$$\eta = -\ln\left(\tan\left(\frac{\theta}{2}\right)\right). \tag{3.43}$$

While the use of η instead of y is well justified for high momentum particles in high energy physics, the calculation of y needs information about the energy and momentum of a particle. To acquire this information particles need to be identified, while η is only dependent on the angle of particles. Hence, experiments often use η instead of y.

When colliding hadrons, one can distinguish between elastic and inelastic collisions. In elastic collisions, only kinematic properties of colliding hadrons are changed and the total kinetic energy is conserved. In inelastic collisions, the total kinetic energy is reduced. This reduction of kinetic energy is used to excite hadrons or to produce new particles. Hence, the total cross section σ_{Total} can be written as sum of the inelastic cross section σ_{Inel} and the elastic cross section σ_{El}.

$$\sigma_{\mathrm{Total}} = \sigma_{\mathrm{Inel}} + \sigma_{\mathrm{El}} \tag{3.44}$$

Furthermore, the cross section can be expressed in dependence of final state variables, called differential cross section [6]. The Lorentz invariant differential cross section in dependence of the momentum $\vec{p}$ is given by $E\,\mathrm{d}^3\sigma/\mathrm{d}p^3$, where E is the single particle energy. Using observables extracted from meson measurements, the Lorentz invariant spectrum of final state particles is given by [3]:

$$E\frac{\mathrm{d}^3 N_{\mathrm{dens}}}{\mathrm{d}p^3} = \frac{1}{2\pi p_{\mathrm{T}}} \frac{\mathrm{d}^2 N_{\mathrm{dens}}}{\mathrm{d}p_{\mathrm{T}}\mathrm{d}y} \tag{3.45}$$

N_{dens} is the number density per collision.

The momentum transfer between partons in an inelastic collision is not fixed. It is possible to divide collisions in two categories, depending on their momentum transfer. In soft processes protons collide as a whole and only a small of amount of momentum is transferred. In hard processes the substructure of the protons are colliding, while these hard processes occur at

$p_{\mathrm{T}} \gtrapprox 2\,\mathrm{GeV}/c$. Most particles are created in soft processes and their particle production spectra can be described with an exponential $E\,\mathrm{d}^3\sigma/\mathrm{d}p^3 \propto e^{-\alpha p_{\mathrm{T}}}$. As already mentioned in Chap. 3.1, soft processes cannot be treated perturbatively but phenomenological models have to be used. Interactions of the hard process occur on short timescales $1/Q \ll 1/\Lambda$ [15], leading to fluctuations to appear frozen, creating a snapshot of the hadron structure with resolution $1/Q$. The factorization theorem [16] formalizes this. Here, the particle production cross section is written as a convolution (written as $\otimes$) of Parton Distribution Functions (PDFs), Fragmentation Functions (FFs) and respective process-dependent partonic cross sections. PDFs can be understood as probability densities to find a parton with a given momentum, while they have to be modified for nucleons inside a nucleus, called nPDFs [17][3]. FFs describe how quarks and gluons transform into color-neutral particles like hadrons and photons [17]. If two protons collide, the differential inclusive hadron (h) production cross section with incoming partons a and b is given by [18]:

$$\sigma_{pp\to hX} \approx \sum_{abjd} \int dx_a \int dx_b \int dz_j f_{a/p}(x_a,\mu_f) \otimes f_{b/p}(x_b,\mu_f) \otimes d\sigma_{ab\to jd}(\mu_f,\mu_F,\mu_R) \otimes D_{j\to h}(z_j,\mu_F) \tag{3.46}$$

x_a and x_b are the initial momentum fractions carried by the interacting partons and z_j is the momentum fraction of h. $f_{a/p}(x_a,\mu_f)$ and $f_{b/p}(x_b,\mu_f)$ are the two PDFs, while the differential cross section for the parton scattering process is given by $d\sigma_{ab\to jd}(\mu_f,\mu_F,\mu_R)$ and $D_{j\to h}(z_j,\mu_F)$ is the FF for parton j to hadron h. Furthermore, μ_f and μ_F are the factorization scales and μ_R is the renormalization scale.

The particle production spectrum created by hard processes can be described by:

$$E\,\mathrm{d}^3\sigma/\mathrm{d}p^3 \propto p_{\mathrm{T}}^{-n} \tag{3.47}$$

Various parametrizations are used to describe particle production spectra over the whole p_{T} range. In this work, the Tsallis-function [19] has been used for the cross section measurement of the ω meson. Its distribution is given by:

$$E\frac{\mathrm{d}^3\sigma}{\mathrm{d}p^3} = \frac{C}{2\pi}\frac{(n-1)(n-2)}{nT[nT+m(n-2)]}\left(1+\frac{m_{\mathrm{T}}-m}{nT}\right)^{-n} \tag{3.48}$$

C, T and n are free fit parameters, while m and m_{T} are the respective rest mass and transverse mass of the particle. For the measurement of the η meson cross section, a two-component model (TCM) fit [20] has been used. The TCM fit is defined by:

$$E\frac{\mathrm{d}^3\sigma}{\mathrm{d}p^3} = A_e \exp(-E_{\mathrm{T,\ kin}}/T_e) + \frac{A}{\left(1+\frac{p_{\mathrm{T}}^2}{T^2 \cdot N}\right)^N} \tag{3.49}$$

with

$$E_{\mathrm{T,\ kin}} = \sqrt{p_{\mathrm{T}}^2 + m^2} - m \tag{3.50}$$

$E_{\mathrm{T,\ kin}}$ is the transverse kinetic energy with the respective transverse momentum p_{T} and rest mass m. A modified TCM fit with two additional free parameters M and T_2 to account for deviations from the powerlaw behavior for momenta greater than $p_{\mathrm{T}} \approx 50\,\mathrm{GeV}$ is being is defined by:

$$E\frac{\mathrm{d}^3\sigma}{\mathrm{d}p^3} = A_e \exp(-E_{\mathrm{T,\ kin}}/T_e) + \frac{A}{\left(1+\frac{p_{\mathrm{T}}^2}{T^2 \cdot N}\right)^N} + \frac{A}{\left(1+\frac{p_{\mathrm{T}}^2}{T_2^2 \cdot M}\right)^M} \tag{3.51}$$

The modified TCM is always used for the measurement of the π^0 meson cross section shown in this work, when the TCM fit is mentioned.

3.4.1 PYTHIA

After extracting the raw yields of a desired meson, these yields have to be corrected for efficiency and acceptance. This is realized with help of Monte Carlo (MC) simulations and the event generator used in this work is PYTHIA [21]. There are different versions of PYTHIA. It was first written in FORTRAN and completely rewritten in C++ in PYTHIA version 8.100. This thesis is using PYTHIA version 8.2 with the Monash 2013 tune [22]. The development began in 1978 with JETSET, which merged with PYTHIA. It focuses on high energy collisions with center of mass energies greater than 10 GeV. In PYTHIA the Lund string-model [23][24] is used for hadronisation. In this model $\mathrm{q\bar{q}}$ pairs are connected by strings representing the strength of the color field described by Eq. 3.5. The energy stored in this string increases linearly with the separation of the $\mathrm{q\bar{q}}$ pair, if the Coulomb term is neglected. If the energy in the string is high enough to produce a new $\mathrm{q'\bar{q}'}$ pair it may break, splitting the system into two separate systems of $\mathrm{q'\bar{q}}$ and $\mathrm{q\bar{q}'}$, where each of these systems is connected via strings as well. This process continues if the invariant mass of the newly created strings remains large

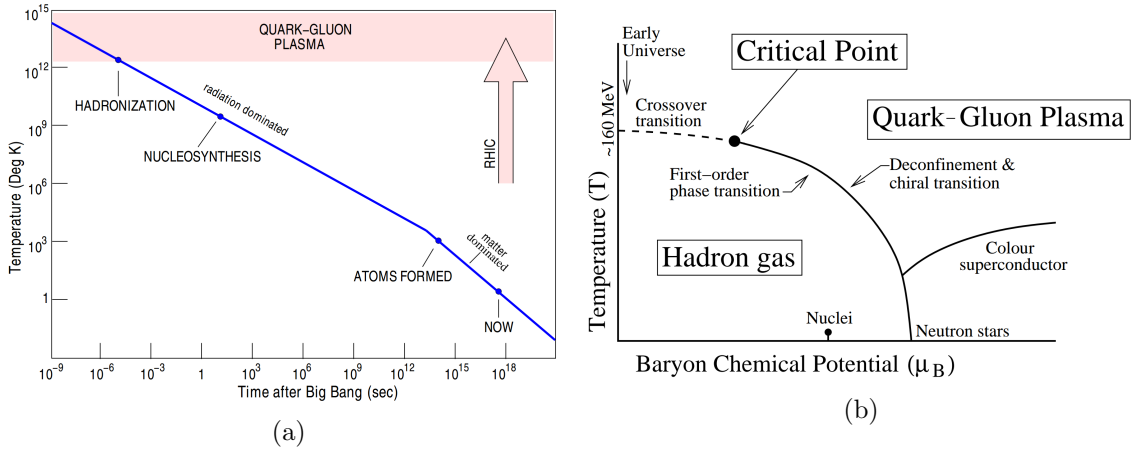

Figure 3.7: **(a):** Temperature in the universe after the Big Bang **(b):** Schematic representation of QCD phase diagram [2].

enough. The flavor composition of the q'$\bar{\text{q}}$' pairs is derived by tunneling probabilities with a suppression of heavy quark production ($u : d : s : c \approx 1 : 1 : 0.3 : 10^{-11}$).

3.5 Quark-Gluon Plasma (QGP)

As described in Sec. 3.1, at normal baryon densities and energies quarks are bound in hadrons. The Quark-Gluon Plasma (QGP) is a state of matter in which quarks can be seen as quasi-free particles due to high energies and baryon densities. The confinement and chiral symmetry breaking are not present anymore in the QGP. Fig. 3.7b shows a schematic representation of the QCD phase diagram, dependent on the baryon chemical potential μ_B and temperature T. At very high baryon densities or μ_B, nucleons start to overlap with each other and cease to exist as individual particles [5]. In this case, gluons and quarks are able to exist quasi-free in the volume of the nucleus. On the other hand, at very high energies the pion density and number of impacts between them are enhanced that much due to nucleon-nucleon interactions, that quarks and gluons cannot be dedicated to a specific hadron [5]. In other words, quarks and gluons in a QGP are able to travel distances that exceed the size of hadrons [25].

Fig. 3.7a shows the development of the temperature in the universe after the Big Bang. The QGP was present until $\approx 10\,\mu$s after the Big Bang [2]. Current collider experiments like ALICE try to investigate this short-lived state. The critical temperature T_c for a phase transition to the QGP can be calculated by LQCD. The results of the calculations depend on the number of quark flavors, quark masses, the interaction potentials and the lattice spacing. It lies between 150 MeV and 200 MeV [26][27]. At low μ_B and high T, there is a crossover rather than a first-order transition. Therefore, the temperature is also indicated as pseudocritical temperature (T_{pc}) [3]. Fig. 3.8 shows an example of the energy density $\epsilon(T)$

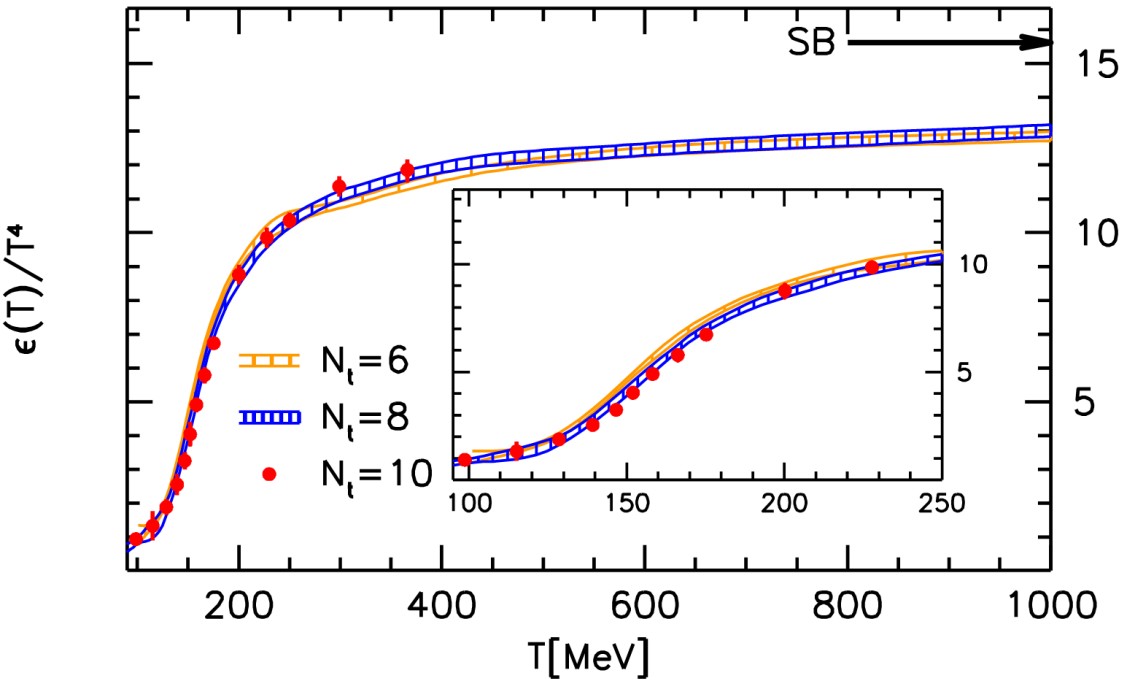

Figure 3.8: Energy density $\epsilon(T)$ normalized by T^4 for different amount of lattice points in temporal direction [28].

normalized by T^4 for different LQCD calculations. It can be seen, that the energy density rises significantly at $\approx 160\,\mathrm{MeV}$. This can be explained by an increase of the degrees of freedom due to the deconfinement transition of the quarks and gluons. The initial energy density ϵ_{Bj} in a collision can be estimated by the Bjorken Formula [29][30]:

$$\epsilon_{Bj}(t) = \frac{1}{A_T}\frac{1}{t}\frac{dE_T}{dy} \tag{3.52}$$

A_T is the transverse overlap region of two colliding nuclei at the formation time t_0 early after the collision and $\frac{dE_T}{dy}$ is the rapidity density of the transverse energy $E_T = \sqrt{p_\mathrm{T}^2 + m^2}$ at mid-rapidity. The critical energy density ϵ_c for the phase transition of the QGP is $0.7 \pm 0.2\,\mathrm{GeV/fm^3}$ [31], while the energy density for the $0\% - 5\%$ most central collisions in $\sqrt{s} = 2.76$ TeV has been estimated to be at least $12.3 \pm 1.0\,\mathrm{GeV/fm^3}$ [32]. Hence, the energy densities created during Pb–Pb are sufficient to create the QGP. Fig. 3.9 shows the evolution of heavy-ion collisions at LHC energies. The Lorentz-contracted heavy-ions are displaced before the collision, represented by the impact parameter b, which describes the distance between the centers of the nuclei. This distance defines the geometrical overlap in the collision and is therefore connected to the number of nucleons, which participate in an inelastic interaction N_part. In addition to that, it is connected to the total number of inelastic nucleon-nucleon collisions N_coll. All nucleons that do not participate in the collision

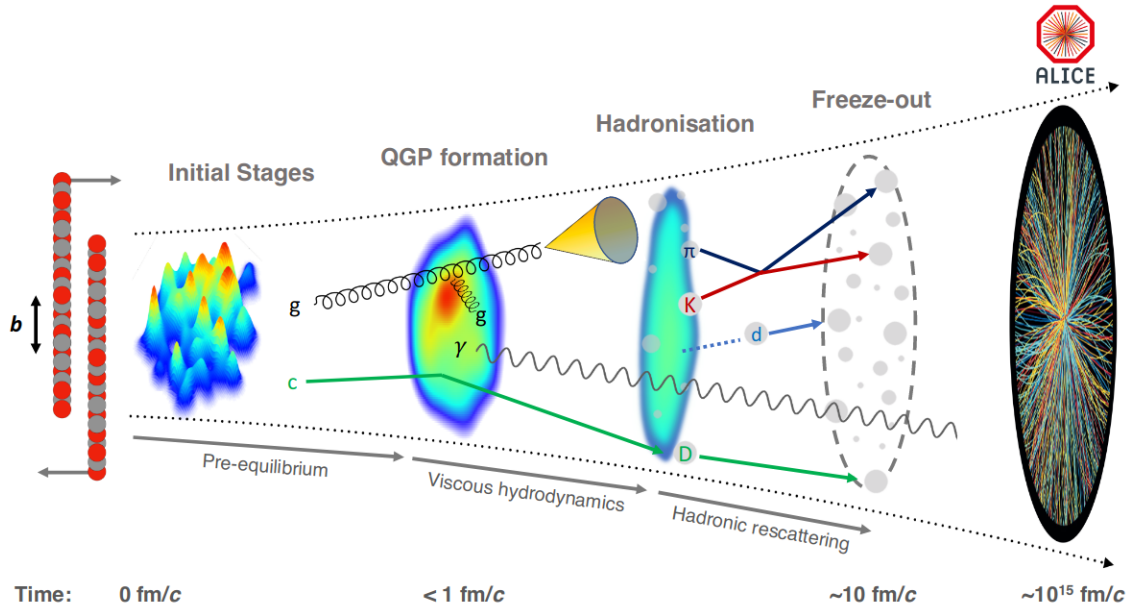

Figure 3.9: Schematic evolution of heavy-ion collisions at the LHC [3].

are called spectators. This leads to the definition of the centrality c_{cent} [33]. If the impact parameter b is zero, the collision is head-on and called central with $c_{\text{cent}} = 0\,\%$. If b is very large, the collision is called peripheral and the centrality is approaching $c_{\text{cent}} = 100\,\%$. As b is directly connected to N_{part}, the amount of produced particles gives a handle how central a collision was. The QGP occurs at a time of the order of $\approx 1\,\text{fm}/c$. Most strongly interacting particles inside the QGP have a free path length much smaller than the formed size of the QGP and interact multiple times, driving the expansion [3]. The active volume is expanding rapidly and cools down. As soon as the temperature is cooled below the critical temperature T_c, hadronisation starts. While further cooling down, the energy density may still be large enough to change the chemical composition of produced particles by inelastic interactions until the chemical freeze-out temperature T_{chem} is reached. While the produced particle composition is fixed, elastic interactions can continue until the temperature of the active volume is below the kinetic freeze-out temperature T_{kin} at a time of $10\,\text{fm}/c$ after the initial collision [3].

Even though the QGP is expected to be created at Pb–Pb collisions, baseline measurements are needed to properly interpret the influence of the QGP on particle production. Proton-proton (pp) and proton-Lead (p–Pb) collisions can serve as those baseline measurements. Neither of these two systems are expected to produce the QGP. pp collisions can be used to probe the QCD vacuum, while p–Pb collisions give valuable information about cold nuclear matter. As particles traversing the QGP interact with it and lose energy via elastic scatterings and gluon radiation, the ratio of measured particle yields in heavy-ion (AA) collisions (like

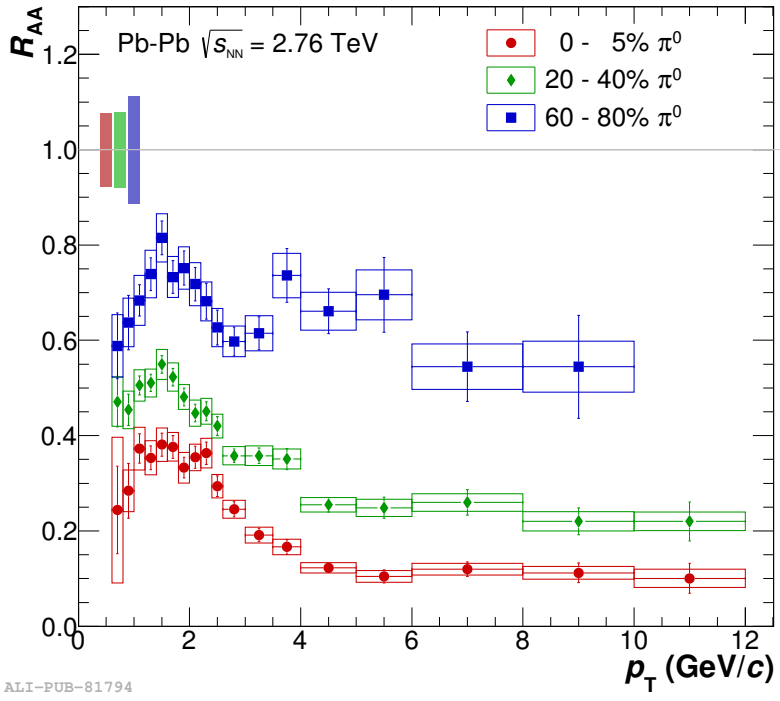

Figure 3.10: R_{AA} of π^0-meson production in Pb–Pb collisions at $\sqrt{s} = 2.76$ TeV for different centrality classes [34].

Pb–Pb) and pp collisions is an important observable to understand the properties of the QGP. This ratio is called R_{AA} and has to be normalized by the average overlap function $\langle T_{AA} \rangle$. $\langle T_{AA} \rangle$ is defined as ratio of the average number of N_{coll} and the inelastic cross section of the nucleon-nucleon collision and centrality of interest. The R_{AA} is given by [3]:

$$R_{AA}(p_T) = \frac{1}{\langle T_{AA} \rangle} \frac{dN_{AA}/dp_T}{d\sigma_{pp}/dp_T} \tag{3.53}$$

Analogously, the ratio of p–Pb collisions and pp collisions is defined by the R_{pA} Without the QGP or initial state nuclear effects, the R_{AA} is expected to be one. The R_{AA} is expected to be below 1 for high p_T inclusive hadrons, due to the energy loss of partons, also known as jet quenching. As total particle multiplicities do not increase with the number of collisions N_{coll}, but with the number of participants N_{part}, the R_{AA} is expected to be suppressed at low p_T and to approach unity with increasing p_T, if no other nuclear effects apply. Fig. 3.10 shows the R_{AA} of π^0-meson production in Pb–Pb collisions at $\sqrt{s} = 2.76$ TeV for different centrality classes. A suppression occurs for all centrality classes. However, the suppression becomes stronger for more central collisions.

Another important probe to investigate the properties of the QGP are direct photons. Direct photons are defined as photons, not originating from decays. [35] They are produced during different stages of the collision and do not interact strongly. Hence, they are able to escape

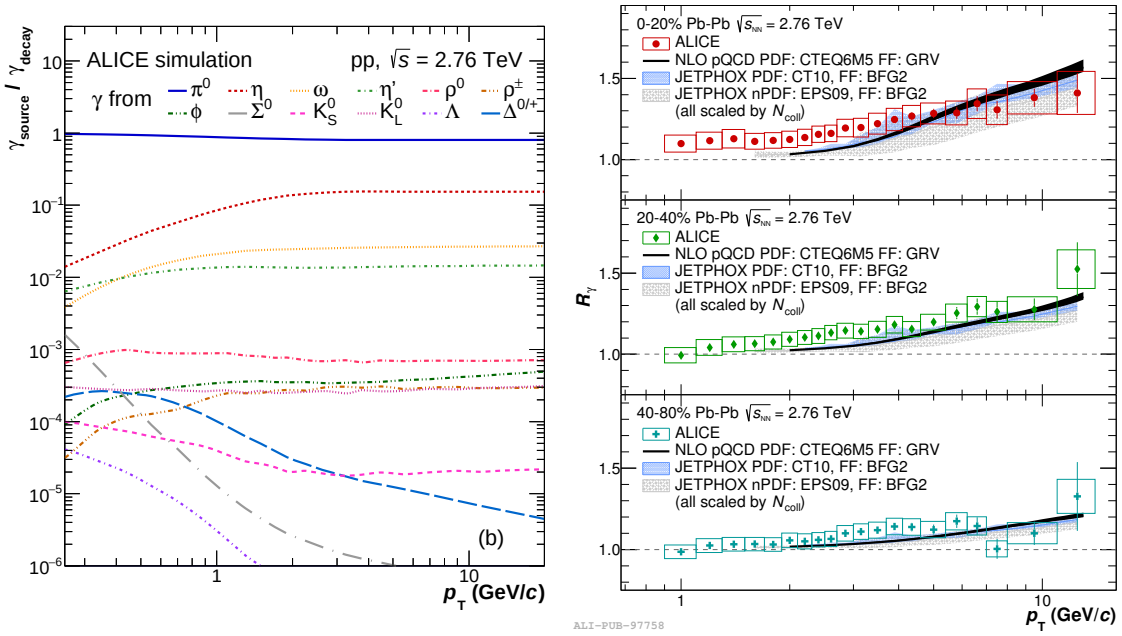

Figure 3.11: **Left:** Fraction of primary decay photons from different particle sources to the total amount of primary decay photons. [37]. The shown functions have been simulated for pp collisions at $\sqrt{s} = 2.76$ TeV. The three largest contributions are the π^0, the η and the ω meson. **Right:** Double ratio R_γ measured for different centrality classes in Pb–Pb collisions at $\sqrt{s} = 2.76$ TeV compared to different pQCD calculations [35].

the QGP nearly unaffected. Direct photons can be separated into two categories: Prompt photons and thermal photons. Thermal photons are emitted by the hot plasma and give important information of the temperature of the QGP. Prompt photons are produced in initial hard parton scatterings, containing information on the nuclear effect on the parton distributions [36]. At low p_T ($p_\mathrm{T} \lesssim 4\,\mathrm{GeV}$) thermal photons dominate the amount of direct photons, while at high p_T values ($p_\mathrm{T} \gtrsim 5\,\mathrm{GeV}$) prompt photons dominate [3]. While the p_T dependent spectrum of thermal photons can be described by an exponential, prompt photons follow a powerlaw shape. To measure the number of direct photons γ_direct, the number of decay photons γ_decay has to be subtracted from the number of inclusive photons $\gamma_\mathrm{inclusive}$.

$$\gamma_\mathrm{direct} = \gamma_\mathrm{inclusive} - \gamma_\mathrm{decay} = (1 - \frac{1}{R_\gamma})\gamma_\mathrm{inclusive} \tag{3.54}$$

R_γ is the direct photon excess, also known as double ratio. To calculate R_γ, precise knowledge of the number of decay photons is needed. The number of primary decay photons from different decay sources, normalized by the total number of decay photons, can be seen in Fig. 3.11 (left). The three largest contribution of decay photons to the total amount of decay photons are the π^0, the η and the ω meson. Hence, precise measurements of their production cross sections are important to properly extract the amount of direct photons. As

the number of decay photons originating from π^0 mesons is about an order of magnitude larger than the number of decay photons from other mesons, a precise measurement of production cross section of this meson is crucial. As a double ratio value above one corresponds to a measurement of direct photons, it can be seen in Fig. 3.11 (right) that it is possible to measure direct photons over the whole shown p_{T} range.

4 Experimental Setup

This chapter will give an introduction to the Large Hadron Collider (LHC) [38], located a the European Organization for Nuclear Research (CERN). CERN is a very important research facility in the field of high-energy physics and was founded in the year 1954 by the Conseil Européen pour la Recherche Nucléaire, where its acronym is derived from. While CERN started with 12 countries involved in its founding, the number of member states increased to 23 until this day. The introduction of the Large Hadron Collider (LHC) will be followed by an overview of the A Large Collider Experiment (ALICE) [39] and its sub-detectors.

4.1 Large Hadron Collider (LHC)

The LHC is located at (CERN) across the border of Switzerland and France in Geneva. It is a 26.7 km long synchrotron accelerator, build in the existing tunnel of the Large Electron-Positron (LEP) collider, lying between 45 m and 170 m under the surface. The LHC is a particle-particle collider and has two separate rings with counter rotating beams, realized by a "two-in-one" super-conducting magnet design. Cooling the superconducting magnets down to a temperature of 1.9 K with the help of superfluid helium, magnetic fields of 8.33 T can be generated. The accelerator was build to enable proton-proton collisions with an energy of up to 7 TeV per beam or $\sqrt{s} = 14$ TeV in total, while the machine is also able to accelerate heavy-ions like Pb. Up until this day energies per nucleon pair of $\sqrt{s} = 13$, 8, and 5 TeV have been reached for pp, p-Pb and Pb-Pb collisions respectively. Nuclei are not accelerated as separate particles, but instead they are accelerated as so-called bunches. For protons, each bunch consists of around 10^{11} nuclei with a maximum amount of 2808 bunches per beam. For Pb ions, a bunch can yield $7 \cdot 10^7$ nuclei while 592 bunches per beam are possible. Protons or heavy-ions have to be pre-accelerated via several stages before they are injected to the LHC. A scheme of the LHC accelerator complex can be found in Fig. 4.1. First protons, coming from a bottle of hydrogen gas, are stripped from their electrons. The stripped protons are then injected in the Linear Accelerator (LINAC2, accelerated to 50 MeV), followed by the Proton Synchrotron Booster (PSB or BOOSTER, accelerated to 1.4 GeV), the Proton Synchrotron(PS, accelerated to 25 GeV) and the Super Proton Synchrotron(SPS, accelerated

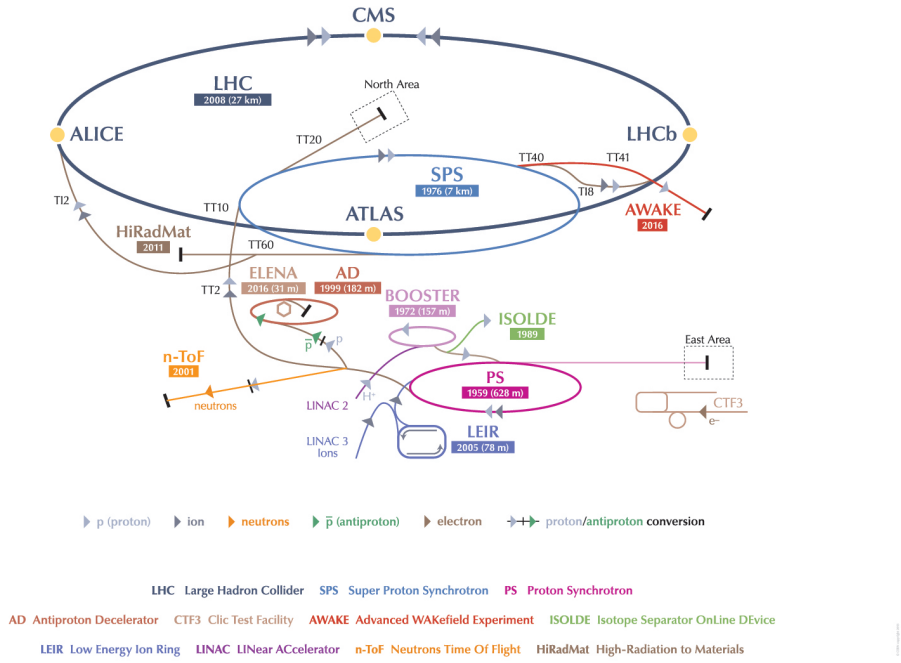

Figure 4.1: Scheme of the CERN accelerator complex [40]. The LHC is drawn with a dark blue line. Smaller accelerators are used to pre-accelerate ions before injecting them into the LHC. Four experiments are located at the interaction points (yellow dots): ALICE, CMS, ATLAS and LHCb.

to 450 GeV). After this acceleration chain, the protons with an energy of 450 GeV are injected to the LHC. As can be seen in Fig. 4.1, the LHC has four interaction points, marked by yellow dots. Each of these interaction points are covered by a large detector system: A Large Ion Collider Experiment (ALICE) [39], Compact Muon Solenoid (CMS) [41], A Toroidal LHC ApparatuS (ATLAS) [42] and LHC beauty experiment (LHCb) [43]. ATLAS and CMS are general purpose detectors. Both experiments were built to use high interaction rates in pp and heavy-ion (A–A) collisions. In the year 2012 the Higgs boson was discovered by these two experiments. Besides the goal of searching for the Higgs boson, ATLAS and CMS were designed to increase our understanding of physics beyond the Standard Model (SM). LHCb on the other hand was designed to study rare decays of b and c quarks and Charge Parity (CP) violation. It shall be noted that the interaction points of ATLAS, CMS and LHCb are shared by smaller experiments like TOTal Elastic and diffractive cross section Measurement (TOTEM), LHC forward (LHCf) or Monopole and Exotics Detector At the LHC (MoEDAL), which expand the capabilties of the LHC even further. This work analyzes data, recorded at ALICE, which will be introduced in the next section.

4.2 A Large Ion Collision Experiment (ALICE)

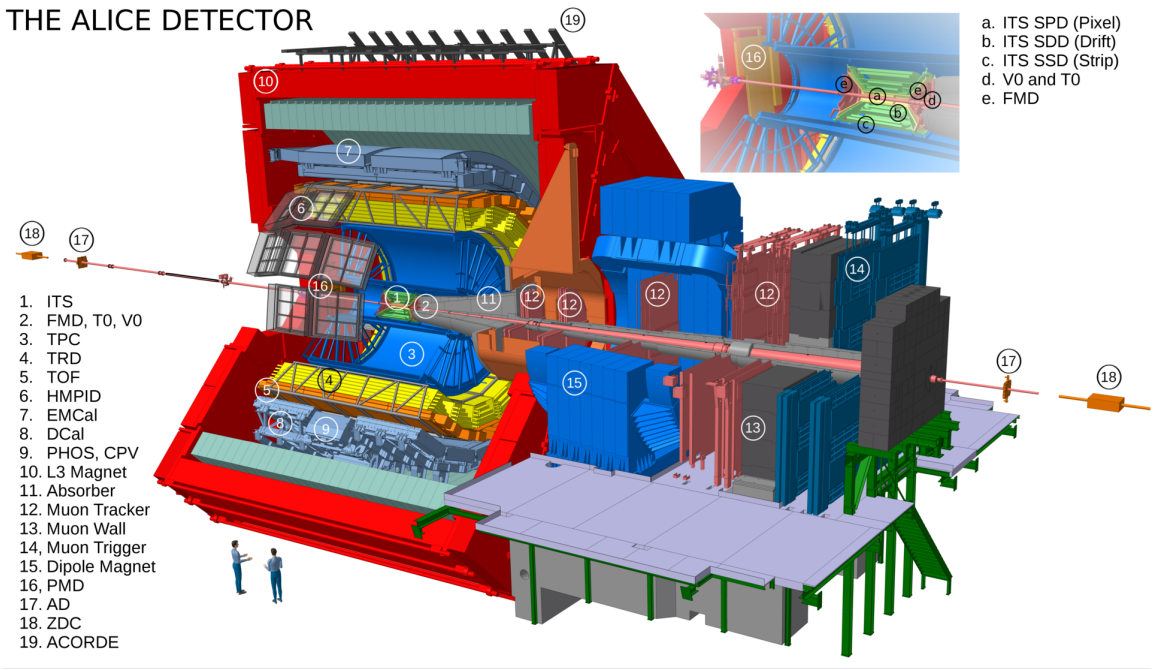

Figure 4.2: Detector configuration of ALICE in Run 2 [44].

A Large Ion Collision Experiment (ALICE) [39][45] is a general-purpose heavy-ion detector, located at the LHC near Geneva and is build to give a deeper understanding of QCD, which describes strong interactions of the SM. A 3D schematic of the ALICE detector can be found in Fig. 4.2. It focuses on the properties of the QGP, a state of strongly interacting matter expected to be formed in A–A (heavy-ion) collisions at extreme values of temperature and energy density. Besides A–A collisions, ALICE is taking data for pp or p–A (collision of proton with heavy-ion) collisions as well. While the energy densities reached in these systems are not sufficient to form the QGP, they are important to understand the underlying collision dynamics and distinguish them from properties of the QGP. Heavy-ion collisions produce a large amount of charged particles, which are challenging to track. The amount of charged particles N_{charged} per pseudorapidity interval η is given by $\mathrm{d}N_{\text{charged}}/\mathrm{d}\eta$. ALICE is designed to measure $\mathrm{d}N_{\text{charged}}/\mathrm{d}\eta$ at mid rapidity of $\mathrm{d}N_{\text{charged}}/\mathrm{d}\eta = 8000$ [39] . The amount of charged particles per pseudorapidity measured in $\sqrt{s} = 13$ TeV is shown in Fig. 4.3 [46]. Furthermore, ALICE is capable to measure in a large dynamic momentum range from tens of MeV/c to over 100 GeV/c, providing excellent Particle IDentification (PID) up to 20 GeV/c [39]. In addition to that, ALICE is able to reconstruct neutral particles that decay into photons, making use of three different calorimeters. While having the dimensions of $16 \cdot 16 \cdot 26\,\mathrm{m}^3$, the experiment has a weight of $\approx 10000\,\mathrm{t}$, which is in the same magnitude as the famous $\approx 300\,\mathrm{m}$ large “Tour Eiffel” in Paris. The detector system can be separated

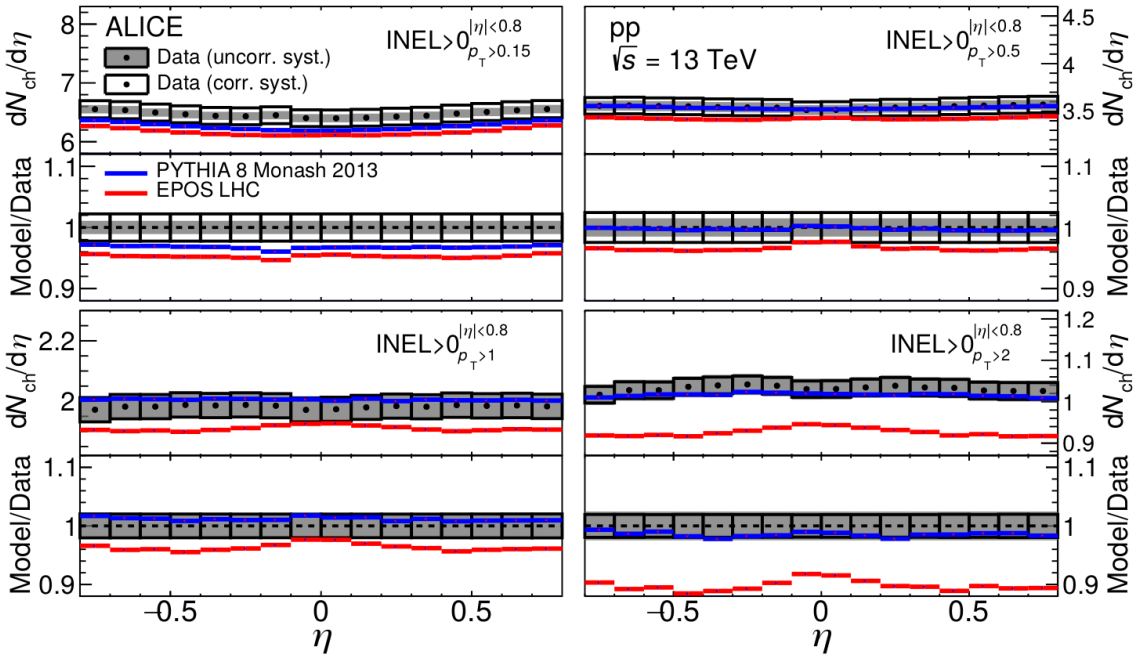

Figure 4.3: Amount of charged particles per pseudorapidity interval $\mathrm{d}N_{\mathrm{charged}}/\mathrm{d}\eta$ for different event classes in comparison to different MC simulations [46].

into the central barrel detectors, the forward detectors and the cosmic-ray trigger detector. ALICE and its sub-detectors use a global orthogonal Cartesian coordinate system. Here, the z-axis is parallel to the mean beam direction pointing in the direction opposite to the muon spectrometer and the x-axis is aligned with the local horizontal pointing to the LHC center, perpendicular to the z-axis. The y-axis is defined perpendicular to the x-axis and the z-axis, pointing upwards. These definitions of x-, y- and z-coordinates will also be used in this work. An overview of the different detector systems will be given in the following sections.

4.2.1 Central Barrel Detectors

As shown in Fig. 4.2, many detectors are located inside the red solenoid magnet. These detectors are called central barrel detectors. As the magnet is reused from the L3 experiment at the LEP, it is called L3 solenoid magnet. It is able to produce a magnetic field of 0.5 T in operation mode to bend the tracks of charged particles and allows to determine their momentum. A list of the central barrel detectors and their acceptance is given in Tab. 4.1.

Inner Tracking System (ITS)

The inner tracking system (ITS) [39][50][49] is the closest detector to the beam line and its layout is shown in Fig. 4.4. Its main purpose is the vertex reconstruction, the separation

Table 4.1: Acceptance of central barrel detectors. [39][45][47][48]

Detector	η in polar	φ in azimuth	Main Purpose
ITS Layer 1 (SPD)	$\|\eta\| < 2.0$	$0° < \varphi < 360°$	Tracking, Vertex
ITS Layer 2 (SPD)	$\|\eta\| < 1.4$	$0° < \varphi < 360°$	Tracking, Vertex
ITS Layer 3+4 (SDD)	$\|\eta\| < 0.9$	$0° < \varphi < 360°$	Tracking, PID
ITS Layer 5+6 (SSD)	$\|\eta\| < 1.0$	$0° < \varphi < 360°$	Tracking, PID
TPC	$\|\eta\| < 0.9$	$0° < \varphi < 360°$	Tracking, PID
TRD	$\|\eta\| < 0.8$	$0° < \varphi < 360°$	Tracking, $e^{\pm}$ id, PID
TOF	$\|\eta\| < 0.9$	$0° < \varphi < 360°$	PID
PHOS	$\|\eta\| < 0.12$	$\Delta\varphi = 70°$	Photons
EMCal	$\|\eta\| < 0.7$	$80° < \varphi < 187°$	Photons and Jets
DCal (6 modules)	$\|\eta\| < 0.7$	$260° < \varphi < 320°$	Photons and Jets
(2 modules)	$0.22 < \|\eta\| < 0.7$	$320° < \varphi < 327°$	
HMPID	$\|\eta\| < 0.6$	$1° < \varphi < 59°$	PID
ACORDE	$\|\eta\| < 1.3$	$30° < \varphi < 150°$	Cosmics

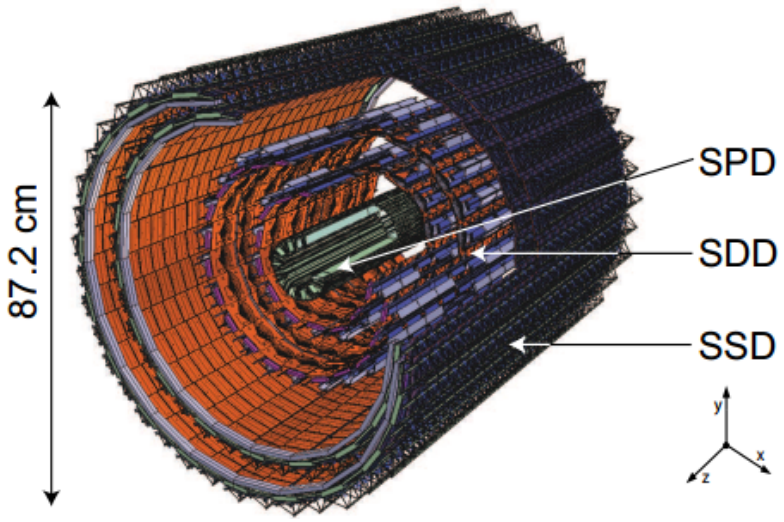

Figure 4.4: Layout of ITS [49]. It can be separated in the several detectors SSD, SDD and SPD with two layers each.

of primary and secondary vertices, the tracking of charged particles, as well as their identification for momenta below 100 MeV/c [50], as these particles cannot be tracked by the TPC. Furthermore, the ITS improves the momentum and angle resolution of the particles reconstructed by the TPC. The ITS is made of 6 individual layers of cylindrical silicon detectors and covers the full azimuthal range with a pseudorapidity of $|\eta| < 0.9$. The ITS can be split into three different detector systems. Starting from the center, the first two layers are Silicon Pixel Detectors (SPD), followed by two layers of Silicon Drift Detectors (SDD) and two layers of Silicon Strip Detectors SSD. The SPD is the fundamental detector for the

vertex reconstruction. As it is operating closest to the interaction point, the track density is the highest for this detector. Therefore, its sensor matrix has the best granularity of $256 \cdot 160$ cells with a size of $50\,\mu$m in $r\varphi$ and $50\,\mu$m in z [39]. The particle identification is using the specific energy loss dE/dx of charged particles. Here, the four layers of SPD and the SSD are used to provide signal amplitude information, while the two or three lowest amplitude signals are used to calculate a truncated mean.

Time Projection Chamber (TPC)

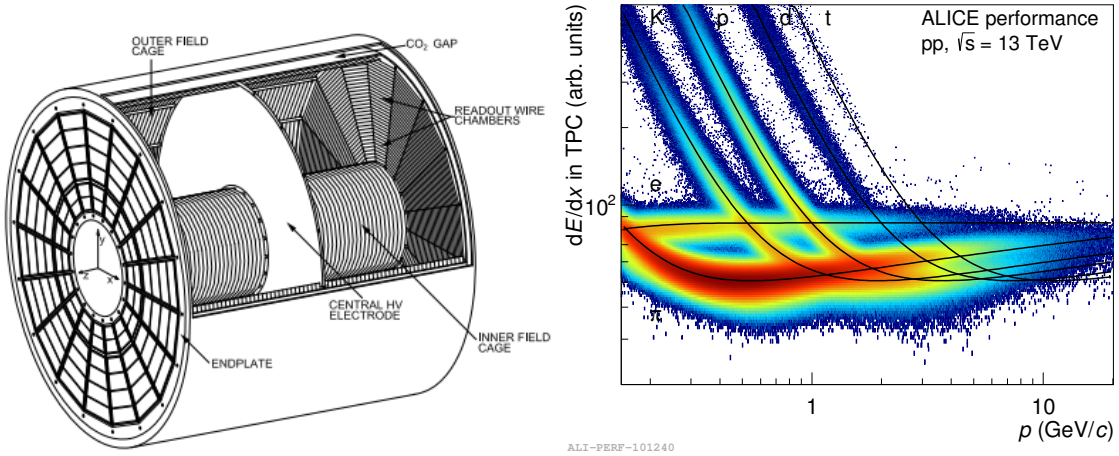

Figure 4.5: **Left:** Schematic view of the TPC [51]. **Right:** Specific energy loss dE/dx measured with the TPC for different particles [44].

The Time Projection Chamber (TPC) [51] is the main tracking detector of ALICE. Fig. 4.5 shows the schematic layout of the TPC. It covers the full azimuthal range with a pseudorapidity of $|\eta| < 0.9$. For tracks with reduced length, a pseudorapidity of $|\eta| < 1.5$ is possible [39]. The TPC is able to cover momenta from $0.1\,\mathrm{GeV}/c$ to $100\,\mathrm{GeV}/c$ [39], while it has good PID capabilties via specific energy loss ($\mathrm{d}E/\mathrm{d}x$) measurements. The TPC was designed to handle the charged particle multiplicities up to $dN_{\mathrm{charged}}/d\eta = 8000$. This results in approximately 20000 primary and secondary tracks in the TPC [39]. The detector is of cylindrical shape, while the active volume has an inner radius of $\approx 80\,\mathrm{cm}$ and an outer radius of $\approx 250\,\mathrm{cm}$. The central axis of the TPC cylinder is positioned along the beam direction with a length of $\approx 500\,\mathrm{cm}$. The active volume is separated along its center, perpendicular to the beam direction, by a $22\,\mu$m thick aluminized mylar foil, called central high voltage electrode. The endplates are separated in 18 trapezoidal sectors, including individual MultiWire Proportional Chambers (MWPC) with cathode pad readout. A voltage of $100\,\mathrm{kV}$ is applied between the endplates and the central high voltage electrode. Charged particles traversing the active volume create ionized gas molecules along their path. Due to the electric field,

these electrons drift towards the endplates and are detected by the MWPC. While the pads of the MWPC give information of the x- and y-coordinates, as well as the deposited energy, the drift time is used to calculate the z-coordinate. This enables the TPC to measure three-dimensional tracks. The drift time of $\approx 90\,\mu$s is also the limiting factor for the luminosity in pp collisions. In addition to that, being inside the L3 magnet allows the detector to measure the momentum of charged particles.

Transition Radiation Detector (TRD)

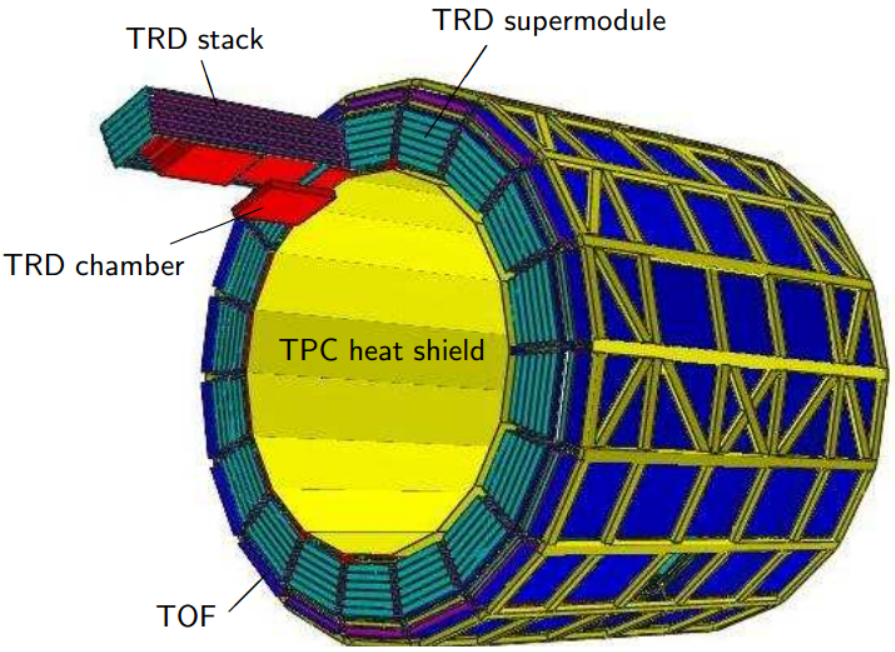

Figure 4.6: Schematic view of the TRD [39]. The cylindrical detector surrounds the TPC and can be separated in the several super modules. Each super module is made of several stacks.

The Transition Radiation Detector (TRD) [39][52] is a cylindrical detector with an inner radius of 2.9 m and an outer radius of 3.68 m. The central axis of the TRD cylinder is positioned along the beam direction with a length of ≈ 700 cm, surrounding the TPC. The TRD consists of 540 individual detector modules, arranged in 18 super modules. Each super module is arranged in 5 stacks along the z-axis and 6 layers in radial direction. The modules are drift chambers consisting of 48 mm thick radiators followed by 30 mm thick drift sections and MWPCs with pad readout. While the TPC already provides good PID information, the specific energy loss of electrons is similar to other charged particles for high momenta, as can be seen in Fig. 4.5 (right). The main purpose of the TRD is to resolve this issue and identify electrons for momenta above 1 GeV/c. In average, charged particles traversing the

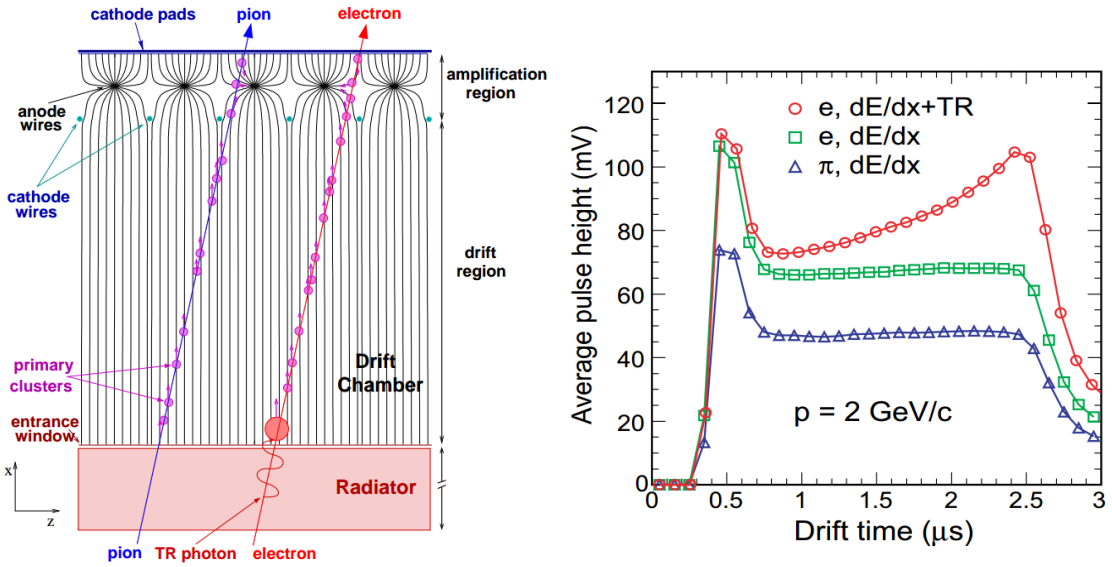

Figure 4.7: **Left:** Schematic cross-sectional view of a TRD detector module [39]. **Right:** Average pulse height as a function of drift time for electrons and pions [39].

radiators with high velocities ($\gamma > 1000$) generate 1.45 X-ray photons in the energy range of 1 to 30 keV, called transition radiation (TR). Particles traversing the modules as well as the generated TR ionize gas molecules, while the resulting electrons drift towards the anode wires of the MWPCs and are detected. Fig. 4.7 (right) shows the average pulse height of electrons and pions with a momentum of 2 GeV/c as a function of the drift time. As can be seen, the produced TR of light electrons can be used to distinguish them from heavier particles like pions. A more detailed description of the particle identification with the help of the likelihood method will be discussed in Sec. 5.

Time of Flight Detector (TOF)

The Time of Flight Detector (TOF) [39] is designed for PID of pions and kaons below 2.5 GeV/c and protons up to 4 GeV/c. It consists of Multigap Resistive Plate Chambers (MRPCs), arranged in a cylindrical frame with an inner radus of 370 cm and an outer radius of 399 cm, as shown in Fig. 4.8. TOF covers a pseudo-rapidty of $|\eta| < 0.9$ over full azimuth. The detector has a modular structure while it can be separated in 18 sectors in φ and 5 segments in z direction. It is using the time of flight information of traversing particles for PID, which complements to the PID capabilties of the ITS and TPC.

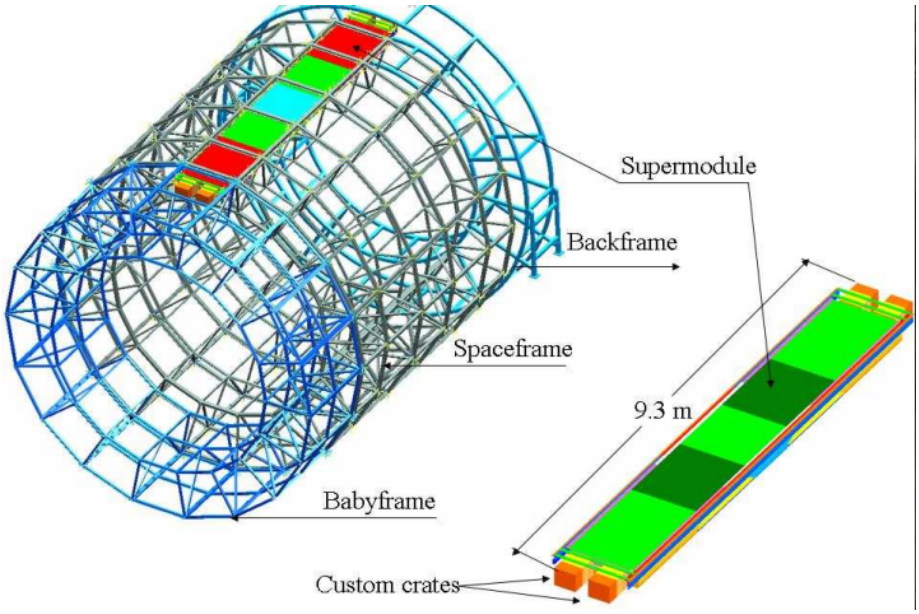

Figure 4.8: Schematic view of the ALICE spaceframe with one TOF supermodule [39].

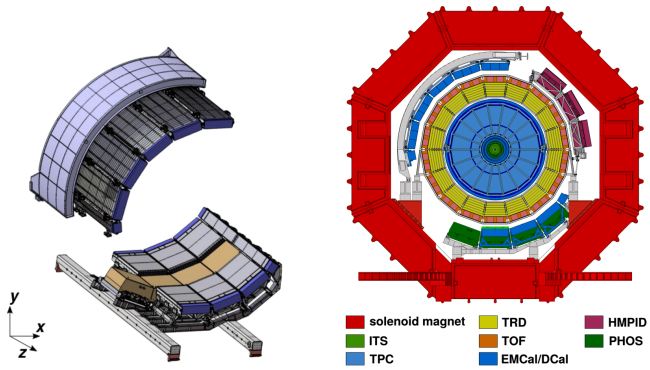

Figure 4.9: **Left:** Schematic view of EMCal and DCal in blue and grey with the PHOS in brown in between the DCal [48]. **Right:** Cross-sectional view of the ALICE central barrel detectors [48].

Photon Spectrometer (PHOS)

The PHOton Spectrometer (PHOS) [53][47] is an electromagnetic calorimeter with a coverage of $\Delta\varphi = 70°$ in azimuth and $|\eta| < 0.125$ in pseudorapidity, while it is positioned at a radial distance of 460 cm. The PHOS can be separated into 4 modules and can be seen in the ALICE cross-sectional view in Fig. 4.9. Three of these modules have 56 rows · 64 columns $\hat{=}$3584 detection elements, while the fourth module has 56 rows · 32 columns. Each detection element, also called cell, is made of a lead tungstate crystal ($PbWO_4$) with a size of $22 \cdot 22 \cdot 180\,mm^3$, whose signal is measured by an Avalanche Photo-Diode (APD) with a size of $5 \cdot 5\,mm^2$, processed by a low-noise preamplifier. Operating the crystals at a temperature

of -25° C amplifies the yield of light in the crystals and increases it by a factor of three compared to room temperature. The resolution of the calorimeter is given by [54]:

$$\frac{\sigma_E}{E} = \sqrt{\left(\frac{a}{\sqrt{E}}\right)^2 + \left(\frac{b}{E}\right)^2 + (c)^2} \tag{4.1}$$

Here, E is the energy of incident particles and σ_E is the resolution. $a/\sqrt{E}$ is called stochastic term and describes the statistical fluctuations in the energy deposition. b/E is called noise term and describes deviations that occur during to the energy reconstruction by electronic noise. c is the constant term, which includes all contributions, which are not dependent on the energy of the incident particle. The energy resolution extracted from test beam data for PHOS is given by[47]:

$$\frac{\sigma_E}{E} = \sqrt{\left(\frac{0.013\,\mathrm{GeV}}{\sqrt{E}}\right)^2 + \left(\frac{0.0358\,\mathrm{GeV}^{1/2}}{E}\right)^2 + (0.0112)^2} \tag{4.2}$$

MWPCs in front of the PHOS are used as a Charged Particle Veto (CPV). Compared to the EMCal and DCal the acceptance of the PHOS is low, but its granularity and therefore its resolution is significantly better. PHOS is generating trigger inputs to the L0 and L1 levels of the ALICE Central Trigger Processor (CTP), while only the L0 trigger is used in this analysis.

Electromagnetic Calorimeters (EMCal and DCal)

The Dijet Calorimeter (DCal) [55][48] can be considered as an acceptance extension of the ElectroMagnetic Calorimeter (EMCal) [39][56][48]. In this analysis, the EMCal and DCal will be treated as a combined detector. The combined detector is also commonly called EMC or simply EMCal after this section. It is utilizing the so-called Shashlik design, using 77 alternating layers of lead and plastic scintillators. Incident particles create showers in the lead absorber layers, which are then producing light in the scintillator layers. Wavelength shifting fibers guide the light to APDs, where the signal is measured. The EMC can be separated into three different sizes of supermodules (SMs): full-size, 2/3-size and 1/3-size. Full-sized SMs consist of $12 \cdot 24 = 288$ modules, while 2/3-sized SMs consist of $12 \cdot 16 = 192$ modules and 1/3-sized SMs consist of $4 \cdot 24 = 96$ modules. The EMCal uses 10 full-sized and 2 1/3-sized SMs resulting in a coverage of $80^\circ < \varphi < 187^\circ$ in azimuth and $|\eta| < 0.7$ in pseudorapidity. The DCal uses 6 2/3-sized and 2 1/3-sized SMs. The DCal can be split in two separate parts with the PHOS positioned in between those two parts. The

coverage of these parts is $260^\circ < \varphi < 320^\circ$ in azimuth with $0.22 < |\eta| < 0.7$ in pseudorapidity and $320^\circ < \varphi < 327^\circ$ in azimuth with $|\eta| < 0.7$. A schematic view of the EMC can be found in Fig. 4.9. Each module has a size of $12 \cdot 12 \cdot 24.6$ consisting of $2 \cdot 2$ optically isolated towers, also called cells, with a size of $6 \cdot 6 \cdot 24.6$ resulting in a spatial resolution of $\Delta\eta \cdot \Delta\varphi = 0.0143 \cdot 0.0143$. The energy resolution extracted from test beam data for EMC is given by [48]:

$$\frac{\sigma_E}{E} = \sqrt{\left(\frac{0.15\,\mathrm{GeV}}{\sqrt{E}}\right)^2 + \left(\frac{0.02\,\mathrm{GeV}^{1/2}}{E}\right)^2 + (0.01)^2} \tag{4.3}$$

Compared to PHOS, EMC has a lower granularity and lower resolution. The large EMC acceptance on the other hand, results in a considerable amount of increased number of measured photons in comparison. For the measurement of highly energetic particles, EMC provides L0 and L1 trigger decisions. As already mentioned, the combination EMC of EMCal and DCal is always meant when the EMCal acronym is used in the following chapters.

High-Momentum Particle Identification Detector (HMPID)

The High-Momentum Particle Identification Detector (HMPID) is build to identify hadrons at $p_\mathrm{T} > 1\,\mathrm{GeV}/c$, especially for the discrimination of π/K and K/p up to $3\,\mathrm{GeV}/c$ and $5\,\mathrm{GeV}/c$ on a track-by-track basis [39]. The detector is based on proximity-focusing Ring Imaging Cherenkov (RICH) counters and covers a pseudo-rapidty of $|\eta| < 0.9$, while it has an azimuthal coverage of $1.2^\circ < \varphi < 58.8^\circ$. Its total active detector area is $10.7\,\mathrm{m}^2$ separated into seven modules with a size of $1.5 \cdot 1.5\,\mathrm{m}^2$.

ALICE COsmic Ray DEtector (ACORDE)

The ALICE COsmic Ray DEtector (ACORDE) is an array of plastic scintillator counters, located on top of the L3 magnet [39]. It is able to provide a fast trigger signal to measure cosmic multi-muon events with help of the TPC, TOF and TRD. Furthermore, single muon trajectories can be used to calibrate the ALICE tracking detectors. The typical rate of muons reaching the ALICE detector is $4.5\,\mathrm{Hz}/\mathrm{m}^2$. ACORDE covers a pseudorapidty of $|\eta| < 1.3$ and $\varphi < 60^\circ$ in azimuth.

Table 4.2: Acceptance of forward detectors and muon spectrometer [39][45].

Detector	η in polar	φ in azimuth	Main Purpose
V0			
V0A	$2.8 < \eta < 5.1$	$0° < \varphi < 360°$	Charged Particles
V0C	$-3.7 < \eta < -1.7$	$0° < \varphi < 360°$	Charged Particles
T0			
T0A	$4.6 < \eta < 4.9$	$0° < \varphi < 360°$	Time, Vertex
T0C	$-3.3 < \eta < -3.0$	$0° < \varphi < 360°$	Time, Vertex
PMD	$2.3 < \eta < 3.9$	$0° < \varphi < 360°$	Photons
FMD			
FMD1	$3.6 < \eta < 5.0$	$0° < \varphi < 360°$	Charged Particles
FMD2	$1.7 < \eta < 3.7$	$0° < \varphi < 360°$	Charged Particles
FMD3	$-3.4 < \eta < -1.7$	$0° < \varphi < 360°$	Charged Particles
ZDC			
ZN	$\lvert\eta\rvert < 8.8$	$0° < \varphi < 360°$	Forward Neutrons
ZP	$6.5 < \eta < 7.5$	$\varphi < 10°$	Forward Protons
ZEM	$4.8 < \eta < 5.7$	$\lvert 2\varphi\rvert < 32°$	Photons
Muon Spectrometer			
MCH	$-4.0 < \eta < -2.5$	$0° < \varphi < 360°$	Muon Tracking
MTR	$-4.0 < \eta < -2.5$	$0° < \varphi < 360°$	Muon Triggering

4.2.2 Forward Detectors and Muon Spectrometer

The forward detectors consist of five separate detectors: The V0, the T0, the Photon Multiplicity Detector (PMD), the Forward Multiplicity Detector (FMD) and the Zero Degree Calorimeter (ZDC) [39][45]. The acceptances of these detectors can be found in Tab. 4.2.

The V0 consists of two segments: The V0A and the V0C. Each of these segments is located at one side of the interaction point with a pseudorapidity region of $2.8 < \eta < 5.1$ for the V0A and $-3.7 < \eta < -1.7$ for the V0C. They are made out of arrays of 32 individual plastic scintillator counters, segmented into four detector rings, read out by photomultiplier tubes. The V0 is able to provide a Minimum Bias (MB) trigger for the central barrel detectors. For the MB trigger, it is possible to require a signal in at least one of the detector segments V0A and V0C (V0OR or INT1) or to require a coincidence between those segments (V0AND or INT7). Furthermore, the V0 is able to help on the determination of the centrality, due to the number of registered particles and participates in luminosity measurements.

Similar to the V0, the T0 detector consists of two segments: The T0A and the T0C. Each of these consists of 12 Cherenkov counters based on a fine-mesh photomultiplier tube coupled to a quartz radiator. The T0C is located in a pseudorapidity region of $-3.3 < \eta < -3.0$ at

a distance of 72.7 cm away from the nominal vertex, while for the T0A the pseudorapidity region is $4.6 < \eta < 4.9$ at a distance of 375 cm. The T0 gives the start time (T0) for the TOF detector, independent of the collision vertex. In addition to that, the T0 provides the vertex position, providing a L0 trigger if the vertex position is within given boundaries, discriminating against beam-gas interactions. As it generates the earliest trigger signal, these signals are generated online without offline corrections.

The PMD is build to measure the multiplicity and spatial distribution in the forward pseudorapidity region, while it is also able to provide estimations of the transverse electromagnetic energy and reaction plane. The detector uses a preshower method, sandwiching a converter between two planes of proportional gas counters.

The FMD is a silicon strip detector dedicated to the measurement of charged particle multiplicities and determination of the reaction plane. It can be separated into several detector rings, called FMD1, FMD2 and FMD3.

The ZDC is a quartz sampling calorimeter, which makes use of the Cherenkov radiation generated in a dense absorber. There exist two sets of ZDCs, located on either side of the interaction point with a distance of 116 m. They are completed by two additional Zero degree ElectroMagnetic calorimeters (ZEMs) with a distance of 7 m to the interaction point. The ZDC is designed to measure the centrality in a heavy-ion collision by determining the number of spectators and can be separated into two detectors: The Zero degree Neutron calorimeter (ZN), the Zero degree Proton calorimeter (ZP).

Muon spectrometer

The muon spectrometer is located in the forward direction, operating in the pseudorapidity region of $-4.0 < |\eta| < 1.3$ [39][45]. Its goal is to measure the complete spectrum of heavy-quark vector-meson resonances, that decay into $\mu^+\mu^-$. It consists of a passive front absorber, a high-granularity tracking system, a large dipole magnet, a passive muon-filter wall, planes of trigger chambers and an inner beam shield. The tracking system consists of five stations with two pad chambers each, called Muon Chambers (MCH), while the trigger system for single-muon and multi-muon triggering is called Muon TriggeR (MTR) At high luminosity runs, the muon spectrometer will take data with a limited number of ALICE detectors, whose readout can take high data rates (ZDC, SPD, PMD, T0, V0 and FMD).

Table 4.3: Selection of triggers important to this work. [45]

Trigger	Different Acronyms	Condition
MB		
MBand	V0AND INT7	Signals in V0A and V0C
EMCal		
EGA	EG1	EMCal L1, following EMCal L0
EGA2	EG2	like EGA, with a lower threshold
PHOS		
PHI7		PHOS energy deposit in coincidence with MBand

4.2.3 Triggering

The different detectors described in Sec. 4.2 are read-out after the trigger decision has been generated by the Central Trigger Processor (CTP) of ALICE. Different detectors can give trigger inputs, which are evaluated by the CTP every machine clock cycle ($\approx 25\,\text{ns}$). The trigger decision consists of three levels, which are generated at certain times after the collision [45]:

- Level 0 (L0) after $\approx 0.9\,\mu\text{s}$:
- Level 1 (L1) after $\approx 6.5\,\mu\text{s}$:
- Level 2 (L2) after $\approx 100\,\mu\text{s}$

The L0 uses information from detectors with fast read-out capabilities like V0 or T0. If an event is accepted by the L0, it is further evaluated by the L1. The latency between these trigger decisions is caused by the computation times of TRD and EMCal, as well as the propagation times from ZDC. After the L0 and L1 decisions have been sent to the detectors, their data is buffered in the front-end electronics. As mentioned in Sec. 4.2.1, the drift time of the TPC is $\approx 90\,\mu\text{s}$. Due to this, the L2 decision is taken after $\approx 100\,\mu\text{s}$. While the L2 decision triggers the sending of the event data to the Data Acquisition system (DAQ) and the High Level Trigger system (HLT), all events accepted by the L1 are also accepted by the L2. The HLT filters these events, while its main task is to build events and to compress the data. A list of triggers used in this work can be found in Tab. 4.3.

4.2.4 Software Framework and LEGO Trains

This work is making use of the analysis frameworks AliROOT [57] and AliPhysics [58], which are extensions of the ROOT [59] framework. ROOT is an object-oriented analysis framework based on C++ [60]. It is written for large scale data analysis and started in context of the NA49 [61] experiment at CERN, which generated 10 TB of raw data. The goal of ROOT is to provide a basic framework with a common set of features needed for data analysis of this scale. It offers a wide variety of tools like fitting, efficient data storage or visualization. While it is also possible to save plots in the desired format like pdf, ROOT has an own data format called root files, enabling the storage of multiple objects in a compressed format. AliROOT extents ROOT with classes and functions, needed for the data analysis in ALICE. This includes multiple available Monte Carlo (MC) event generators like PYTHIA or HIJING [62]. As a detailed description of the detector geometry is contained in the framework, particle transport tools like GEANT3 [63], GEANT4 [64] and FLUKA [65] can be used to propagate particles through the detector material including detector responses similar to data. The simulated events contain the complete information, that is available to real data. Furthermore, simulated events contain the complete true information of the generated particles. Hence, it is possible to compare reconstructed yields to the number of generated particles and therefore obtain reconstruction efficiencies and purity estimates. After processing the raw data of real data and MC, event information is saved to Event Summary Files (ESD). An even more compressed data format compared to ESD files are Analysis Object Data (AOD) files. They contain a minimum set of information relevant for an analysis, which reduces the necessary computing power for it. This work is using AOD files to safe computing resources. The amount of data, recorded by ALICE is in average 100 MB/s [66]. Even though AODs store a compressed version of the data, the total size of the recorded data is still very large. To handle this large amount of data, the LHC Computing Grid (LCG), which is linking computer centers all over the world, has been developed. The access of the LCG is realized with the Lightweight Environment for Grid Operations (LEGO) system, which has access to the latest code in AliPhysics. AliPhysics is the central analysis framework of ALICE. The code in AliPhysics, that has been used in this work to run over events, select particles with properties of interest and store their relevant information to histograms or trees into root files, can be found in the folder “PWGGA/GammaConv”. With help of these root files, the contained histograms and trees are further processed offline. The corresponding software that extracts raw yields, calculates correction factors and corrected yields or combines different measurements can be found at [67].

4.2.5 Tracking and Vertex Reconstruction in ALICE

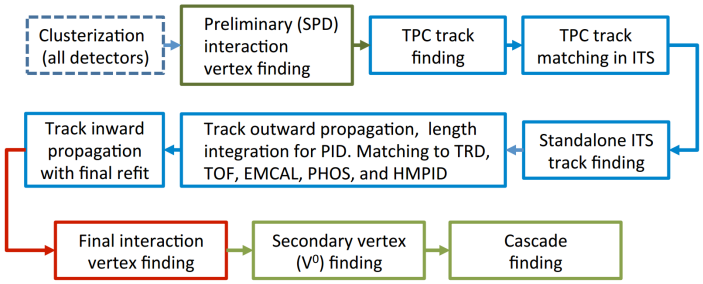

Figure 4.10: Event reconstruction flow in ALICE [45].

In this section, the tracking and vertex reconstruction procedure [39][45] in the central barrel system of ALICE will be discussed. A scheme of the reconstruction procedure can be found in Fig. 4.10. After clusterization of hit signals in the detectors, it starts with the determination of a preliminary primary vertex, using the two innermost layers of the ITS, the SPD. Here, pairs of reconstructed points in the two layers, close in azimuth in the transverse plane, are selected and their z-coordinates are used to estimate the z-position of the primary vertex. It is the space point to which the tracklets, defined by straight lines between the pairs of clusters, converge. The same procedure is performed in the traverse plane and the resulting estimate of the primary vertex is used to correct the z-coordinate. The bending of tracks due to the magnetic field is neglected at this point, as the distances are short. The resolution on the primary vertex is dependent on the track multiplicity and is one order of magnitude larger in pp collisions ($\approx 150\,\mu$m) compared to heavy-ion collisions ($\approx 10\,\mu$m). The preliminary primary-vertex position can be used as seed for the tracking procedure. This is performed in three steps, based on an inward-outward scheme, which starts with the TPC on its own. It uses a Kalman filter for track finding and fitting, whose result is highly dependent on the initial seed values for the track parameters and their covariance matrix. These seeds are generated by using the space points reconstructed in the TPC, calculated from the center of gravity of 2D clusters (pad-row and time), while for high particle densities a more sophisticated cluster unfolding is performed. Two different sets of seeds are calculated. For one set it is assumed, that the track originated from the primary vertex, while for the second set it is assumed that the track originated from elsewhere. Starting from the most outer pad rows and using the primary vertex as a constraint for the first pass, the seeds are propagated inwards, updated with the nearest cluster, if they fulfill a proximity cut, until the inner wall of the TPC is reached. After this, the seeding is repeated without the primary vertex constraint. This procedure is repeated for different seeds, while it is possible to reconstruct the same physical track multiple times. Hence, if two tracks are exceeding a certain limit of common clusters, between 25 % and 50 %, one of them is rejected. Only tracks that have

50 % of the expected track clusters with minimum number of 20 clusters are accepted. Furthermore, the specific energy loss is used to assign a most-probable-mass to the track, while the minimum mass that is being assigned is the pion mass. When the reconstructed track reaches the inner wall of the TPC, the track is propagated to the outer ITS layers, similar to the track reconstruction in the TPC. If during the propagation more than one space-time point is within the search window, a track for each point is followed to the innermost ITS layer. This can result in multiple track candidates for each TPC track, where only the best quality track is kept. After all TPC tracks have been propagated, remaining clusters are used for track reconstruction in a ITS only approach. When this reconstruction step is complete, the Point of Closest Approach (PCA) to the preliminary interaction vertex is extrapolated for all tracks and the tracks are propagated outwards with the previously found clusters. As soon as the TRD or the TOF is reached, the tracks are matched with the tracklets of the corresponding detector and propagated further to match signals of PHOS, EMCal and HMPID. For the update of the track kinematics, only detectors within the outer radius of the TPC are used, while the information of other detectors is saved for PID. For the last track reconstruction step all tracks are propagated inwards with previously found clusters, starting from the outer wall of the TPC and the final primary vertex is determined. In this work, so-called hybrid tracks [68] are used for the measurement of charged pions as the SPD was partly switched off during many run periods. Besides good global tracks, disussed in this section, the hybrid track sample includes complementary tracks constrained to the primary vertex. Complementary tracks do not have SPD hits, but use an ITS fit.

Not all particles in ALICE are produced at the primary vertex. Some particles are produced due to decays or conversions and are called secondary particles, produced at a secondary vertex. Tracks of neutral particles that decay into two charged particles of opposite charge form a V-like shape and are therefore called V^0 candidates. After calculating the PCA of the V^0 candidate, it is required that the distance of the two tracks at the PCA is less than 1.5 cm. Furthermore, the PCA needs to be be closer to the primary vertex than the closest clusters of the two tracks and for a momentum greater than 1.5 GeV/c, $\cos\theta_{V^0}$ has to be greater than 0.9. Here, θ_{V^0} is the angle between the total momentum of the V^0 candidate and the straight line connecting the PCA and the primary vertex. Two different algorithms for finding V^0 candidates are available in ALICE: The on-the-fly and the offline V^0-finder. The on-the-fly V^0-finder is running during the global track reconstruction process and has access to raw cluster information for tracking. This improves the position and momentum resolution of the reconstructed tracks in comparison to the offline V^0-finder, which is running on stored ESD files. However, the offline V^0-finder can be rerun on analysis level, which enables adjustments to the selection criteria. This work is using the on-the-fly V^0-finder.

5 Service Task on Likelihood Method for Particle Identification with TRD

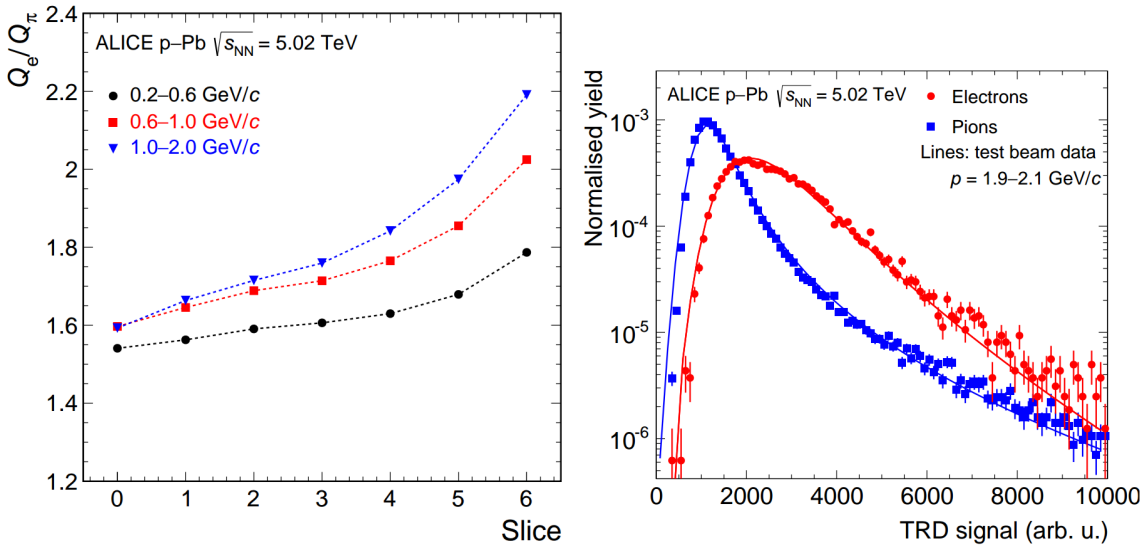

Figure 5.1: **Left:** Ratio of average signals of electrons to average signals of pions for the seven tracklet slices [52]. Lower slice numbers are farther away from the radiator, while the TR photons are absorbed predominatly close to the radiator. **Right:** Total integrated charge normalized to the tracklet length for electrons and pions [52].

As described in Sec. 4.2.1, the TRD is built to identify electrons for momenta above 1 GeV/c, where the specific energy loss of electrons is similar to other charged particles. For the electron identification (eID), the clusters along a tracklet are redistributed into $N_{\text{slices}} = 7$ slices during the track reconstruction. Each of these slices corresponds to a detector thickness of approximately 5 mm and enables a time evolution of the signal. The seven slices are numbered starting from zero and ending at six. Slices with higher numbers are closer to the radiator. Fig. 5.1 (left) shows the ratio of average signals of electrons to average signals of pions for the seven tracklet slices. TR photons are absorbed predominatly close to the radiator or at large slice numbers. The performance of the eID is described by two different oberservables: The electron efficiency and the pion efficiency. The electron efficiency is defined as the probability to correctly identify an electron. The pion efficiency on the other hand is defined as the fraction of pions which are identified as an electron. There are multiple methods to perform

PID like the truncated mean method, the likelihood method or neural networks [52]. This work will focus on the likelihood method [69][52] and only electrons and pions are considered, as pions are the main source of background in hadron collisions. Fig. 5.1 (right) shows an example of the total integrated charge distribution for electrons and pions in arbitrary units. After normalization, these distributions describe the conditional probability function $P(Q|k)$ to measure a total charge Q in the TRD for a particle species k. The likelihood $L(e|Q)$ that a particle with a given charge deposit is an electron is given by [69]

$$L(e|Q) = \frac{P(Q|e)}{P(Q|e) + P(Q|\pi)} \tag{5.1}$$

This equation is only considering a single charge measurement. As described in Sec. 4.2.1, the TRD consists of six layers in radial direction. Each of these layers i measures a separate total charge Q^i. These separate charge measurements can be combined into a charge vector $\vec{Q} = (Q^0, Q^1, ..., Q^5)$. If a set of multiple charge measurements is obtained, the combined likelihood can be calculated. This combined likelihood $L(e|\vec{Q})$ over all species k and layers i is given by [69]

$$L(e|\vec{Q}) = \frac{P(\vec{Q}|e)}{\sum_k P(\vec{Q}|k)} \tag{5.2}$$

Here, the combined probability $P(\vec{Q}|k)$ for a given particle species k is given by

$$P(\vec{Q}|k) = \prod_i P^i(Q^i|k) \tag{5.3}$$

If the TRD readout chambers are properly calibrated it can be assumed that $P^i = P$. Therefore, $P(\vec{Q}|k)$ can be written as:

$$P(\vec{Q}|k) = \prod_i P(Q^i|k) \tag{5.4}$$

The likelihood method can be performed in multiple dimensions. This means, that the charge signals q_s^i of the different slices s and layers i are combined in different ways. These different variations of the likelihood method are called LQ1D, LQ2D, LQ3D and LQ7D, where the number in the acronyms is the corresponding dimension number. The one-dimensional likelihood method is called LQ1D and combines the charge information of all slices and therefore uses the total integrated charge for each layer. The equations, which have been discussed until this point correspond to the LQ1D method. The two-dimensional likelihood method (LQ2D) evaluates the combined charge signal of the first four slices and the last three slices separately, while the LQ3D method evaluates the signals of the first three, the next two

and the last two slices and the LQ7D method evaluates the signals of all slices individually. The calculation of the resulting likelihood will be discussed on the example of the LQ2D method, while the calculation for LQ3D and LQ7D method is performed analogously. The charge information for each of the slice combinations j for layer i are given by Q_j^i. In case of the LQ2D method, the charge information of the two available slice combinations Q_0^i and Q_1^i are given by:

$$Q_0^i = \sum_{s=0}^{3} q_s^i \text{ and } Q_1^i = \sum_{s=3}^{N_{\text{slices}}} q_s^i \tag{5.5}$$

Analogously to Eq. 5.2, Eq. 5.3 and Eq. 5.4, the combined likelihood over all species k and layers i for the LQ2D method is given by

$$L(e|\vec{Q_0}, \vec{Q_1}) = \frac{P(\vec{Q_0}, \vec{Q_1}|e)}{\sum_k P(\vec{Q_0}, \vec{Q_1}|k)} \tag{5.6}$$

with the combined probability $P(\vec{Q_0}, \vec{Q_1}|k)$:

$$P(\vec{Q_0}, \vec{Q_1}|k) = \prod_i P(Q_0^i, Q_1^i|k) \tag{5.7}$$

and

$$P(Q_0^i, Q_1^i|k) = \prod_j P(Q_j^i|k) \overset{\text{LQ2D}}{=} P(Q_0^i|k) \cdot P(Q_1^i|k) \tag{5.8}$$

In practice, the charge distributions are fitted by a Gaussian function convoluted with a Landau function, called Langau function F_{Langau} in context of this work. The function has

Table 5.1: Parameters of the Langau distribution and their meaning.

Parameter	Meaning
$P_{0,\text{Langau}}(\beta\gamma)$	Width of Landau density
$P_{1,\text{Langau}}(\beta\gamma)$	Most probable value of Landau density
$P_{2,\text{Langau}}(\beta\gamma)$	Total area
$P_{3,\text{Langau}}(\beta\gamma)$	Width of Gaussian
$P_{4,\text{Langau}}(\beta\gamma)$	Exponential slope

five free parameters $P_{l,\text{Langau}}(\beta\gamma)$, whose meaning can be found in Tab. 5.1. During the Service Task, it has been investigated if a reduction of the number of free fit parameters of the Langau function is beneficial. It turned out that this caused worse results or even caused the fit to fail and was therefore not further propagated. After parametrizing the charge distributions for different particles, the resulting values of $P_{l,\text{Langau}}(\beta\gamma)$ are plotted

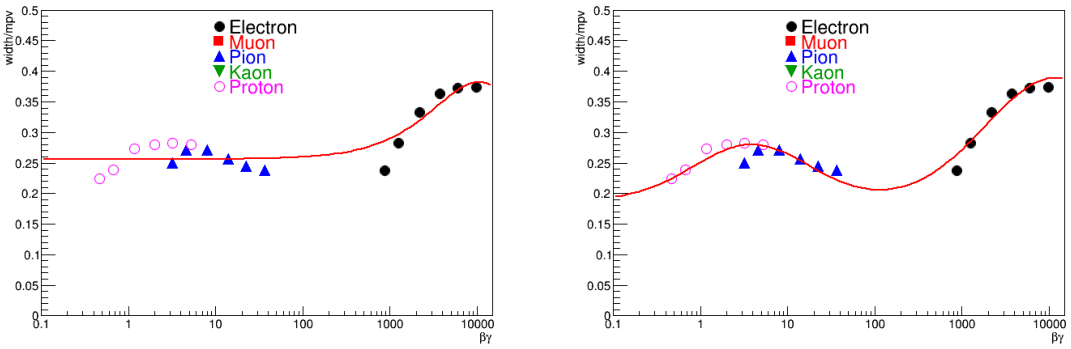

Figure 5.2: Parametrization of $P_{0,\text{Langau}}(\beta\gamma)$. **Left:** No changes applied to the parametrization. **Right:** Changes investigated during the Service Task are applied to the parametrization.

against $\beta\gamma$, parameterized and stored for the calculation of the likelihood. It was investigated, which influence the quality of the fit for the $P_{l,\text{Langau}}(\beta\gamma)$ parametrization has on the PID performance. As an example, the parametrization of $P_{0,\text{Langau}}(\beta\gamma)$ is shown with and without improvements in Fig. 5.2. While clear improvements to the parametrization could be realized, the total PID performance could not be enhanced. Hence, the changes to the parametrization are neglected.

Before this Service Task, the likelihood method treated particles and antiparticles as the same particles and generated a combined set of parameters for them. This work expanded the method to generate a set of separate parameters for particles and antiparticles in addition to the generation of combined parameters. The analyzer is able to select the generated parameters of choice with help of a track charge variable $V_{\text{Track Charge}}$. A value of $V_{\text{Track Charge}} = 0$ selects the generated parameters for combined particles and antiparticles, while a value of $V_{\text{Track Charge}} = 1$ selects the generated parameters for positively charged particles and a value of $V_{\text{Track Charge}} = 2$ selects the generated parameters for negatively charged particles. Fig. 5.3 shows the performance in dependence of momentum of the different generated parameters.

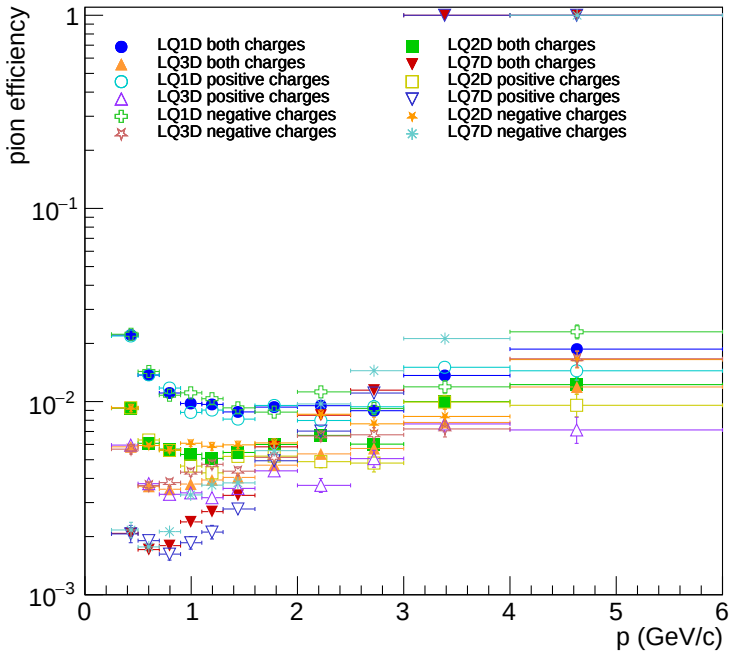

Figure 5.3: Pion efficiency in dependence of momentum for different particle charges. Only tracks, which consist of at least 6 tracklets are used.

6 Dataset and Event Selection

This work was performed using data from proton-proton (pp) collisions at $\sqrt{s} = 13$ TeV, that was recorded from 2016 to 2018 during Run 2 of LHC operation. The data of each year is furthermore split into separate periods, which can be split into subsets of runs. Each run corresponds to a time interval of continuous data taking without changes of the detector configurations or interruptions. The periods used in this work, as well as their corresponding Monte Carlo (MC) productions, can be found in Tab. 6.1. In this work, the data recorded in 2016 will be called LHC16, while the data recorded in 2017 will be called LHC17 and the data recorded in 2018 will be called LHC18. As it is possible, that certain detectors did not operate under stable conditions or were turned off completely during various runs, extensive quality assurance (QA) has been performed per run (runwise), per period (periodwise) and per year (yearwise). While assuring the quality of the data, the resulting list of good runs (runlists) differ for the different reconstruction systems. This work focussed on the quality assurance of the PHOS detector observables. As the PHOS runlist was intended to also be used for the PCM-PHOS method, QA for the PCM method was performed on the list of runs, that have been declared good for PHOS. The quality assurance in the EMCal system has been performed within the ALICE collaboration, explicitly by Joshua König[1]and Adrian Florin Mechler [1]. The runlists for the different systems differ slightly and the resulting number of events can be found in Tab. 6.5. A more detailed explanation of the most important observables will be given during this work. If not stated otherwise, all comparisons of global observables shown in this work are based on the PHOS runlist, while observables directly connected to a specific method use the corresponding runlist of this method.

The amount of runs used in this work is so large, that it is not possible to properly show different QA observables and distinguish between the separate runs. This is illustrated as an example in Fig. 6.1. It shows the fraction of events with the reconstructed primary vertex condition $|Z_{\mathrm{Vtx}}| > 10\,\mathrm{cm}$, while the details of this figure are discussed in Sec. 6.2. Due to the large amount of runs, QA observables will only be shown for the example period LHC18f. As the dataset consists of many runs, also a small percentage of crashed jobs in the LEGO train system can result in missing runs in the example plots. It shall also be mentioned,

[1]Institut für Kernphysik, Universität Frankfurt, Frankfurt, Germany

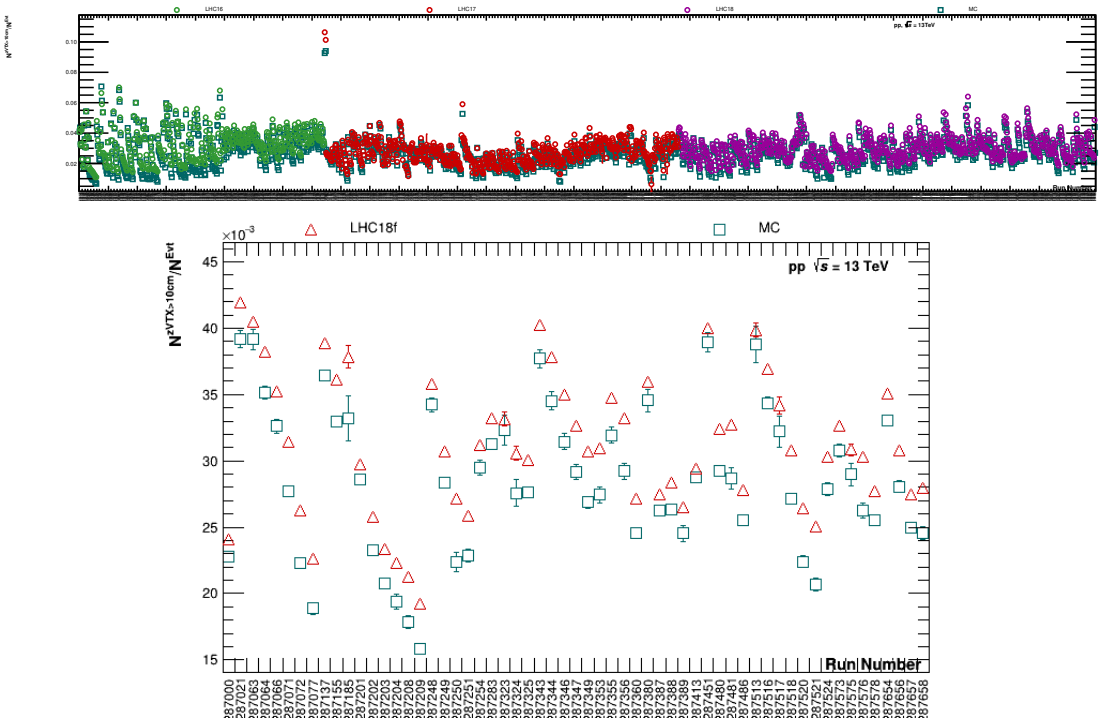

Figure 6.1: Fraction of rejected events, due to the reconstructed primary vertex condition $|Z_{\mathrm{Vtx}}| > 10\,\mathrm{cm}$ to the total number of collected events. **Top:** All available runs that have been checked during quality assurance in comparison to MC are shown. As it can be clearly seen, the number of runs is too large, to show them in one plot. Due to this reason only a fraction of runs will be shown for runwise comparisons. **Bottom:** The runs of the example period LHC18f and their anchored MC productions are shown. The trend between the different runs is reproduced by the MC simulation.

that due to the huge amount of available events, not the whole dataset was sampled in one iteration, but parts of the MC events have been produced in extra productions. The runwise QA was partly performed without these extra productions to safe resources on the LCG, only reducing the amount of events and increasing statistical fluctuations without changing other observables. All runlists used for the analysis can be found in Sec. A.5.

6.1 Monte Carlo (MC) Simulation Selection

As described in Sec. 3.4.1, the event generator used to correct the extracted raw yields of mesons for efficiency and acceptance is PYTHIA 8.2 with the Monash 2013 tune. The anchored MC productions for the MB dataset can be found in Tab. 6.1. They were produced with approximately the same number of events per period as in data, also called 100 % sampling. As the EG1, EG2 or PHI7 enhance the available number of photons for high p_{T}, it is essential to either generate a huge amount of MC events or to use adjusted MC productions.

Dataset (LHC16)	Anchored MC set	Dataset (LHC17)	Anchored MC set	Dataset (LHC18)	Anchored MC set
LHC16d (pass1)	LHC17f6	LHC17c (pass1)	LHC18d3	LHC18b (pass1)	LHC18g4
LHC16e (pass1)	LHC17f9	LHC17e (pass1)	LHC17h1	LHC18d (pass1)	LHC18g5
LHC16g (pass1)	LHC17d17	LHC17f (pass1)	LHC18d3	LHC18e (pass1)	LHC18g6
LHC16h (pass1)	LHC17f5	LHC17h (pass1)	LHC18c12b	LHC18f (pass1)	LHC18h2
LHC16i (pass1)	LHC17d3	LHC17i (pass1)	LHC17k4	LHC18g (pass1)	LHC18h4
LHC16j (pass1)	LHC17e5	LHC17j (pass1)	LHC17h11	LHC18h (pass1)	LHC18h4
LHC16k (pass2)	LHC18f1	LHC17k (pass1)	LHC18c13	LHC18i (pass1)	LHC18h4
LHC16l (pass2)	LHC18d8	LHC17l (pass1)	LHC18a8	LHC18j (pass1)	LHC18h4
LHC16o (pass1)	LHC17d16	LHC17m (pass1)	LHC17l5	LHC18k (pass1)	LHC18h4
LHC16p (pass1)	LHC17d18	LHC17o (pass1)	LHC18a9	LHC18l (pass1)	LHC18j1
		LHC17r (pass1)	LHC18a1	LHC18m (pass1)	LHC18j4
				LHC18n (pass1)	LHC18k1
				LHC18o (pass1)	LHC18k2
				LHC18p (pass1)	LHC18k3

Table 6.1: Datasets of the years 2016, 2017 and 2018 separated into the used periods. The datasets in MB are anchored to their corresponding MC sets.

Dataset	Anchored MC set	Number of p_{T} intervals	Number of events per p_{T} interval in millions	minimum photon energy E_{γ} in detector acceptance
Normal Jet Jet MC				
LHC16	LHC19a1	20	32.5	-
LHC17	LHC18f5	20	40	-
LHC18	LHC19d3	20	40	-
γ enhanced Jet Jet MC				
LHC16	LHC20b1b2	6	5.47	3.5 GeV in DCal or PHOS acceptance
LHC16	LHC20b1c2	8	5.47	7 GeV in DCal or PHOS acceptance
LHC17	LHC18l6b2	6	8	3.5 GeV in DCal or PHOS acceptance
LHC17	LHC18l6c2	8	8	7 GeV in DCal or PHOS acceptance
LHC18	LHC19i3b2	6	8	3.5 GeV in DCal or PHOS acceptance
LHC18	LHC19i3c2	8	8	7 GeV in DCal or PHOS acceptance

Table 6.2: Anchored MC of the years 2016, 2017 and 2018 for triggered datasets.

Hence, different productions were used for triggered data, which can be found in Tab. 6.2. These productions are called Jet-Jet (JJ) MC and generate events in separate $p_{\mathrm{T,hard}}$ intervals, while only events containing jets, that exceed 5 GeV in transversal energy are accepted. The initial conditions have to be generated multiple times (N_{trials}) to obtain the targeted number of events $N_{\mathrm{evt.\ gen.}}$ per $p_{\mathrm{T,hard}}$ interval. As particles are not added arbitrarily, compared to MB productions, Jet-Jet productions follow the same compositions and energy distributions as MB productions. However, the spectrum of Jet-Jet productions has to be weighted and

min $p_{\mathrm{T,hard}}$ (GeV/c)	max $p_{\mathrm{T,hard}}$ (GeV/c)	ω_{JJ}
5	7	43.8875
7	9	13.6334
9	12	6.81745
12	16	2.68138
16	21	0.981202
21	28	0.391851
23	36	0.127982
36	45	0.0467046
45	57	0.0206898
57	70	0.00752808
70	85	0.00319537
85	99	0.00122745
99	115	0.000644337
115	132	0.000322367
132	150	0.0001689
150	169	9.19213e-05
169	190	5.35627e-05
190	212	3.01741e-05
212	235	1.75063e-05
235	10000	2.80928e-05

Table 6.3: Weights of the normal Jet-Jet MC productions LHC19a1, LHC18f5 and LHC19d3.

can only be used at high p_{T}, as the minimum momentum transfer is 5 GeV/c. These weights ω_{JJ} are calculated by:

$$\omega_{\mathrm{JJ}} = \frac{\sigma_{\mathrm{evt.}}}{N_{\mathrm{trials}} N_{\mathrm{evt.\ gen.}}} \tag{6.1}$$

Here, $\sigma_{\mathrm{evt.}}$ is the average cross section for the generated events according to the simulation. As the amount of extracted ω mesons in the Jet-Jet MC productions LHC19a1, LHC18f5 and LHC19d3 is sufficient, these MC productions have been used for measurement of the ω meson. This is not the case for the π^0 and η meson measurement. Therefore, the γ enhanced Jet-Jet MC productions have been used for these measurements. For each produced event, these MC productions require one γ, which exceeds a certain energy threshold to point towards the detector. Two different energy thresholds have been used in these MC productions. In this work, the Jet-Jet MC productions without γ enhancement are called JJMC. Furthermore, the γ enhanced Jet-Jet MC productions with an energy threshold of 3.5 GeV are called lowJJMC and the γ enhanced Jet-Jet MC productions with an energy threshold of 7 GeV are called highJJMC. The weights for JJMC can be found in Tab. 6.3 and need to be applied in every event for each particle. The corresponding weights for lowJJMC and highJJMC are shown

min $p_{\mathrm{T,hard}}$ (GeV/c)	max $p_{\mathrm{T,hard}}$ (GeV/c)	ω_{JJ} for LHC20b1b2	ω_{JJ} for LHC18l6b2	ω_{JJ} for LHC19i3b2
5	7	0.0318163	0.0343221	0.0343118
7	9	0.0280099	0.0287842	0.0287709
9	12	0.0271878	0.0282014	0.028205
12	16	0.0208271	0.0207503	0.0207509
16	21	0.0130291	0.0132192	0.0132104
21	10000	0.0181411	0.0180455	0.0180347
min $p_{\mathrm{T,hard}}$ (GeV/c)	max $p_{\mathrm{T,hard}}$ (GeV/c)	ω_{JJ} for LHC20b1c2	ω_{JJ} for LHC18l6c2	ω_{JJ} for LHC19i3c2
8	10	0.000528778	0.000583836	0.000583836
10	14	0.00121486	0.00124525	0.00124525
14	19	0.00132257	0.00133701	0.00133701
19	26	0.00132752	0.00132045	0.00132045
26	35	0.00102868	0.0010136	0.0010136
35	48	0.000741674	0.000738478	0.000738478
48	66	0.000437791	0.00043112	0.00043112
66	10000	0.000350834	0.00035756	0.00035756

Table 6.4: Weights of the γ enhanced Jet-Jet MC productions LHC20b1b2, LHC18l6b2, LHC19i3b2, LHC20b1c2, LHC18l6c2 and LHC19i3c2.

in Tab. 6.4. To only select events with properties also found in real collisions, it is required that jets have momenta of $p_{\mathrm{T}} < 3.0 \cdot p_{\mathrm{T,hard}}$.

6.2 Event Selection

Different event selection criteria have to be fulfilled, so that events are considered in the analysis of this work. First, an offline event selection was applied. This is making use of available central barrel trigger decision information and applies a Physics Selection (PS). The PS rejects events, which are not of physics type. This includes for example calibration events or events assigned to contamination of noise or beam-gas interactions. In addition to the PS, the reconstructed primary vertex Z_{Vtx} of a selected event has to be within $|Z_{\mathrm{Vtx}}| < 10\,\mathrm{cm}$ with respect to the center of ALICE in z-direction. This selection ensures a good vertex resolution. Fig. 6.1 shows the fraction of events with the condition $|Z_{\mathrm{Vtx}}| > 10\,\mathrm{cm}$, where the trend of the different runs in data is well described by MC. The reconstruction of the primary vertex is required to contain at least one tracklet and can be calculated, using global tracks or only ITS tracks in case of low p_{T} tracks [70]. The number of normalized events $N_{\mathrm{evt,\,norm}}$,

used to normalize the measured spectra have to account for the discussed selection criteria and is given by:

$$N_{\text{evt, norm}} = N_{\text{Tr,}|Z_{\text{Vtx}}|<10\,\text{cm}} + \frac{N_{\text{Tr,}|Z_{\text{Vtx}}|<10\,\text{cm}}}{N_{\text{Tr,}|Z_{\text{Vtx}}|<10\,\text{cm}} + N_{\text{Tr,}|Z_{\text{Vtx}}|>10\,\text{cm}}} \cdot N_{\text{Tr, no vtx}} \tag{6.2}$$

Here, "Tr" is the chosen MB, EMCal or PHOS trigger, while $N_{\text{Tr, no vtx}}$ is the number of events without a primary vertex. $N_{\text{Tr,}|Z_{\text{Vtx}}|<10\,\text{cm}}$ and $N_{\text{Tr,}|Z_{\text{Vtx}}|>10\,\text{cm}}$ are the number of events with their primary vertex inside and outside $|Z_{\text{Vtx}}| = 10\,\text{cm}$. This normalization takes events without a reconstructed vertex into account by using the approximation, that the vertex position of these events is similar to events with a reconstructed vertex.

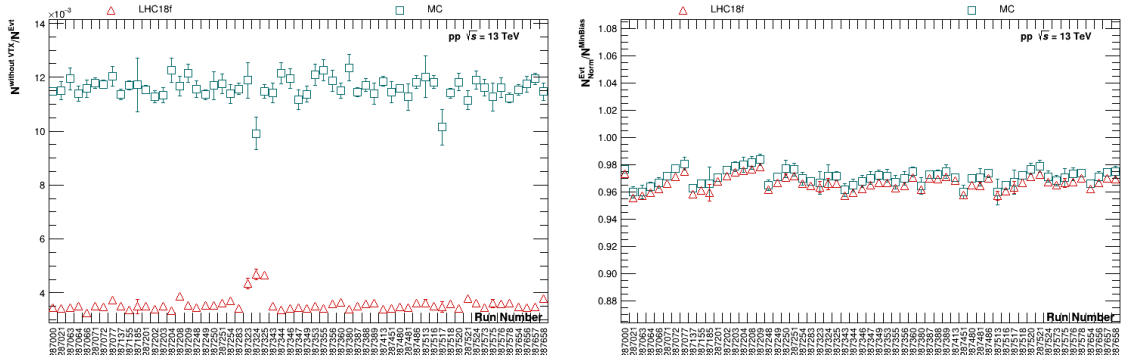

Figure 6.2: Runwise comparison of observables for LHC18f in comparison to the anchored MC. **Left:** Fraction of rejected events due to not having a reconstructed primary vertex to all collected events. **Right:** Fraction of normalized events $N_{\text{evt, norm}}$ to all MB events.

The fraction of normalized events $N_{\text{evt, norm}}$ to all events in MB are shown in Fig. 6.2 (right). Fig. 6.3 shows the distribution of the z-vertex position and number of good tracks for data in comparison to MC. It can be seen, that trends in data are followed by MC.

In-bunch pileup can occur due to the high luminosities and limited data taking rates that can be measured in ALICE. To reduce the fraction of in-bunch pileup, only events with a single reconstructed primary SPD vertex are considered. Background originating from beam-gas interactions is further reduced by cutting on the correlation of clusters and tracklets in the SPD by:

$$N_{\text{Clusters}} < 4 \cdot N_{\text{Tracklets}} + 65 \tag{6.3}$$

This cut is vizualized in Fig. 6.4. Out-of-bunch pileup occurs, if the readout time of detectors is too slow to distinguish between multiple bunch-crossings. The EMCal and PHOS have fast readout capabilities and out-of-bunch pileup can be rejected by a cut on the cluster time (timing cut), if these detectors are included. For PCM, out-of-bunch pileup can become

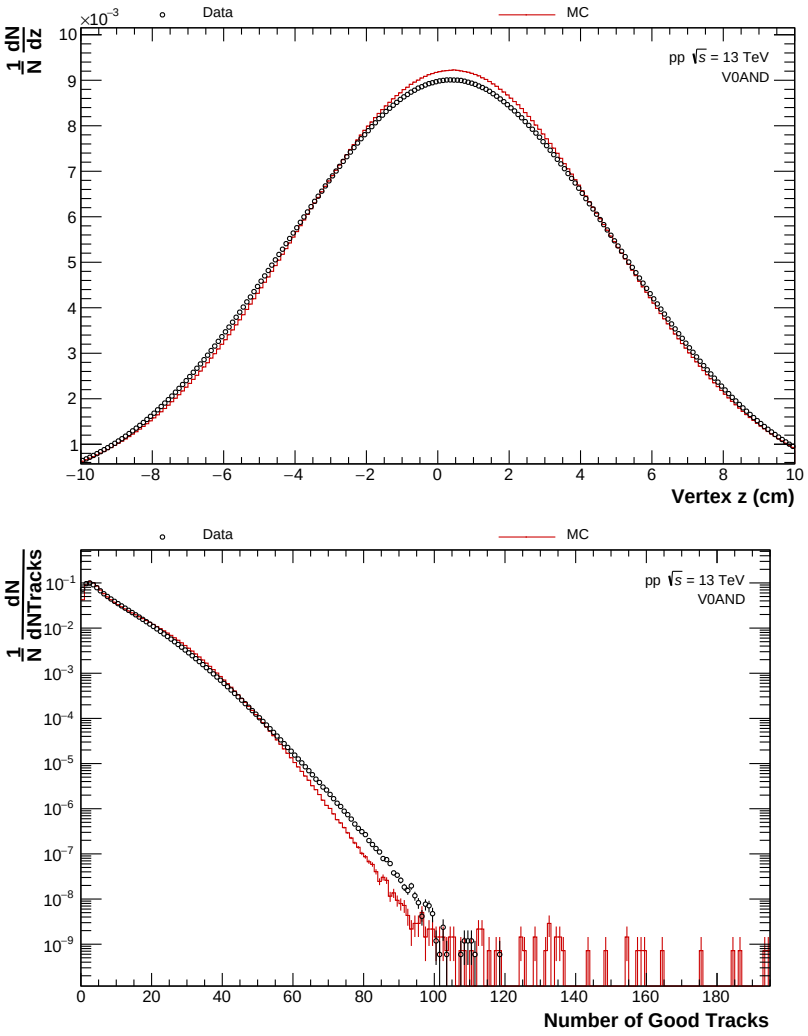

Figure 6.3: Comparison of z-vosition of collision vertex (**top**) and number of good tracks (**bottom**) in data to MC.

relevant, as the TPC with its slow tracking capabilities is mandatory for this reconstruction method. However, the measurement of ω mesons requires the measurement of primary tracks of charged pions and it is required for primary tracks to have at least one cluster in the SPD, which has fast readout capabilities. Hence, out-of-bunch pileup is negligible.

To convert measured invariant yields into invariant cross sections, the luminosity $\mathcal{L}$ for the chosen trigger condition is required. If A accounts for the acceptance and efficiency of the trigger and σ_{Inel} is the inelastic cross section, the collision rate $\mathrm{d}N/\mathrm{d}t$ is given by [71]

$$\frac{\mathrm{d}N}{\mathrm{d}t} = A \cdot \sigma_{\text{Inel}} \cdot \mathcal{L} = \sigma_{\text{Trigger}} \cdot \mathcal{L} \tag{6.4}$$

While A is acquired by adjusted simulations, σ_{Trigger} is determined by measuring the LHC luminosity and interaction rates simultaneously with help of van der Meer (vdM) scans.

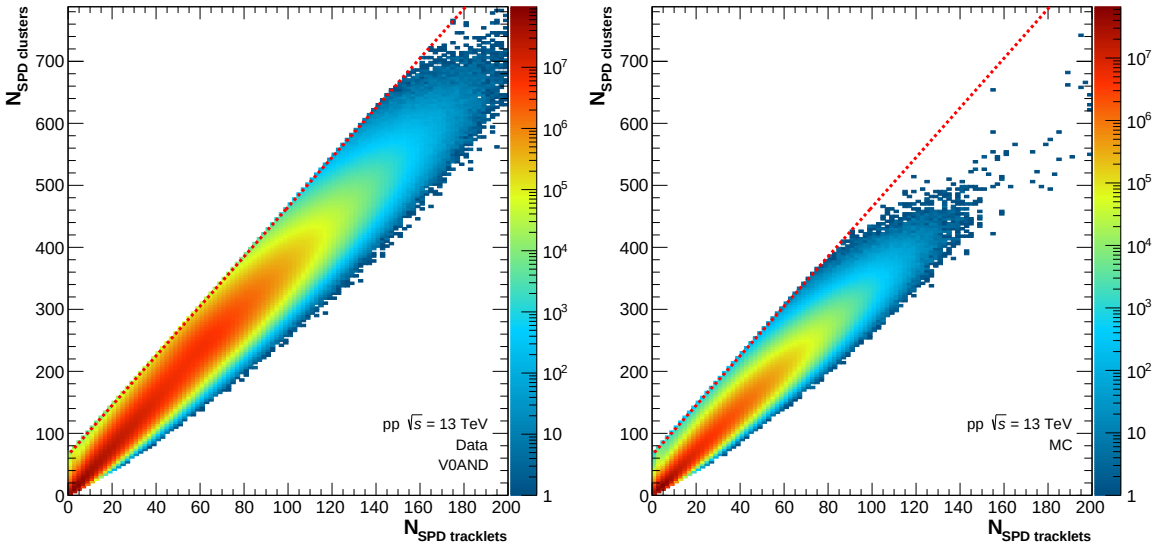

Figure 6.4: Number of SPD clusters vs. number of SPD tracklets of data (**left**) and MC (**right**). The cut, described by Eq. 6.3, is represented by a dotted red line.

Events have certain trigger decision flags applied to them, which can be used to select events with certain trigger conditions. For MB, events with the trigger flag V0AND (INT7) were selected. It requires a coincident signal in both V0 detectors and a cross section $\sigma_{\text{MB, INT7}}$ of $57.8 \pm 1.2\,\text{mb}$ [72] was measured. The analysis of the high energy events, triggered by EMCal uses the EG1 and EG2 flags. For the PHOS trigger, the PHI7 flag was used. Events, which contain multiple analyzed event flags are only considered for one trigger, to reject overlapping triggers. This removes the correlation of the statistical uncertainties between different triggers. The EMCal and the PHOS trigger require certain energy deposits in the detectors and enhance the trigger capabilities of the INT7 trigger significantly, described by the so-called trigger rejection factor (TRF). These properties will be discussed in more detail in section Sec. 6.3. The integrated luminosity $\mathcal{L}_{\text{Int}}$ quantifies the size of a given dataset and can be calculated as:

$$\mathcal{L}_{\text{Int}} = \int \mathcal{L}\mathrm{d}t = \frac{N_{\text{Events}}}{\sigma_{\text{Trigger}}} = \frac{N_{\text{evt, norm}}}{\sigma_{\text{MB, INT7}}} \cdot \text{TRF} \tag{6.5}$$

$N_{\text{evt, norm}}$ is the normalized number of events, calculated with Eq. 6.2. The number of events for the different runlists and the resulting $\mathcal{L}_{\text{Int}}$ can be found in Tab. 6.5.

6.3 High Energy Triggered Data

As discussed in the previous section, besides the MB trigger, the high energy triggers EG1 and EG2 of EMCal are used to enhance the available number of photons at high p_{T}. Furthermore,

Method	Trigger	$N_{\text{evt, MB}}$	$N_{\text{evt, norm}}$	$\mathcal{L}_{\text{Int}}$ in nb^{-1}	TRF
PCM	MB	$1.93614 \cdot 10^9$	$1.85872 \cdot 10^9$	32.2 ± 0.7	1.0
EMCal	MB	$1.62159 \cdot 10^9$	$1.56192 \cdot 10^9$	27.0 ± 0.6	1.0
EMCal	EG2	$1.34969 \cdot 10^8$	$1.30456 \cdot 10^8$	985.0 ± 43.1	436.5 ± 16.5
EMCal	EG1	$9.40122 \cdot 10^7$	$9.07874 \cdot 10^7$	8550.2 ± 377.2	5443.5 ± 208.3
PHOS	MB	$1.75519 \cdot 10^9$	$1.69377 \cdot 10^9$	29.3 ± 0.6	1.0
PCM-EMCal	MB	$1.53249 \cdot 10^9$	$1.47733 \cdot 10^9$	25.6 ± 0.6	1.0
PCM-EMCal	EG2	$1.34969 \cdot 10^8$	$1.30456 \cdot 10^8$	958.0 ± 31.9	424.5 ± 10.6
PCM-EMCal	EG1	$9.40122 \cdot 10^7$	$9.07902 \cdot 10^7$	8314.2 ± 280.2	5293.1 ± 135.2
PCM-PHOS	MB	$1.75519 \cdot 10^9$	$1.69377 \cdot 10^9$	29.3 ± 0.6	1.0

Table 6.5: Number of events for different reconstruction methods. The TRFs for MB datasets are defined to be unity. Therefore no error is given in these cases.

the PHI7 trigger of PHOS has been investigated. This section will explain the EMCal triggers, followed by the PHOS trigger.

The EG1 and EG2 are EMCal L1 triggers that require a certain energy deposit in a sliding window of 4x4 cells. This is possible across multiple Trigger Region Units (TRUs), while the triggers require a coincident signal in both V0 detectors. A TRU in the EMCal covers the area of a third full-size SM corresponding to 8x48 cells. [73]. The energy deposit thresholds are set on ADC level before the detector energy calibration is completed and can therefore only be given approximately. The threshold for the EG2 and EG1 are $E_{\text{Thre,EG2}} \approx 3.5\,\text{GeV}$ and $E_{\text{Thre,EG1}} \approx 8\,\text{GeV}$. If the EG1 or EG2 trigger is fired, an event flag is set, which allows for the selection of triggered events for the analysis. High energy triggers were not enabled for all runs. Hence, runs without triggered events have been removed in the existing EMC and PCM-EMCal runlists, when running the analysis for the EG1 and EG2 trigger. An analogous procedure has been applied to the PHOS runlist for the PHI7 trigger. High energy triggers enhance the measured cluster spectra, shown in Fig. 6.5 (left), as well as the resulting yields. The spectra are normalized by the number of events of the respective triggers. This enhancement is accounted for by the so-called Trigger Rejection Factor (TRF). For the TRF, the cluster spectra (normalized by the number of events) of the different triggers are divided by the cluster spectrum (normalized by the number of events) of MB. The ratios of the different cluster spectra can be seen in Fig. 6.5 (right). In the threshold region of the different triggers, a strong rise in the ratio, called turn-on, can be observed. The turn-on is followed by a plateau region, which is parametrized multiple times with a constant, while each time the lower energy boundary of the parametrization range $R_{\text{lower boundary}}$ is slightly varied, making use of the cluster intervals (binning). In comparison to the chosen lower boundary value, $R_{\text{lower boundary}}$ starts from 2 intervals (bins) earlier and goes up to 9 intervals higher

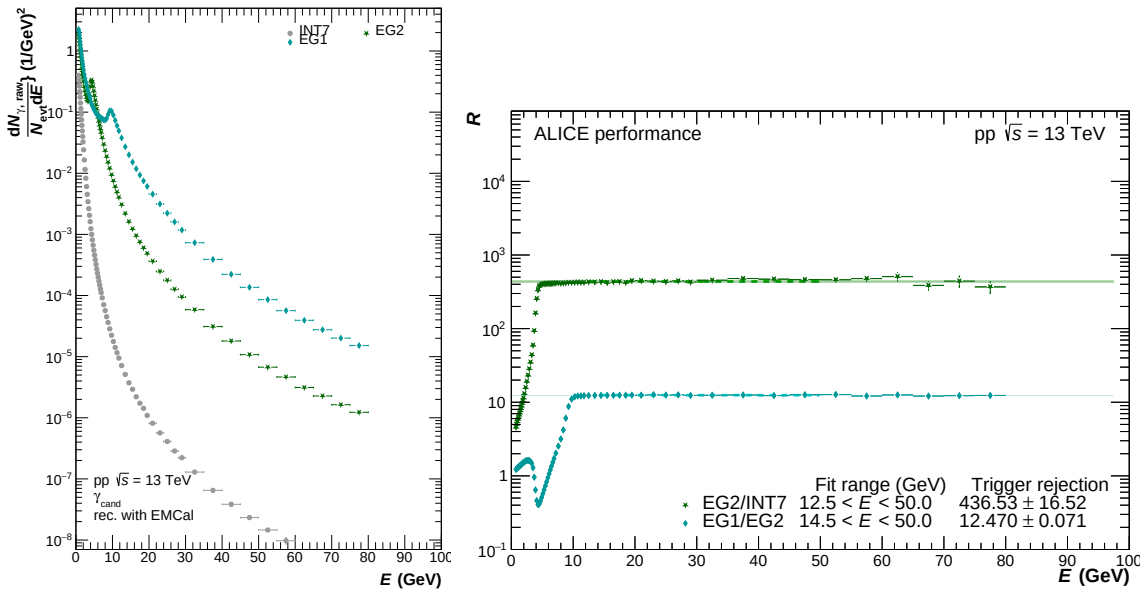

Figure 6.5: **Left:** Cluster spectra for different triggers, normalized by the number of events for the respective trigger. **Right:** TRF for EG2 and EG1

in the cluster intervals (binnings). This results in different constant values for the plateau region, which are again parametrized with a constant, defining the TRF. Its uncertainty is estimated as largest deviation of the different parametrizations to the determined TRF. Technically, triggers with higher energy threshold are divided by the trigger with the next highest threshold to reduce statistical uncertainties. For the total TRF, the separate TRFs have to be multiplied and for the MB dataset, the TRF is defined to be unity. Recent discussions suggest an additional correction for the TRF, taking the trigger efficiency into account. However, this correction has shown to be of the order of 2 % for the π^0 cross section, which is covered by the estimated systematic uncertainty of the explained TRF calculation approach. As the trigger is not implemented in the MC production, it has to be mimicked. This mimicking has been implemented within the ALICE collaboration. In this work, the dedicated AliEmcalTriggerMaker task [74] has been used. It is replicating the 4x4 cells sliding window, which is used in data. The resulting TRFs in MC can be seen in Fig. 6.6, where a good agreement with data can be observed. The values of the TRFs are documented in Tab. 6.5

The PHI7 is a PHOS L0 trigger and analogous to the EG1 and EG2 triggers, an event flag is created if the trigger is fired. It needs a certain energy deposit in a sliding window of 4x4 cells, limited in a TRU, while the triggers require a coincident signal in both V0 detectors. A full PHOS module consists of 8 TRUs, while two TRUs share a direct link to the ALICE DAQ (DDL). The PHOS detector consists of three full sized modules and one half sized module. This results in a total of 14 DDLs, which are numbered from 6 to 19. The energy

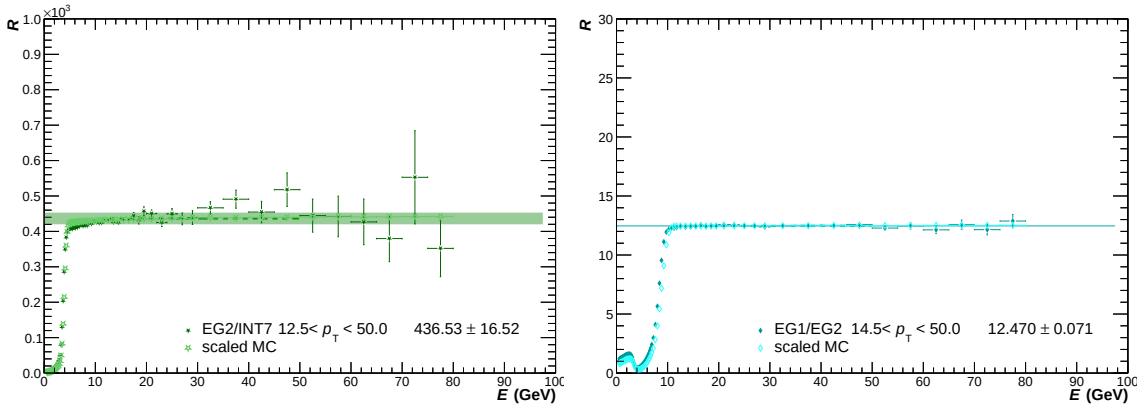

Figure 6.6: **Left:** TRF for EG2 in comparison to MC. **Right:** TRF for EG1 in comparison to MC.

deposit threshold for the PHI7 is $E_{\mathrm{Thre,PHI7}} \approx 4.0\,\mathrm{GeV}$. However, besides the event flag, the information of the position of the 4x4 slide window that fired the trigger is stored for PHOS. This gives the possibility to check, if a certain cluster has fired the trigger during the analysis. A cluster is only considered to have triggered, if its highest energy cell is not flagged bad by a specific bad channel map (BCM) for triggers. This BCM is not identical to the general PHOS BCM, discussed in Sec. 6.4. All clusters, which are used for any of the described cluster spectra of this section have to be flagged as good by the corresponding general BCM of EMCal or PHOS.

During this thesis, three different approaches have been implemented to mimic the trigger in MC. As a first approach, the trigger mimicking in MC for PHI7 is realized by requiring each event to have at least one cluster that exceeds a given threshold. The threshold value is not constant but gets sampled from a Gaussian distribution with the two parameters $\sigma_{\mathrm{Mimicking}}$ and $\mu_{\mathrm{Mimicking}}$. $\sigma_{\mathrm{Mimicking}}$ is corresponding to the width of the turn-on region and $\mu_{\mathrm{Mimicking}}$ is corresponding to its position, while both parameters have to be tuned iteratively. As soon as a new event is analyzed, a uniform random value between zero and one is generated for each cluster. This random value is compared to the turn-on parametrization at the given energy deposit value of the cluster. If the random value is lower than the turn-on parametrization, the cluster is considered to have fired trigger event flag.

In a second approach to mimic the trigger, the possibility to check if a specific cluster has fired the trigger is also implemented in MC. For this trigger mimicking approach, the cluster spectrum of the PHI7 trigger is divided by the cluster spectrum of the MB trigger for each DDL. Analogous to the calculation of the TRF in EMCal, the resulting ratios show a turn-on followed by a plateau region, where the plateau can give an effective trigger rejection factor for a certain DDL. The ratios are parametrized by a function that describes the turn-on and converges to a constant for high energies at the plateau. This is shown in Fig. 6.7 (top

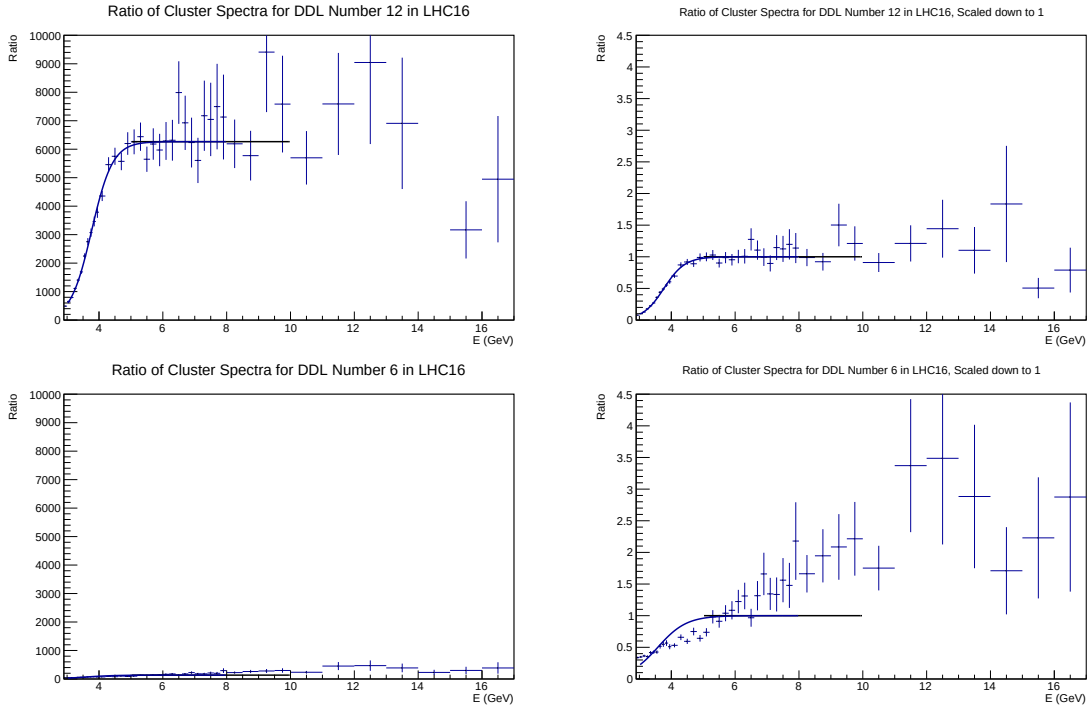

Figure 6.7: Ratio of cluster spectra of the PHI7 and MB trigger. **Left:** Clusters normalized by the number of events are divided. **Right:** Left cluster ratios are scaled down, so that the parametrization function in the plateau region is one. **Top:** DDL 12 for LHC16. **Bottom:** DDL 6 for LHC18. DDL 6 for LHC18 does not function properly and clusters are not allowed to fire the trigger in this DDL for LHC18 data.

left) for the example DDL 12 for LHC16. As available clusters are separated on 14 DDLs, the available number of photons for each DDL is limited. Due to this reason, the described ratios are created per year, instead of creating these ratios per period or per run. Ratios can differ significantly between different DDLs and years. DDL 6 for LHC18, shown in Fig. 6.7 (bottom), is an example DDL, that does not work properly and is marked as a "bad DDL" for the trigger decision. Besides the "bad DDL" flag, a "maybe bad DDL" flag has been introduced. The analyzer can decide, whether clusters that are positioned on a DDL with one of these flags are allowed to fire the trigger. To acquire a quantification, if a DDL behaves properly or is "bad" or "maybe bad", the number of clusters in PHI7 triggered data above an energy deposit of 1 GeV, normalized by the number of events, have been compared to the MC simulation for each year and is shown in Fig. 6.8. The quality flags for the different DDLs, that have not considered to be good can be found in Tab. 6.6. In Fig. 6.7 (right), the ratios and the parametrization functions shown in Fig. 6.7 (left) are scaled down by a high energy constant, so that the high energy plateau becomes one. The trigger decision is implemented similar to the first mimicking approach. As soon as a new event is analyzed, a uniform random value between zero and one is generated for each cluster. This random

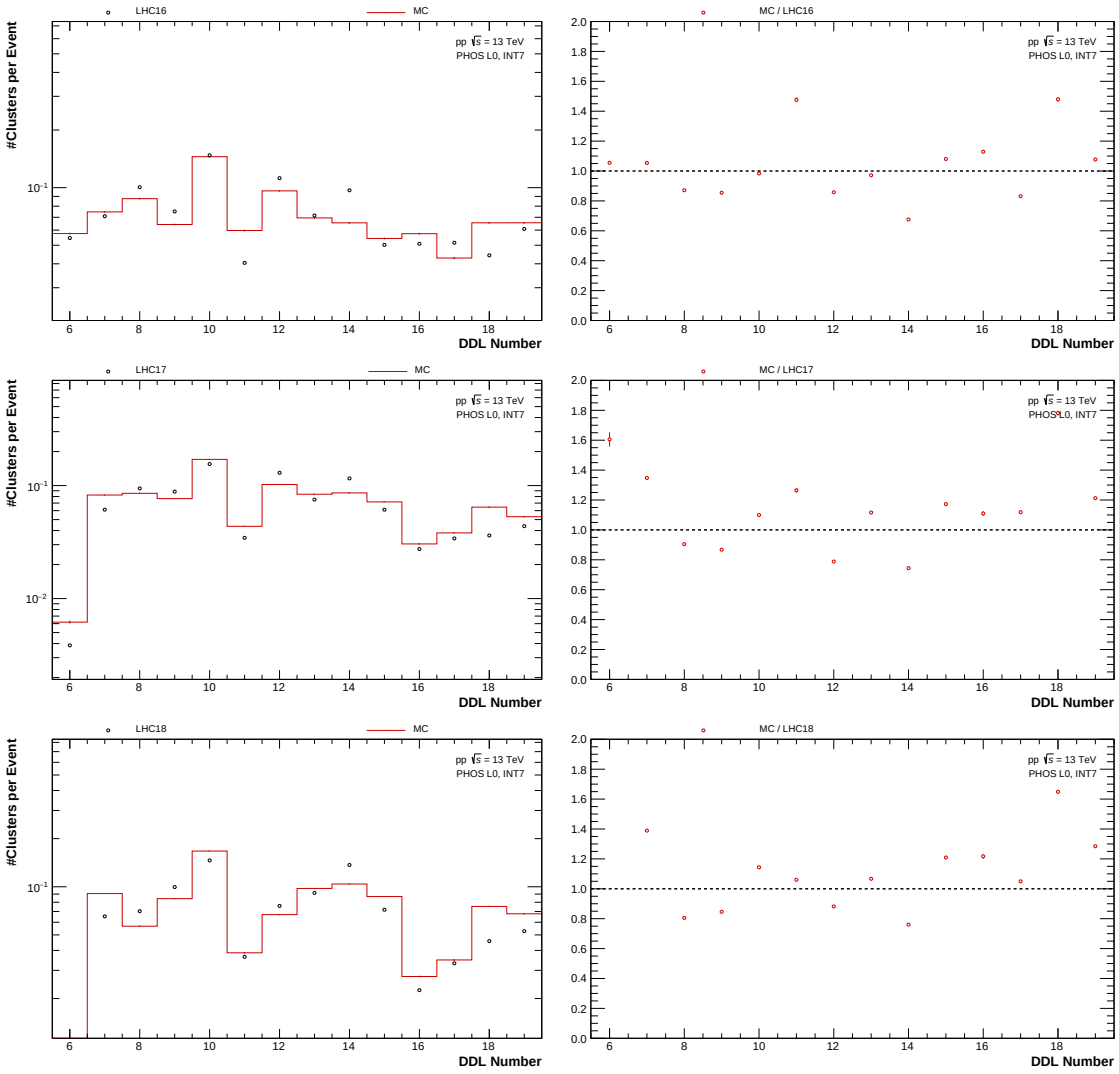

Figure 6.8: **Left:** Number of clusters above an energy deposit of 1 GeV per event and per number of good tracks. **Right:** Ratio of data and MC of the spectra shown in (left). **Top to Bottom:** Data and MC of LHC16, LHC17 and LHC18.

value is compared to the turn-on parametrization for the corresponding DDL, whose plateau has been scaled down to one, at the given energy deposit value of the cluster. If the random value is lower than the parametrization function, the cluster is considered to have fired the trigger.

Up until this point, the trigger mimicking assumes a trigger efficiency of 100 % in the plateau region. In the third approach to mimic the trigger, also the trigger efficiency is implemented in MC. This is realized by making use of the fact, that the MB data set also contains events with a PHOS L0 trigger flag. Two specific cluster histograms are used in this approach:

- Only clusters, which have been flagged as good by the general BCM and the BCM for triggers are filled into the histogram

Periods (Years)	DDL number	Quality Flag
LHC16	11	maybe bad
LHC16	14	maybe bad
LHC16	16	maybe bad
LHC16	18	bad
LHC17	6	bad
LHC17	7	maybe bad
LHC17	18	bad
LHC18	6	bad
LHC18	18	bad

Table 6.6: Quality flags for the different DDLs, that have not considered to be good.

- Only clusters, which have been flagged as good by the general BCM and the BCM for triggers are filled into the histogram, while events that are used for this histogram have to fulfill the additional condition that the MB event has also the PHOS L0 trigger flag assigned to it

The shape of the ratio of these histograms is similar to the example spectra shown in Fig. 6.7, while the plateau is representing the trigger efficiency of a given DDL. In contrast to the second mimicking approach, the ratios are parametrized without scaling the parametrizations to one. By comparing a uniform random value between zero and one to the parametrization functions during the analysis, the cluster triggering decision is mimicked, similar to the second mimicking approach. The resulting ratio for the example DDL 12 in LHC16 can be found in

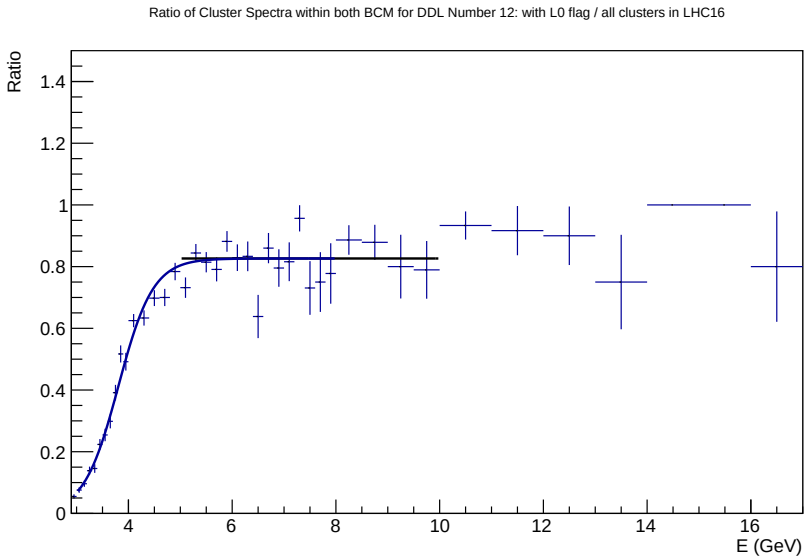

Figure 6.9: Ratio of MB cluster spectrum with PHOS L0 trigger flag and cluster spectrum of all MB events. This ratio is shown for the example DDL 12 in the LHC16.

Fig. 6.9.

The exclusion of triggered clusters, due to the BCM for triggers has to be accounted for in the TRF. Hence, various cluster spectra histograms, which are only filled for specific clusters, have been added for the MB trigger as well as the PHI7 trigger:

- Only clusters, which have been flagged as good by the general BCM and the BCM for triggers are filled into the histogram
- Only the highest energy clusters in an event, that has also been flagged as good by the general BCM and the BCM for triggers are filled into the histogram
- Only triggered clusters are filled into the histogram

Which cluster histograms need to be used for the calculation of the TRF is dependent on the analysis decision, if one of the clusters, used to create neutral meson candidates needs to have fired the trigger or not. Furthermore, it may also depend on the decision which trigger mimicking approach is used for MC. During this work, the implementation of the framework for the determination of the TRF, as well as the implementation of the trigger mimicking in MC has been performed. Final investigations on the TRF were performed in close collaboration with Adrian Florin Mechler[2], which lead to the completion of the π^0 and η measurement in the triggered dataset. Hence, the extracted meson yields shown in this thesis, which use the PHI7 trigger and were adjusted by the TRF, were not produced during this work, but were provided by Adrian Florin Mechler. Here, only PHI7 triggered events with at least one cluster, that fired the trigger, are taken into account. The clusters to reconstruct the neutral meson candidates are not required to have fired the trigger. The cluster spectra, which are used to calculate the TRF, are using all available clusters, which are flagged as good by the general BCM for the PHI7 triggered dataset and require all clusters of the MB triggered dataset to additionally be flagged as good by the BCM for triggers. It has turned out, that requiring clusters in the cluster spectrum of the PHI7 triggered dataset to additionally be flagged as good by the BCM for triggers has a negligible effect on the plateau region, where the TRF is extracted from. Furthermore, the second mimicking approach has been selected. This mimicking approach uses the DDL turn-on curves, while the plateau regions of these turn-on curves are scaled down to one. Clusters on DDLs that are flagged as "bad DDL" are not allowed to fire the trigger. Using the described cluster spectra, the TRF is calculated analogous to the EMCal triggers. Fig. 6.10 shows the TRF for PHOS in data in comparison to MC.

[2]Institut für Kernphysik, Universität Frankfurt, Frankfurt, Germany

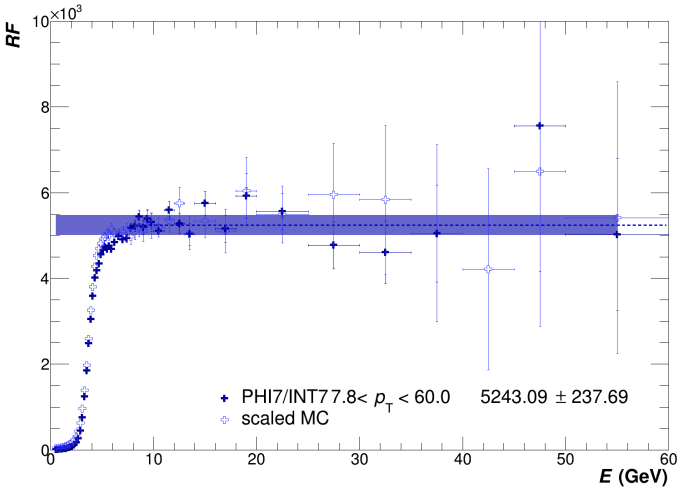

Figure 6.10: TRF for PHOS in data compared to MC.

6.4 Quality Assurance (QA)

As already mentioned in the beginning of this chapter, extensive Quality Assurance (QA) has been performed on a run-by-run (runwise) basis, as well as per period (periodwise) and per year (yearwise). The goal of the QA is the selection of good runs and good clusters for the physics analysis. It can be separated in different modules: The event QA for event-related observables, the photon QA for conversion photon-related observables, the cluster QA for cluster-specific observables and finally the primary track QA for primary track related observables. The runs used for the QA have been preselected by the ALICE Data Preparation Group (DPG), who ensured that the tracking in the ITS and TPC work properly for these runs. Here, it shall be mentioned that the amount of runs excluded during the QA process in LHC16 was significantly higher than for LHC17 and LHC18. This shows that the quality of the preselected data has improved during the years. Runs that have been discarded by the DPG can change during time. Hence, the used runlists have been compared again to the DPG runlists during the year 2020 and runs that were not flagged as good by the DPG have been removed, even if they were considered to be good in the QA performed during this work. This also includes runs with incomplete TPC acceptance, which were considered to be good during the QA of data of 2016. As discussed already, this work was focussing on the QA for the PCM and the PHOS detector. This includes the event QA, the conversion photon QA, the cluster QA and the primary track QA. Additional QA for the EMCal has been performed within the ALICE collaboration. The first iteration of the QA was the runwise event QA. In runwise QA, it is important that monitored observables are in the same order of magnitude between data and MC. However, it even more important that monitored trends between runs for certain observables in data are followed by MC. This means, that the changes of detector

properties during different runs are properly covered by the simulation. For observables which were not simulated, the monitored trends are used to find runs which behave significantly different from other runs of the period. If the trend of data is not followed in MC, it is checked if there is a valid reason for the observed behavior. If this is not the case, the runs are discarded. Only runs, which pass the QA are shown in this section. While more event properties have been checked, the main observables in the event QA to distinguish good from bad runs were:

- Mean number of good tracks
- Root mean square (RMS) of number of good tracks
- Number of conversion γ candidates
- Fraction of pileup
- Fraction of good events
- Fraction of events with a z-vertex position outside 10 cm with respect to the center of ALICE
- Fraction of events without a primary vertex
- Position of z-vertex
- Mass position of neutral pions

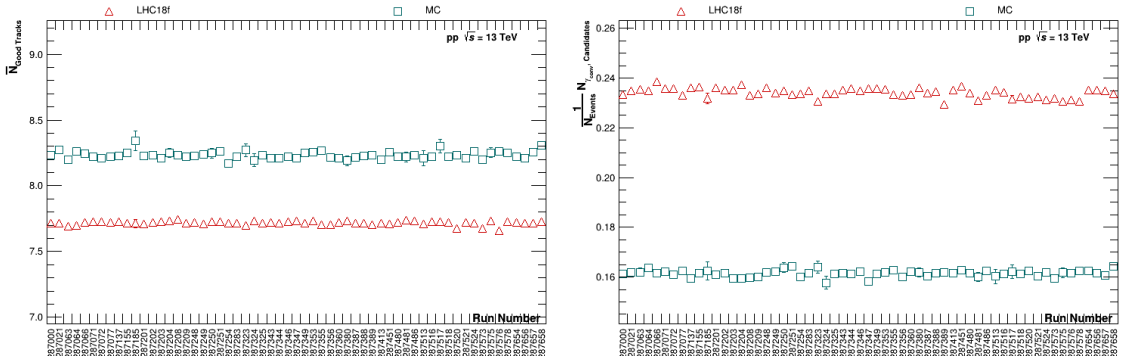

Figure 6.11: Runwise comparison of observables for LHC18f in comparison to the anchored MC. **Left:** Mean number of good tracks **Right:** Number of conversion γ candidates

Fig. 6.11 and Fig. 6.12 show the most important event QA quantities for LHC18f. As it can be seen, the trends that occur in data are followed well in MC. After documenting suspicious runs and removing bad runs from the runlist, the runwise conversion photon QA was performed. Here, the main observables to distinguish good from bad runs have been:

- $n\sigma_{e^\pm}$ for the specific energy loss $\mathrm{d}E/\mathrm{d}x$ for electrons in the TPC

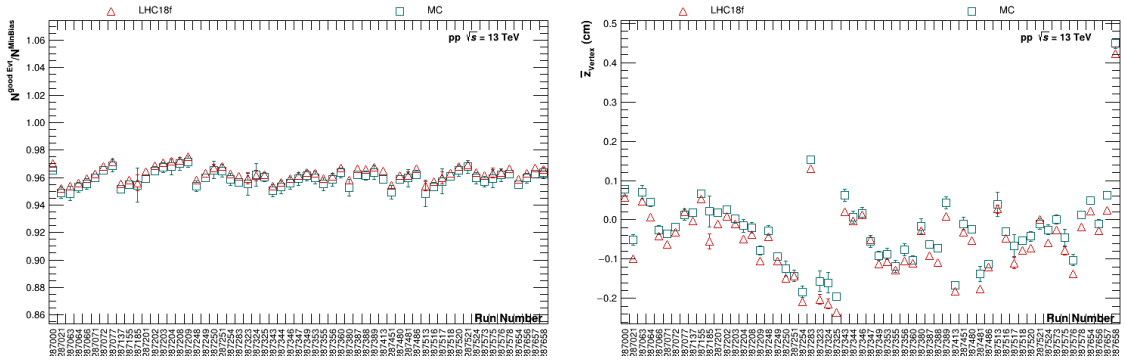

Figure 6.12: Runwise comparison of observables for LHC18f in comparison to the anchored MC. **Left:** Fraction of good events **Right:** Position of z-vertex

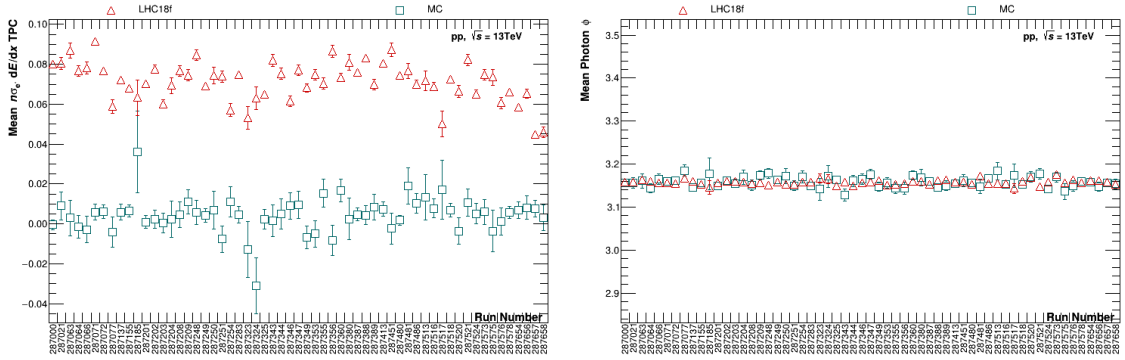

Figure 6.13: Runwise comparison of observables for LHC18f in comparison to the anchored MC. **Left:** $n\sigma$ for the specific energy loss $\mathrm{d}E/\mathrm{d}x$ for electron in the TPC. **Right:** Photon φ.

- Photon η
- Electron η
- Photon φ
- Number of TPC clusters for electrons

Example observables for the combined years are shown in the appropriate sections. Fig. 6.13, Fig. 6.14 and Fig. 6.15 show the most important photon QA quantities for LHC18f. Similar to the event QA, it can be seen that the trends that occur in data are reproduced well in MC. The differences, that can be seen for $n\sigma_{e^\pm}$ are small compared to the selection cut of $-3 < n\sigma_{e^\pm} < 4$, which is applied for the physics analysis of this work. After bad runs were removed from the runlists, periodwise and yearwise checks have been performed.

In the following, the cluster QA will be described. The main observable to distinguish good from bad runs in the cluster QA was the number of clusters, normalized by the number of events. Furthermore, the cluster QA focuses on finding bad cells or channels in a detector and marking them as bad in a specific detector map, called bad channel map (BCM). This part of

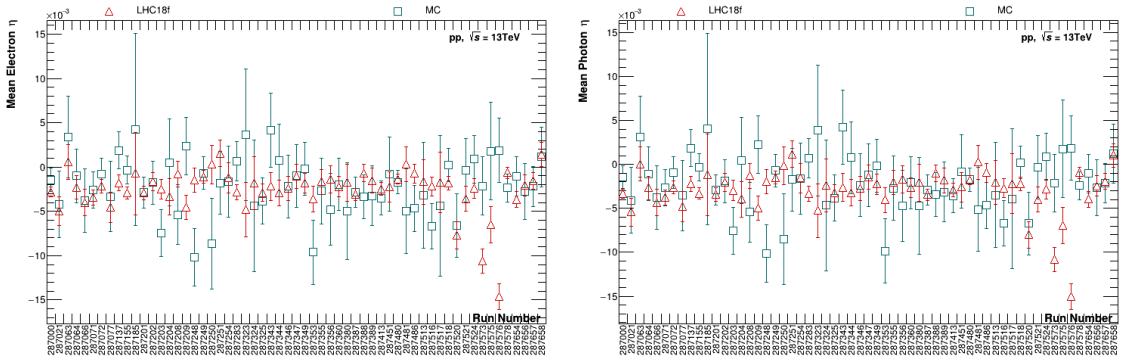

Figure 6.14: Runwise comparison of observables for LHC18f in comparison to the anchored MC. **Left:** Electron η. **Right:** Photon η.

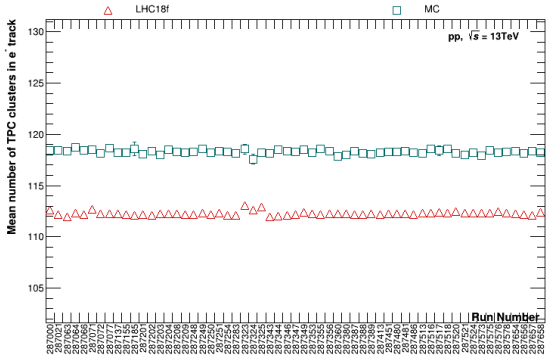

Figure 6.15: Runwise comparison of number of TPC clusters for electrons for LHC18f in comparison to the anchored MC.

the cluster QA will be called cell QA. Each cell has a unique cellID and cells that have already been flagged as bad within the ALICE collaboration are also considered to be bad for this work and were taken from the already existing BCM in OADB/PHOS/PHOSBadMaps.root in AliPhysics. This BCM will be called basic BCM in the following. The information whether a cell is bad is stored for a group of subsequent runs that have similar distributions of bad channels, so called runranges. The runranges in the basic BCM are mostly based on periods, while periods with very few runs have been combined. The same runranges have been taken for the cell QA, while some periods have been split further. The decision if runranges had to be split is based on the η-φ distribution of clusters. This is done by investigating if the regions, where many photons are measured in comparison to the rest of the modules are changing between different runs. Fig. 6.16 shows the η-φ distribution of PHOS clusters for different runranges in the example period LHC16k. Bad channels are identified in a two step procedure. First, cells are marked as suspicious depending on criteria introduced in the following, and as a second step, these suspicious cells are checked in detail. Five different observables have been used to decide, which cells are suspicious:

- Width of cell energy distribution in dependence of the mean cell energy

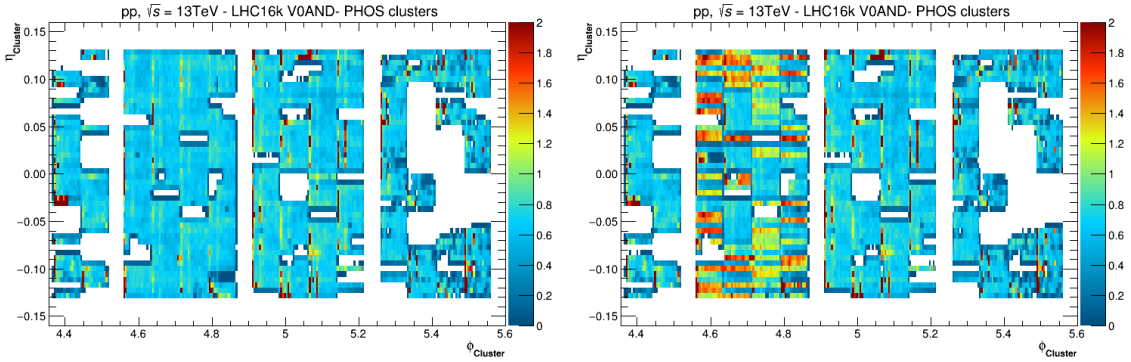

Figure 6.16: η-φ distribution of PHOS clusters for different run ranges in LHC16k normalized by the number of events and global average cluster density per cell. **Left:** Run 256512 to 256944. **Right:** Run 257011 to 257144.

- Ratio of number of cells with an energy from L to 30 GeV to number of cells with an energy from 0 GeV to L, with the variable integration limit L.
- Width of the cell time distribution in dependence of the mean cell time
- Number of all fired cells normalized by the number of events
- Ratio of fired cells to cells which fired at a time $|t| < 0.02\,\mu$s.

These observables are shown in Fig. 6.17 for the data taking period LHC16j. The dotted lines indicate thresholds and all cells outside these thresholds are marked as suspicious. These lines are chosen in a way, that only cells that do not follow the common distribution of all cells are marked as suspicious. To decide if a cell is bad, the energy and timing distributions of all suspicious cells have been checked. While the energy distribution is compared to MC, the simulation does not provide timing information. To better judge the behavior of cells, their timing information is compared to random good cells. Examples of a good and a bad cell are shown in Fig. 6.18. The cell energy distribution in data of the good cell is in reasonable agreement with MC, while the cell time distribution shows the expected behavior. None of these statements hold for the bad cell. The selection of good and bad cells can be subjective for some cells. To catch bad cells, which passed this QA step, an algorithm has been used on good cells, which compares how often a cell fired to how often neighboring cells fired. For each cell, the number how often a cell has fired is compared to their 100 neighboring cells, based on the CellID and a mean $\mu_{\text{neighbors}}$ as well as a standard deviation $\sigma_{\text{neighbors}}$ is calculated. Cells which are firing significantly more or less often than the mean are called hot or cold cells and are flagged as bad. The decision if a cell is hot or cold is made on a selection window of $\mu_{\text{neighbors}} \pm (n_{\text{neighbors}} \cdot \sigma_{\text{neighbors}})$. This means, lower values of $n_{\text{neighbors}}$ result in a more strict BCM compared to higher values of $n_{\text{neighbors}}$. On the other hand, a

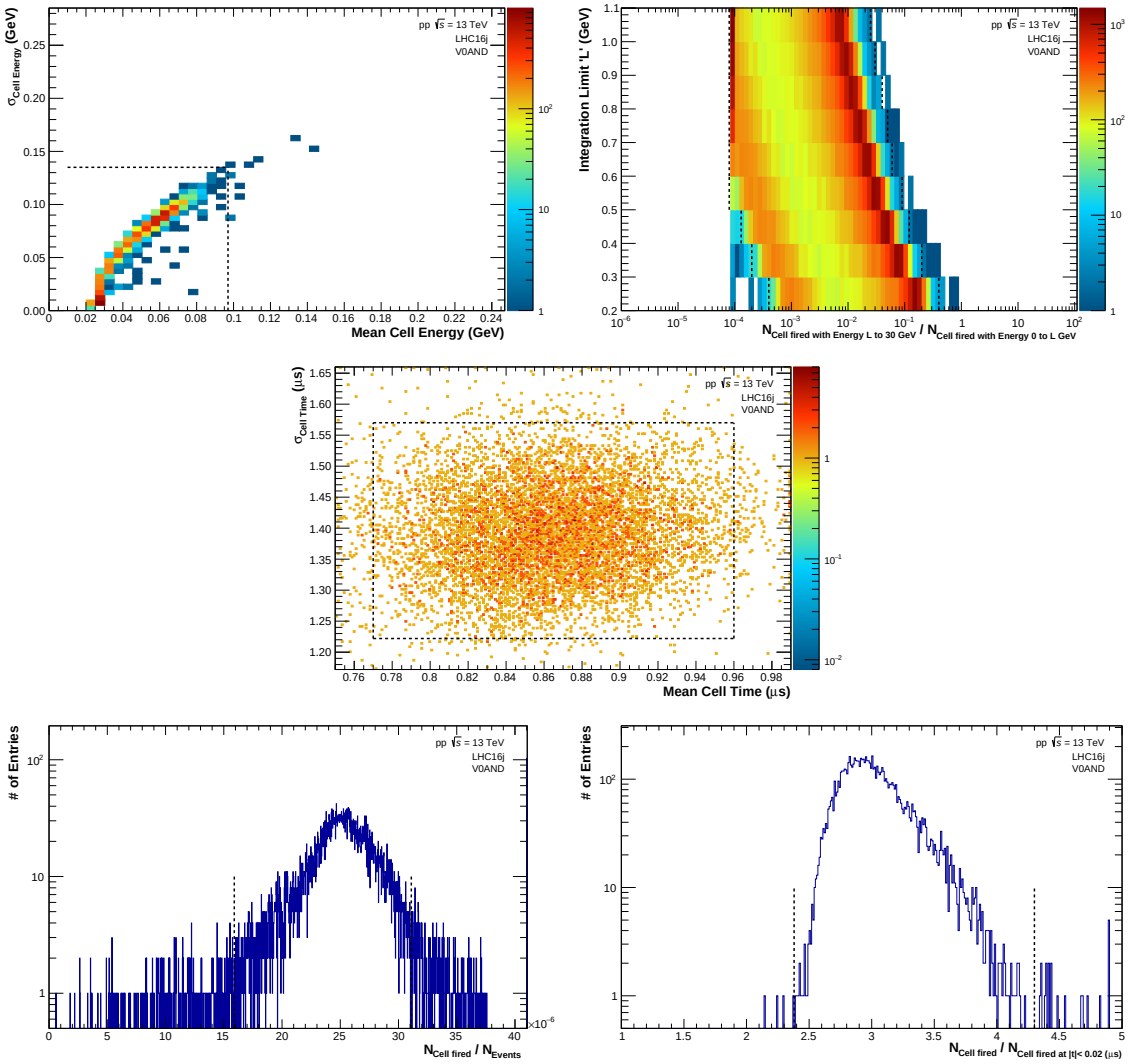

Figure 6.17: Observables which are used to decide, which cells are suspicious and need to be checked for example period LHC16j. **Top Left:** Width of cell energy distribution in dependence of the mean cell energy. **Top Right:** Ratio of number of cells with an energy from L to 30 GeV to number of cells with an energy from 0 GeV to L, with the variable integration limit L. **Middle:** Width of the cell time distribution in dependence of the mean cell time. **Bottom Left:** Number of all fired cells normalized by the number of events. **Bottom Right:** Ratio of fired cells to cells which fired at a time $|t| < 0.02\,\mu$s.

value of $n_{\text{neighbors}} = \infty$ means, that no additional cells are flagged by this algorithm. Three different BCMs have been created, while all of these BCM include the basic BCM:

- Only suspicious cells, that have been flagged as bad due to their energy and time distribution are added to the basic BCM. This is equivalent to $n_{\text{neighbors}} = \infty$.
- In addition to the suspicious cells, that have been flagged as bad due to their energy and time distribution, hot and cold cells are selected with $n_{\text{neighbors}} = 5.5$.

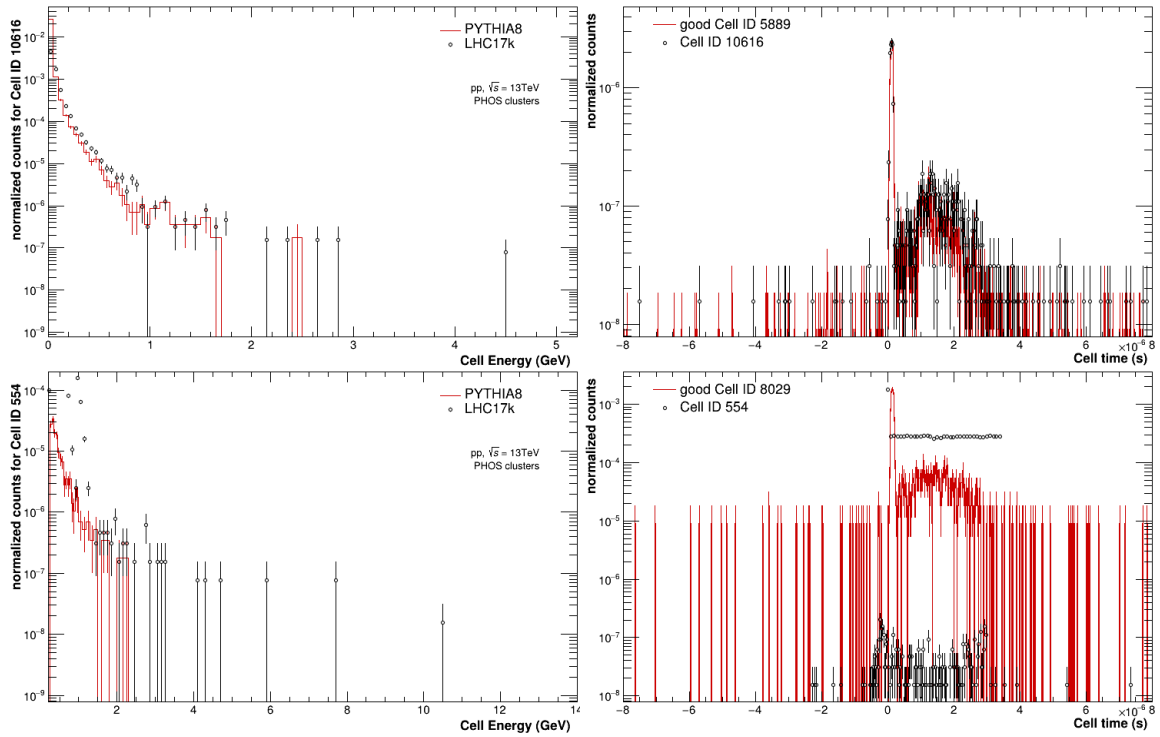

Figure 6.18: Observables of example cells to decide if a suspicious cell is of good or bad quality. **Left:** Energy distribution of an example cell. The distribution in data is compared to MC. **Right:** Time distribution of an example cell. As the time is not available for MC, the cell is compared to a different cell of good quality. **Top:** Cell of good quality. **Bottom:** Cell of bad quality.

- In addition to the suspicious cells, that have been flagged as bad due to their energy and time distribution, hot and cold cells are selected with $n_{\text{neighbors}} = 1.5$.

A π^0 meson analysis with the PHOS and PCM-PHOS method has been performed multiple times, where these three BCMs and the basic BCM were applied. A comparison of the resulting corrected yields can be found in Fig. 6.19. The concept of corrected yields will be explained in detail in Chap. 9. The entries of the legend is ordered in a way, that lower entries include all bad channels in their BCM from upper entries. It can be seen that there are no significant differences anymore, regardless if $n_{\text{neighbors}}$ was chosen to be 5.5 or 1.5. As a lower number means more cells that have been marked bad, the BCM with $n_{\text{neighbors}} = 5.5$ was chosen for the analysis.

In the following, the primary track QA will be described. Primary tracks are of special importance for the measurement of charged pions. The main observables for the primary Track QA have been:

- $n\sigma_{\pi^\pm}$ for the specific energy loss $\mathrm{d}E/\mathrm{d}x$ in the TPC
- Distance of Closest Approach (DCA)

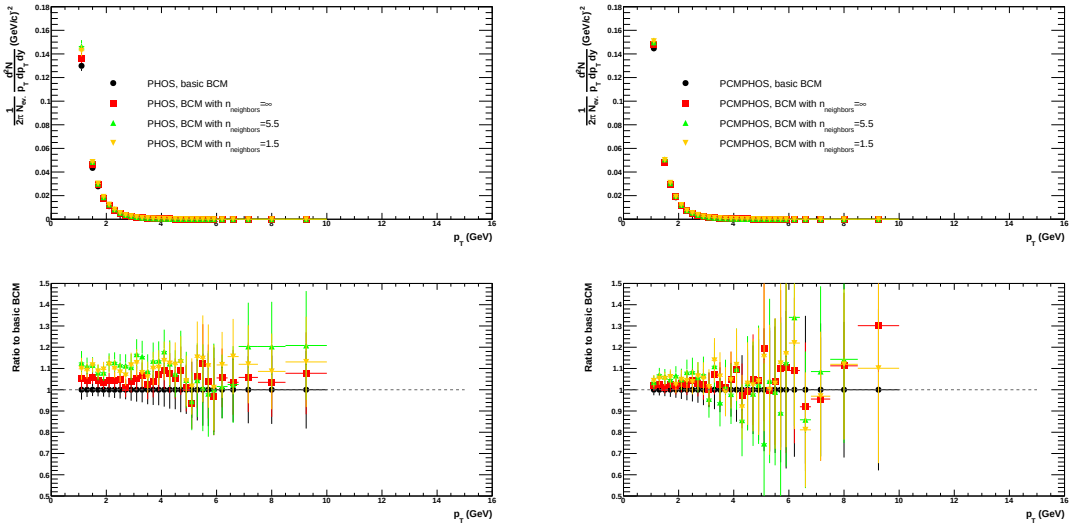

Figure 6.19: **Top:** Corrected yields of π^0 meson with different BCMs applied. **Bottom:** Ratio of corrected yields with different BCMs applied corrected yield with basic BCM applied. **Left:** π^0 meson reconstructed with PHOS method. **Right:** π^0 meson reconstructed with PCM-PHOS method.

- Charged pion p_{T}
- Charged pion η
- Charged pion φ

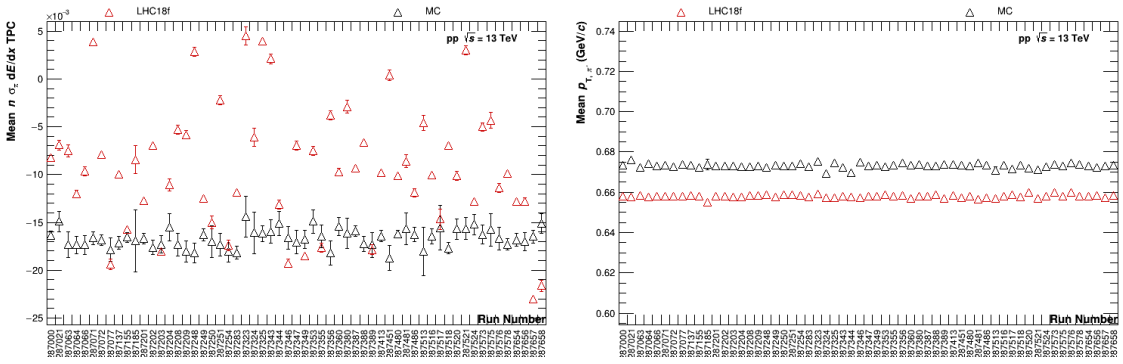

Figure 6.20: Runwise comparison of observables for LHC18f in comparison to the anchored MC. **Left:** Specific energy loss distribution for pions in TPC. **Right:** p_{T} of π^-s.

Fig. 6.20, Fig. 6.21 and Fig. 6.22 show the most important primary track QA quantities for LHC18f. As positive charged pions show a similar behavior, only negative charged pions are shown here. The trends that occur in data are mostly followed well in MC. Similar to the $n\sigma_{e^\pm}$ distribution in the conversion photon QA, the differences that can be seen for $n\sigma_{\pi^\pm}$ are small compared to the selection cut of $-3 < n\sigma_{\pi^\pm} < 3$, which is applied for the physics analysis of this work.

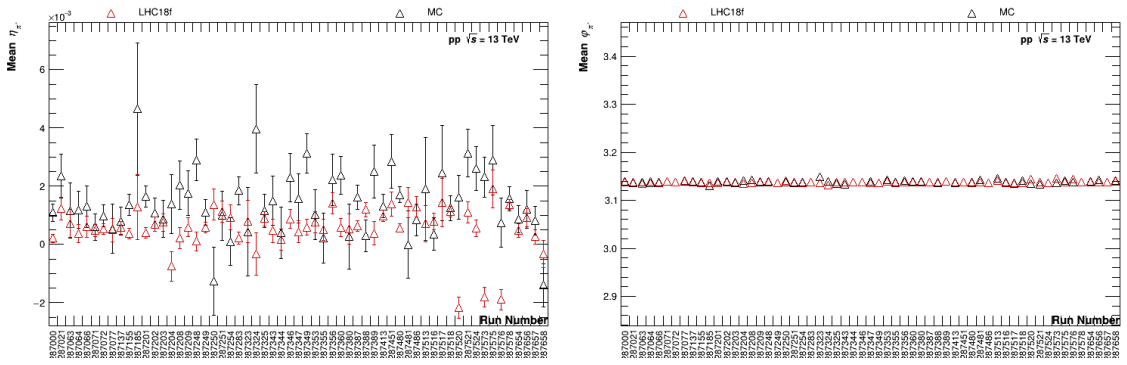

Figure 6.21: Runwise comparison of observables for LHC18f in comparison to the anchored MC. **Left:** η of π^-s. **Right:** φ of π^-s.

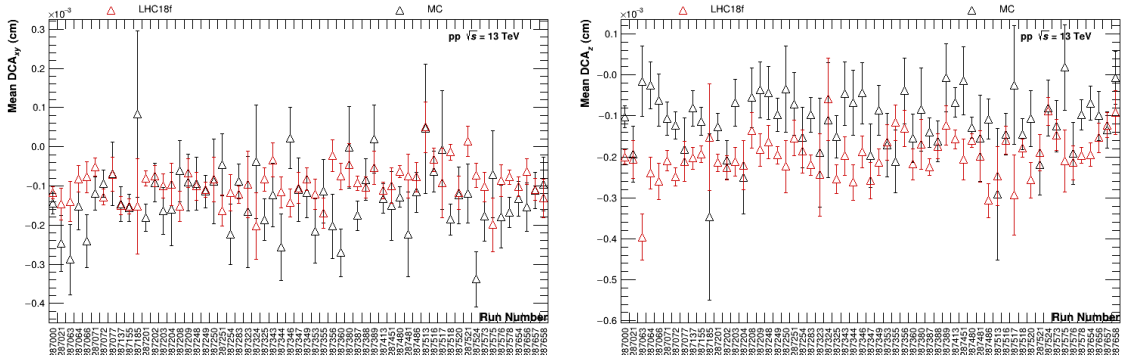

Figure 6.22: Runwise comparison of observables for LHC18f in comparison to the anchored MC. **Left:** DCA in xy-direction. **Right:** DCA in z-direction.

7 Charged Pion Selection

Table 7.1: Track and PID cuts applied for charged pions.

Cut	Value
Pseudorapidity	$\lvert\eta_{\pi^\pm}\rvert < 0.9$
Minimum number of crossed pad rows in TPC	$N_{\text{cr. rows, TPC}} > 70$
Minimum ratio of crossed rows over findable clusters	$R_{\text{cr. rows find. cls, TPC}} < 0.8$
Maximum fraction of shared clusters with other tracks	$F_{\text{shared cls, TPC}} < 0.4$
Maximum number of shared clusters with other tracks	$N_{\text{shared cls, TPC}} < 10$
Minimum number of TPC clusters	$N_{\text{cls, TPC}} > 80$
Minimum number of TPC PID clusters	$N_{\text{PID cls, TPC}} > 50$
DCA to primary vertex	$\text{DCA}_{\text{XY}} < 2.4\,\text{cm}$ and $\text{DCA}_{\text{Z}} < 3.2\,\text{cm}$
χ^2 of TPC track fit per cluster	$\chi^2/N_{\text{cls, TPC}} < 4$
χ^2 of ITS track fit per cluster	$\chi^2/N_{\text{cls, ITS}} < 36$
χ^2 of global track fit per cluster	$\chi^2/N_{\text{cls, global}} < 36$
Transverse Momentum	$p_{\text{T}} > 100\,\text{MeV}/c$
Invariant Mass of $\pi^\pm$	$m_{\pi^+\pi^-} < 850\,\text{MeV}/c^2$
require refit in ITS and TPC	yes
cluster requirement ITS	hit in any SPD layer
Energy loss $\text{d}E/\text{d}x$ in TPC	$-3 < n\sigma_{\pi^\pm} < 3$

The ω meson in this work is reconstructed, using its decay channel $\omega \to \pi^+\pi^-\pi^0$. As shown in Tab. 3.3, charged pions ($\pi^\pm$) have a mean lifetime of $(2.6033 \cdot 10^{-8} \pm 0.00004)\,\text{s}$. This is sufficient to traverse through the ALICE detector before decaying. Hence, $\pi^\pm$ can be measured and identified directly, using their global hybrid track information in the ITS and TPC with an additional refit. The applied cuts can be found in Tab. 7.1. It is required for all tracks to be within the rapidity range of $\lvert\eta_{\pi^\pm}\rvert < 0.9$, equivalent to the dimensions of the TPC. The track reconstruction procedure is described in Sec. 4.2.5 and tracks, which could not to be properly refitted are excluded from the analysis. The refit furthermore requires

χ^2 to be below 4 per TPC cluster. To improve the track quality, a cut on the maximum amount of shared TPC clusters and on its fraction to all clusters has been applied. A total number and a relative fraction is used for this cut, as the momentum dependent curvature of a track influences the number of track points that can be found. To separate the $\pi^{\pm}$ from secondary particles, a DCA cut to the primary vertex has been used. The DCA distributions

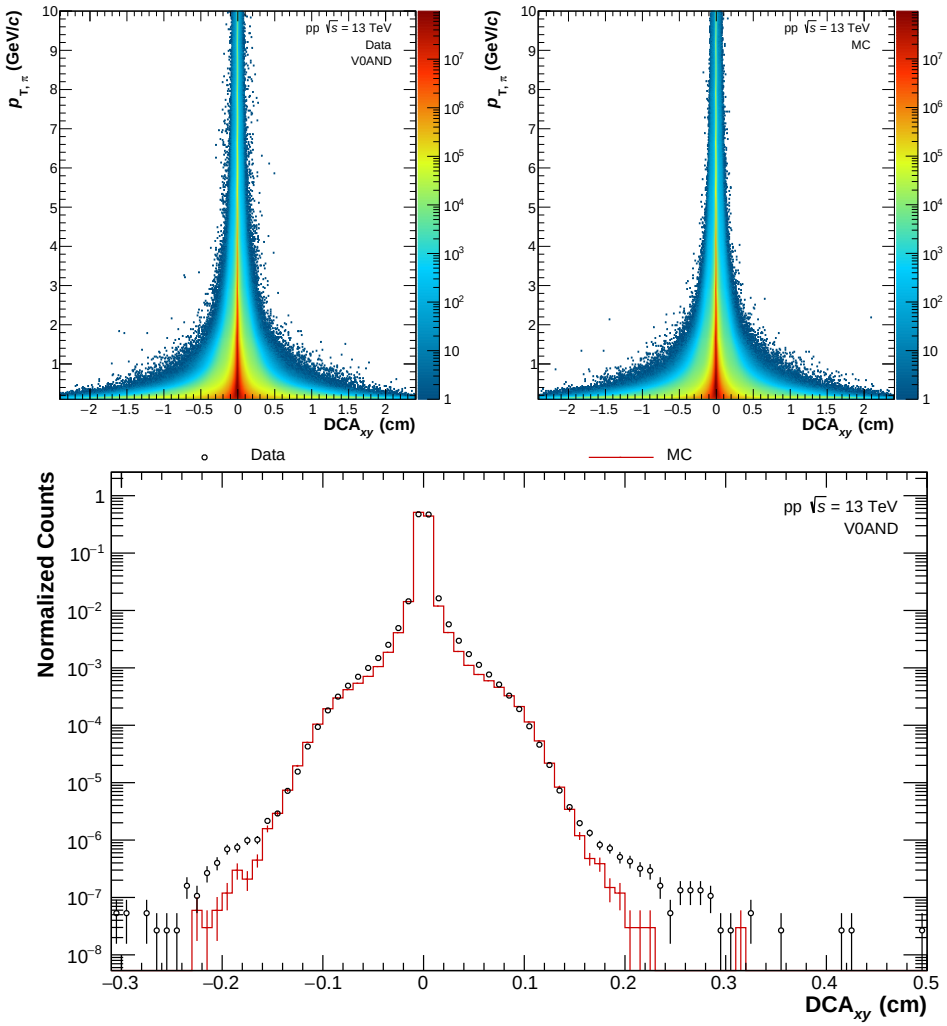

Figure 7.1: **Top:** DCA in x-y-direction of charged pions for data (**left**) and MC (**right**). **Bottom:** Comparison of charged pion DCA in z-direction between data and MC. The shown distribution is a projection over the whole p_{T} range.

in x-y-direction and z-direction of charged pions for data and MC in dependence of p_{T} can be found in Fig. 7.1 and Fig. 7.2. The DCA distribution in x-y-direction in data is in good agreement with MC. The DCA distribution in z-direction is in good agreement below $|0.5|$ cm and deviates for larger $\mathrm{DCA_Z}$. However, as a very lose cut of $\mathrm{DCA_Z} < 3.2\,\mathrm{cm}$ is used and the amount of normalized counts is many orders of magnitude smaller for distances above $|0.5|$ cm, the $\mathrm{DCA_Z}$ distribution is considered to be in reasonable agreement between data

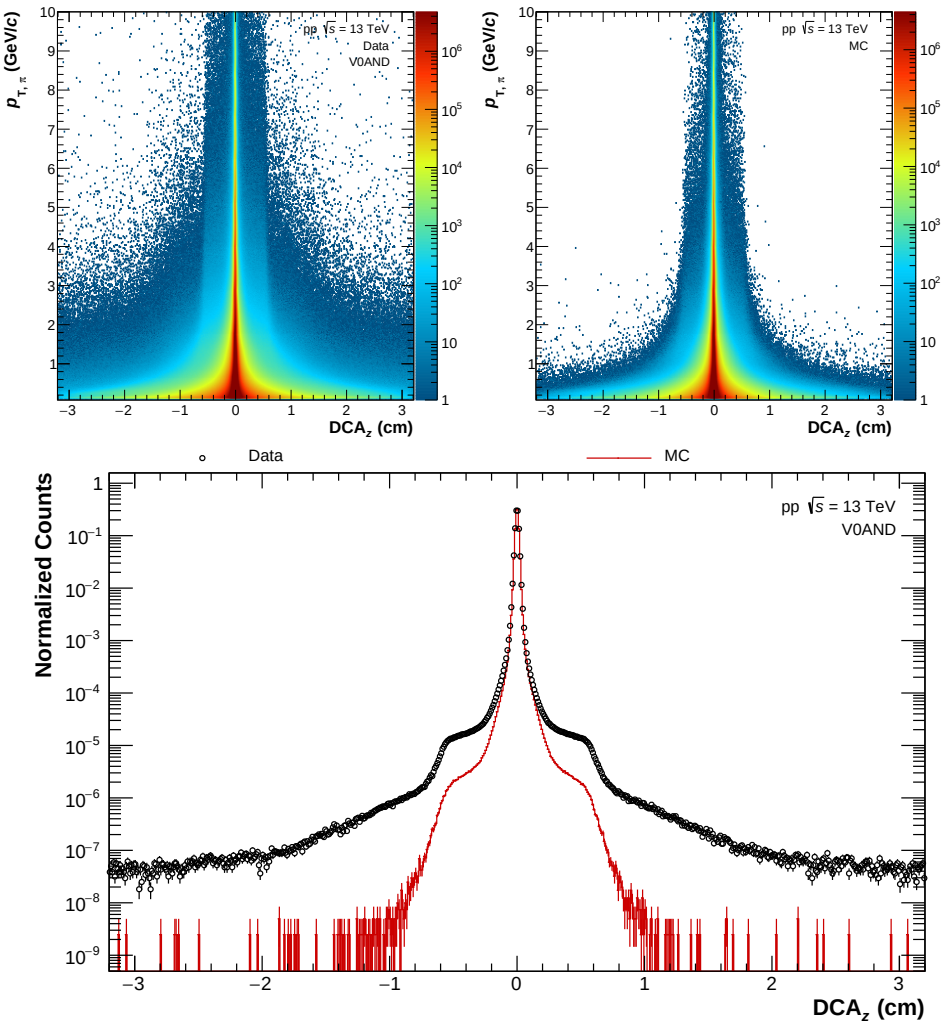

Figure 7.2: **Top:** Charged pion DCA in z-direction of charged pions for data (**left**) and MC (**right**). **Bottom:** Comparison of charged pion DCA in z-direction between data and MC. The shown distribution is a projection over the whole p_{T} range.

and MC. Furthermore, tracks with a transverse momentum of smaller than 100 MeV/c have been rejected. The charged pion distributions of η, φ and p_{T} can be found in Fig. 7.3 and Fig. 7.4 (Left). As can be seen, these distributions in data are in very good agreement with the MC simulation. Only the π^- distributions are shown, as the distributions for π^+ are similar.

Charged pion tracks are identified via their specific energy loss $\mathrm{d}E/\mathrm{d}x$ in the TPC. A cut of $n\sigma_{\pi^{\pm},\,\mathrm{TPC}}$ around the expected energy loss for charged pions is applied to select the desired tracks and is defined by:

$$n\sigma_{\pi^{\pm},\,\mathrm{TPC}} = \frac{\mathrm{d}E/\mathrm{d}x\,|_{\mathrm{meas}} - \langle \mathrm{d}E/\mathrm{d}x \rangle}{\sigma_{\mathrm{Bethe\ Bloch}}} \tag{7.1}$$

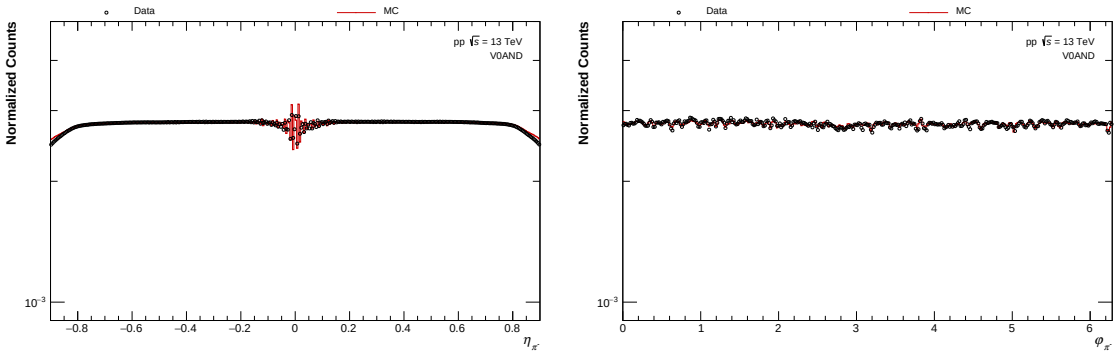

Figure 7.3: η (**left**) and φ (**right**) distribution of π^- mesons in data compared to MC. The distributions are normalized by the number of events.

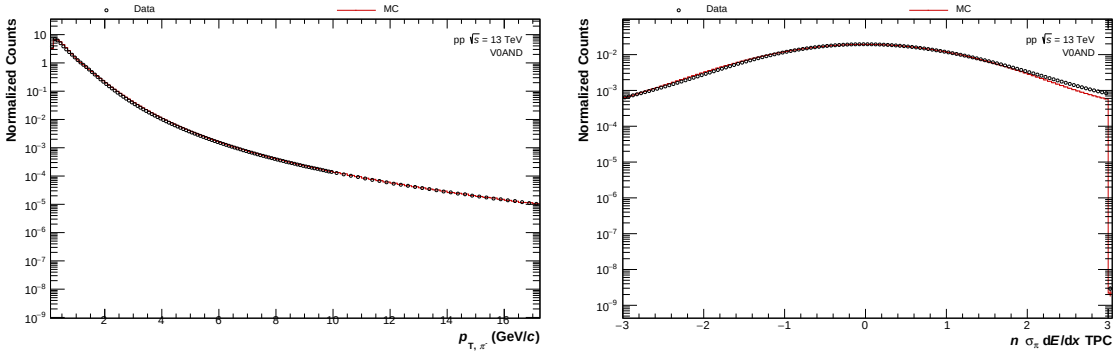

Figure 7.4: **Left:** p_{T} distribution of π^- in data compared to MC. The distribution is normalized by the number of events and the p_{T} interval width. **Right:** Comparison of energy loss $\mathrm{d}E/\mathrm{d}x$ for TPC tracks between data and MC.

Here, $\mathrm{d}E/\mathrm{d}x\,|_{\mathrm{meas}}$ is the measured energy loss and $\langle \mathrm{d}E/\mathrm{d}x \rangle$ is the expected energy loss due to the Bethe-Bloch equation (Eq. 3.15) and the TPC calibration with the resolution $\sigma_{\text{Bethe Bloch}}$.

Fig. 7.5 shows the energy loss $\mathrm{d}E/\mathrm{d}x$ for TPC tracks before and after the PID cut has been applied. As can be seen, the $\mathrm{d}E/\mathrm{d}x$ distribution of charged pions has an overlap with different particles. Ordering the overlap regions from low p_{T} to high p_{T}, the corresponding particles are electrons, kaons, protons and deuterons. The applied PID cut is resulting in one band in the $\mathrm{d}E/\mathrm{d}x$ distribution around the charged pions. The remaining contamination could be reduced by using the PID capabilities of other detectors like the TOF or TRD. The effect of the inclusion of the PID capabilities of the TOF detector has been investigated during this work. However, while it did result in slightly better signal to background ratios for the ω reconstruction, the number of lost reconstructed ω mesons was significant. Therefore, besides the TPC, no additional PID detectors have been used in the final analysis. The contamination in MC is more visible than in data. The direct comparison of $\mathrm{d}E/\mathrm{d}x$ is shown in Fig. 7.4 (right). Here, it can be observed that the deviation between the distributions can

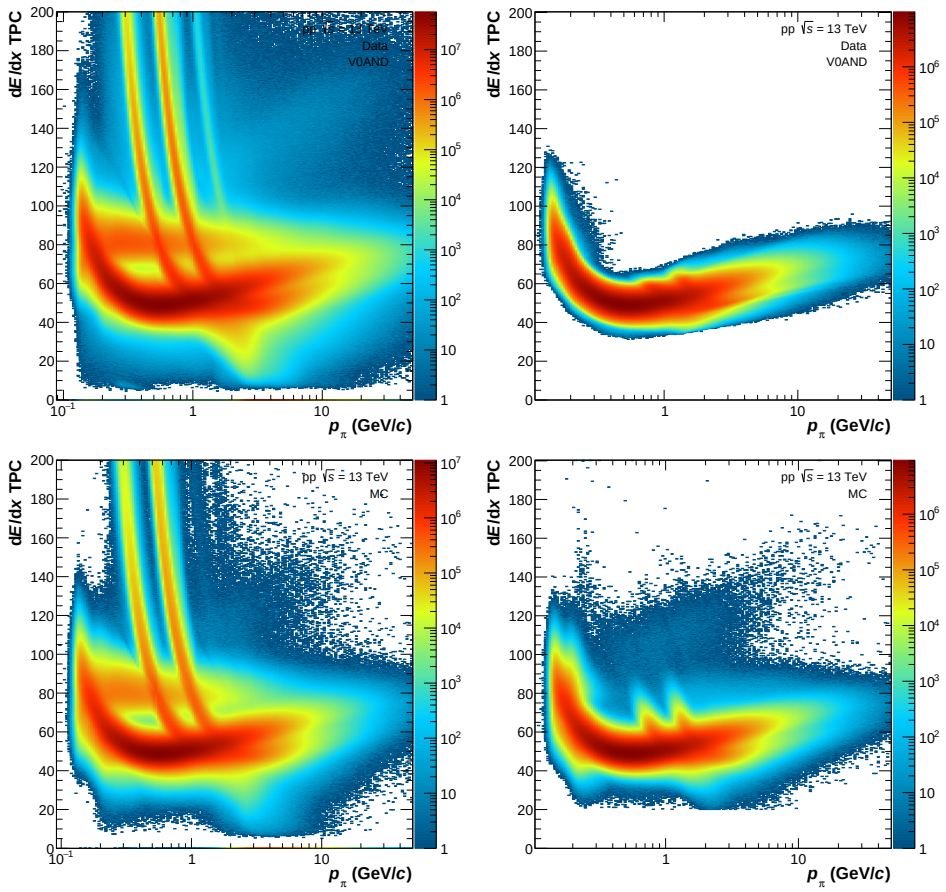

Figure 7.5: Energy loss $\mathrm{d}E/\mathrm{d}x$ for TPC tracks before (**left**) and after (**right**) the PID cuts for π^+ and π^- have been applied for data (**top**) and MC (**bottom**).

be considered minor. Furthermore, a cut of $m_{\pi^+\pi^-} < 850\,\mathrm{MeV}/c^2$ has been applied on the invariant mass $m_{\pi^+\pi^-}$ of charged pion pairs. The choice of this cut is further explained in Sec. 10.2.

8 Photon Reconstruction

The photon measurement in ALICE can be realized in two different ways. Either by measuring them directly with help of the calorimeters EMCal and PHOS or by reconstructing them with the Photon Conversion Method (PCM). In this work, both variants will be used. While this section will discuss the principles of both variants, the direct measurement of photons will focus on the PHOS detector. The reason for this is, that the focus of the π^0 measurement during this work is on the PHOS detector, while calibration and QA of the EMCal detector has been performed within the ALICE collaboration. Furthermore, the principle of the photon measurement is similar in both detectors. However, the EMCal is an important detector for the ω meson cross section measurement, performed in this work, and its most important properties shall be discussed.

8.1 Photon Reconstruction with Photon Conversion Method (PCM)

While photons are stable in vacuum, they have the probability to convert into an e^+e^--pair with the help of a nearby charged scattering partner. In ALICE, photons that convert into e^+e^--pairs in the inner detector material generate charged tracks, which can be measured with the ITS and TPC, as long as the photons are converted within a radius of $R_{\text{conv}} < 180\,\text{cm}$. These tracks can be used to reconstruct V^0-candidates with a secondary vertex with one of the two available V^0-finder algorithms discussed in Sec. 4.2.5. In this analysis, the on-the-fly V^0-finder is used, as it provides improved position and momentum resolution compared to the offline V^0-finder.

The Photon Conversion Method (PCM) makes use of the found V^0-canditates to reconstruct the originating photon. Previous analysis [75][76][77] have shown, that the precision of the reconstructed conversion point can be improved by recalculating the secondary vertex with the requirement, that e^+e^--pairs are parallel at the point of their creation, as photons do not have a mass. This recalculation is also being used in this work. To identify e^+e^--pairs and

Track & V0 cuts		
V0-finder	On-the-Fly	
Cut on R_{conv}	5 cm $< R_{\mathrm{conv}} <$ 55 cm or 72 cm $< R_{\mathrm{conv}} <$ 180 cm	for all reco. methods for all reco. methods, except PCM-PHOS for π^0 and η meson
Line cut	$R_{\mathrm{conv}} > \lvert Z_{\mathrm{conv}}\rvert \cdot S_{\mathrm{ZR}} - Z_0$ with $S_{\mathrm{ZR}} = \tan(2 \cdot \arctan(\exp(-\eta_{\mathrm{cut}})))$, $\eta_{\mathrm{cut}} < 0.8$ and $Z_0 = 7\,\mathrm{cm}$	
Fraction of measured TPC clusters to findable TPC clusters	$> 60\%$	
minimum track p_{T} cut	$p_{\mathrm{T,track}} > 0.05$ GeV/c	
minimum photon momentum	$p_{\mathrm{T},\gamma} > 0.02$ GeV/c	
η-cut for tracks & Secondary vertexs (V^0s)	$\lvert\eta_{\mathrm{track,\ V0,\ cms}}\rvert < 0.8$	
Cut on Z_{conv}	$\lvert Z_{\mathrm{conv}}\rvert$ < 240 cm	
PID cuts		
$n\sigma_{e^\pm}$ TPC dE/dx	$-3 < n\sigma_{e^\pm} < 4$	
$n\sigma_{\pi^\pm}$ TPC dE/dx	0.4 GeV/c $< p <$ 3.5 GeV/c: $p >$ 3.5 GeV/c:	$n\sigma_{\pi^\pm} > 1$ $n\sigma_{\pi^\pm} > 0.5$
Photon cuts		
1D χ^2_γ/ndf cut	χ^2_γ/ndf< 50	
2D χ^2_γ/ndf, $\lvert\psi_{\mathrm{pair}}\rvert$ cut	$\lvert\psi_{\mathrm{pair}}\rvert < 0.18 \cdot \exp(-0.055\chi^2_\gamma)$	
elliptic 2D q_{T} cut (Armenteros)	$q_{\mathrm{T}} < q_{\mathrm{T,max}} \cdot \sqrt{1-\alpha^2/\alpha^2_{\mathrm{max}}}$ with $\alpha_{\mathrm{max}} = 0.95$ and $q_{\mathrm{T,\ max}} = 0.125 \cdot p_{\mathrm{T}}$ (GeV/c) limited by $q_{\mathrm{T,\ max}} = 50.0\,\mathrm{MeV}/c$	
$\cos(\theta_{\mathrm{point}})$	> 0.85	
Reject too close V0s	$\Delta R_{\mathrm{conv}} < 6$, $\quad \mathrm{V}^0\measuredangle < 0.02$	

Table 8.1: Cut applied for V^0 candidates, tracks and photons for the PCM method.

enhance the purity of conversion photons in the V^0 sample, various different cuts have been applied.

To reject V^0 candidates, originating from π^0 and η Dalitz decays, only conversion radii of $R_{\mathrm{conv}} > 5\,\mathrm{cm}$ are allowed. Furthermore, as can be seen in the material budget studies shown in [78], the conversion probability in the range of $55\,\mathrm{cm} < R_{\mathrm{conv}} < 72\,\mathrm{cm}$ is not yet understood and V^0 candidates within this conversion radius are rejected. Due to lack of statistics, a set of specific correction factors for the PHOS acceptance cannot be obtained. Investigations [78] have shown, that the available correction factors in the $72\,\mathrm{cm} < R_{\mathrm{conv}} < 180\,\mathrm{cm}$ applied to the PHOS acceptance deteriorate slightly the agreement. Therefore, the π^0 and η analysis in PCM-PHOS do not use this region. As shown in the appendix figure Fig. A.36, excluding

V^0 candidates with conversion radii within $72\,\text{cm} < R_{\text{conv}} < 180\,\text{cm}$ reduces the number of extracted ω meson candidates by $\approx 30\,\%$. This results in statistical fluctuations in the corrected yield in the order of $10\,\%$, without showing a systematic effect. Due to this reason, photons with conversion radii within $72\,\text{cm} < R_{\text{conv}} < 180\,\text{cm}$ are not excluded for the ω reconstruction. The concept of raw yields and corrected yields is explained in detail in Chap. 9.

Tracks and V^0 candidates have to lie within the acceptance of the TPC and the ITS. Therefore, they are required to be within $|Z_{\text{conv}}| < 240\,\text{cm}$ and $R_{\text{conv}} < 180\,\text{cm}$. These quantities use the center of the detector for their determination. To reduce possible edge effects, a pseudorapidity of $\eta_{\text{track, V0, cms}} < 0.8$ is chosen. As the pseudorapidity of a V^0 candidate is calculated using the angle of its 3-momentum and the z-R-plane, while the starting point of the track is not considered, V^0 candidates have the possibility to lie outside the acceptance of the TPC and the ITS. To reject these candidates a so-called "line-cut" is applied, requiring the condition:

$$R_{\text{conv}} > |Z_{\text{conv}}| \cdot S_{\text{ZR}} - Z_0 \tag{8.1}$$

with $S_{\text{ZR}} = \tan(2 \cdot \arctan(\exp(-\eta_{\text{cut}})))$ and $Z_0 = 7\,\text{cm}$. Charged tracks need to have a momentum of at least $50\,\text{MeV}/c$ and at least $60\,\%$ of findable clusters. The reason for a relative value of findable clusters instead of a total number is, that the momentum dependent curvature and length of a track can differ for secondary particles.

The track identification of $e^{\pm}$ is based on their specific energy loss $\mathrm{d}E/\mathrm{d}x$ in the TPC. Analogously to Eq. 7.1, a cut of $n\sigma_{\text{e}^{\pm}, \text{TPC}}$ around the expected energy loss of $\text{e}^{\pm}$ is used to select $\text{e}^{\pm}$ candidates.

$$n\sigma_{\text{e}^{\pm}, \text{TPC}} = \frac{\mathrm{d}E/\mathrm{d}x\,|_{\text{meas}} - \langle\, \mathrm{d}E/\mathrm{d}x \,\rangle}{\sigma_{\text{Bethe Bloch}}} \tag{8.2}$$

Also here, $\mathrm{d}E/\mathrm{d}x\,|_{\mathrm{meas}}$ is the measured energy loss and $\langle \mathrm{d}E/\mathrm{d}x \rangle$ is the expected energy loss due to the Bethe-Bloch equation (Eq. 3.15) and the TPC calibration with the resolution $\sigma_{\mathrm{Bethe\ Bloch}}$. While the Bethe-Bloch parametrization for the expected energy loss is obtained in a central calibration step by parametrizing various different particle species, the particle distributions can still deviate slightly from the expected energy loss. Hence, an additional calibration step of the average energy loss for electrons has been performed during this work. For this, the mean average loss for different intervals of η, p_{T} and the number of TPC clusters is plotted against $n\sigma_{\mathrm{e}^{\pm},\,\mathrm{TPC}}$. An example of these distributions can be found in Fig. 8.1, while further distributions can be found in [79]. The distributions are fitted for each interval and a recalibration factor dependent on η, p_{T} and the number of TPC clusters is extracted. These recalibration factors are calculated separately for each period and are then applied on analysis level.

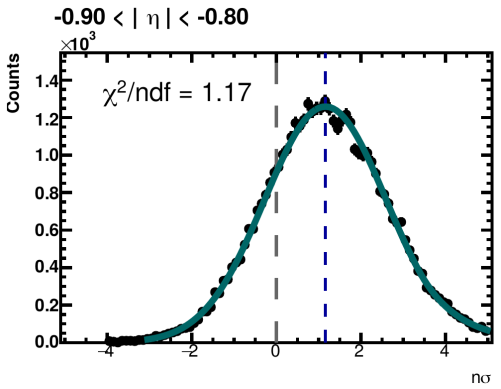

Figure 8.1: $\mathrm{d}E/\mathrm{d}x$ distribution for the p_{T} interval of 0.1 to 0.2 GeV/c and 0 to 60 TPC clusters.

The $\mathrm{d}E/\mathrm{d}x$ distribution in the TPC without a PID selection cut can be found in Fig. 8.2 (left). The $e^{\pm}$ are selected along the $e^{\pm}$ line within $-3 < n\sigma_{e^{\pm}} < 4$. As the $\pi^{\pm}$ band overlaps with the electron band above $\approx 4\,\mathrm{GeVc}$, a track cut along the $\pi^{\pm}$ line dependent on the track momentum p is applied. From momenta between $0.4\,\mathrm{GeV}/c$ and $3.5\,\mathrm{GeV}/c$, tracks within $n\sigma_{\pi^{\pm}} > 1$ and for momenta above $3.5\,\mathrm{GeV}/c$ tracks within $n\sigma_{\pi^{\pm}} > 0.5$ are rejected. Fig. 8.2 (middle) shows the $\mathrm{d}E/\mathrm{d}x$ distribution in the TPC after the PID selection cuts have been applied. The distributions, shown in Fig. 8.2 (right) are acquired after all photon selection criteria are applied. To further increase the purity of the $e^{\pm}$ sample the information of other PID detectors like the TRD or TOF could be used. However, in the end this would significantly reduce the number of available neutral mesons. Furthermore, as reconstructed photons are combined with charged pions to reconstruct ω mesons, a small amount of contamination is negligible. Therefore, no further PID is applied.

Photons are reconstructed using the KFParticle package, which can be found in AliROOT. It is using a Kalman Filter approach [80][81] and a cut on $\chi^2_\gamma/\mathrm{ndf} < 50$ is applied to improve the quality of selected photons. Furthermore, the topology of the decay is used to even further

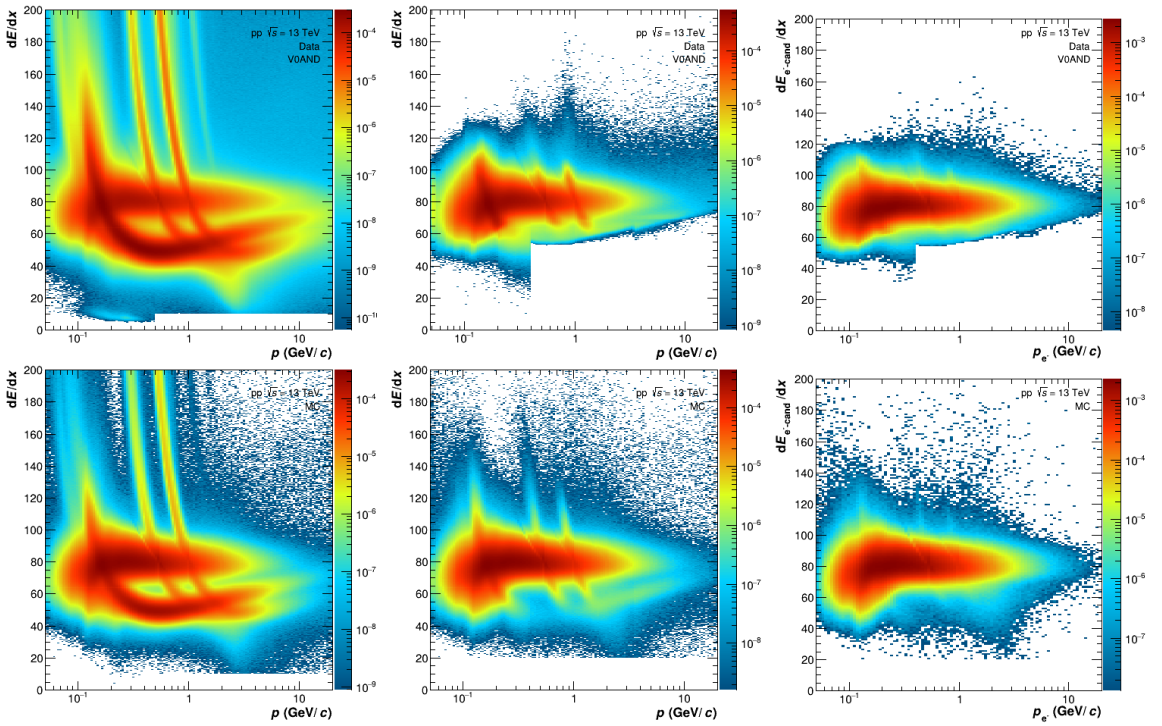

Figure 8.2: Energy loss $\mathrm{d}E/\mathrm{d}x$ for TPC tracks before (**left**) and after (**middle**) the PID cuts for e^+ and e^- have been applied for data (**top**) and MC (**bottom**). The distribution on the **right** are acquired after all photon selection criteria are applied.

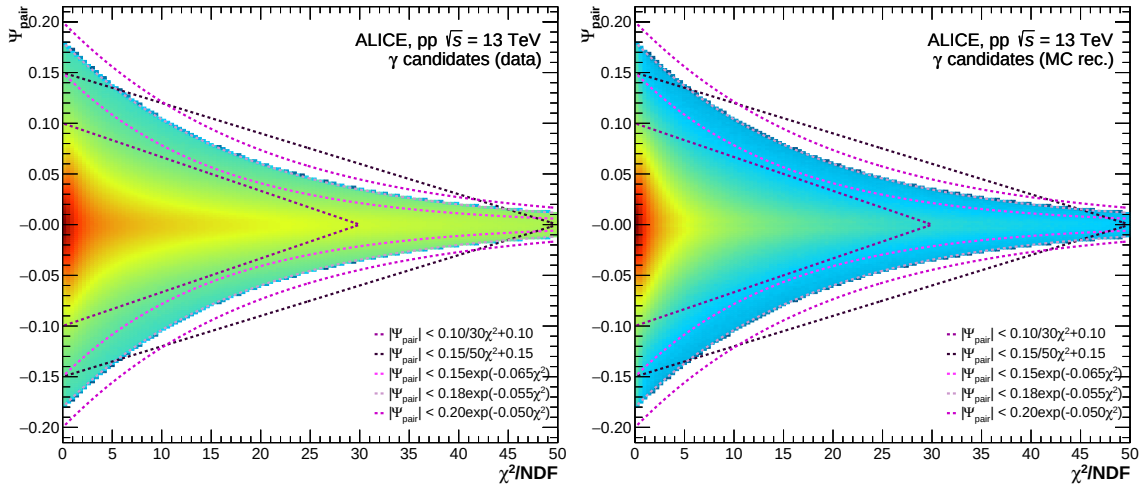

Figure 8.3: Comparison of χ^2/ndf (**left**) and ψ_{pair} (**right**) distributions of the photon candidates in data and different MC contributions. ψ_{pair} against χ^2/ndf for data (**left**) and MC (**right**).

improve this quality. The angle between the plane of e^+e^--pairs and the plane perpendicular to the magnetic field is given by $\psi_{\mathrm{pair}} = \arcsin(\theta_{\mathrm{Opening},e^\pm}/\zeta_{\mathrm{Pair}})$ and is calculated after the tracks are propagated for 50 cm from the conversion point in radial direction. $\theta_{\mathrm{Opening},e^\pm}$ is the opening angle between the e^+e^--pair in polar direction and ζ_{Pair} is defined by their momenta

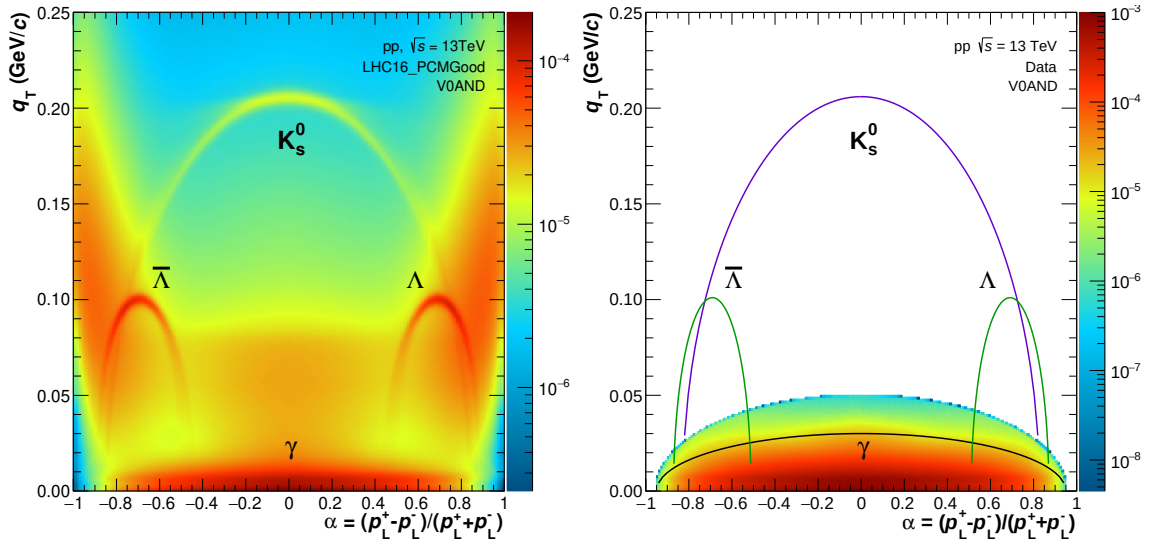

Figure 8.4: Armenteros-Podolanski-Plot of all V^0 candidates after the basic track and V0 cuts (left) and after all cuts are applied (right).

$\vec{p_{e^\pm}}$ with $\zeta_{\text{Pair}} = \arccos((\vec{p_{e^+}} \cdot \vec{p_{e^-}})/(|\vec{p_{e^+}}| \cdot |\vec{p_{e^-}}|))$. A comparison of the distributions of χ^2/ndf and ψ_{pair} for data and MC can be found in Fig. 8.3, where it can be observed that photons are centered around $\psi_{\text{pair}} = 0$. A two-dimensional cut of $|\psi_{\text{pair}}| < 0.18{*}\exp(-0.055\chi^2)$ is applied to reject particles from decays or arbitrary combinations. Furthermore, the pointing angle θ_{Pointing} is defined as angle between the photon vector and the vector that connects the primary vertex, while it is required that $\cos(\theta_{\text{Pointing}}) > 0.85$.

To reject contributions from K^0_S, Λ and $\bar{\Lambda}$ particles, a combination of the longitudinal momentum asymmetry of two charged particles with opposite charge α and the projection q_{T} of the momentum of a daughter particle to its mother particle (the V^0 candidate) is used. With $\theta_{\text{Mother,Daughter}}$ being the angles between mother and daughter particles, p being the momenta of the daughter particles and $p_{\text{L}}^{\pm}$ being the longitudinal momenta of the daughter particles, α and q_{T} are defined as

$$\alpha = \frac{p_{\text{L}}^{+} - p_{\text{L}}^{-}}{p_{\text{L}}^{+} + p_{\text{L}}^{-}} \tag{8.3}$$

and

$$q_{\text{T}} = p \cdot \sin(\theta_{\text{Mother,Daughter}}). \tag{8.4}$$

Decays with two particles of the same mass are symmetrical distributed along α. This is true for photons converting into e^+e^--pairs as well for K^0_S particles, which predominantly decays in $\pi^+\pi^-$-pairs. On the other hand, Λ and $\bar{\Lambda}$ particles dominantly decay into a proton (antiproton) and a π^- (π^+) resulting in an asymmetric decay with $|\alpha| \approx 0.7$. The Armenteros-

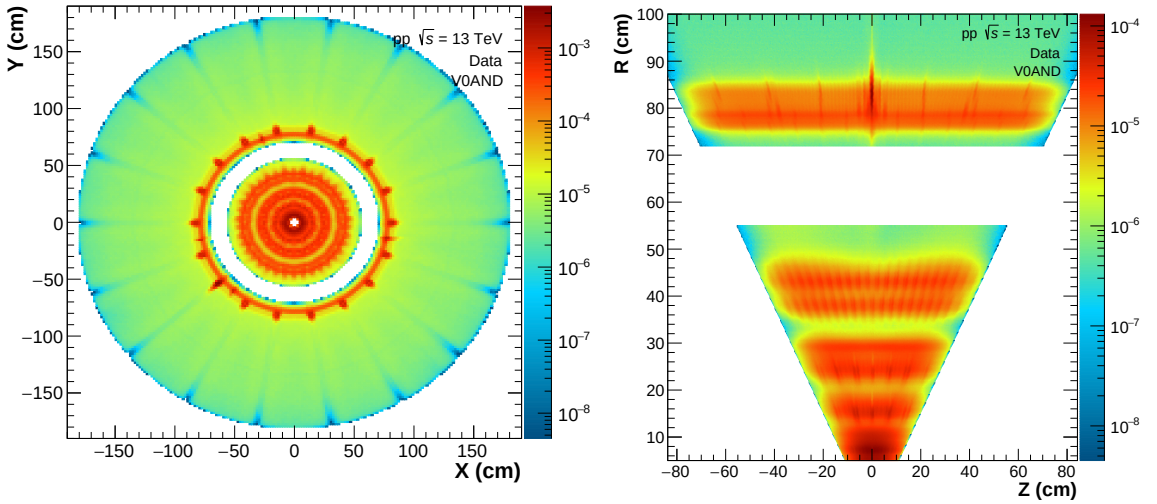

Figure 8.5: Conversion points of gamma candidates in the xy-plane (left) and zR-plane (right) in ALICE.

Podolanski-Plot is plotting q_{T} against α and can be found in Fig. 8.4 (left). In this thesis an elliptical cut of $q_{\mathrm{T}} < q_{\mathrm{T,max}} \cdot \sqrt{1-\alpha^2/\alpha^2_{\mathrm{max}}}$ with $\alpha_{\mathrm{max}} = 0.95$ and $q_{\mathrm{T,\,max}} = 0.125 \cdot p_{\mathrm{T}}\,(\mathrm{GeV}/c)$ is applied. Furthermore, $q_{\mathrm{T,\,max}}$ is limited to a maximum value of $q_{\mathrm{T,\,max}} = 50.0\,\mathrm{MeV}/c$. Fig. 8.4 (right) shows the remaining photon candidates after all cuts have been applied. As can be seen, only a small fraction of Λ and $\bar{\Lambda}$ particles are able to survive the cuts. Fig. 8.5 visualizes the photon conversion points in the xy-plane (left) and zR-plane (right). Conversions predominantly occur within the layers of the ITS and the field cage of the TPC. The line cut can be seen in the rectangular form in the zR-plane. The conversion probability has been studied, while Material Budget weights have been calculated in [78]. By implementation of these material budget weights, the systematic uncertainty on the material budget is significantly reduced compared to previous analysis.

8.2 Photon Reconstruction with Calorimeters

The two calorimeters EMCal and PHOS have been used to reconstruct photons during this work. Photons, electrons and positrons, that hit a calorimeter produce electromagnetic showers in the calorimeter, that expand over multiple adjacent cells. The energy deposited in a cell is E_{cell}. These cells are grouped into so-called clusters with an energy E_{cluster} by algorithms called clusterizers. Heavier particles, also called minimum ionizing particles (MIPs), only lose a fraction of their energy in the calorimeters. For the clusterizing process, two energy thresholds, called seed energy E_{seed} and aggregation energy $E_{\mathrm{aggregation}}$, are needed.

Cluster cuts	PHOS	EMCal
clusterizer	Unfolding	Clusterizer V3
minimum seed energy E_{seed}	50 MeV	500 MeV
minimum cell energy $E_{\text{aggregation}}$	15 MeV	100 MeV
minimum cluster energy E_{cluster}	0.3 GeV	0.7 GeV
minimum number of $N^{\text{cells}}_{\text{cluster}}$	1 for $E_{\text{cluster}} < 1$ GeV, 2 for $E_{\text{cluster}} \geq 1$ GeV	1 for $E_{\text{cluster}} < 4$ GeV, 2 for $E_{\text{cluster}} \geq 4$ GeV
long cluster axis σ^2_{long}	open for $E_{\text{cluster}} < 1$ GeV, $0.1 < \sigma^2_{\text{long}} < 100$ for $E_{\text{cluster}} \geq 1$ GeV	open for $E_{\text{cluster}} < 1$ GeV, $0.1 < \sigma^2_{\text{long}} < 0.50$ for $E_{\text{cluster}} \geq 4$ GeV
Cluster time t_{cluster}	$< \lvert 30 \rvert$ ns & timing cut efficiency	$-20\,\text{ns} < t_{\text{cluster}} < 25\,\text{ns}$
Opening angle	> 0.005	
Trackmatching	$\lvert\eta\rvert < 0.02$, $\lvert\varphi\rvert < 0.08$	$\Delta\eta \leq 0.01 + (p_{\text{T}} + 4.07)^{-2.5}$ $\Delta\phi \leq 0.015 + (p_{\text{T}} + 3.65)^{-2}$ $E_{\text{cluster}}/p_{\text{track}} < 1.75$
Exotic cluster cut	none	$F_+ < 0.97$ & $N_{\text{T-Card}}$ for $E_{\text{cluster}} > 50\,\text{GeV}$

Table 8.2: Standard cuts for the PHOS and EMCal cluster selection.

The EMCal clusterizer uses a seed energy of $E_{\text{seed}} = 500\,\text{MeV}$ and an aggregation energy of $E_{\text{aggregation}} = 100\,\text{MeV}$, while these thresholds for the PHOS clusterizer are $E_{\text{seed}} = 50\,\text{MeV}$ and $E_{\text{aggregation}} = 15\,\text{MeV}$. The threshold values are chosen to reject minimum MIPs and detector noise, while differences in these energy thresholds and the cuts are mostly originating from the different granularity and resolution of the two detectors. Generally, a clusterizer sorts all cells according to their energy and starting with the highest energy cell, unclustered cells with $E_{\text{cell}} > E_{\text{seed}}$ are used to build new clusters. Adjacent cells to the cluster are added to the cluster, as long as $E_{\text{cell}} > E_{\text{aggregation}}$. This step is repeated as long as there are available cells with a common edge to the cluster, that fulfill the condition $E_{\text{cell}} > E_{\text{aggregation}}$. For EMCal, the V3 clusterizer is used. In addition to the condition $E_{\text{cell}} > E_{\text{aggregation}}$, this clusterizer requires the energy of a newly added cell to be lower than the energy of the adjacent cluster cell. While this enables the V3 clusterizer of EMCal to handle overlapping clusters, the PHOS clusterizer uses an unfolding method on clusters with multiple local maxima, after the clusters have been created. The unfolding method then splits clusters and uses their local minima as new cluster edges. After a cluster has been created, the clusterizer continues to build new clusters with unclustered cells starting with the next highest energy cell, as long as the condition $E_{\text{cell}} > E_{\text{seed}}$ is hold.

As described in Sec. 6.4, bad channels are flagged by a BCM. For the EMCal, only cells which are not flagged as bad are added to a cluster during a re-clusterization process. PHOS uses a different approach. For each cluster it is checked if the cluster is positioned at a cell position, that is flagged as bad. In this case, the cluster is rejected for the analysis entirely.

The resulting cluster consists of $N_{\text{cluster}}^{\text{cells}}$ cells with specific cell energies $E_{\text{cell, i}}$ and the total energy of a cluster E_{cluster} is calculated by:

$$E_{\text{cluster}} = \sum_{i}^{N_{\text{cluster}}^{\text{cells}}} E_{\text{cell, i}} \tag{8.5}$$

While photons create clusters of circular shape, charged particles are bend in the magnetic field and hit the calorimeter in an angle, leading to clusters of elliptical shape. This property can be described by σ^2_{long}, which corresponds to the long axis of the ellipse. It is defined by:

$$\sigma^2_{\text{long}} = 0.5 \cdot \left(\sigma^2_{\Phi\Phi} + \sigma^2_{\eta\eta} + \sqrt{\left(\sigma^2_{\Phi\Phi} - \sigma^2_{\eta\eta}\right) + 4\sigma^4_{\Phi\eta}}\right) \tag{8.6}$$

The coefficients σ_{ab} are weighted by the cell energies and are calculated by:

$$\sigma_{ab} = \sum_{i}^{N_{\text{cluster}}^{\text{cells}}} \frac{\omega_i a_i b_i}{\omega_{tot}} - \sum_{j}^{N_{\text{cluster}}^{\text{cells}}} \frac{\omega_j a_j}{\omega_{tot}} \sum_{k}^{N_{\text{cluster}}^{\text{cells}}} \frac{\omega_k b_k}{\omega_{tot}} \tag{8.7}$$

with $\omega_{tot} = \sum_i^{N_{\text{cluster}}^{\text{cells}}} \omega_i$ and $\omega_i = \max(0, 4.5 + \log(E_{\text{cell, i}}/E_{\text{cluster}}))$. Neutrons hitting the detector create clusters with one high energetic cell, surrounded by low energetic cells. These clusters are rejected with a cut of $\sigma^2_{\text{long}} > 0.1$ in both calorimeters. Furthermore, to reject contributions from low energetic electrons and merging clusters at high momenta in the EMCal, a cut of $\sigma^2_{\text{long}} < 0.5$ is applied. Obviously, a cut on σ^2_{long} requires clusters with $N_{\text{cluster}}^{\text{cells}} \geq 2$. As low energy photons can create clusters with only one cell, a cut on $N_{\text{cluster}}^{\text{cells}} \geq 2$ is applied for energies above 1 GeV for PHOS and 4 GeV for EMCal and the cut on σ^2_{long} is therefore only applied above these energies.

Fig. 8.6 (left) shows the timing distribution t_{cluster} for PHOS clusters for different cluster energies. It can be seen, that the timing uncertainty is reduced for higher energies. To reduce the amount of out-of-bunch pileup, a cut on t_{cluster} is used. The chosen timing-window for EMCal is $-20\,\text{ns} < t_{\text{cluster}} < 25\,\text{ns}$, while a timing window of $|t_{\text{cluster}}| < 30\,\text{ns}$ is applied for PHOS. No proper timing information is available for MC and the amount of lost photon clusters due to this cut has to be accounted for by the so-called timing efficiency. This efficiency describes the fraction of lost reconstructed π^0 mesons due to an applied timing cut in comparison to a loose timing cut. Investigations within the ALICE collaboration have

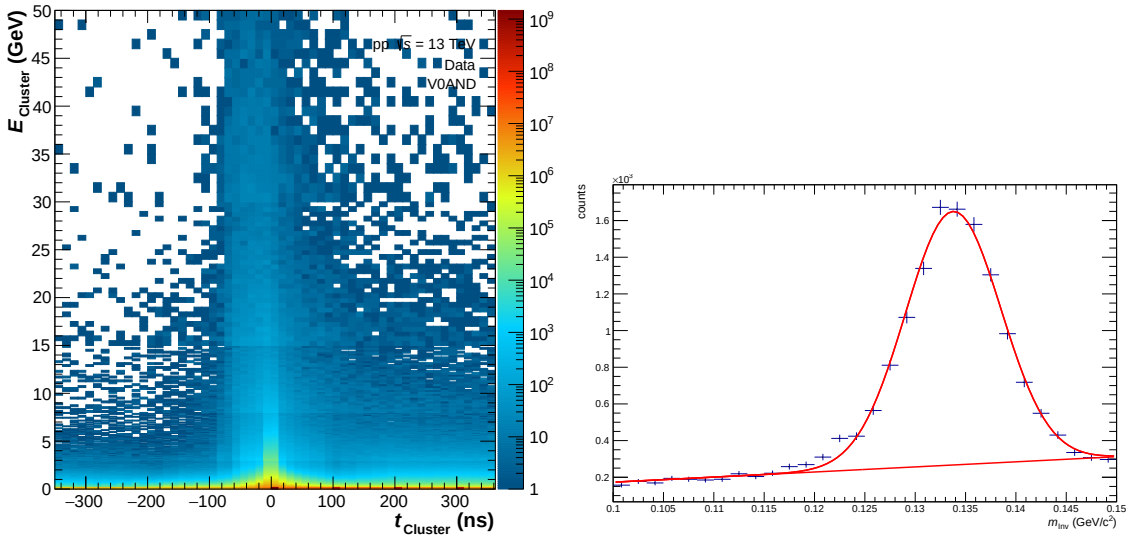

Figure 8.6: **Left:** Timing distribution for PHOS clusters. The timing uncertainty becomes smaller for higher energies. Contributions from different bunch crossings are visible. **Right:** Fit of invariant mass distribution for an example interval between 12.8 and 15.15 GeV/c^2 for $|t_{\text{cluster, probe}}| < 30$ ns.

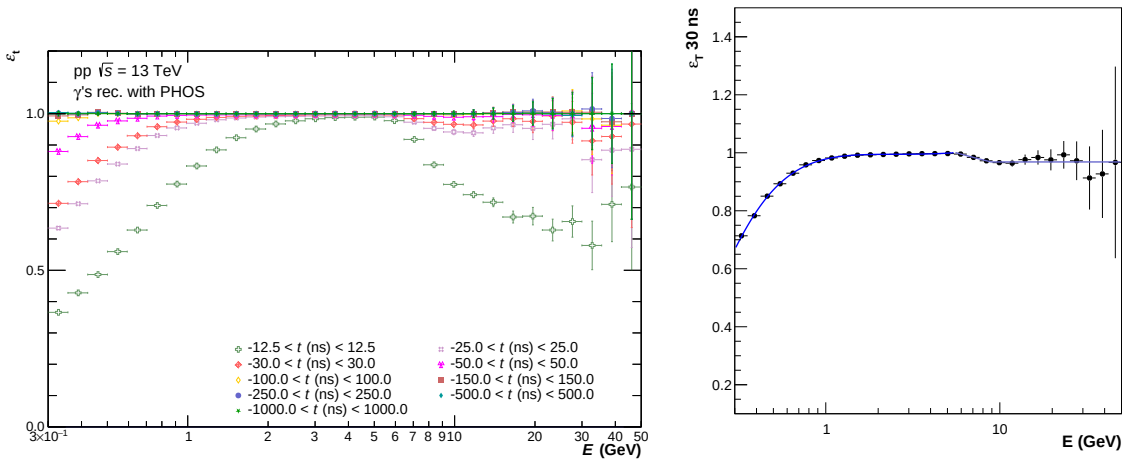

Figure 8.7: **Left:** Timing efficiency for different timing cuts on clusters for PHI7 triggered sample. **Right:** Fit on timing efficiency for a timing cut of $|t_{\text{cluster, probe}}| < 30$ ns for PHI7 triggered sample.

shown, that this effect is negligible for EMCal and no timing efficiency will be applied in this case. However, it has shown to have a significant effect for the PHOS detector.

For the timing efficiency, π^0 meson yields are reconstructed in a simple invariant mass analysis. Here, two photons with cluster energies $E_{\text{cluster},1}$ and $E_{\text{cluster},2}$ are combined to calculate the invariant mass m_{Inv} of π^0 candidates with:

$$m_{\text{Inv}} = \sqrt{2E_{\text{cluster},1}E_{\text{cluster},2}(1-\cos(\theta_{1,2}))} \tag{8.8}$$

Here, the two photons that form a π^0 candidates are also called legs in this work. $\theta_{1,2}$ is the angle between the three-momentum vectors of those legs. The basic principles of an invariant mass analysis will be explained for the energy correction in this section, while a more detailed explanation will be given in Chap. 9. The PHI7 triggered data set has been used for the number of photons for higher energies, as this number is significantly lower for the MB triggered data set. However, the MB triggered data has been used to estimate the systematic uncertainty. To ensure a good timing information, one leg, called tag, is required to have a cluster energy $E_{\text{cluster,tag}}$ between 2.0 and 5.5 GeV/c^2. Furthermore, the tag needs to be within the timing window of $|t_{\text{cluster, tag}}| < 30$ ns. The second leg is called probe, while only probes within the timing window of $|t_{\text{cluster, probe}}| < 1000$ ns are selected. By applying different timing cuts on the probe, the yield of reconstructed π^0 candidates reduces. The invariant mass distributions for different probe energy $E_{\text{cluster,probe}}$ intervals and different probe timing cuts are parametrized with a Gaussian with an additional linear background. An example for these parametrizations for $|t_{\text{cluster, probe}}| < 30$ ns and 12.8 GeV $< E_{\text{cluster,probe}} <$ 15.15 GeV can be found in Fig. 8.6 (right). After the linear background parametrization has been subtracted, the yields are acquired by integrating in a given mass window between 120 and 150 GeV/c^2. By dividing these yields for different probe timing cuts by the yield of an open probe timing cut of $|t_{\text{cluster, probe}}| < 1000$ ns, the timing efficiency is calculated for different probe energies and timing cuts, shown in Fig. 8.7 (left). The timing efficiency is parametrized in a low and a high energy part, which can be seen in Fig. 8.7 (right) for $|t_{\text{cluster, probe}}| < 30$ ns. During the analysis in MC, a random value between 0 and 1 is generated and the generated value is compared to the timing efficiency value at an energy E_{cluster} of a given cluster. If the generated value is above the timing efficiency value, the cluster is rejected.

To remove clusters originating from charged particles like $e^{\pm}$, a method called track-matching is used. For track-matching, charged tracks are propagated to the calorimeter surface where it compared to nearby clusters in η and ϕ. If tracks are pointing too close to a cluster, this cluster is rejected. The exact parameters for the used track-matching can be found in Tab. 8.2.

It is important, that the cluster energies in data and MC are similar to each other. For this purpose an energy calibration, also called fine-tuning or non-linearity correction, has been performed for PHOS during this work, while the fine-tuning for EMCal has been performed within the ALICE collaboration. First, it shall be explained how the energy calibration was performed in general before details of the PHOS implementation during this work are discussed. Similar to the timing efficiency, the energy calibration is based on an invariant mass analysis of π^0 mesons, where the invariant mass m_{π^0} is calculated by Eq. 8.8. Here, either both photons or just one photon can be measured by the calorimeter. In the latter

case, the second photon is acquired with help of PCM, while this reconstruction method is called PCM-EMCal or PCM-PHOS, dependent on the used calorimeter. If both photons are measured by a calorimeter, the neutral pion reconstruction method is commonly named the same as the used detector itself. For the EMCal and PHOS method, only symmetric decays are used. This is realized with a cut on the asymmetry $\alpha_{\gamma_1\gamma_2} < 0.1$ on the momenta p_{γ_i} of both photons with:

$$\alpha_{\gamma_1\gamma_2} = \frac{|p_{\gamma_1} - p_{\gamma_2}|}{p_{\gamma_1} + p_{\gamma_2}} \tag{8.9}$$

In this case, the energy of both photons E_{γ_i} is nearly the same and can be approximated by $E_{\gamma_1} \approx E_{\gamma_2} \approx E_\gamma$ and Eq. 8.8 simplifies to:

$$m_{\pi^0} = \sqrt{2E_\gamma^2(1-\cos(\theta_{1,2}))} = \sqrt{E^{\pi^0}(1-\cos(\theta_{1,2}))} = \sqrt{p_{\mathrm{T}}^{\pi^0}(1-\cos(\theta_{1,2}))} \tag{8.10}$$

The invariant mass m_{π^0} distributions are generated for various cluster energy intervals. The resulting histograms H_{SB} consist of a signal on top of an additional background. The background is estimated by an event-mixing histogram H_{B}, where more details will be explained in Sec. 9. The estimated background is normalized to H_{SB} outside the signal region and then subtracted from H_{SB} resulting in a signal histogram H_{S}. The resulting signal distributions in

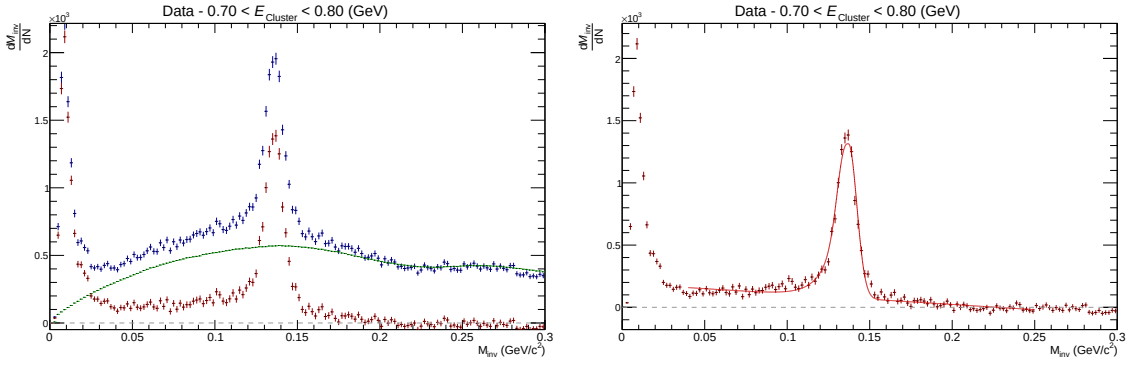

Figure 8.8: Invariant mass distribution for PHOS energy calibration for 0.7 GeV $< E_{\mathrm{cluster}} <$ 0.8 GeV. **Left:** Comparison of signal with additional background (blue) to normalized event mixing background (green) and the signal distribution (red). **Right:** Signal distribution fitted with a Gaussian with an exponential tail on the left plus an additional linear function.

data and MC are parametrized with a Gaussian with an exponential tail on the left plus an additional linear function and the mass positions are acquired. An example of these distributions for 0.7 GeV $< E_{\mathrm{cluster}} <$ 0.8 GeV is shown in . One approach to calculate the energy calibration is to parametrize the mass positions in data and MC individually by $F_{\pi^0,\,\mathrm{Ind.}}$. The resulting energy calibration is then calculated by building the ratio $F_{\pi^0,\,\mathrm{Ind.,\,R.}}$ of $F_{\pi^0,\,\mathrm{Ind.}}$ for

data and MC. Another approach to calculate the energy calibration is to parametrize the ratio between the mass positions in data and MC directly by $F_{\pi^0,\,\mathrm{R.}}$. The parametrization functions of the ratios are used as correction factor for the energy of MC clusters.

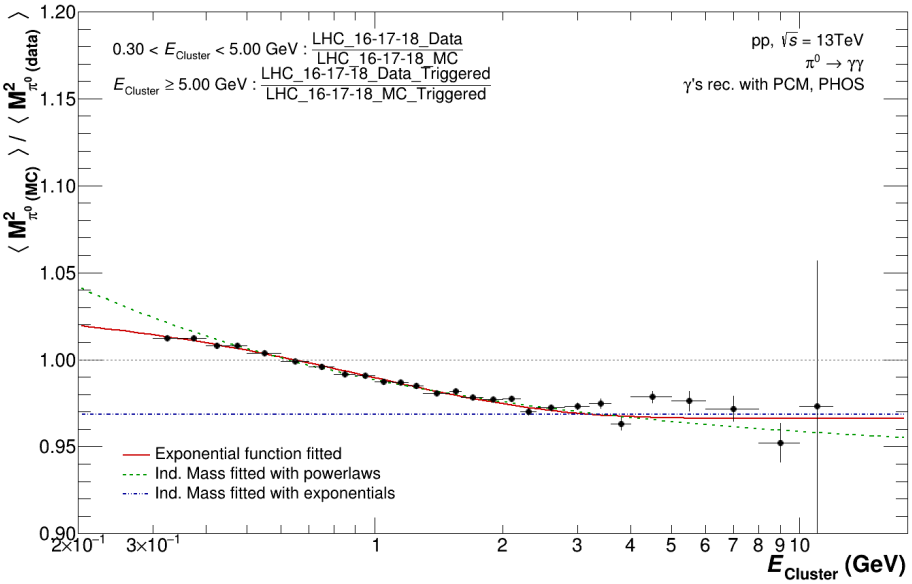

Figure 8.9: Ratio of mass position of MC and data for PCM-PHOS method in first cluster energy calibration iteration. While different parametrizations are shown, the exponential function has been used for the calibration.

For PHOS, multiple iterations of the calibration have been performed on the LHC16 dataset. Each calibration step is added to the previous calibration multiplicative. At first, the PCM-PHOS has been used to generate an energy correction for PHOS clusters. The ratio between the mass position of MC and data for the PCM-PHOS method for the first cluster energy calibration iteration can be found in Fig. 8.9. After this, a high-p_{T} constant fit to the ratio of the π^0 mass position in data to the Particle Data Group (PDG) [10] value between 1 and 12 GeV was used to shift the mass position in data and MC by the inverse of the fit value. At last, the PHOS method has been used on top of the previous correction to reduce the difference between the cluster energies in data and MC even further. The resulting mass position in data and MC for PHOS and PCM-PHOS are plotted in Fig. 8.10. The distributions of this plot have been acquired after a full signal reconstruction described in Sec. 9 has been performed. The observed deviation is below 1 % over the whole p_{T} range and can be considered as in good agreement.

The EMCal studies within the ALICE collaboration showed, that there exist clusters where the leading cell contains nearly all cluster energy. These clusters, also called exotics, are believed to be artificial clusters originating from the readout electronics. These clusters are rejected by an exotic cluster cut, whose parameters can be found in Tab. 8.2. F_+ is the

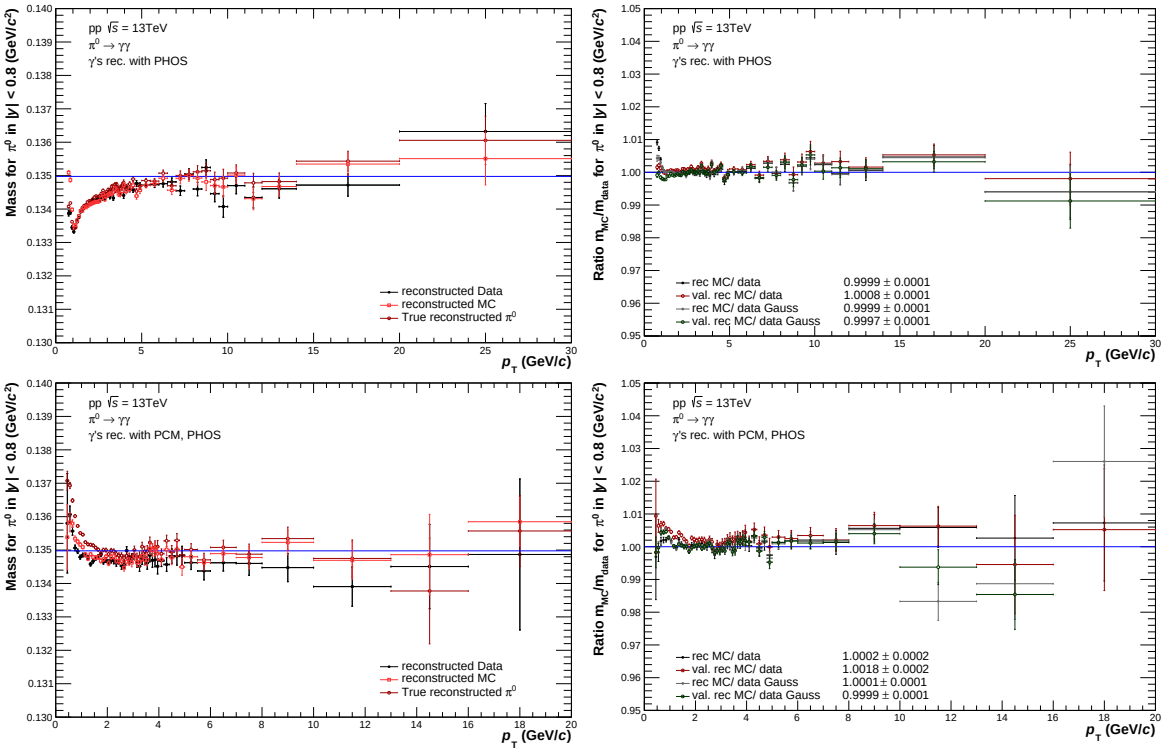

Figure 8.10: **Left:** Reconstructed π^0 masses for data, MC and true reconstructed MC for MB. The π^0 reconstruction is performed with the PHOS calorimeter on **top**, while PCM-PHOS has been used in **bottom**. **Right:** Ratio of MC distributions to data.

energy fraction of the leading cell to the sum of the energy of the leading cell and the four adjacent cells and has to be smaller than 0.97. A T-Card is a readout unit of the EMCal, which consists of 2×8 cells. As clusters increase in size with increasing energy, it is very unlikely that physical clusters can exist in only one T-Card above a certain energy threshold. Therefore, clusters only contain cells in one T-Card are rejected for $E_{\mathrm{cluster}} > 50\,\mathrm{GeV}$.

9 Measurement of π^0 and η Meson Production Cross Sections

The π^0 and η mesons are the lightest neutral mesons, making them one of the most abundant particles created in ultrarelativistic pp collisions. In the analysis presented in this thesis, both mesons are reconstructed via their dominant decay into two photons. As described in Sec. 8.2, photons in ALICE can either be measured directly with help of the calorimeters EMCal or PHOS or be measured by making use of their probability to convert into e^+e^--pairs. If both photons for the neutral meson reconstruction are measured with a calorimeter, the reconstruction method is called the same as the used detector. This means, that the acronyms PHOS or EMCal can be used for both cases: For the name of the calorimeter itself or for the reconstruction method based on these detectors. Furthermore, if both photons are measured by making use of e^+e^--pairs, the reconstruction method is called Photon Conversion Method (PCM). If one photon is acquired with a calorimeter and the second photon is acquired using PCM, the reconstruction method is called PCM-EMCal or PCM-PHOS, dependent on the used calorimeter.

To measure the production cross section of these mesons an invariant mass based analysis is performed. The invariant mass m_{Inv} of two photons is calculated according to Eq. 8.8. As the π^0 and η meson candidates are measured via their decay into two photons and to distinguish the calculated invariant mass of these mesons from the peak position $m_{\pi^0(\eta)}$ in Eq. 9.2 and the invariant mass $m_{\pi^+\pi^-\pi^0}$ of ω meson candidates, the invariant mass of the π^0 and η meson candidates is also called $m_{\gamma\gamma}$ in this thesis. While this work is using the PHOS and PCM-PHOS method to reconstruct $m_{\gamma\gamma}$, the reconstruction of $m_{\gamma\gamma}$ with the remaining methods have been done accordingly within the ALICE collaboration. This also includes the merged EMCal (mEMC) and the PCM-Dalitz reconstruction method. The mEMC is a purity based reconstruction method for merged EMCal clusters. PCM-Dalitz is a hybrid reconstruction method, utilizing PCM and a Dalitz-decay. The mEMC and PCM-Dalitz method will not be further explained during this thesis. The combination of the different reconstruction methods for the π^0 and η meson were performed in close collaboration with the "Soft Photons and Neutral Mesons Physics Analysis Group" within the ALICE collaboration,

Meson cuts	PHOS	PCM-PHOS
pseudorapidity	$\lvert\eta_{\pi^0(\eta)}\rvert < 0.8$	$\lvert\eta_{\pi^0(\eta)}\rvert < 0.8$
minimum opening angle $\theta_{\text{Min, }\pi^0(\eta)}$ in mrad	5	5
energy asymmetry	$\lvert\alpha_{\pi^0(\eta)}\rvert < 1$	$\lvert\alpha_{\pi^0(\eta)}\rvert < 1$

Table 9.1: Standard cuts for the PHOS and EMCal meson selection.

analogously to the combination of different ω meson reconstruction methods. As the details on the combination procedure of ω mesons can be found in Chap. 10, no details on the combination procedure of π^0 and η mesons are discussed in this chapter.

It shall be explicitly mentioned, that the final determination of the choice of the possible TRF for the PHOS detector has not been performed during this work, as explained in Sec. 6.3. Investigations, on the correct choice of the possible TRF calculations, implemented during this work, was continued in close collaboration with Adrian Florin Mechler[1]. As the determination, which TRF calculation should be chosen has not been performed during this work, the last but very important analysis step, the determination of the systematic uncertainties for π^0 and η mesons, has also not been performed for this thesis, but where determined in collaboration with Adrian Florin Mechler, after the TRF had been decided. Due to this reason, the figures that show corrected yields, cross sections or comparisons to other measurements in this chapter, were provided by the ALICE collaboration.

To perform the invariant mass based analysis, $m_{\gamma\gamma}$ and p_{T} of the meson candidates are filled in a 2D-histogram for each neutral meson candidate. This histogram is then projected to multiple p_{T} intervals. The choice of the p_{T} intervals is based on the reduction of statistical uncertainties and the increase of the p_{T} resolution, while still providing a stable signal extraction for as many methods as possible. This also includes the PCM, EMCal and PCM-EMCal method.

The black distribution (SigBG) in Figs. 9.1 shows the $m_{\gamma\gamma}$ distribution of all neutral meson candidates, that pass the selection criteria discussed in this work. This distribution is the sum of the desired neutral meson signal and a background. The background consists of a mainly combinatorial background, originating from uncorrelated photon pairs and an additional remaining background from falsely identified particles. There are multiple ways to describe the combinatorial background. This work is using the event-mixing approach. In comparison to parametrizing the background, the event-mixing method is using a physics based approach. It creates a background distribution by ensuring that no correlation between two combined photons exists, by only combining photons from different events. This is realized by different

[1]Institut für Kernphysik, Universität Frankfurt, Frankfurt, Germany

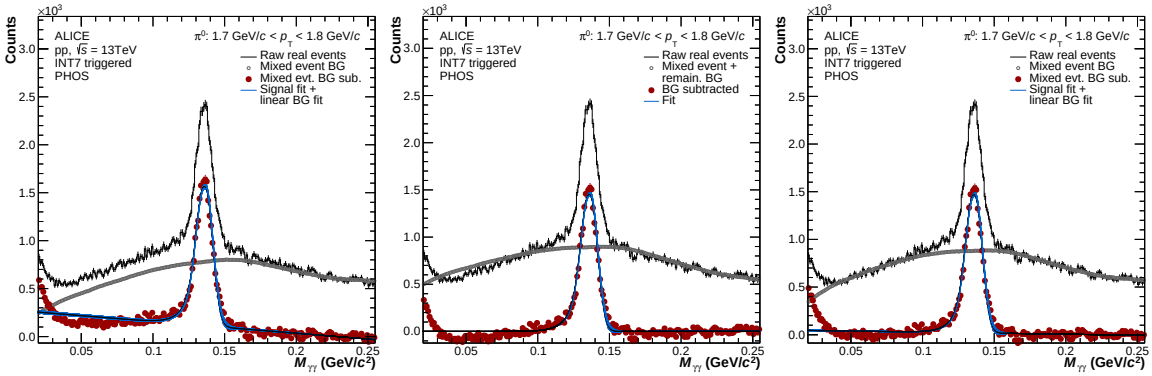

Figure 9.1: Example distributions of $m_{\gamma\gamma}$ for $1.7\,\text{GeV} < p_\text{T} < 1.8\,\text{GeV}$ for PHOS in the MB triggered data set of LHC16. The black distribution shows all meson candidates for the chosen p_T inverval. The gray dots show the estimated background distribution. The red dots are acquired by subtracting the black distribution by the gray dots and correspond to the signal distribution. **Left:** Background distribution is acquired by event mixing. The background is then normalized to the signal distribution on the right side of the peak. The remaining background is estimated by a linear function, but not yet subtracted. After subtracting the remaining linear background distribution the **middle** plot is acquired. **Right:** The ratio of the event mixing background to all meson candidates is parametrized outside the peak region and the event mixing background is scaled by this parametrization. No remaining background is subtracted for this method, as it is included in the mixed event distribution.

Event Mixing Class	Bin Number	Bin Value for PHOS	Bin Value for PCM-PHOS
Photon multiplicity N_γ	1	2	1
	2	3	2
	3	4	3
	4	≥ 4	≥ 3
z-vertex position Z_Vtx in cm	1	-50 to -3.38	-50 to -3.38
	2	-3.38 to -1.61	-3.38 to -1.61
	3	-1.61 to -0.23	-1.61 to -0.23
	4	-0.23 to 1.07	-0.23 to 1.07
	5	1.07 to 2.45	1.07 to 2.45
	6	2.45 to 4.25	2.45 to 4.25
	7	4.25 to 50.0	4.25 to 50.0

Table 9.2: Intervals for event-mixing buffers.

buffers, which store the photon candidates of up to 80 events. If an event buffer has reached this limit, the first added event is deleted to store the photon candidates of the new event. This procedure is called first in first out (FIFO). All photons of the actual event are paired with all photons of the corresponding FIFO buffer. The background shape depends on the primary z-vertex position Z_Vtx and the photon multiplicity N_γ. Hence, a buffer for different Z_Vtx and N_γ bins is used, while all photons of an event are combined with all photons in

Method	$m_{\gamma\gamma}$ of π^0 in GeV/c^2	$m_{\gamma\gamma}$ of η in GeV/c^2
PHOS	$0.19 < m_{\gamma\gamma} < 0.3$	$0.62 < m_{\gamma\gamma} < 0.79$
PCM-PHOS	$0.17 < m_{\gamma\gamma} < 0.3$	$0.58 < m_{\gamma\gamma} < 0.79$

Table 9.3: Integration ranges for scaling event-mixing BG.

the event buffer with corresponding Z_{Vtx} and N_γ to generate background meson candidates. The different intervals for Z_{Vtx} and N_γ, used for the event-mixing buffers can be found in Tab. 9.2. The invariant mass of the resulting background meson candidates and its transverse momentum is filled in a 2D-histogram and projected to multiple p_{T} intervals analogously to SigBG.

The background distributions in the three example plots of Figs. 9.1 are represented by gray dots. Two different approaches to use the event-mixing background have been investigated during this work. The background distribution in Fig. 9.1 (left) was acquired by integrating SigBG and the event-mixing background outside the peak region and using the integral to scale the event-mixing background to SigBG. The corresponding integration ranges to scale the background can be found in Tab. 9.3. After the background has been subtracted, the raw signal distribution remains, shown in red dots. This distribution is parametrized with a function $F_{\pi^0(\eta)}$, consisting of a Gaussian with a tail on the left side on top on a polynomial function. $F_{\pi^0(\eta)}$ is defined as:

$$F_{\pi^0(\eta)} = A \cdot \left(G(m_{\gamma\gamma}) + \exp\left(\frac{m_{\gamma\gamma} - m_{\pi^0(\eta)}}{\lambda} \right) \cdot (1 - G(m_{\gamma\gamma})) \cdot \theta_{\mathrm{H}} \left(m_{\pi^0(\eta)} - m_{\gamma\gamma} \right) \right) + P_0 + P_1 \cdot m_{\gamma\gamma} + P_2 \cdot m_{\gamma\gamma}^2 + P_3 \cdot m_{\gamma\gamma}^3 \quad (9.1)$$

with

$$G(m_{\gamma\gamma}) = \exp\left(-0.5 \left(\frac{m_{\gamma\gamma} - m_{\pi^0(\eta)}}{\sigma_{m_{\pi^0(\eta)}}} \right)^2 \right) \quad (9.2)$$

The Gaussian $G(m_{\gamma\gamma})$ is defined by the width $\sigma_{m_{\pi^0(\eta)}}$ and the mean position $m_{\pi^0(\eta)}$. The amplitude of the reconstructed meson is given by A. While the exponential tail is driven by λ, the Heavyside step function θ_{H} ensures, that the tail only occurs on the left side of the meson peak. The remaining background is described by a linear function with the parameters P_0 and P_1. The second and third order polynomial parameters P_2 and P_3 are not used in the shown distributions, but were used to check its effect on the background description. The resulting parametrization is shown as blue line in Fig. 9.1 (left). The exponential tail is originating from late photon conversions, as well as energy loss due to bremsstrahlung for

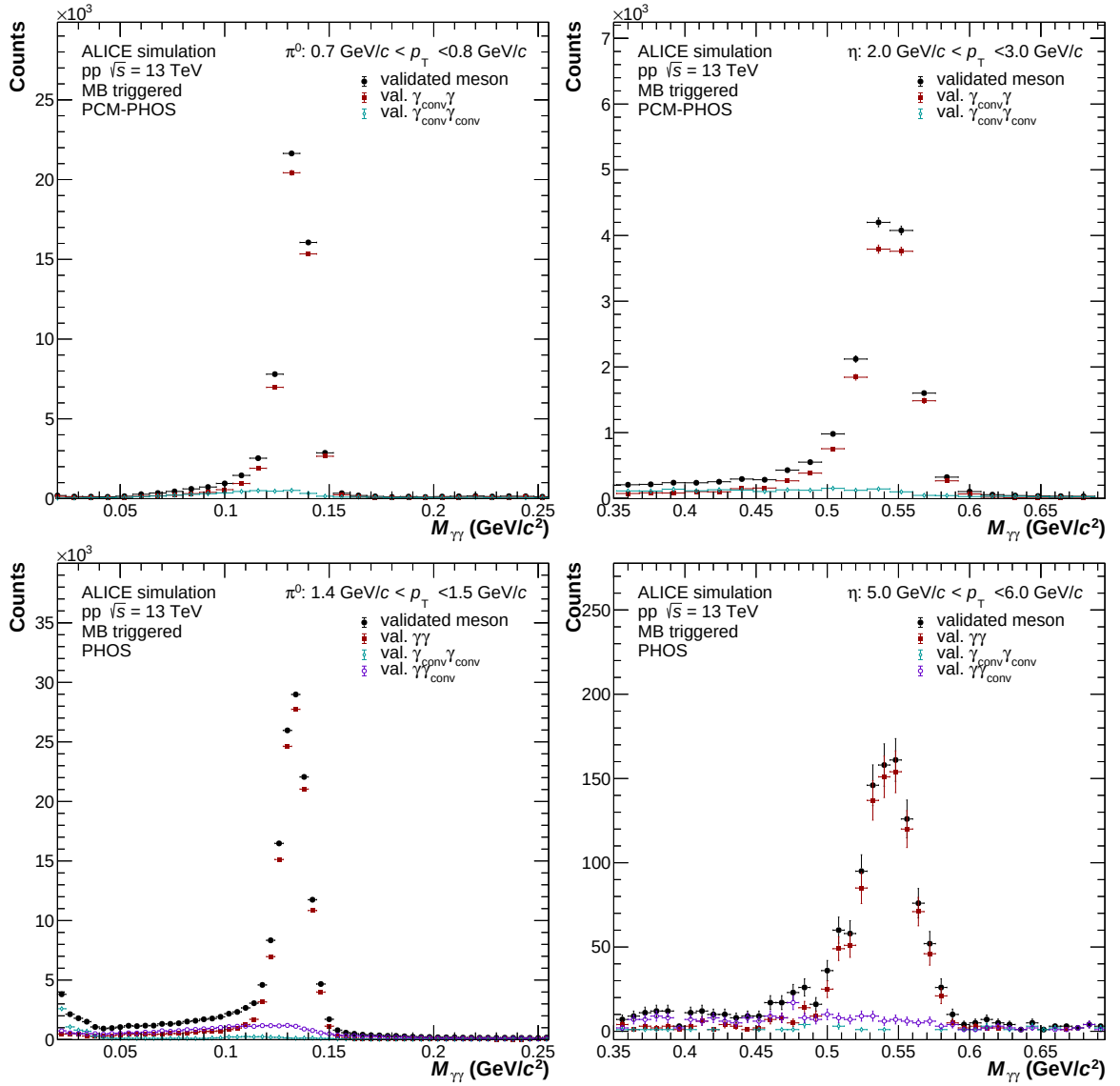

Figure 9.2: Different contributions to the $m_{\gamma\gamma}$ distribution for example p_{T} intervals for validated π^0 (left) and η (right) mesons for MC, reconstructed with PCM-PHOS (top) and PHOS (bottom) for the MB triggered data set.

PCM-PHOS. Photon conversions are called late photon conversions, if they occurred outside the radial distance at which tracking with help of the TPC is still possible. However, in comparison to EMCal and PCM-EMCal, the effect of late photon conversions is negligible for PHOS and PCM-PHOS, leading to almost symmetrical signal shapes for PHOS. This can be seen in Fig. 9.2, which presents example p_{T} intervals of the $m_{\gamma\gamma}$ distribution for validated π^0 and η mesons in MC, reconstructed with PCM-PHOS and PHOS for the MB triggered data set. The black distributions show all validated mesons, while the red points represent the expected photon pairs. The purple points, in the case of PHOS, show meson candidates, where the leading cell of one cluster is an electron originating from a late photon

Method	$m_{\gamma\gamma}$ of π^0 in GeV/c^2	$m_{\gamma\gamma}$ of η in GeV/c^2
PHOS	$m_{\pi^0} - 0.035 < m_{\gamma\gamma} < m_{\pi^0} + 0.023$	$m_{\eta} - 0.05 < m_{\gamma\gamma} < m_{\eta} + 0.035$
PCM-PHOS	$m_{\pi^0} - 0.038 < m_{\gamma\gamma} < m_{\pi^0} + 0.018$	$m_{\eta} - 0.080 < m_{\gamma\gamma} < m_{\eta} + 0.040$

Table 9.4: Integration ranges of π^0 and η to acquire raw yields.

Method	$m_{\gamma\gamma}$ of π^0 in GeV/c^2	$m_{\gamma\gamma}$ of η in GeV/c^2
PHOS	$0.04 < m_{\gamma\gamma} < 0.3$	$0.35 < m_{\gamma\gamma} < 0.79$
PCM-PHOS	$0.05 < m_{\gamma\gamma} < 0.3$	$0.35 < m_{\gamma\gamma} < 0.79$

Table 9.5: Fit range of event-mixing BG for BGratio approach.

conversion. In case of the cyan points, both photons originate from photon conversions. For PCM-PHOS, only one of these photons is originating from late conversions, while both photons are originating from late conversions in case of PHOS.

Subtracting the remaining background, described by the polynomial part of the parametrization, results in Fig. 9.1 (middle). The remaining red distribution is used to extract the raw yield for the corresponding meson. The extraction of the raw yield $N^{\pi^0(\eta)}$ is using the mean meson mass $m_{\pi^0(\eta)}$ from the parametrization to integrate the red distribution by bin counting in a given window around the peak position. The corresponding integration windows can be found in Tab. 9.4.

However, as can be seen in Fig. 9.1 (middle), a first order polynomial is not enough to describe the remaining background properly. To improve the description of the remaining background, a different approach to use the event-mixing background has been investigated in this work. This approach will be called BGratio and is used as standard method for the π^0 and η analysis, performed in this work. For BGratio, the ratio of SigBG to the event-mixing BG is calculated and parametrized for each p_{T} interval. The parametrization function of Eq. 9.1 has been used to parametrize the ratio in the ranges given in Tab. 9.5, while the second order polynomial parameter P_2 is also used in this approach. After that, the event-mixing BG is scaled by the polynomial part of the parametrization function and subtracted from SigBG. No remaining BG is subtracted in this approach, as it is included in the mixed event distribution. An example of the resulting signal and background distributions can be found in Fig. 9.1 (right). The extraction of the meson raw yields is performed analogously to the first event-mixing approach, while a significant improvement can be observed. Detailed plots of the signal extraction for each p_{T} interval for PHOS and PCM-PHOS can be found in Sec. A.3. The plots show the signal distributions in data, using the MB and PHI7 trigger, and shape

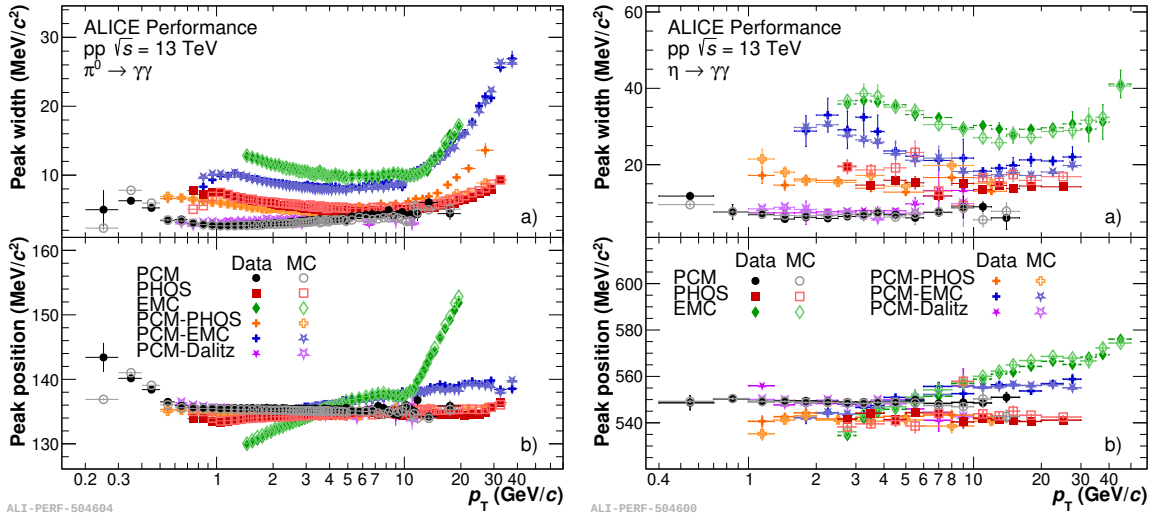

Figure 9.3: Mass position and width of π^0 (left) and η (right) meson in data and MC for different reconstruction methods from invariant mass fit using Eq. 9.1.

comparisons of the signal distributions in data and MC. As can be seen, the signal extraction is working well for both systems over the whole p_T range in which the different triggers are used (Tab. 9.6), while the shapes of the resulting signal distributions are in good agreement between data and MC. As described below, it was decided within the ALICE collaboration to only use one trigger for a given p_T interval. However, the figures shown in Sec. A.3 also illustrate the signal distributions in data for p_T intervals, which have been used to cross-check the measured cross sections of the different triggers, as the signal extraction has been implemented and performed during this work. Fig. 9.3 shows the mass position and width of π^0 (left) and η (right) mesons in data in comparison to MC for different reconstruction methods. A slight increase in width for data in comparison to MC can be observed for PCM-PHOS at momenta above $p_T = 15\,\mathrm{GeV}/c$. This increase in width is covered by the systematic uncertainties, by varying the integration windows, shown in Tab. 9.5. The mass positions and widths in PHOS and PCM-PHOS are acquired from fitting the BG subtracted invariant mass distribution with Eq. 9.1. Besides the slight increase in width, data and MC are in good agreement for the π^0 and η meson, while the lower number of measured η mesons results in larger statistical fluctuations.

In addition to the selection criteria for photons discussed in Sec. 8, the selection of π^0 and η mesons require further conditions. To avoid edge effects of the central barrel detector, which covers a pseudorapidity window of $\eta_{\text{central barrel}} = 0.9$, both mesons need to be reconstructed within a pseudorapidity of $|\eta_{\pi^0(\eta)}| < 0.8$. A minimum opening angle of $\theta_{\text{Min, }\pi^0(\eta)} = 5\,\mathrm{mrad}$ between the two photon vectors of the meson candidates is chosen. This cut has is based on

the detector resolution and assures that the event mixing background, is properly reproduced. Furthermore, the energy asymmetry $\alpha_{\pi^0(\eta)}$ is defined as:

$$\alpha_{\pi^0(\eta)} = \frac{E_{\gamma_1} - E_{\gamma_2}}{E_{\gamma_1} + E_{\gamma_2}} \tag{9.3}$$

Here, E_{γ_1} and E_{γ_2} are the energies of the two photons. However, as $\alpha_{\pi^0(\eta)}$ is distributed over the complete range but is not necessarily distributed symmetrical around zero, no cut on this distribution has been applied.

After the raw yields have been extracted, these yields are converted to invariant cross sections $E\,\mathrm{d}^3\sigma/\mathrm{d}p^3$, calculated by:

$$E\frac{\mathrm{d}^3\sigma}{\mathrm{d}p^3} = \frac{1}{2\pi}\frac{1}{p_\mathrm{T}}\frac{1}{N_{\mathrm{evt,\ trigger}}}\frac{1}{\epsilon_{\mathrm{reco,\ }\pi^0(\eta)}\cdot A_{\pi^0(\eta)}}\frac{1}{BR}\frac{N^{\pi^0(\eta)} - N_{\mathrm{Sec}}^{\pi^0(\eta)}}{\Delta y \Delta p_\mathrm{T}}\sigma_{\mathrm{Trigger}} \tag{9.4}$$

$N_{\mathrm{evt,\ trigger}}$ and $\sigma_{\mathrm{Trigger}}$ are the number of events and the cross section of the used trigger as described in Sec. 6.2, including the TRF. BR is the branching-ratio of the decay for the reconstructed meson, which can be found in Tab. 3.3. $N^{\pi^0(\eta)}$ is the extracted raw yield for a given rapidity and momentum interval $\Delta y \Delta p_\mathrm{T}$. $N_{\mathrm{Sec}}^{\pi^0(\eta)}$ is the number of secondary mesons, which originate from decays of K_S^0, K_L^0 and Λ particles. $\epsilon_{\mathrm{reco,\ }\pi^0(\eta)}$ and $A_{\pi^0(\eta)}$ are the reconstruction efficiency and the geometrical detector acceptance and are often shown as combined quantity:

$$\epsilon = 2\pi y \epsilon_{\mathrm{reco,\ }\pi^0(\eta)} \cdot A_{\pi^0(\eta)} \tag{9.5}$$

However, to consider the low branching-ratio of the Dalitz decay and the purity P, needed for the merged EMCal (mEMC) analysis, Eq. 9.5 is adjusted for π^0 and η mesons in this work:

$$\epsilon = 2\pi y \epsilon_{\mathrm{reco,\ }\pi^0(\eta)} \cdot A_{\pi^0(\eta)} \cdot BR/P \tag{9.6}$$

For all reconstruction methods, except mEMC, the purity is defined as $P = 1$. If the correction of $\sigma_{\mathrm{Trigger}}$ is not yet applied, the resulting yield is also commonly called corrected yield. A more detailed explanation of the different contributions to convert the extracted raw yields to invariant cross sections is provided in the next passages.

As already described in Sec. 6.3, extracted yields from triggered data sets have to be scaled by the TRF. It has been decided to use all clusters and not only triggered clusters in the analysis. As explained, the cluster spectra, which are used to calculate the TRF are using all available clusters to be flagged as good by the general BCM for the PHI7 triggered dataset

Trigger and MC Simulation	p_T range for π^0 in PHOS	p_T range for π^0 in PCM-PHOS	p_T range for η PHOS	p_T range for η in PCM-PHOS
MB trigger corrected by normal MC	$0.7\,\mathrm{GeV}/c < p_T$ & $p_T < 10\,\mathrm{GeV}/c$	$0.5\,\mathrm{GeV}/c < p_T$ & $p_T < 10\,\mathrm{GeV}/c$	$2.5\,\mathrm{GeV}/c < p_T$ & $p_T < 10\,\mathrm{GeV}/c$	$1\,\mathrm{GeV}/c < p_T$ & $p_T < 10\,\mathrm{GeV}/c$
PHI7 trigger corrected by lowJJMC	$10\,\mathrm{GeV}/c < p_T$ & $p_T < 16\,\mathrm{GeV}/c$	$10\,\mathrm{GeV}/c < p_T$ & $p_T < 14\,\mathrm{GeV}/c$	$10\,\mathrm{GeV}/c < p_T$ & $p_T < 16\,\mathrm{GeV}/c$	$10\,\mathrm{GeV}/c < p_T$ & $p_T < 14\,\mathrm{GeV}/c$
PHI7 trigger corrected by highJJMC	$16\,\mathrm{GeV}/c < p_T$ & $p_T < 35\mathrm{GeV}/c$	$14\,\mathrm{GeV}/c < p_T$ & $p_T < 30\mathrm{GeV}/c$	$16\,\mathrm{GeV}/c < p_T$ & $p_T < 30\mathrm{GeV}/c$	$14\,\mathrm{GeV}/c < p_T$ & $p_T < 30\,\mathrm{GeV}/c$

Table 9.6: p_T ranges for different triggers, corrected by different MC simulations for π^0 and η meson in PHOS and PCM-PHOS.

and require all clusters of the MB triggered dataset to additionally be flagged as good by the BCM for triggers. The corrected meson yields of p_T intervals, which were measured with multiple triggers are only used to validate the measurements of different triggers. For each p_T interval, only one trigger with a specific MC has been used, documented in Tab. 9.6.

The acceptance $A_{\pi^0(\eta)}$ and the efficiency are extracted from MC. $A_{\pi^0(\eta)}$ is calculated by the ratio of all meson candidates $N^{\pi^0(\eta)}$, whose daughter particles lie within the geometrical limits of the analysis and all generated meson candidates in that rapidity window $|y| < y_{\max}$:

$$A_{\pi^0(\eta)}(p_T) = \frac{N^{\pi^0(\eta)}_{|y|<y_{\max},\text{ with daughter particles within acceptance}}}{N^{\pi^0(\eta)}_{|y|<y_{\max}}} \tag{9.7}$$

Two different efficiencies have been studied in this work. On the one hand, it can be checked whether a meson candidate is a combination of two photons, which originate from the desired meson. The meson candidates for which this statement is true, are called validated or true meson candidates. By counting these candidates in the integration windows given in Tab. 9.4, the fraction of validated meson candidates to all the generated meson candidates within $A_{\pi^0(\eta)}$ can be calculated. This results in the validated efficiency $\epsilon_{\text{true, }\pi^0(\eta)}$, also called true efficiency. On the other hand, the signal extraction, that has been described in this chapter, can also be performed in MC. By comparing the extracted meson yields to the number of generated meson candidates, the reconstruction efficiency $\epsilon_{\text{reco, }\pi^0(\eta)}$, also called normal efficiency, can be calculated. If the signal extraction would be flawless, both efficiencies would be identical. However, as different signal extraction methods do not describe the background shape perfectly, differences are expected. This can be seen in the various meson signal shape comparison plots in Chap. A.3, where it can be observed that the validated signal is not zero outside the peak region. However, the signal extraction minimizes the background outside the peak region by construction. Hence, this work is using $\epsilon_{\text{reco, }\pi^0(\eta)}$ to take these effects into account. Fig. 9.4 shows ϵ for the π^0 and η meson in data and MC for different reconstruction

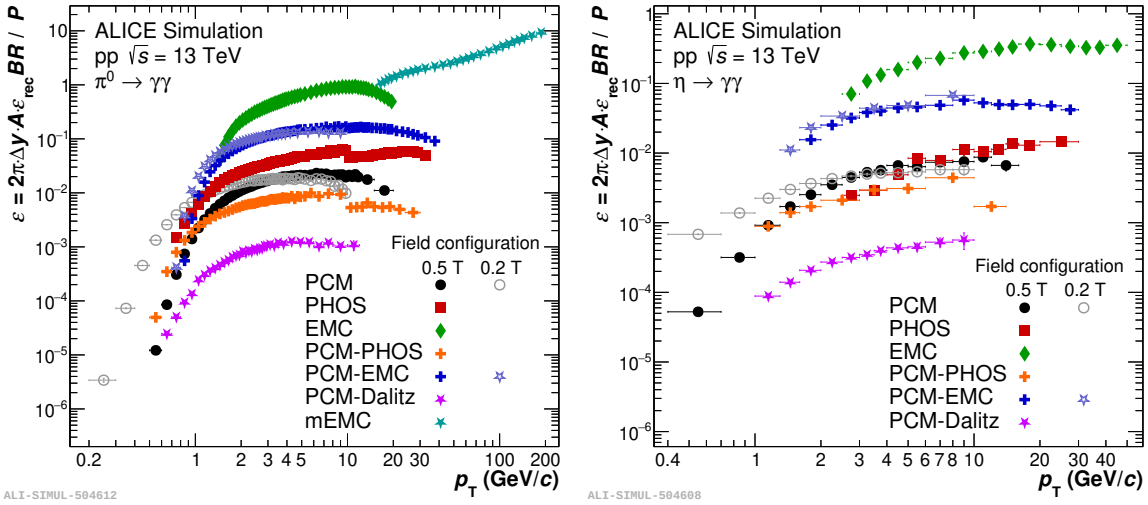

Figure 9.4: Acceptance times Efficiency ϵ for π^0 (left) and η (right) meson in data and MC for different reconstruction methods.

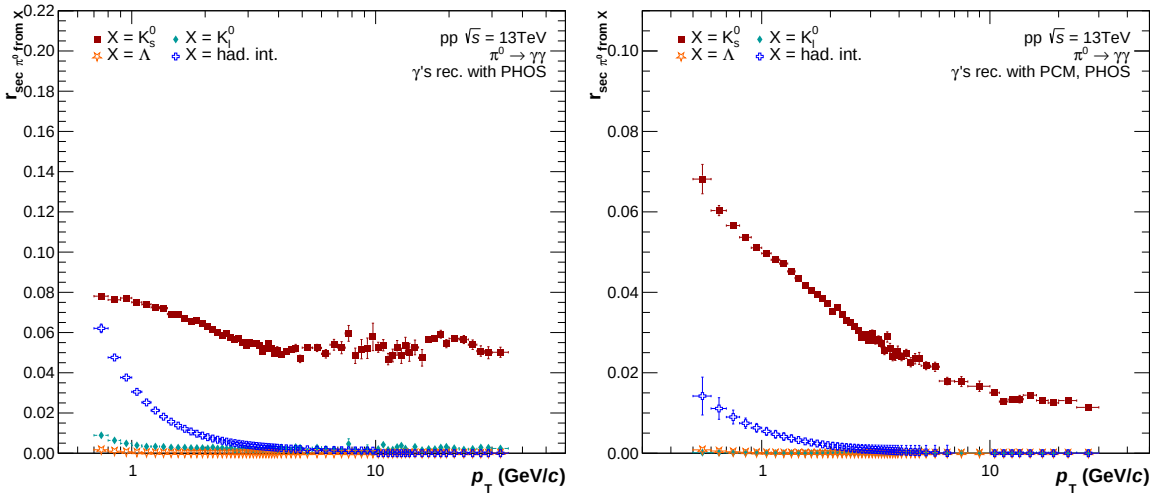

Figure 9.5: Ratio of different secondary π^0 distributions to the total π^0 yield for PHOS (left) and PCM-PHOS (right).

methods. The drop of ϵ for PHOS and PCM-PHOS is originating from the reduction in efficiency due to the PHI7 triggered analysis.

Secondary mesons are defined as mesons originating from weak particle decays and hadronic interactions in the detector material. While hadronic interactions are estimated by MC, π^0 mesons originating from weak particle decays have to be corrected for. The amount of secondary π^0 mesons from weak decays is driven by K^0_S, K^0_L and Λ. Measurements of the productions of these particles are used to obtain the invariant yields of secondary π^0 mesons, while the full decay kinematics is being accounted for. The ratios of different secondary π^0 distributions to the total π^0 yield for PCM-PHOS and PHOS are shown in Fig. 9.5.

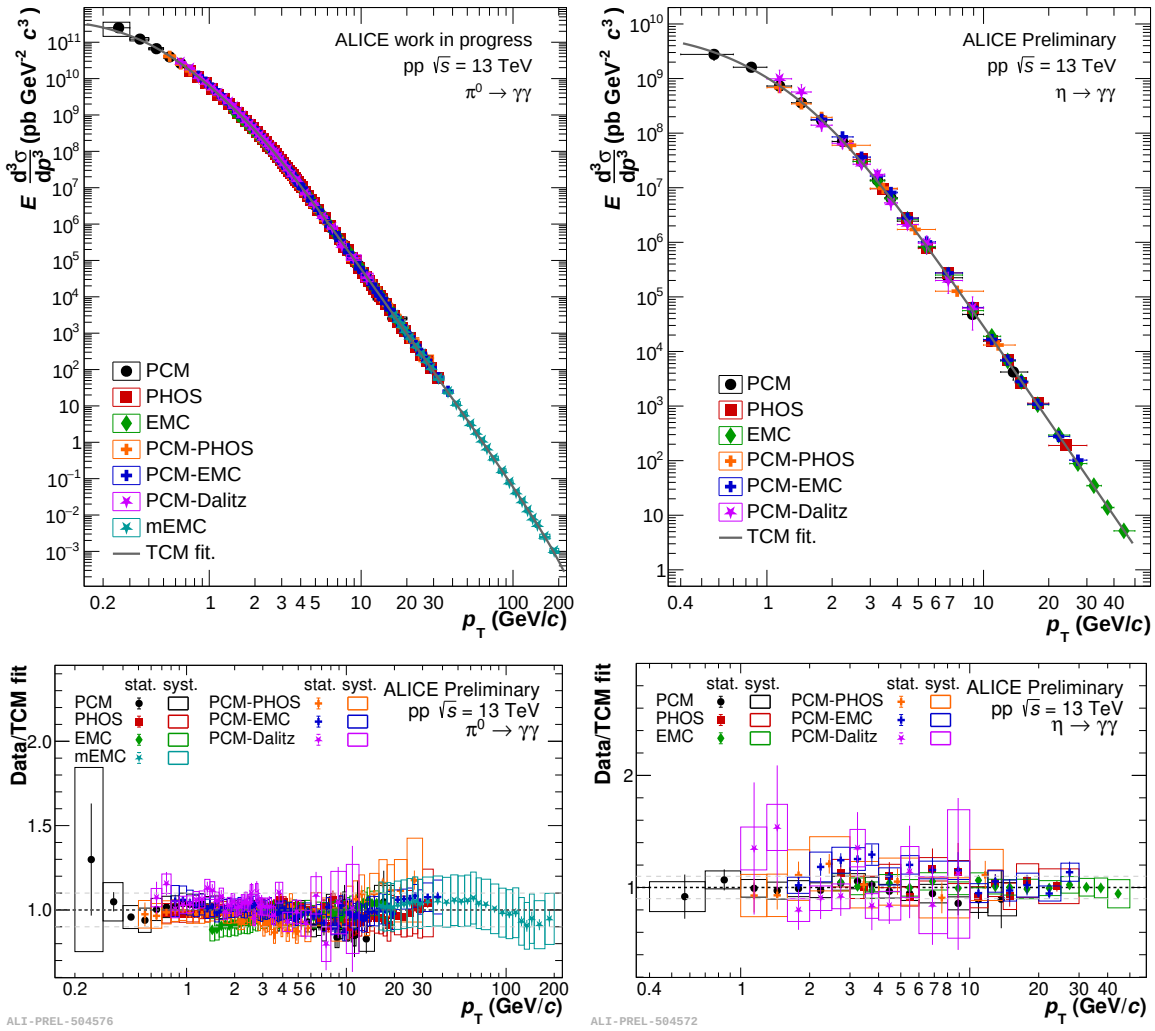

Figure 9.6: **Top:** Invariant cross section for the measurement of π^0 (left) and η (right) mesons for PHOS and PCM-PHOS in comparison to the invariant cross sections to different reconstruction methods in $\sqrt{s} = 13$ TeV. The reconstruction methods fitted with a common TCM fit. **Bottom:** Ratio of the different reconstruction methods in $\sqrt{s} = 13$ TeV to the TCM fit.

After the fully corrected invariant cross section has been acquired for PHOS and PCM-PHOS with help of Eq. 9.4, they are combined with the acquired cross sections from EMCal, PCM-EMCal, PCM, mEMC and PCM-Dalitz. The cross sections of p_{T} intervals, which were measured with multiple reconstruction methods are combined with help of the Best Linear Unbiased Estimate (BLUE) method [82][83][84]. This method considers the statistical and systematic uncertainties, as well as their correlations, to acquire a combined spectrum with better precision than the separate measurements. For the following plots of this section, the vertical error bars represent the statistical uncertainties, while the boxes represent the systematic uncertainties. Fig. 9.6 (top) is showing the invariant cross section for the measurement of π^0 (left) and η (right) mesons for PHOS and PCM-PHOS in comparison to the

invariant cross sections to different reconstruction methods in $\sqrt{s} = 13$ TeV. The combined π^0 and η spectra are parametrized with a TCM function, as defined by Eq. 3.51 and Eq. 3.49, and the ratio of the different reconstruction methods to this fit is shown in Fig. 9.6 (bottom). The TCM fits have been performed on the combined spectrum shown in Fig. 9.7. As it can be observed, the majority of the different reconstruction methods do align within uncertainties. While the low p_{T} regime is dominated by PCM, the high p_{T} regime is dominated by reconstruction methods that make use of the calorimeter triggers. The mEMC measurement is enhancing the available p_{T} range to up to 200 GeV. for π^0 mesons. The larger fluctuations for the η in comparison to the π^0 are originating from the larger statistical uncertainties.

The invariant cross sections of the π^0 and η mesons are calculated in p_{T} intervals with finite widths and are steeply falling. Hence, the center of an interval does not represent the cross section of this interval and needs to be corrected. This is realized by shifting the cross section either in p_{T} or in its value. A shift in p_{T} is commonly known as horizontal shift or x-shift, while a shift in its value is commonly known as vertical shift or y-shift. Both approaches are viable. For π^0 and η mesons a shift in p_{T} has been chosen for the invariant cross section, while a shift of their value has been chosen for their ratio, as both spectra would have a different shift. A TCM function is used to parametrize the underlying spectrum and calculate the center of mass for each p_{T} interval. The parametrization is then used to shift the spectra accordingly. While the TCM fit is determined on the combined spectrum, the resulting shifts are also applied to the shown individual cross sections and all following plots in this section have the bin shift applied.

The combination of the different reconstruction methods is shown in Fig. 9.7 (left) together with its ratio to the common TCM fit (right). The invariant cross sections are compared to PYTHIA 8.2 as well as different NLO calculations. The NLO calculations for the π^0 meson are using the PDFs CT18 [85] or CT14 [86] together with the FFs NNFF1.0 [87] or DSS14 [88]. The NLO calculation for the η meson is using the PDF CT18 with the FF AESSS. The factorization scale value μ used for the PDFs is $0.5 \geq \mu < 2.0$. The combined invariant cross sections cover a momentum range of $0.2\,\mathrm{GeV}/c < p_{\mathrm{T}} < 200\,\mathrm{GeV}/c$ for π^0 mesons and $0.4\,\mathrm{GeV}/c < p_{\mathrm{T}} < 50\,\mathrm{GeV}/c$ for η mesons. The PYTHIA simulation is overestimating the π^0 meson production for low p_{T} by up to 50 %, while a similar behavior was already observed for charged pions [89]. The shape of the PYTHIA distribution is not matching the measured data. With increasing p_{T}, it is getting closer to the measured distribution until it is within the uncertainties at $p_{\mathrm{T}} > 50\,\mathrm{GeV}/c$. The comparison of the η meson to the PYTHIA simulation shows a similar behavior. PYTHIA significantly overestimates the measured data at low p_{T}, while its shape is not well described. With increasing p_{T}, the simulation is getting closer to the measured distribution until it is crossing with the measurement at $p_{\mathrm{T}} \approx 15\,\mathrm{GeV}/c$.

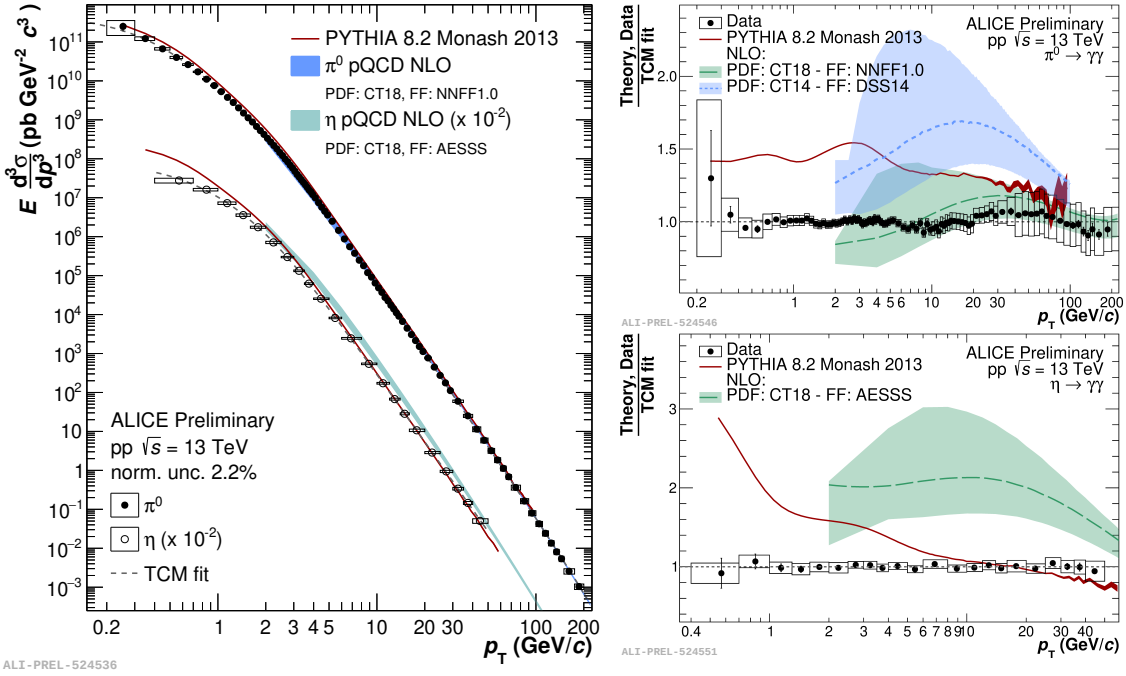

Figure 9.7: **Left:** Invariant cross section of the combined measurements of π^0 and η mesons in $\sqrt{s} = 13$ TeV, parametrized with a modified TCM fit. The invariant cross section is compared to the PYTHIA 8.2 simulation, using the Monash 2013 tune [22], as well as differentNLO calculations. **Right:** Ratio of the shown distributions to the TCM fit. The π^0 is shown on top, while the η is shown on bottom.

The NLO calculations using CT14 with DSS14 for the π^0 and CT18 with AESSS for the η are overestimating the measured spectra. However, the NLO calculation using CT18 with NNFF1.0 for the π^0 is describing the spectrum quite well. It is in agreement with the measurement within uncertainties, while also describing the shape of the spectrum. Similar observations have been made in [90], where the cross section of the π^0 measurement has been compared to a NLO calculation using the PDF CT18 with the FF DSS14 and to a NLO calculation using the PDF CT18 with the FF NNFF1.0. Here, the NLO calculation using the FF NNFF1.0 is describing the cross section of the π^0 measurement significantly better in comparison to the NLO calculation using the FF DSS14. As only the FF changed in these two NLO calculations, the benefit of using novel fitting approaches, like the neural network based approach used for NNFF1.0, is illustrated.

The reconstruction of π^0 and η mesons is quite similar and uses the same decay channel. Due to this, for each reconstruction method, the p_{T} ranges in which the η can be reconstructed is likely to also be covered in the π^0 reconstruction. Hence, the η/π^0 ratio can be calculated for each reconstruction method separately and be combined to one spectrum analogously to the η or π^0 spectra with help of the BLUE method. The benefit of this method is, that the systematic uncertainties can be calculated on the ratio itself. As certain uncertainties cancel

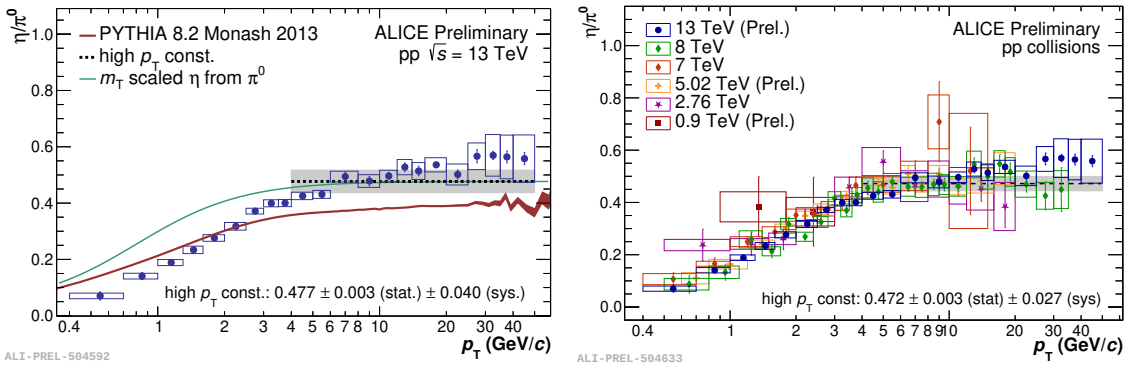

Figure 9.8: Combined η/π^0 spectrum for $\sqrt{s} = 13$ TeV. **Left:** In comparison to the PYTHIA 8.2 simulation as well as m_T scaling. The high p_T constant is determined to be $0.477 \pm 0.003(\text{stat}) \pm 0.040(\text{sys})$. **Right:** In comparison to different pp collisions in ALICE.

in the ratio, the resulting systematic uncertainties are reduced. Fig. 9.8 shows the combined η/π^0 ratio in comparison to PYTHIA 8.2 simulation as well as a prediction from m_T scaling (left) and in comparison to different pp collisions in ALICE (right). It has been shown in [91], that the spectra of π^0 and η mesons are similar, when they are plotted as functions of m_T, which is known as m_T scaling [92]. The term m_T scaling is describing the procedure to estimate the cross sections of different mesons by a universal function defined as:

$$E\frac{\mathrm{d}^3\sigma}{\mathrm{d}p^3} = Sf_\pi\left(\sqrt{p_T^2 + m_h^2}\right) = Sf_\pi\left(\sqrt{m_T}\right) \tag{9.8}$$

S is the relative normalized, obtained by the high p_T fit of the ratio, m_h is the rest mass of the corresponding hadron or meson and f_π is a universal function dependent on the transverse mass m_T. Here, the unmodified TCM fit, described by Eq. 3.49, has been used for f_π. It can be seen that the ratio in data is significantly lower than the distribution, that is expected from m_T scaling for $p_T < 4\,\text{GeV}/c$. This behavior has already been observed in the past [93][94][95][96] and can be explained by a large amount of feed-down (π^0 mesons from decays of heavy particles) to the π^0 distribution at low p_T. PYTHIA is underestimating the measured ratio for high p_T. The comparison to previous measurements shows a good agreement between the different measurement within their uncertainties, while enhancing the p_T coverage to up to $p_T = 50\,\text{GeV}/c$.

10 Measurement of ω Meson Production Cross Section

ω meson cuts	
Pseudorapidity	$\lvert\eta_{\omega}\rvert < 0.85$
Charged Pion Mass	$m_{\pi^+\pi^-} < 850\,\mathrm{MeV}/c^2$
π^0 meson cuts	
Pseudorapidity	$\lvert\eta_{\pi^0}\rvert < 0.8$
Mass Cut in MeV/c^2	$3\sigma_{\pi^0}$ around π^0 mass, where mass and width have been obtained as p_{T} dependent parametrizations
maximum p_{T}	$25\,\mathrm{GeV}/c$ for EMCal

Table 10.1: Overview of the ω and π^0 selection criteria for the ω reconstruction.

The previous chapters discussed the selection of charged and neutral pions, using different reconstruction techniques. This chapter is dedicated to the measurement of the production cross section of the ω meson via its $\omega \rightarrow \pi^+\pi^-\pi^0$ decay channel. ω mesons are reconstructed via their invariant mass m_{Inv} in p_{T} intervals, which is calculated using the four-momentum vectors of all $\pi^+\pi^-$ π^0 combinations in a given event. To distinguish the calculated invariant mass of ω meson candidates from the peak position m_{ω} in Eq. 10.3 and the invariant mass $m_{\gamma\gamma}$ of the π^0 and η meson candidates, the invariant mass of ω meson candidates is also called $m_{\pi^+\pi^-\pi^0}$ in this thesis. While π^+ and π^- are directly measured, using their track information, the π^0 is reconstructed via its decay into two photons. The reconstruction method for the ω meson is named after the reconstruction method for the neutral pion: PCM, EMCal, PCM-EMCal, PHOS and PCM-PHOS. A detailed description of the π^0 reconstruction for the PHOS and PCM-PHOS method has been given in Chap. 9. All five different reconstruction methods have been used to reconstruct π^0 candidates for the ω production cross section measurement with the help of the MB trigger. Furthermore, the EG1 and EG2 trigger extend the available p_{T} range of the ω reconstruction for the EMCal and PCM-EMCal method. For

all plots of this chapter, the vertical error bars represent the statistical uncertainties, while the boxes represent the systematic uncertainties. To reduce the impact of the π^0 mass resolution on the ω production cross section measurement, the reconstructed invariant mass of the ω meson candidates $m_{\omega,\,\mathrm{reco.}}$ is corrected by the nominal π^0 meson mass position $m_{\pi^0,\,\mathrm{PDG}}$ provided by the PDG. The corrected invariant mass of ω meson candidates $m_{\pi^+\pi^-\pi^0}$ is calculated by

$$m_{\pi^+\pi^-\pi^0} = m_{\omega,\,\mathrm{reco.}} - (m_{\pi^0,\,\mathrm{reco.}} - m_{\pi^0,\,\mathrm{PDG}}), \tag{10.1}$$

where $m_{\pi^0,\,\mathrm{reco.}}$ is the reconstructed invariant mass of π^0 mesons according to Eq. 8.8. While the resulting ω mass width is reduced by this correction, a fraction of the influence of the π^0 still remains.

For the ω meson reconstruction, π^0 candidates are selected according to their invariant mass information. As explained in Chap. 9, the π^0 signal is parametrized and its mass position and width is extracted. The π^0 mass position and width distributions for the PCM, EMCal and PCM-EMCal methods were provided by the collaboration, while these distributions for the PHOS and PCM-PHOS method were extracted during this work. For the ω meson reconstruction, the information of the π^0 mass and width acquired by the π^0 measurement for all used reconstruction methods has been parametrized in dependence of p_T. Fig. 10.1 (top) shows the parametrization of the mass position and width distribution for π^0 mesons in MC for the EMCal reconstruction method. The mass position and width distributions are given by the m_{π^0} and σ_{π^0} parameter in Eq. 9.1. π^0 candidates are selected within a $3\sigma_{\pi^0}$ window around the mass position. The invariant mass distributions of the π^0 candidates, used for the ω reconstruction with the help of the EMCal method in the JJMC sample, for the EG2 trigger before and after this invariant mass cut is applied can be found in Fig. 10.1 (bottom). The trigger turn-on is resulting in a second accumulation of π^0 candidates above $4\,\mathrm{GeV}/c$. As it can be observed, the π^0 candidates selected by EMCal are limited to $p_\mathrm{T} < 25\,\mathrm{GeV}/c$. The reason for this is that photons of high energy clusters are starting to merge in the detector and cannot be measured as separate clusters anymore. Therefore, the π^0 analysis for the EMCal is limited to $p_\mathrm{T} < 20\,\mathrm{GeV}/c$. However, studies of the π^0 signal shape during this work have shown that the π^0 selection for the ω reconstruction can be increased. The π^0 selection of the other reconstruction methods are not limited by p_T. Furthermore, to avoid edge effects of the central barrel with a pseudorapidity of 0.9, the pseudorapidity of selected π^0 is required to be $|\eta_{\pi^0}| < 0.8$. For the same reason, the pseudorapidity of ω meson candidates is required to be $|\eta_\omega| < 0.85$. In addition to that, as already mentioned in Chap. 7 and described in Sec. 10.2, the invariant mass of $\pi^\pm$-pairs have to be $m_{\pi^+\pi^-} < 850\,\mathrm{MeV}/c^2$.

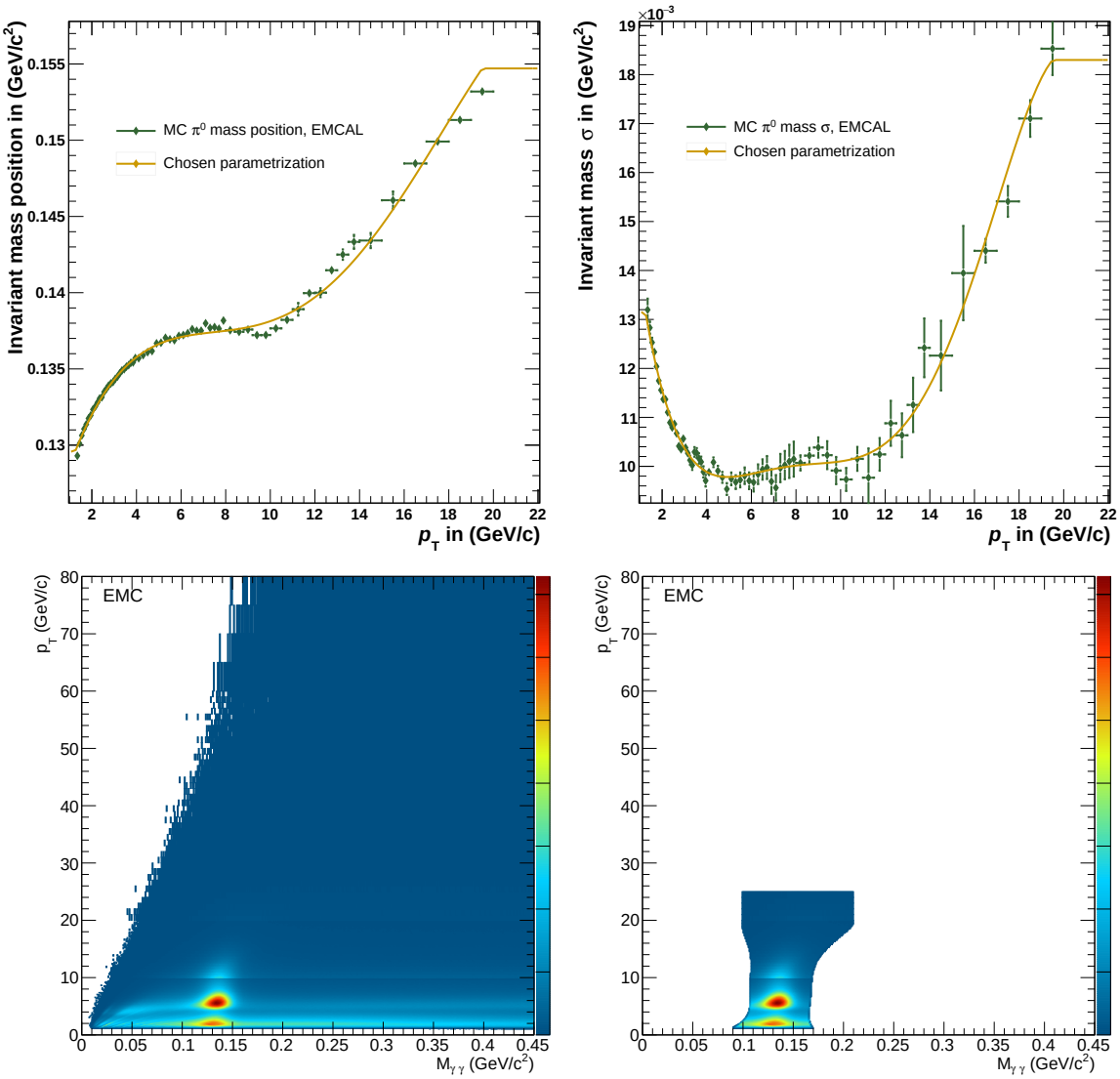

Figure 10.1: **Top:** Parametrization of π^0 invariant mass position (left) and width in terms of σ_{π^0} (right) in MC for EMCal. The parametrizations of the different reconstruction methods are becoming constant above and below certain momentum thresholds. **Bottom:** Invariant mass distribution of π^0 candidates in MC for EMCal before (left) and after (right) the selection cut within a $3\sigma_{\pi^0}$ window on their invariant mass is applied. The trigger turn-on is resulting in a second accumulation of π^0 candidates above 4 GeV/c.

In principle, the invariant mass analysis for ω mesons is performed analogously to the π^0 analysis explained in Chap. 9. Fig. 10.2 show the example distributions of the invariant mass $m_{\pi^+\pi^-\pi^0}$ for ω candidates for all reconstruction methods and triggers. The black diamonds (SigBG) show all meson candidates for the chosen p_{T} interval, while the green line shows the estimated background (BG) distribution. By subtracting the green line from the black diamonds, the red signal distribution remains. The same procedure is performed in MC. Various BG description methods have been investigated during this work and will be discussed

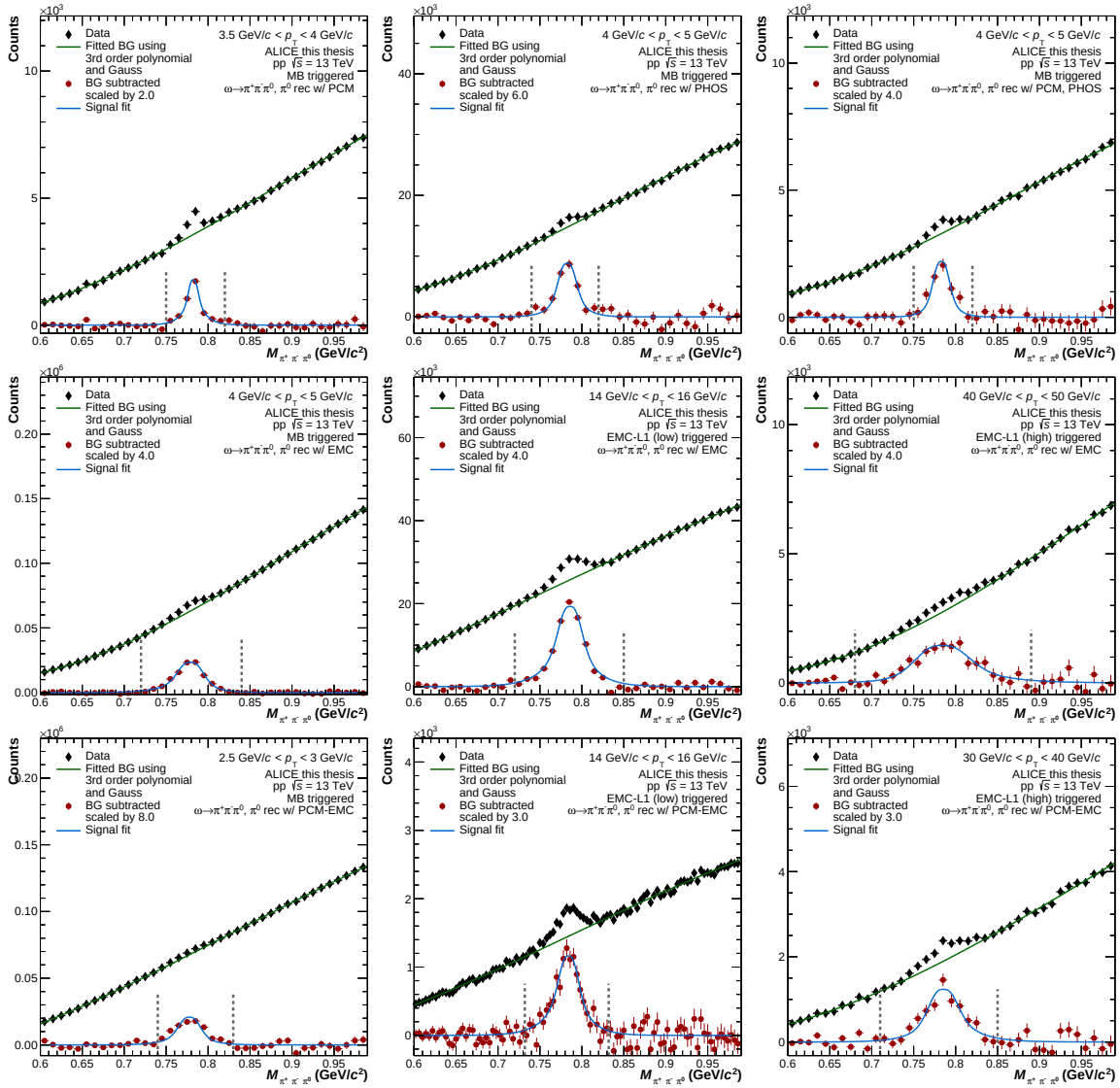

Figure 10.2: Example $m_{\pi^+\pi^-\pi^0}$ distributions of ω meson for different reconstruction methods and triggers. The black diamonds show all meson candidates for the chosen p_{T} interval. The green lines show the estimated BG distribution. The red dots are acquired by subtracting the black diamonds by the green lines and correspond to the signal distribution. The used reconstruction methods and triggers are given in the respective legends.

in detail in Sec. 10.2. For this analysis, a Gaussian on top on a third order polynomial has been chosen as parametrization for the BG description. The parametrization function is given by

$$F_{\omega,\,\mathrm{BG}} = A \cdot G(m_{\pi^+\pi^-\pi^0}) + P_0 + P_1 \cdot m_{\pi^+\pi^-\pi^0} + P_2 \cdot m^2_{\pi^+\pi^-\pi^0} + P_3 \cdot m^3_{\pi^+\pi^-\pi^0} \qquad (10.2)$$

with

$$G(m_{\pi^+\pi^-\pi^0}) = \exp\left(-0.5\left(\frac{m_{\pi^+\pi^-\pi^0} - m_\omega}{\sigma_\omega}\right)^2\right). \tag{10.3}$$

$m_{\pi^+\pi^-\pi^0}$ is the invariant mass of meson candidate of the combined π^+, π^- and π^0. The Gaussian $G(m_{\pi^+\pi^-\pi^0})$ is defined by the width σ_ω and the mean position m_ω. The amplitude of the reconstructed ω meson distribution is given by A. P_0, P_1, P_2 and P_3 are the free parameters of the underlying polynomial parametrization. Besides the example p_T intervals shown in Fig. 10.2, further p_T intervals can be found in Sec. A.4.2. The chosen BG parametrization is able to describe all reconstruction methods over the whole p_T range. After the BG subtraction, the remaining ω meson signal, represented by the red dots, is parametrized with $F_{\omega,\,\mathrm{Signal}}$. This parametrization function is given by a Gaussian with an exponential tail on both sides of the peak:

$$\begin{aligned} F_{\omega,\,\mathrm{Signal}} = A \cdot G(m_{\pi^+\pi^-\pi^0}) + \\ A \cdot \exp\left(\frac{m_{\pi^+\pi^-\pi^0} - m_\omega}{\lambda_1}\right) \cdot (1 - G(m_{\pi^+\pi^-\pi^0})) \cdot \theta_\mathrm{H}\left(m_\omega - m_{\pi^+\pi^-\pi^0}\right) + \\ A \cdot \exp\left(-\frac{m_{\pi^+\pi^-\pi^0} - m_\omega}{\lambda_2}\right) \cdot (1 - G(m_{\pi^+\pi^-\pi^0})) \cdot \theta_\mathrm{H}\left(m_{\pi^+\pi^-\pi^0} - m_\omega\right) \end{aligned} \tag{10.4}$$

The definition of the different parameters are similar to Eq. 10.2. In addition to that, the Heavyside step function θ_H is used to apply the exponential tail, parametrized by λ_1 and λ_2, to only one side of the ω peak. For PCM, PCM-PHOS and PHOS, the same exponential tail parameter is used on both sides of the peak, with $\lambda = \lambda_1 = \lambda_2$. The lambda parameters λ, λ_1 and λ_2 are fixed to the values acquired by the true MC signal parametrizations. Therefore, the only free parameters of this parametrization are the amplitude A, the peak width σ_ω and the mean position m_ω. As a BG parametrization is used, no remaining BG is subtracted.

The raw signal for the ω meson in a given p_T interval is extracted by integrating (counting) the $m_{\pi^+\pi^-\pi^0}$ spectrum in a given mass window around m_ω (bin counting). As the width of the ω meson increases with p_T, the true MC signal parametrizations with a simple Gaussian is used to acquire the width $\sigma_{\omega,\,\mathrm{Gauss}}$ distribution of the ω meson for the different reconstruction methods. The definition of true ω mesons is the similar to the definition for true π^0 and η mesons, explained in Chap. 9. An ω meson candidate in MC is called validated or true ω meson, if the three pions that have been used to reconstruct the ω meson candidate are originating from the same validated ω meson. The integration is performed within a $3\sigma_{\omega,\,\mathrm{Gauss}}$ window around m_ω. The integration range is indicated by the vertical dotted grey lines around

the peaks in Fig. 10.2. As explained for the π^0 and η meson in Chap. 9, the extracted yields are converted into invariant cross sections $E\,\mathrm{d}^3\sigma/\mathrm{d}p^3$. This conversion is performed by:

$$E\frac{\mathrm{d}^3\sigma}{\mathrm{d}p^3} = \frac{1}{2\pi}\frac{1}{p_\mathrm{T}}\frac{1}{N_{\mathrm{evt,\ trigger}}}\frac{1}{\epsilon_{\mathrm{reco,\ }\omega}\cdot A_\omega}\frac{1}{BR}\frac{N^\omega}{\Delta y\Delta p_\mathrm{T}}\sigma_\mathrm{Trigger} \tag{10.5}$$

Corrected yields are raw yields, that are corrected by all correction terms of Eq. 10.5 without σ_Trigger. The different terms are similar to the π^0 and η reconstruction. $N_{\mathrm{evt,\ trigger}}$ and σ_Trigger are the number of events and the cross section of the used trigger, as described in Sec. 6.2. As described in Sec. 6.3, the raw yields of the photon triggers EG2 and EG1 are enhanced and have to be normalized by the use of corresponding TRFs, which are included in σ_Trigger. BR is the branching-ratio of the $\omega \to \pi^+\pi^-\pi^0$ decay, which can be found in Tab. 3.3. In addition to that, it includes the branching-ratio of $\pi^0 \to \gamma\gamma$. $\epsilon_{\mathrm{reco,\ }\omega}$ and A_ω are the reconstruction efficiency and the geometrical detector acceptance and are often shown as combined quantity $\epsilon_\omega = 2\pi y \epsilon_{\mathrm{reco,\ }\omega}\cdot A_\omega$. They follow the same principles as $\epsilon_{\mathrm{reco,\ }\pi^0(\eta)}$, $A_{\pi^0(\eta)}$ and ϵ of Chap. 9. A_ω can be extracted from MC by comparing all generated ω mesons, whose daughter particles also lie within the chosen reconstruction acceptance η_ω to all ω mesons within η_ω. N^ω is the extracted ω raw yield for a given rapidity and momentum interval $\Delta y\Delta p_\mathrm{T}$. In contrast to the correction of π^0 mesons in Eq. 9.4, no secondary correction needs to be applied as the number of particles that are able to decay into ω mesons is negligible. The distributions of m_ω, m_ω and ϵ_ω will be shown in Sec. 10.5 in Fig. 10.14.

10.1 Different Signal Extraction Methods

When the BG is approximated to only originate from uncorrelated combinations of π^+, π^- and π^0 mesons, the BG can be described by different mixing techniques. Three different mixing techniques to ensure that no correlations between the combined mesons exist have been investigated during this work: Event-mixing, sideband-mixing and likesign-mixing. Fig. 10.3 shows an example p_T interval for event-mixing (left), sideband-mixing (middle) and likesign-mixing (right). The most obvious approach would be to use the same BG description method, as it is used in the π^0 analysis: The event-mixing. This method uses FIFO buffers to store π^+, π^- and π^0 candidates dependent on the primary z-vertex position Z_Vtx and photon multiplicity N_γ with up to 50 events in each FIFO buffer. The uncorrelated event-mixing BG is created by combining π^+, π^- and π^0 mesons to ω candidates, where at least one of the three pions is originating from a different event. The decision which pions are selected from the same event and which pions are taken from the FIFO buffers has shown to be negligible and shall not be further discussed in this work, while the sum of the different possibilities is

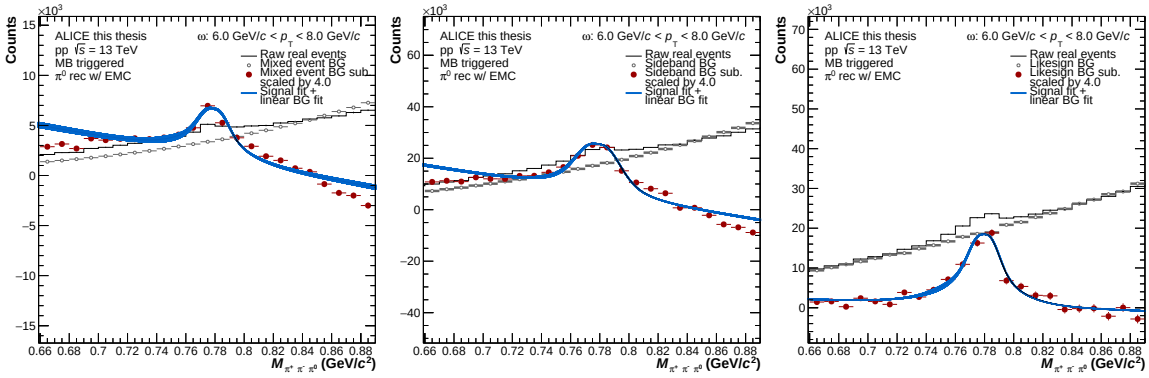

Figure 10.3: Example $m_{\pi^+\pi^-\pi^0}$ distributions of ω meson candidates $6\,\text{GeV} < p_\text{T} < 8\,\text{GeV}$ for EMCal in the MB triggered data set. The black diamonds show all meson candidates for the chosen p_T interval. The green line shows the estimated BG distribution. The red dots are acquired by subtracting the black diamonds by the green line and correspond to the signal distribution. An additional first order polynomial is used for the remaining BG. **Left:** The BG is described by event-mixing. **Middle:** The BG is described by sideband-mixing. **Right:** The BG is described by likesign-mixing.

used as BG. The sideband-mixing and likesign-mixing methods are using pions of the same event. Sideband-mixing is only using π^0 candidates for the reconstruction of an uncorrelated ω-BG, that have an invariant mass m_{π^0} outside the π^0 peak region. The π^0 candidates have been selected within $10\,\text{MeV}/c < m_{\pi^0} < 50\,\text{MeV}/c$ and $180\,\text{MeV}/c < m_{\pi^0} < 220\,\text{MeV}/c$. For the likesign-mixing technique, only charged pions of the same charge are combined with neutral pions to reconstruct ω candidates. Hence, the combinations $\pi^-\pi^-\pi^0$ and $\pi^+\pi^+\pi^0$ are possible. The histograms of the different mixing techniques are normalized to SigBG on the right side of the peak before they are subtracted. The remaining BG is described by a linear function. Neither the event-mixing nor the sideband-mixing method are able to describe the BG in the $m_{\pi^+\pi^-\pi^0}$ spectrum of the ω meson. While the likesign-mixing method does manage to describe the $m_{\pi^+\pi^-\pi^0}$ spectrum significantly better, it does not manage to describe all momenta. This is most prominent for very low p_T, where the signal to BG ratio becomes low. The reason, why event-mixing and sideband-mixing are not able to describe the ω-BG at all is partly due to the fact, that the total BG is not only consisting of combinatorial BG. This can be seen in Fig. 10.4 (left and middle), where different contributions to ω meson BG for $5.0\,\text{GeV}/c < p_\text{T} < 6.0\,\text{GeV}/c$ (left) and $12.0\,\text{GeV}/c < p_\text{T} < 14.0\,\text{GeV}/c$ (middle) in EMCal for MC, using the MB trigger are shown. The blue distribution in these plots is acquired by subtracting all validated ω mesons from the SigBG distribution and can be called true BG. The true BG can be separated in three different distributions:

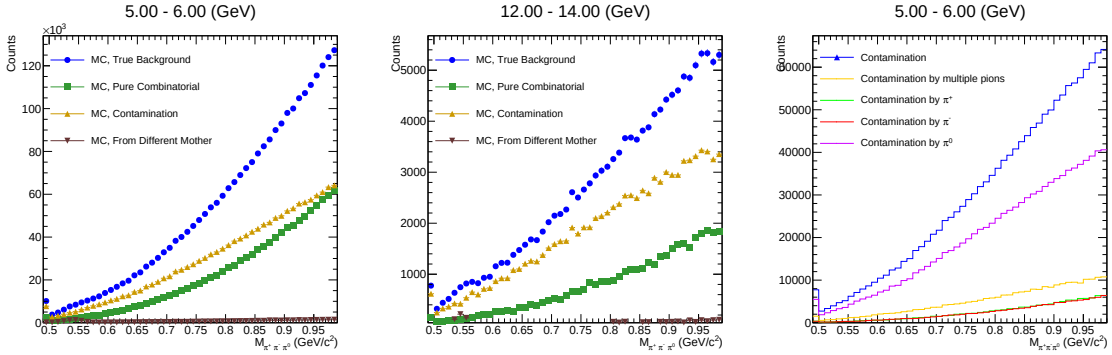

Figure 10.4: **Left** and **Middle**: Different contributions to ω meson BG for 5.0 GeV/c $< p_{\mathrm{T}} <$ 6.0 GeV/c (left) and 12.0 GeV/c $< p_{\mathrm{T}} <$ 14.0 GeV/c (middle) in EMCal for MC, using the MB trigger. The blue distribution is acquired by subtracting all validated ω mesons from the SigBG distribution. The blue distribution is split in three categories: The green distribution consists of ω candidates originating from uncorrelated pions, the combinatorial BG. In the orange distribution at least one pion is not the identified pion, the contamination BG. The brown distribution originates from the same mother meson, which is not the ω meson. **Right**: Different contributions to ω meson contamination BG for 5.0 GeV/c $< p_{\mathrm{T}} <$ 6.0 GeV/c in EMCal for MC, using the MB trigger. The blue distribution shows the total contamination BG. The purple distribution shows the contamination contribution caused by neutral pions. This contribution is generating the majority of the total contamination BG. The green and red distributions shows the contamination contribution caused by charged pions. The orange distribution is describing cases, in which more than one pion is falsely identified.

- Different Mother: All three combined pions are correctly identified and originate from the same mother particle. However, the mother particle is no ω meson. The contribution of BG originating from a different mother is negligible.

- Contamination: At least one of the three combined pions is not the particle, which it is identified as. The contamination BG is generating a significant part of the total BG. As can be seen, the contamination BG becomes even more important for high p_{T}. The contamination BG originates primarily from wrongly identified neutral pions.

- Combinatorial: The remaining BG is originating from uncorrelated combinations of $\pi^+\pi^-\pi^0$. Besides the contamination, the combinatorial BG is the most important BG contribution.

The right plot in Fig. 10.4 is showing different contributions to the ω meson contamination BG for 5.0 $<$GeV/c $p_{\mathrm{T}} <$ 6.0 GeV/c. The largest contribution turned out to be neutral pions. Further p_{T} intervals of the plots shown in Fig. 10.4 can be found in Fig. A.34 and Fig. A.35. To ensure that the BG shape produced in MC is similar to the BG shape in data,

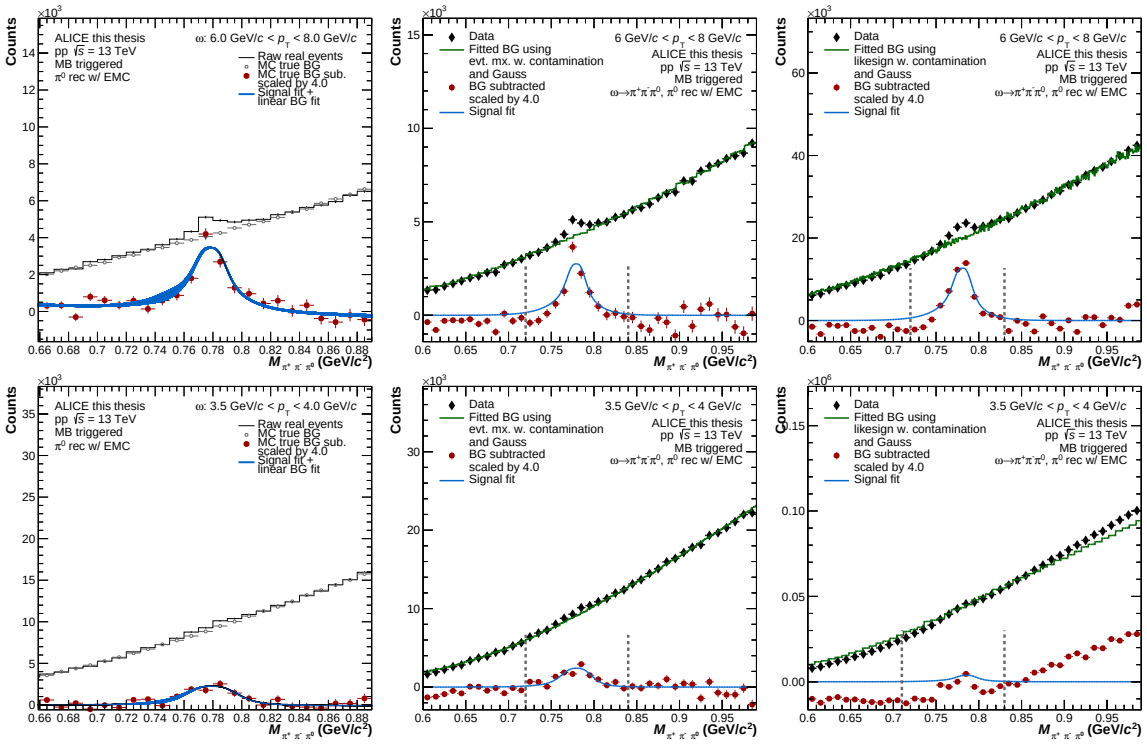

Figure 10.5: Example $m_{\pi^+\pi^-\pi^0}$ distributions of ω meson for $6\,\mathrm{GeV} < p_\mathrm{T} < 8\,\mathrm{GeV}$ (top) and $3.5\,\mathrm{GeV} < p_\mathrm{T} < 4\,\mathrm{GeV}$ (bottom) for EMCal in the MB triggered data set. **Left:** The BG is described by the true MC BG. An additional first order polynomial is used for the remaining BG. **Middle:** The BG is described using a template parametrization using event-mixing from data for combinatorial BG and contamination BG from MC. **Right:** The BG is described using a template parametrization using likesign-mixing from data for combinatorial BG and contamination BG from MC.

the validated ω candidates have been subtracted from SigBG in MC and the resulting histograms have been used as true BG, replacing the mixing technique histograms. An example of this BG description method can be found in Fig. 10.5 (left). The true BG describes the BG better, than any of the described mixing techniques. Therefore, the BG originating from contamination has to be considered and a template parametrization method has been implemented, also called template fit. This parametrization is combining the combinatorial BG histogram with the contamination BG histogram and scales them in a way, that they match the signal shape. While the contamination BG can only be extracted from MC, there are various possibilities for the selection of the combinatorial BG histogram. All three described mixing techniques have been used for the combinatorial BG of the template parametrization. No remaining BG is subtracted for all BG parametrizations described in this chapter. An example of the template parametrization method, using event-mixing and likesign-mixing can be found in Fig. 10.5 (left and right). While, the signal extraction is improved using the template parametrization in comparison to the use of a purely combinatorial BG, the

extracted signals show a high amount of fluctuation and are not able to describe the BG for the whole p_{T} range. The comparison of the discussed BG description methods show that the true MC BG describes the BG shape the best, while likesign mixing is the most promising mixing technique. Furthermore, the likesign-mixing method can be further improved by the use of a template parametrization.

The benefit of the discussed BG description methods is that the BG shape is described by histograms, which are driven by physical principles. While the same cannot be said for a BG parametrization, parametrizing the BG can result in a better description and shall be discussed in the following passage. A previous ω analysis in $\sqrt{s} = 7$ TeV [97] has used a second order polynomial to describe the BG for the most reconstruction methods and p_{T}, while for PHOS a first order polynomial has been used at $p_{\mathrm{T}} > 10\,\mathrm{GeV}/c$. However, a second order polynomial is not able to describe the BG at low p_{T} for the different reconstruction methods in this work and a third order polynomial is needed. A simple polynomial parametrization is only parametrizing the $m_{\pi^+\pi^-\pi^0}$ outside of the peak region and works quite well for low to medium p_{T}. However, as the width of the ω meson starts to increase significantly at $p_{\mathrm{T}} > 15\,\mathrm{GeV}/c$, the $m_{\pi^+\pi^-\pi^0}$ region available for parametrizing is reduced until the simple polynomial parametrization becomes not viable anymore. By adding a peak shape on top of the polynomial, the parametrization can also be used in the peak region and therefore cover the whole p_{T} range. Only the polynomial part of the parametrization is used to subtract the BG from SigBG. To acquire the peak shape, the true MC candidates have been parametrized with different peak functions for each p_{T} interval : A simple Gaussian, a Gaussian with an exponential tail on the left side and a Gaussian with an exponential tail on both sides. Furthermore, the Gaussian with an exponential tail on both sides is parametrized in two variations. One variation uses the same exponential tail parameter on both sides of the peak, resulting in symmetrical peaks. The second variation uses independent exponential tail parameters on the two peak sides. In addition to that, the p_{T} dependent parameters of the different peak function are themselves parametrized to obtain p_{T} dependent parametrizations for each parameter of the different peak functions. These parametrizations can be found in [67]. They should be taken with caution, if the p_{T} range becomes extended at some point in the future by other analysis, as it is not guaranteed, that the polynomial parametrizations behave properly outside the chosen p_{T} range. It turned out, that an exponential tail on both sides of the peak is needed to properly describe the shape of true ω meson signal over the whole p_{T} range. The exponential tail on the right side of the peak becomes prominent for $p_{\mathrm{T}} > 15\,\mathrm{GeV}/c$ and originates from clusters in the EMCal that start to merge. For the MB triggered PCM, PHOS and PCM-PHOS, which are limited in p_{T} in comparison to the EMCal triggers, a Gaussian with symmetrical exponential tails have shown to describe the

signal shape best. In the BG parametrization, the only free parameter of the peak function is the amplitude. The width and tail parameters are fixed on the p_{T} dependent values, extracted from the true MC parametrization. Fixing those parameters reduces the risk of the parametrization itself to create an additional peak shape during the signal extraction procedure for low signal to BG ratios. In addition to that, the parametrization becomes more stable in terms of statistical fluctuations.

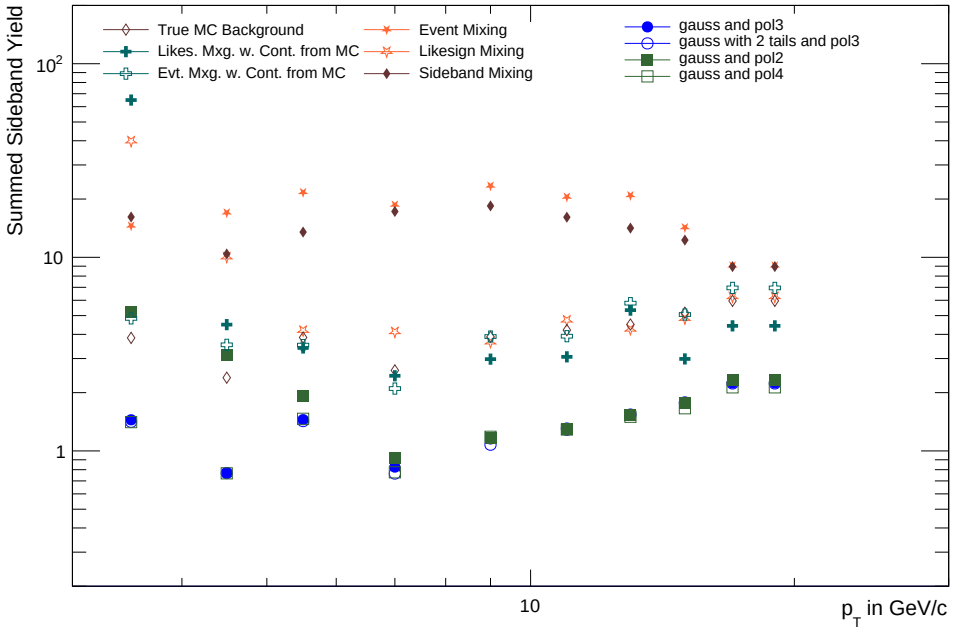

Figure 10.6: Sideband yields of a selection of different BG description methods for MB triggered data, reconstructed with EMCal for different p_{T}.

To quantify how well a certain BG description method performs, the absolute invariant mass interval values on the left side and on the right side of the peak region between $< 0.6\,\mathrm{GeV}/c < m_{\pi^+\pi^-\pi^0} < 0.7\,\mathrm{GeV}/c$ and $< 0.9\,\mathrm{GeV}/c < m_{\pi^+\pi^-\pi^0} < 0.99\,\mathrm{GeV}/c$ are summed after the BG has been subtracted. The resulting values will be called sideband yields during this work. Fig. 10.6 shows the sideband yields of a selection of different BG description methods for MB triggered data, reconstructed with EMCal for different p_{T} intervals. The third and forth order polynomial parametrizations are performing significantly better than all other BG description methods. While the second order polynomial is performing well for $p_{\mathrm{T}} > 7\,\mathrm{GeV}/c$, the benefit of a third order polynomial can be observed for $p_{\mathrm{T}} < 7\,\mathrm{GeV}/c$. As the fourth order polynomial is not improving the sideband yields any further, the BG parametrization is limited to a third order polynomial. Fig. 10.7 shows examples of the $m_{\pi^+\pi^-\pi^0}$ distributions for $3.5\,\mathrm{GeV}/c < p_{\mathrm{T}} < 4\,\mathrm{GeV}/c$ for EMCal in the MB triggered data set for different BG fits. The peak function of a simple Gaussian, as well as the Gaussian with an exponential tail on both sides of the peak, are viable options for the BG description. As it was already

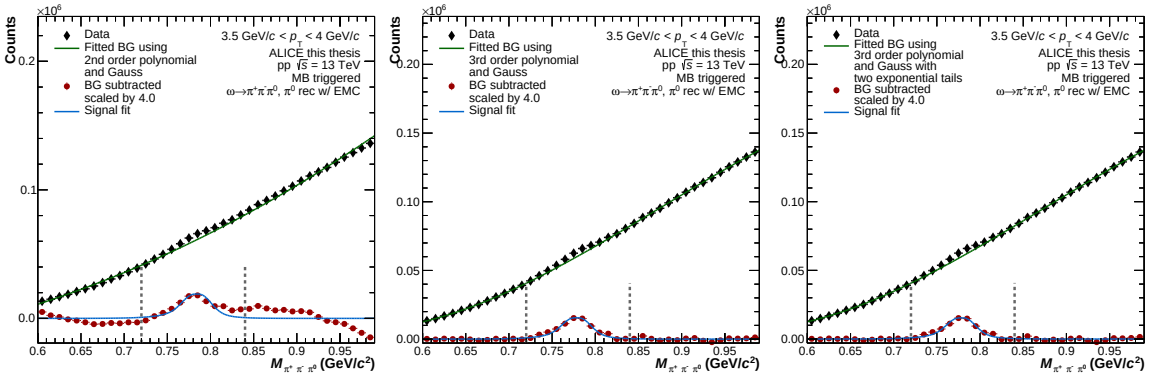

Figure 10.7: Example $m_{\pi^+\pi^-\pi^0}$ distributions of ω meson for $3.5\,\text{GeV} < p_\text{T} < 4\,\text{GeV}$ for EMCal in the MB triggered data set. The BG is described by different parametrization functions. Only the polynomial part of the parametrizations is subtracted as BG. From left to right the used BG parametrization functions are: Second order polynomial with an additional Gaussian on top, third order polynomial with an additional Gaussian on top, and finally a third order polynomial with an additional Gaussian with an exponential tail on both sides of the peak on top.

explained in Chap. 9, two efficiencies are possible for this analysis. It could be observed, that the difference of these efficiencies becomes smaller for a simple Gaussian on top of a third order polynomial in comparison to the Gaussian with an exponential tail on both sides. On the other hand, the Gaussian with an exponential tail on both sides has shown to be even more stable in terms of possible statistical fluctuations. It has been decided to use a simple Gaussian on top on a third order polynomial for the signal extraction of this work, while the option of a Gaussian with an exponential tail on both sides has only been used for the estimation of the systematic uncertainties. The parametrization function of a Gaussian on top on a third order polynomial is given by Eq. 10.2, while by individually fixing P_0, P_1 or P_2 to zero, it could be observed that all polynomial terms are needed to describe the BG properly.

The remaining ω meson signal, after the BG subtraction, is parametrized with $F_{\omega,\,\text{Signal}}$, defined in equation Eq. 10.4. As already described, the same exponential tail parameter is used on both sides of the peak for PCM, PCM-PHOS and PHOS, while the lambda parameters λ, λ_1 and λ_2 are fixed to the values acquired by the true MC signal parametrizations. Hence, the only free parameters of this parametrization are the amplitude A, the peak width σ_ω and the mean position m_ω.

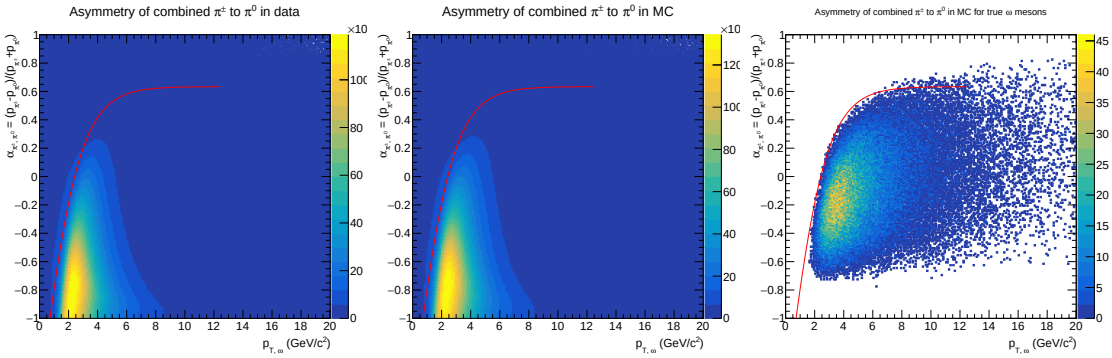

Figure 10.8: Asymmetry distribution $\alpha_{\pi^{\pm},\pi^0}$ of combined charged pions and neutral pions in dependence of the ω-p_{T} for EMCal using the MB trigger. From left to right the plots show $\alpha_{\pi^{\pm},\pi^0}$ for data, MC and validated ω mesons in MC. The red line represents an example cut on the $\alpha_{\pi^{\pm},\pi^0}$ distribution.

10.2 Difference of Efficiencies

Similar to the efficiencies for π^0 and η mesons, a reconstruction and a validated or true efficiency can be calculated for the ω meson. A comparison of the different signal shapes in data and MC for all reconstruction methods can be found in the appendix in Sec. A.4.2. As can be seen, the shape of true ω mesons can deviate from the extracted ω meson shape. This difference can be observed in the appendix figures of Sec. A.4.3, which compares the corrected yields of the different reconstruction methods and triggers . However, the signal shape between data and MC is in good agreement for the whole momentum range of all reconstruction methods. Hence, the reconstruction efficiency has been used for the ω meson reconstruction, while the difference to the true efficiency is considered for the estimation of the systematic uncertainties. As the difference of the two different efficiencies seems to be more prominent in the calorimeter methods in comparison to PCM, the effect of different calorimeter cuts on this difference has been investigated on the basis of corrected yields. This includes the cluster timing, the minimum energy, the number of minimum cells in a cluster and the long axis of the cluster shape. None of these properties did influence the difference of the different efficiencies within statistical uncertainties.

Furthermore, it turned out that the difference of the two efficiencies becomes large for very low p_{T}. As the minimum energy of photons in the EMCal is 700 MeV, predominantly asymmetric decays of low energetic neutral pions and high energetic charged pions are used for the ω reconstruction at low p_{T}. Hence, the influence on the difference of efficiencies of the

asymmetry $\alpha_{\pi^{\pm},\pi^0}$ between the combination of both charged pions and the neutral pion have been investigated. $\alpha_{\pi^{\pm},\pi^0}$ is calculated by:

$$\alpha_{\pi^{\pm},\pi^0} = \frac{p_{\pi_\pm} - p_{\pi_0}}{p_{\pi_\pm} + p_{\pi_0}} \tag{10.6}$$

Fig. 10.8 shows the asymmetry distribution of combined charged pions and neutral pions in dependence of the ω-p_{T} for EMCal, using the MB trigger. An example cut on $\alpha_{\pi^{\pm},\pi^0}$ is represented by a red line and was extracted from the shape of validated ω mesons in MC. Similar to the cluster cut variations, no influence the difference of the different efficiencies within statistical uncertainties could be observed.

In addition to the cluster cut variations and the studies of $\alpha_{\pi^{\pm},\pi^0}$, the influence on the invariant mass distribution $m_{\pi^+\pi^-}$ of the combined charged pions was investigated, as the influence of charged pions become more important at low p_{T}, due to the $\alpha_{\pi^{\pm},\pi^0}$ distribution. Fig. 10.9 (right) shows the different contributions to the invariant mass $m_{\pi^+\pi^-}$ of charged

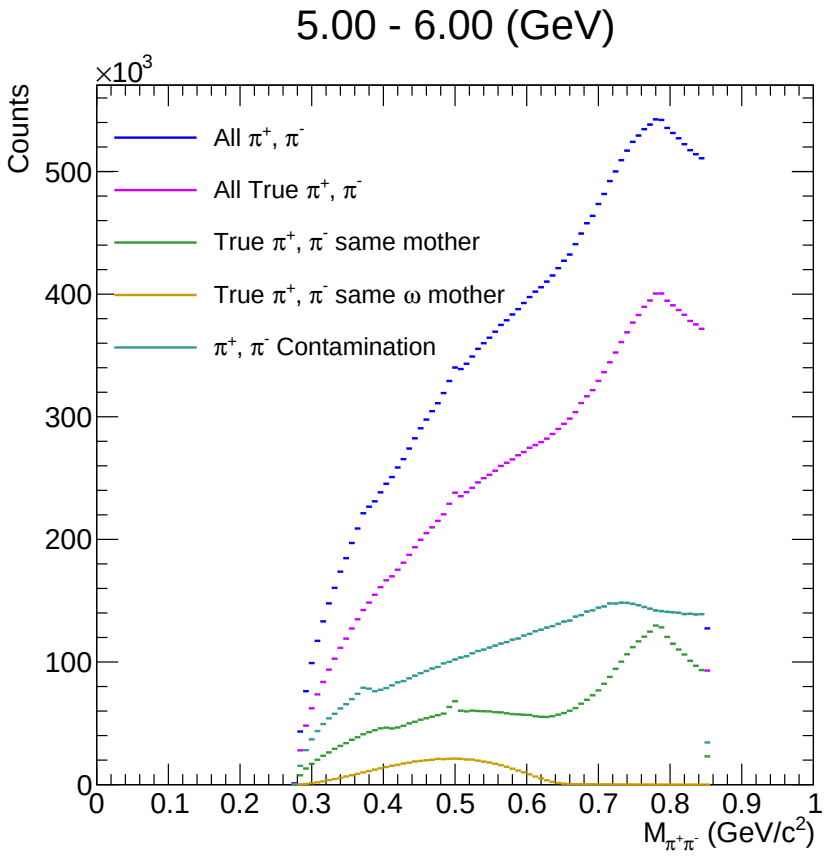

Figure 10.9: Different contributions to invariant mass $m_{\pi^+\pi^-}$ of charged pions for the example p_{T} interval of $5\,\mathrm{GeV}/c < p_{\mathrm{T}} < 6\,\mathrm{GeV}/c$, simulated in MC.

pion pairs for $5\,\mathrm{GeV}/c < p_{\mathrm{T}} < 6\,\mathrm{GeV}/c$, simulated in MC. The invariant mass range of

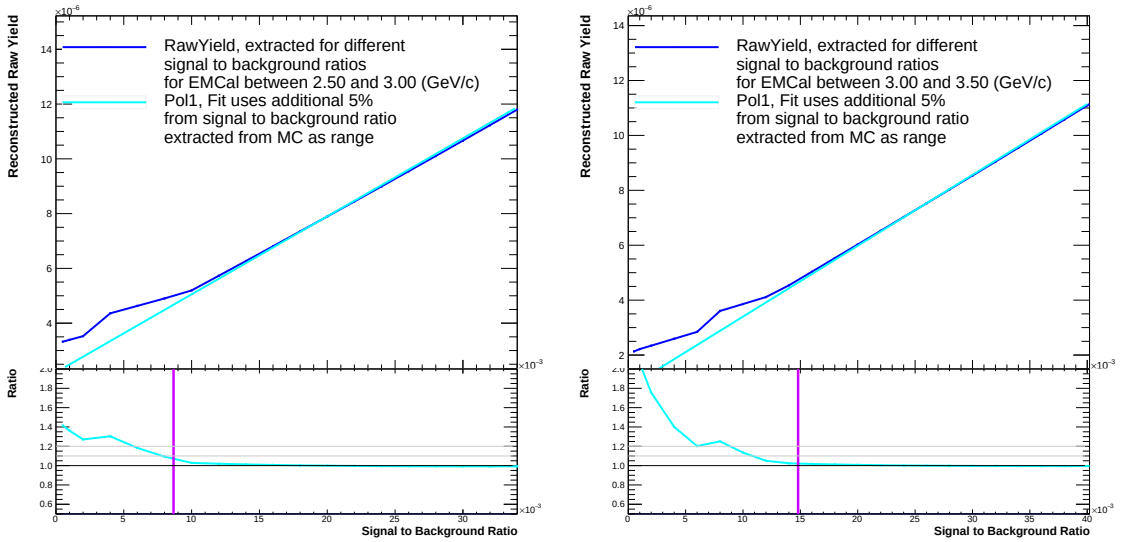

Figure 10.10: Extracted raw yields for different signal to BG ratios for EMCal for 2.50 GeV/c $< p_{\mathrm{T}} <$ 3.0 GeV/c (left) and 3.00 GeV/c $< p_{\mathrm{T}} <$ 3.5 GeV/c (right). The vertical purple line marks the signal to BG ratio that has been determined for the corresponding p_{T} interval in MC. The parametrization is performed in a range from the purple line to additional 5 % in the signal to BG ratio.

charged pions, which originate from the same ω-meson mother can be up to $m_{\pi^+\pi^-} \approx 650$ MeV/c^2. Different cut windows on $m_{\pi^+\pi^-}$ for the selection of charged pion pairs, which are used for the ω reconstruction, have been investigated. It turned out, that the reduction of the open cut of $m_{\pi^+\pi^-} < 850\,\mathrm{MeV}/c^2$ is heavily influencing the shape of the BG shape in the ω meson reconstruction. The resulting BG distribution shapes become more difficult to parametrize with a third order polynomial, while the difference in efficiency could not be improved. Due to this reason, a loose cut on the invariant mass of $m_{\pi^+\pi^-} < 850\,\mathrm{MeV}/c^2$ has been used for this analysis.

As the difference of the two efficiencies become significant for low signal to BG ratios at low p_{T}, the influence of the signal to BG ratio to the signal extraction has been studied. For this study, the true ω mesons are subtracted from SigBG in MC to obtain a p_{T} dependent validated or true BG distribution. The true BG distribution and the true ω mesons can be used to create $m_{\pi^+\pi^-\pi^0}$ distributions with well-defined signal to BG ratios, which can be used to perform a signal extraction. For an ideal signal extraction method, the obtained raw yields are proportional to the signal to BG ratio. However, as the signal extraction is not ideal, deviations from the ideally linear function are expected for low signal to BG ratio values. Fig. 10.10 shows examples the extracted raw yields for different signal to BG ratios for EMCal for 2.50 GeV/c $< p_{\mathrm{T}} <$ 3.0 GeV/c and 3.00 GeV/c $< p_{\mathrm{T}} <$ 3.5 GeV/c. The vertical purple line marks the signal to BG ratio, that has been determined for the corresponding p_{T} interval in MC. In other words, the line marks the signal to BG ratio, which is present in the

analysis. The parametrization range of the first order polynomial function, shown in cyan, is starting from this purple line, while it ends at a signal to BG value equal to the purple line plus additional 5 %. As can be seen, the difference between the cyan parametrization and the reconstructed raw yield is dependent on the signal to BG ratio and the chosen p_{T} interval. The p_{T} interval from $3.00\,\mathrm{GeV}/c < p_{\mathrm{T}} < 3.5\,\mathrm{GeV}/c$ is the first p_{T} interval, which has been used for the ω reconstruction with the EMCal reconstruction method. The BG description of the p_{T} interval of $2.50\,\mathrm{GeV}/c < p_{\mathrm{T}} < 3.0\,\mathrm{GeV}/c$ has been considered to not be adequate, as the signal to BG ratio in this interval is too low to properly extract the raw yield.

10.3 Systematic Uncertainties

The systematic uncertainties of the different reconstruction methods and all triggers are estimated independently of each other, making use of Barlow's criteria [98]. The majority of the systematic uncertainties are evaluated by adjusting the chosen selection criteria for the different reconstruction methods within reasonable limits and investigate the effect on the resulting corrected yields. This procedure is performed in dependence of p_{T} and the variation of selection criteria is performed one at a time. In addition to that, some systematic uncertainties like for example the material budget uncertainty are using the knowledge of intensive studies performed within the collaboration. The different origins of systematic uncertainties are summed in quadrature, while the total systematic uncertainty is given by the square root of this sum. As the number of possible cut variations for each selection criteria is infinite and the processing capabilities of the LCG are limited, a reasonable selection of variations for the selection criteria had to be chosen. Due to this limitation, the largest deviation of the different origins of uncertainties for each interval are acquired by calculating the average of the maximum positive and negative deviation from the standard cut. If the variation of the cut is not performed by loosening and tightening but only tightening the cut, the deviation has been used as maximum deviation and was divided by $\sqrt{2}$. To consider statistical uncertainties, the deviation distributions have been "smoothed" for all origins of systematic uncertainties, except the signal extraction. While smoothing the systematic uncertainties basically means to parametrize the distributions, the smoothing also takes the average of neighboring p_{T} intervals if a certain uncertainty is zero for a given p_{T} interval. The different origins of systematic uncertainties are grouped into different categories and the resulting origins of systematic uncertainties can be found in Tab. 10.2. As most systematic uncertainties are p_{T} dependent, the values given in the table are shown in ranges, reflecting this dependence. For the calculation of the combined statistical and systematic uncertainties, the different reconstruction methods and triggers were combined as explained in Sec. 10.4 and Sec. 10.5. The p_{T} dependent systematic uncertainties of the different uncertainty groups for each reconstruction method are shown in Fig. 10.11. Even more detailed information of the chosen cut variations can be found in the appendix in Sec. A.4.4. The different categories are explained in the following passages.

Signal Extraction:
As already discussed in the previous section, the standard method to describe the BG is a Gaussian on top of third order polynomial. For the signal extraction uncertainty, the used Gaussian on top of the polynomial BG is changed to a Gaussian with an exponential on both sides. In addition to that, the polynomial is increased to fourth order. Furthermore, the

Method	PCM	PHOS	PCM-PHOS	EMCal			PCM-EMCal		
Trigger Unit	MB in %	MB in %	MB in %	MB in %	EG2 in %	EG1 in %	MB in %	EG2 in %	EG1 in %
Signal Extraction	3.7 - 15.5	9.5 - 27.9	4.5 - 27.1	4.0 - 12.8	1.9 - 8.3	4.2 - 16.0	5.2 - 16.4	3.8 - 11.1	5.4 - 22.3
Material	5.0	2.0	2.7	4.2	4.2	4.2	3.3	3.3	3.3
Charged pion rec.	3.5 - 4.4	3.7 - 4.4	3.9 - 4.3	4.2 - 4.6	4.6 - 5.6	4.8 - 6.0	3.9 - 4.4	4.3 - 5.4	4.5 - 5.8
Conv photon rec.	1.9 - 9.9	-	2.5 - 4.6	-	-	-	2.3	2.3 - 2.5	2.3 - 2.8
Calo photon rec.	-	6.1 - 6.4	5.4 - 5.5	2.5 - 3.5	2.6 - 4.2	4.8 - 6.9	2.2 - 7.2	2.2 - 5.1	4.7 - 8.2
Neutral pion rec.	3.2	5.0 - 5.6	5.0 - 5.3	3.1	3.1 - 6.0	3.2 - 10.0	3.1	3.1 - 5.8	3.2 - 9.1
Pileup	0.5	0.7	0.7	0.3	0.3	0.3	0.3	0.3	0.3
Total syst. uncertainty	8.4 - 21.7	13.2 - 29.4	10.8 - 29.0	8.5 - 15.0	7.7 - 12.7	9.6 - 21.4	9.1 - 19.3	8.2 - 15.0	10.1 - 23.8
Statistical uncertainty	9.4 - 35.2	9.3 - 19.5	15.0 - 22.3	4.5 - 7.9	3.7 - 14.9	3.9 - 9.6	5.5 - 19.5	7.3 - 24.4	9.9 - 18.9
Combined stat unc.	3.1 - 35.2								
Combined syst unc.	5.8 - 21.7								

Table 10.2: Systematic uncertainties for different reconstruction methods and triggers. The given ranges reflect the p_{T} dependence of the different origins of systematic uncertainties. The total uncertainties are calculated by combining the different reconstruction methods and triggers, explained in Sec. 10.4 and Sec. 10.5.

integration range and the parametrization range is adjusted. To consider the difference in the two efficiencies, the corrected yield, using the true efficiency, is taken into account. As the polynomial of 2nd order and the different mixing techniques do not properly describe the BG, these methods are not used for the estimation of the systematic uncertainty. The signal extraction uncertainty is the dominant contribution to the total systematic uncertainties for all reconstruction methods over almost the whole p_{T} range and can reach up to 27.9 % for PHOS at 5 GeV/c < p_{T} < GeV/c.

Material Budget:

System	Calculation	Uncertainty in %
PCM	$2 \cdot \sqrt{2.5^2}$	5
EMCal	$2 \cdot \sqrt{1.5^2 + 1.5^2}$	4.24
PHOS	$2 \cdot \sqrt{1^2}$	2
PCM-EMCal	$\sqrt{1.5^2 + 1.5^2 + 2.5^2}$	3.3
PCM-PHOS	$\sqrt{1^2 + 2.5^2}$	2.7

Table 10.3: Overview of systematic uncertainties of the material budget.

Photons can convert to $e^{\pm}$ pairs, due to interactions with the detector material. Hence, precise knowledge on the material budget of the detector is necessary. The material budget can be separated into two parts: The outer and the inner material. All detector material within a radius of $R = 180$ cm, corresponding to the middle of the TPC, is called inner material. Conversions within this radius can be tracked and measured with the PCM method. Intensive studies within the collaboration [78] have shown, that the uncertainty for the inner detector material is 2.5 % per conversion photon. All detector material outside the radius of $R = 180$ cm is called outer material and originates predominantly from the support structures of the TRD and TOF. This material is relevant for photon reconstructions with the help of a calorimeter. Conversions within the outer detector are also called late photon conversions, as described in Sec. 9. The photons originating from these conversions cannot be tracked and may end up in separate clusters, leading to missing π^0 candidates in the invariant mass distribution. The systematic uncertainty for the outer material budget was estimated in [99] to be 4.2 % in total for EMCal or 1.5 % per photon for the TRD and 1.5 % per photon for the TOF. Furthermore, it was estimated to be 2 % in total or 1 % per photon for the PHOS detector [100]. The total systematic uncertainty for the material budget is calculated as square root of the quadratic sum of the inner and outer material, shown in Tab. 10.3.

Charged Pion Reconstruction:
The charged pion reconstruction uncertainty is highly correlated in all reconstruction methods. The different variations of the charged pion cuts include the number of ITS and TPC clusters and the minimum p_{T}. The uncertainty for the ITS-TPC matching efficiency were taken from [101]. The values between the given p_{T} intervals were interpolated linearly by $F_{\text{ITS-TPC Matching}}(p_{\mathrm{T},\,\pi^{\pm}})$, while the values below $0.1\,\mathrm{GeV}/c$ and above $20\,\mathrm{GeV}/c$ in $F_{\text{ITS-TPC Matching}}(p_{\mathrm{T},\,\pi^{\pm}})$ are fixed to the values of these thresholds.
By approximating $p_{\mathrm{T},\,\pi^{\pm}} \approx p_{\mathrm{T},\,\omega}/3$ and knowing that two charged pions are used to reconstruct an ω candidate, the estimation of the uncertainty for the ITS-TPC matching efficiency is calculated by $F_{\text{ITS-TPC Matching}}(p_{\mathrm{T},\,\omega}/3) * 2$. Furthermore, the $n\sigma_{\pi^{\pm}}$ value of the charged pion idenfication and the cut on the combined charged pion mass has been varied. The largest contributions to the charged pion reconstruction uncertainty are the ITS-TPC matching efficiency and the pion identification. The order of magnitude for the systematic uncertainty of the charged pion reconstruction is $\approx 5\,\%$.

Conversion Photon Reconstruction:
The selection criteria of the conversion photon reconstruction can be separated into four groups: Track properties, PID, Kalman Filter properties and K^0_S, Λ and $\bar{\Lambda}$ rejection. Variation of these selection criteria have shown that the largest contributions to the systematic uncertainty are given by changes to Kalman Filter properties χ^2_γ and ψ_{pair} followed by changes to the K^0_S, Λ and $\bar{\Lambda}$ rejection cuts. The total uncertainty is of the conversion photon reconstruction is in the order of $3\,\%$. Its influence grows for low p_{T} and can reach up to $9\,\%$ for the lowest p_{T} interval in PCM.

Calorimeter Photon Reconstruction:
To estimate the systematic uncertainty of the calorimeter photon reconstruction, the energy fine-tuning, the minimum cluster energy E_{cluster}, the minimum number of cells in a cluser $N^{\text{cells}}_{\text{cluster}}$, the cluster timing window t_{cluster} (including the timing efficiency), the cluster shape variable σ^2_{long} and the track-matching variables have been adjusted. As described in [102], using a simple cut on $N^{\text{cells}}_{\text{cluster}}$ is not possible for EMCal, as the number of cells per cluster is not perfectly reproduced by MC. Hence, variations of $N^{\text{cells}}_{\text{cluster}}$ in EMCal and PCM-EMCal are including a correction, performed in PCM-EMCal and EMCal. The systematic uncertainty of the calorimeter photon reconstruction for the MB and EG2 trigger are dominated by the variations of $N^{\text{cells}}_{\text{cluster}}$, σ^2_{long} and the track-matching variables. For the EG1 trigger, the uncertainty of the TRF becomes the dominant contribution. The order of magnitude for the total systematic uncertainty of the calorimeter photon reconstruction is $\approx 5\,\%$.

Neutral Pion Reconstruction:
The selection of π^0 candidates has been performed in an invariant mass window of $3\sigma_{\pi^0}$

around the extracted mass position. By varying the width of the selection window, the purity of the π^0 meson candidates is adjusted. Furthermore, a cut on the energy asymmetry is used to estimate its influence on the π^0 selection. As the ω reconstruction with EMCal, using the EG1 and EG2, is applying a cut on the maximum p_{T} for the π^0 selection, this cut has been reduced and removed. The systematic uncertainty of the π^0 selection is estimated to be between 3.1 % and 10.0 %

Pileup:
To estimate the effect of pileup, the pileup rejection criteria have been loosened. The effect was minor and in the order of 0.5 %. This is also due to the fact, that the invariant mass analysis uses two charged pions on top of a neutral pion candidate to form a correlated ω signal and the uncorrelated BG is well described by the polynomial BG parametrization.

ω/π^0 Ratio:
For the π^0 and η meson reconstruction, the individual reconstruction methods are acquired in similar p_{T} ranges. Therefore, the individual measurements have been used to calculate the η/π^0 ratio. This has the benefit, that systematic uncertainties can be calculated on the ratio itself, while certain uncertainties can cancel each other. However, the individual measurements of the π^0 and the ω meson for the different reconstruction methods differ significantly in their p_{T} ranges. Hence, for the calculation of the ω/π^0 ratio, the combined spectra, shown in Fig. 10.20 and Fig. 9.7, have been used. Before the ratio is calculated, the p_{T} interval limits of the π^0 meson are adjusted (re-binned) to match the p_{T} intervals of the ω meson. After that, the intervals of the ω and π^0 distributions are shifted in $E\,\mathrm{d}^3\sigma/\mathrm{d}p^3$, as explained in Sec. 10.5. As the material budget partly cancels out in the ω/π^0 ratio, the contribution of the material budget uncertainty can be reduced. For this purpose additional invariant cross section distributions of the ω and π^0 meson without the material budget uncertainty have been calculated. The relative total uncertainties with and without material budget uncertainties for each p_{T} interval are given by $U_{\mathrm{meson,\ with}}(p_{\mathrm{T}})$ and $U_{\mathrm{meson,\ without}}(p_{\mathrm{T}})$. Furthermore, the difference of these uncertainties is given by:

$$\Delta U_{\mathrm{meson}}(p_{\mathrm{T}}) = U_{\mathrm{meson,\ with}}(p_{\mathrm{T}}) - U_{\mathrm{meson,\ without}}(p_{\mathrm{T}}) \tag{10.7}$$

The differences $\Delta U_{\mathrm{meson}}(p_{\mathrm{T}})$ of the ω and π^0 meson, $\Delta U_{\omega}(p_{\mathrm{T}})$ and $\Delta U_{\pi^0}(p_{\mathrm{T}})$, are compared to determine if $\Delta U_{\omega}(p_{\mathrm{T}})$ or $\Delta U_{\pi^0}(p_{\mathrm{T}})$ is smaller. Only the smaller uncertainty $\Delta U_{\mathrm{meson,\ smaller}}(p_{\mathrm{T}})$ is used reduce the total systematic uncertainty of the ω/π^0 ratio. As systematic uncertainties are summed in quadrature, $\Delta U^2_{\mathrm{meson,\ smaller}}(p_{\mathrm{T}})$ is subtracted from $U^2_{\mathrm{meson,\ with}}(p_{\mathrm{T}})$, before the ω/π^0 ratio is calculated.

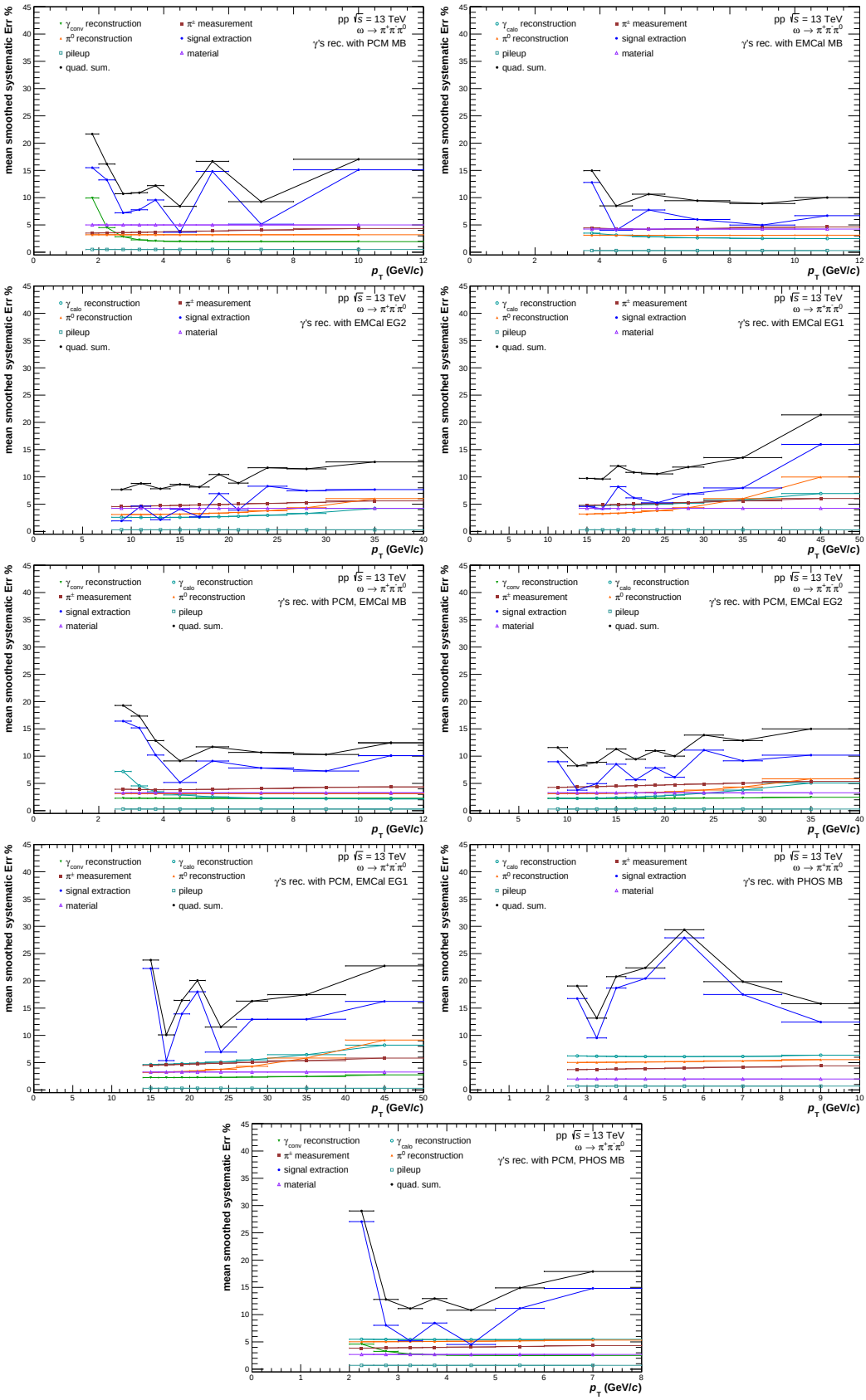

Figure 10.11: Total systematic uncertainties and their contributions for different ω reconstruction methods and triggers as function of p_T. All systematic uncertainties with exception to the signal extraction are smoothed. The used reconstruction methods and triggers are given in the respective legends.

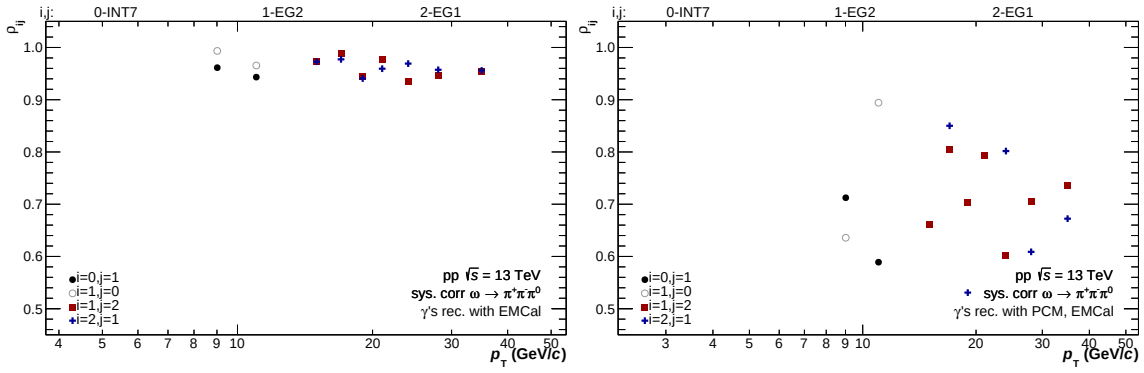

Figure 10.12: $\rho_{i,j}(p_{\mathrm{T}})$ for the different triggers of EMCal (left) and PCM-EMCal (right). The markers are only shown for p_{T} intervals with overlapping triggers.

10.4 Combination of Individual EMCal triggers

The ω meson in EMCal and PCM-EMCal is measured with the help of three different triggers: MB, EG2 and EG1. While the MB trigger is well suited for low p_{T} measurements, the EG2 and EG1 enhance the p_{T} range of the ω meson measurement significantly. Each trigger is analyzed individually, resulting in separate cross sections for each trigger. The p_{T} intervals, that are measured with multiple triggers can be combined to one measurement with improved uncertainties with the help of the Best Linear Unbiased Estimate (BLUE) [82][83][84] method. The BLUE method is taking the statistical and systematic uncertainty of each measurement and their correlation into account. As each trigger is using a separate data sample, the statistical uncertainties of the different triggers are considered completely uncorrelated. In case of the systematic uncertainties, all origins of systematic uncertainties except the signal extraction have been considered to be completely correlated. The total correlation of two measurements i and j is described by the p_{T} dependent correlation factors $\rho_{i,j}(p_{\mathrm{T}})$. The values of $\rho_{i,j}(p_{\mathrm{T}})$ can be between within 0 and 1, where 0 is corresponding to completely uncorrelated and 1 to completely correlated measurements. They are calculated by:

$$\rho_{i,j}(p_{\mathrm{T}}) = \frac{\sqrt{S_i^2(p_{\mathrm{T}}) - U_{i,j}^2(p_{\mathrm{T}})}}{S_i(p_{\mathrm{T}})} \tag{10.8}$$

Here, S_i is the statistical uncertainty of i, while $U_{i,j}$ is uncorrelated error of i with respect to j. The p_{T} dependent correlation factors $\rho_{i,j}(p_{\mathrm{T}})$ for the different triggers of EMCal and PCM-EMCal can be found in Fig. 10.12. For the combination of measurements, each measurement and their uncertainties are multiplied by specific weights $\omega_a(p_{\mathrm{T}})$. To obtain these weights, a correlation matrix $C_{i,j}(p_{\mathrm{T}})$ of size $n_{\mathrm{comb}} \times n_{\mathrm{comb}}$ is used. n_{comb} is the number of measurements which shall be combined and $n_{\mathrm{comb}} = 3$ in the case of the EMCal and

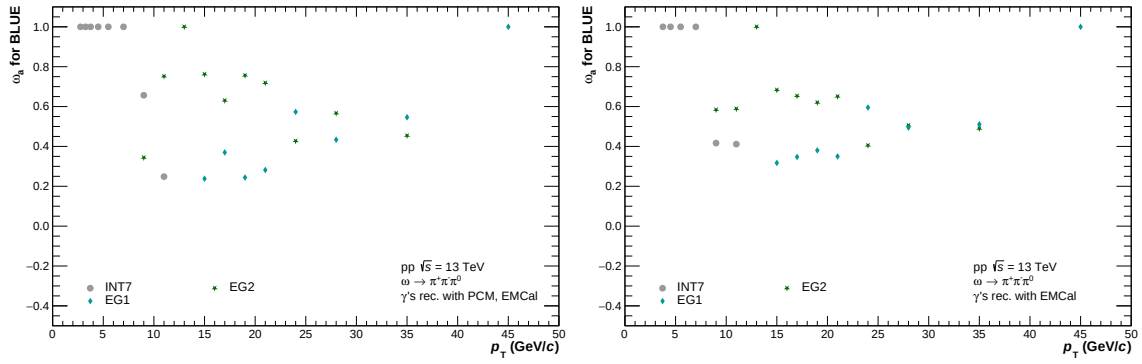

Figure 10.13: $\omega_a(p_T)$ for the different triggers of EMCal (left) and PCM-EMCal (right).

PCM-EMCal triggers. The matrix elements of $C_{i,j}(p_T)$ are called correlation coefficients $c_{i,j}(p_T)$ and are given by:

$$c_{i,j}(p_T) = \frac{\rho_{i,j}(p_T)S_i(p_T)\rho_{j,i}(p_T)S_j(p_T)}{T_i(p_T)T_j(p_T)} \tag{10.9}$$

$T_i(p_T)$ is the p_T dependent total uncertainty and is calculated by the square-root of the quadratic sum of the statistical and systematic uncertainty. With $C^{-1}_{i,j}(p_T)$ being the inverse matrix of $C_{i,j}(p_T)$ and $d_{a,b}(p_T)$ being the matrix elements of $C^{-1}_{i,j}(p_T)$, the weights $\omega_a(p_T)$ of the combination can be calculated by:

$$\omega_a(p_T) = \frac{\sum_{b=1}^{n_{\text{comb}}} d_{a,b}(p_T)}{\sum_{a,b}^{n_{\text{comb}}} d_{a,b}(p_T)} \tag{10.10}$$

Here, a and b are the indices of measurements which are combined and $\omega_a(p_T)$ is the weight applied to measurement a. The weights for the combination of the MB, EG2 and EG1 for EMCal and PCM-EMCal can be found in Fig. 10.13. If $Y_a(p_T)$ is the p_T dependent value of a distribution in measurement a, the BLUE method uses these weights to calculate a weighted average value $\langle Y(p_T)\rangle$ by:

$$\langle Y(p_T)\rangle = \sum_{a=1}^{n_{\text{comb}}} \omega_a(p_T)Y_a(p_T) \tag{10.11}$$

Besides the combination of the invariant cross sections $E\,\mathrm{d}^3\sigma/\mathrm{d}p^3$, observables directly connected to the individually measurements, like the mass position or width, are also combined using $\omega_a(p_T)$. For all upcoming figures of EMCal and PCM-EMCal, that are shown after this section, the different triggers have been combined.

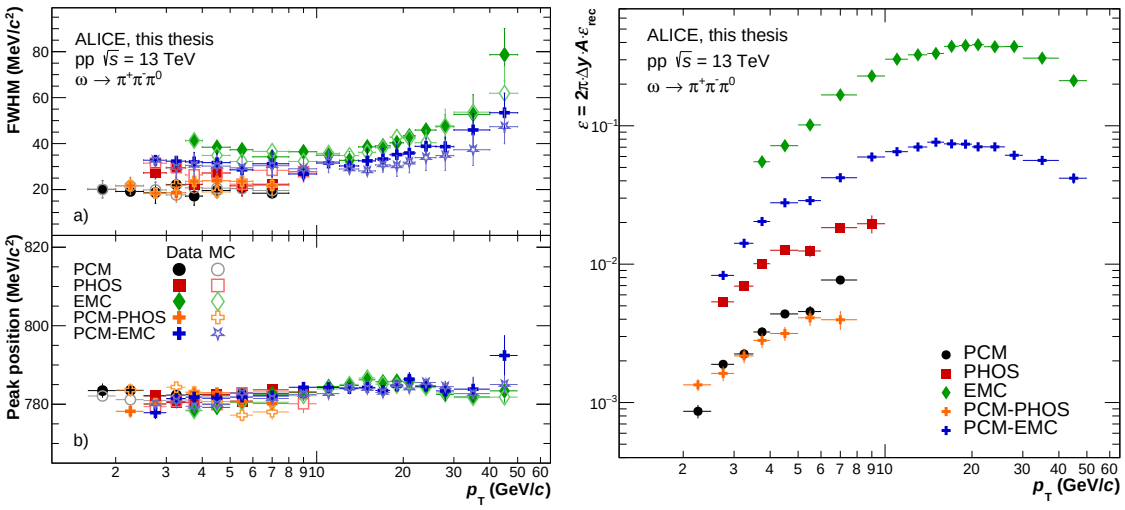

Figure 10.14: **Left:** Peak width (top) and position (bottom) of the ω meson for PCM, EMCal, PCM-EMCal, PHOS and PCM-PHOS in data (full markers) and MC (open markers), obtained from the signal parametrization $F_{\omega,\,\mathrm{Signal}}$. **Right:** Acceptance times efficiency ϵ_ω for the ω meson for the different reconstruction methods.

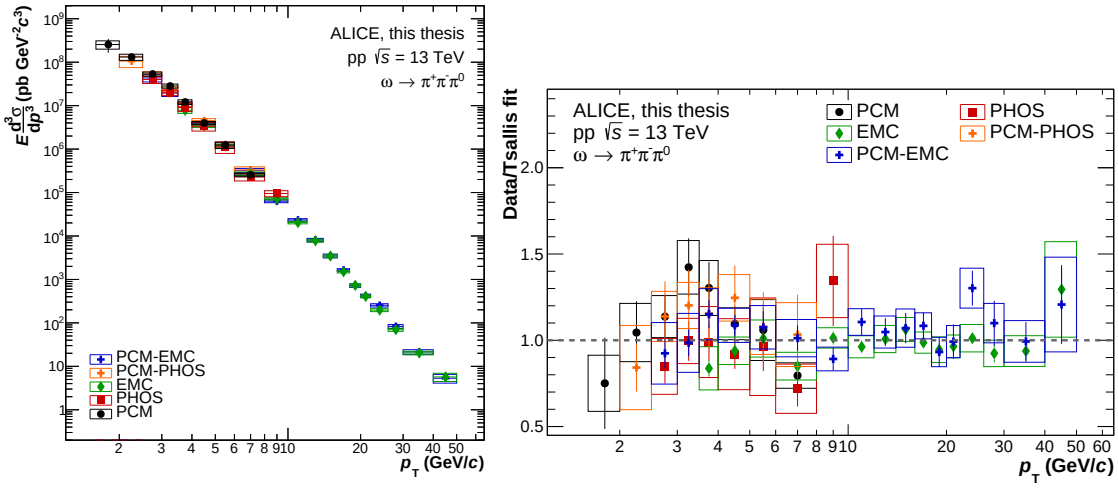

Figure 10.15: **Left:** Comparison to the invariant cross section of the ω production for the different reconstruction methods, used in this thesis. **Right:** Ratio of the invariant cross sections of the different reconstruction methods to the Tsallis function on their combined spectrum.

10.5 Individual ω Production Cross Section Measurements and their Combination

Fig. 10.14 (left) shows the peak width and position of the ω meson for the different reconstruction methods in data and MC, while Fig. 10.14 (right) shows ϵ_ω for the different reconstruction methods. The coverage of p_T for the different reconstruction methods can be

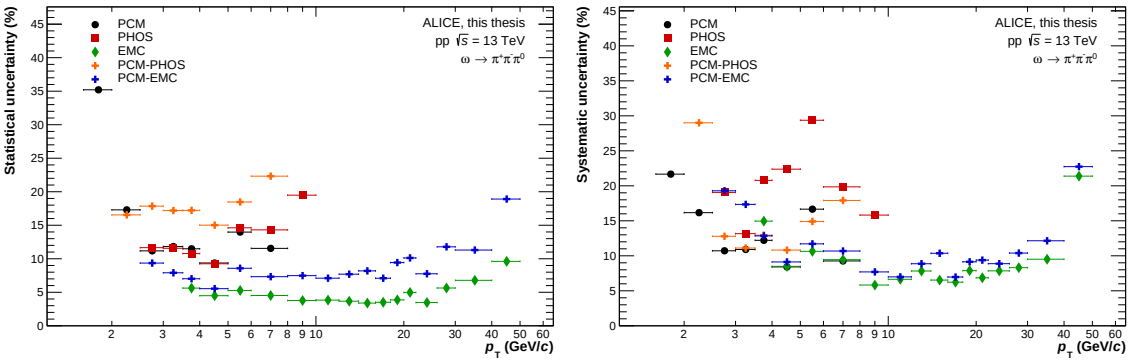

Figure 10.16: Comparisons of the statistical (**left**) and systematic (**right**) uncertainties of the ω production cross section for the different reconstruction methods, used in this thesis.

Method	Coverage of p_T in GeV/c
PCM	1.6–12.0
PCM-EMCal	2.5–50.0
PCM-PHOS	2.0–8.0
EMCal	3.5–50.0
PHOS	2.5–10.0

Table 10.4: Coverage of p_T for the different reconstruction methods, shown in Fig. 10.15.

seen in Tab. 10.4. The distributions align well for all reconstruction methods, while the benefits of the different methods can be clearly seen. PCM is able to reconstruct ω mesons down to 1.6 GeV/c with a FWHM of only $\approx$ 20 GeV/c^2. The benefits of the conversion photon, can also be seen in the width of PCM-PHOS and PCM-EMCal, which is significantly lower than the width of PHOS and EMCal. The increase of width at high p_T for PCM-EMCal and EMCal is originating from merging clusters in the calorimeters at high p_T. The low probability of photons to convert into $e^{\pm}$-pairs can be seen in low values of ϵ_ω for PCM. As the opening angles decrease, due to the Lorentz boost, ϵ_ω increases with p_T. If p_T increases even further, photons cannot be distinguished in the calorimeter anymore and ϵ_ω decreases, while the p_T of neutral pions is limited to 25 GeV/c for EMCal. Fig. 10.15 (left) shows a comparison of the invariant cross sections of all reconstruction methods, used in this work. Fig. 10.15 (right) is showing ω cross sections of Fig. 10.15 (left) divided by a Tsallis function, that has been obtained on the combined spectrum, as explained in chapter Sec. 10.6 and shown in Fig. 10.20. Each reconstruction method is performed independently of each other. The statistical and systematic uncertainties of the reconstruction methods are shown in Fig. 10.16. The different reconstruction methods align well within their statistical and systematic uncertainties. Similarly to the combination of the different triggers, described in Sec. 10.4, the different reconstruction methods are combined, using the BLUE method. In

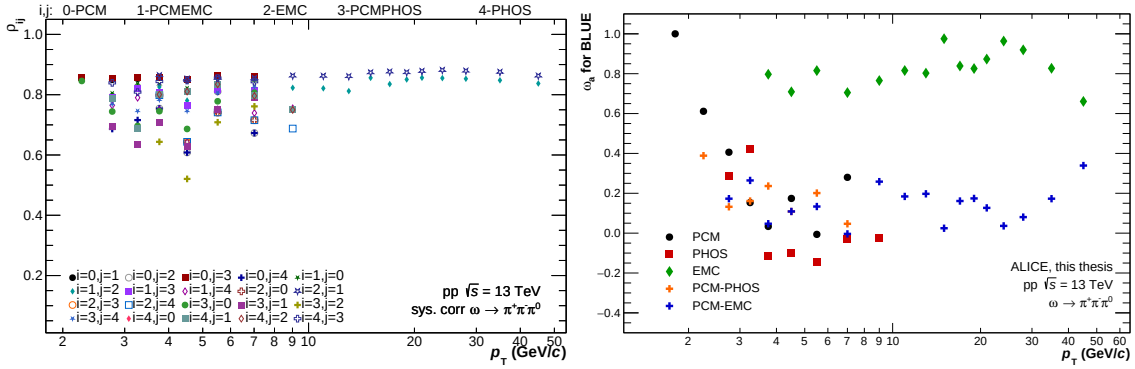

Figure 10.17: Correlation factors $\rho_{i,j}(p_{\mathrm{T}})$ (**left**) and weights $\omega_a(p_{\mathrm{T}})$ (**right**) used for the combination with the help of the BLUE method for PCM, EMCal, PCM-EMCal, PHOS and PCM-PHOS. The correlation factors are only shown, if multiple systems are available for a given p_{T}.

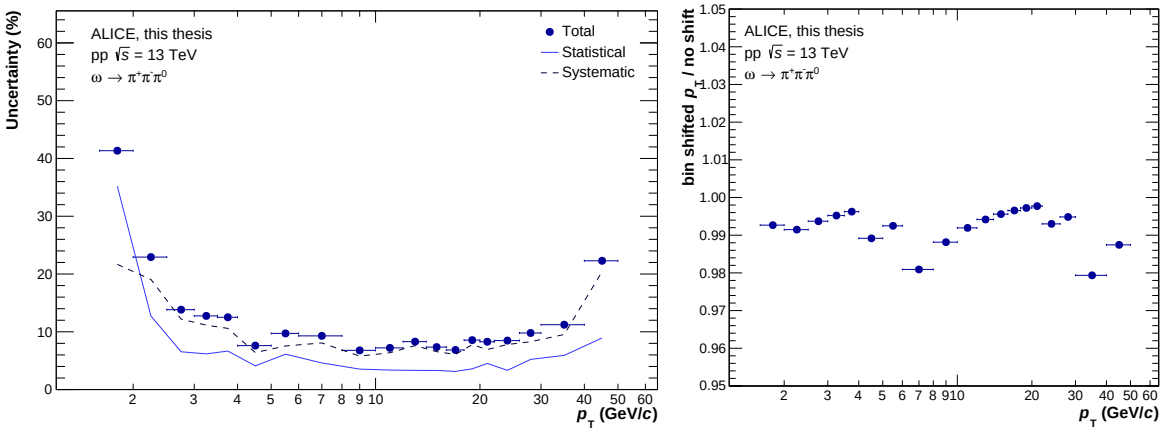

Figure 10.18: **Left:** Statistical and systematic uncertainties as well as the total uncertainty after the combination of the different reconstruction methods. **Right:** interval shift correction for combined ω spectrum in p_{T} (x-shift).

this case, the number of entries n_{comb} in the correlation matrix $C_{i,j}(p_{\mathrm{T}})$ changes to five, to consider all five reconstruction methods. Correlations between the statistical uncertainties of the different reconstruction methods were found to be completely uncorrelated between each other. By comparing the effect of the same cut variations during the estimation of the systematic uncertainties in different reconstruction systems with each other, the correlations of different origins of the systematic uncertainties is estimated. The resulting correlation factors $\rho_{i,j}(p_{\mathrm{T}})$ (left) and weights $\omega_a(p_{\mathrm{T}})$ can be found in Fig. 10.17. The statistical and systematic uncertainties, as well as the total uncertainty after the combination of the different reconstruction methods, can be found in Fig. 10.18. The total uncertainty is dominated by the systematic uncertainty over nearly the whole p_{T} range. Only the first p_{T} interval is dominated by the statistical uncertainties, as it represents the statistical limit of the ω measurement at low p_{T}. Furthermore, the total uncertainty is in the order of 10 % for most p_{T} intervals.

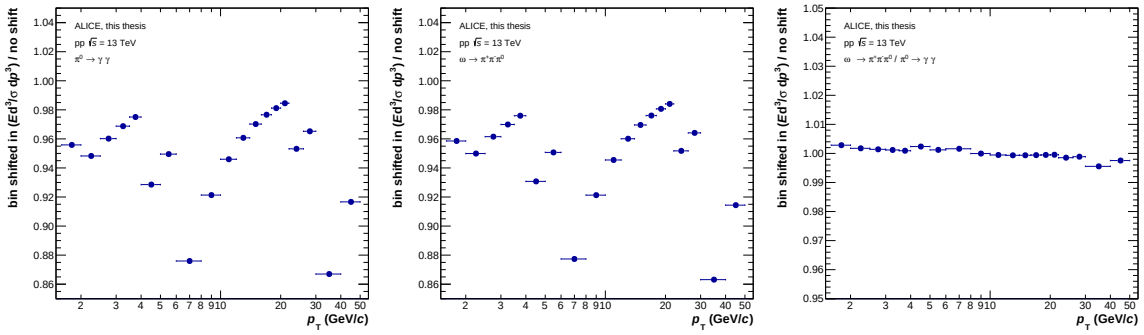

Figure 10.19: Bin shift correction for the ω / π^0 ratio in $E\,\mathrm{d}^3\sigma/\mathrm{d}p^3$ (y-shift). The unshifted ω and π^0 spectra are shifted by their corresponding Tsallis or TCM function in $E\,\mathrm{d}^3\sigma/\mathrm{d}p^3$, before the ratio is build. From left to right, the bin shift corrections are shown for π^0, ω and ω / π^0.

In Chap. 9, the effect of steeply falling spectra on p_T intervals with finite width was discussed. Analogously to the π^0 and η meson, the invariant cross sections of the ω meson are corrected by shifting their values horizontally in p_T (x-shift). The combined ω meson spectrum is parametrized with a Tsallis function, defined by Eq. 3.48. The resulting bin shift corrections are shown in (bottom, right). For the calculation of the ω / π^0 ratio, the unshifted ω and π^0 spectra are shifted in $E\,\mathrm{d}^3\sigma/\mathrm{d}p^3$ (y-shift), as both mesons can have a different shift in p_T. Here, a Tsallis function has been used for the ω spectrum, while a TCM function has been used for the π^0 spectrum. The corresponding bin shift corrections for the ω, the π^0 and the ω / π^0 ratio are shown in Fig. 10.19. The separate corrections for the ω and π^0 ratio nearly completely cancel each other out, resulting in a bin shift correction for the ω / π^0 of less than 1 %. The combined ω spectrum and the ω/π^0 ratio shown in the next section have the corresponding bin shift correction applied.

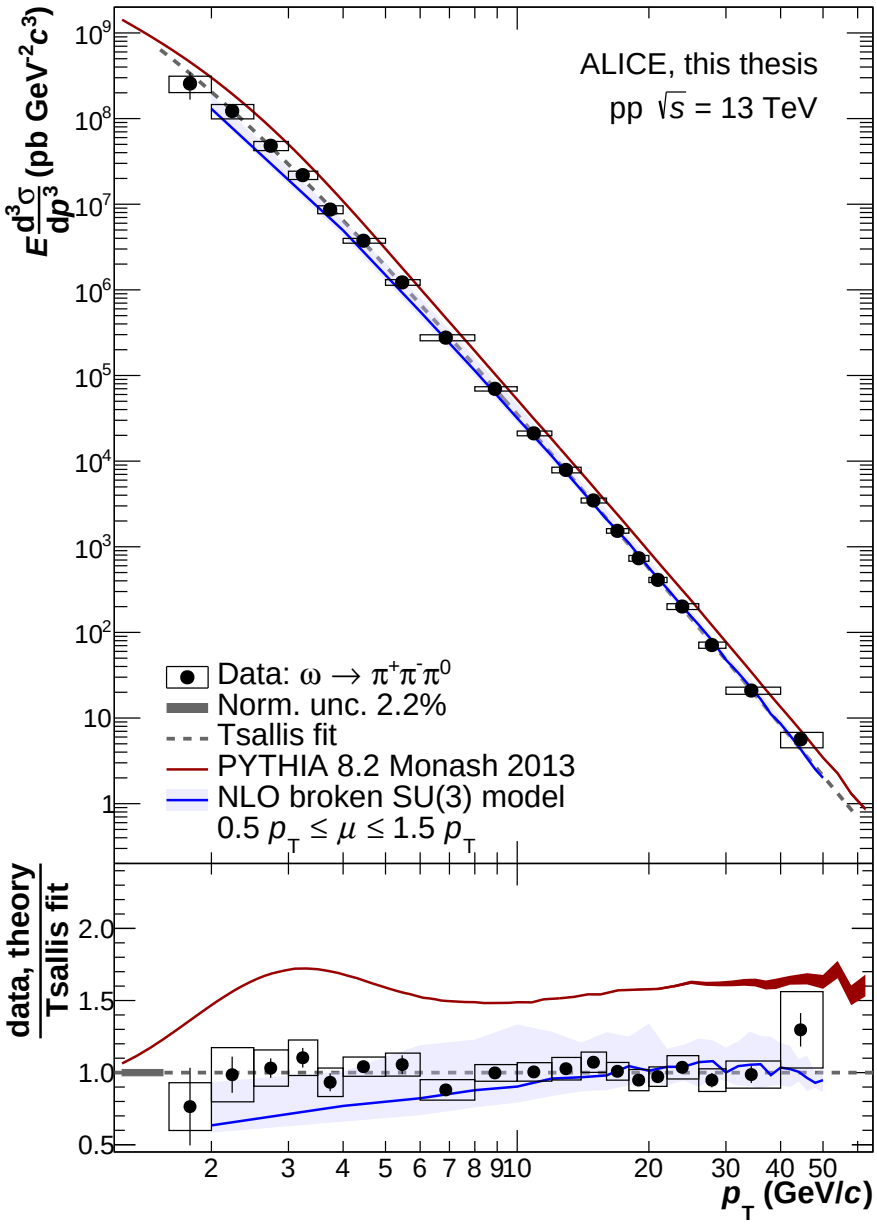

Figure 10.20: Invariant cross section of the ω meson production in $\sqrt{s} = 13$ TeV parametrized with a Tsallis function (top). The invariant cross section is compared to the PYTHIA 8.2 simulation as well as the NLO calculation provided by [103]. The ratio of the described distribution to the Tsallis function is shown in the bottom.

10.6 Results

As described in Sec. 10.5, the individual reconstruction methods of PCM, PHOS, PCM-PHOS, EMCal and PCM-EMCal are combined, using the BLUE method to acquire the invariant cross section of the ω meson production shown in Fig. 10.20 and a bin shift correction in p_{T} direction is applied. Similar to the combined invariant cross section of π^0 and η mesons in Fig. 9.7, the invariant cross section of the ω meson is compared to PYTHIA 8.2, using the Monash

2013 tune. In addition to that, the spectrum is compared to a NLO calculation, provided by [103]. This NLO calculation uses a broken SU(3) model approach for the ω fragmentation. Here, the scale $\mu = p_{\mathrm{T}}$ is used for factorization, fragmentation and renormalisation, while the blue error band denotes the theoretical scale uncertainty, given by the variation of $\mu = 0.5p_{\mathrm{T}}$ and $\mu = 1.5p_{\mathrm{T}}$. The gray bar is the normalization uncertainty. Its value is 2.2 % and is based on the uncertainty of the cross section of the used dataset, determined in [72]. The combined ω spectrum covers a p_{T} range of $1.6\,\mathrm{GeV}/c < p_{\mathrm{T}} < 50\,\mathrm{GeV}/c$. Compared to the previous ω measurement in $\sqrt{s} = 7$ TeV [97], the momentum range is increased by over $30\,\mathrm{GeV}/c$, while the uncertainties have been significantly reduced. The spectrum is parametrized with a Tsallis function, defined by Eq. 3.48 and the resulting parameters and χ^2/ndf are given in Tab. 10.5. The invariant cross section of the ω meson is divided by the Tsallis function and the resulting ratios are shown in the bottom panel. The combined data is well described by the parametrization within uncertainties over the whole p_{T} range. The increased precision of the combined ω spectrum in comparison to the individual cross sections can also be seen in the significantly reduced fluctuations. Similar to the π^0 distribution shown in Fig. 9.7, the PYTHIA 8.2 simulation is overestimating the invariant cross section of the ω meson in data up to 50 %. A similar overestimation was already observed for $\pi^{\pm}$ at high p_{T} in [89], indicating that the Monash 2013 tune may be insufficient to describe the light meson production at the unprecedented transverse momenta and collision energies, that have recently become accessible at the LHC. In contrast to the PYTHIA 8.2 simulation, the NLO distribution is in good agreement with the measured cross section within uncertainties.

Fig. 10.21 is showing the ω/π^0 ratio in $\sqrt{s} = 13$ TeV in comparison to previous measurements in different center of mass energies from 62 GeV to 7 TeV [104][105][106][107][97]. Similar to the invariant cross section of the ω meson, the overall p_{T} coverage of this measurement of $1.6\,\mathrm{GeV}/c < p_{\mathrm{T}} < 50\,\mathrm{GeV}/c$ is increasing the previous momentum range by over $30\,\mathrm{GeV}/c$. The calculated ω/π^0 ratio is in agreement with the previous measurements within the statistical and systematic uncertainties. However, the ω/π^0 ratio is showing a tendency for lower values in comparison, giving a slight hint of lower values for higher collision energies or precision. Furthermore, a slight decrease of the ω/π^0 ratio for high p_{T} can be seen.

$C(\times 10^{10}\mathrm{pb})$	n	$T(\mathrm{GeV})$	χ^2/NDF	NDF
$3.51^{\pm 0.63\ (\mathrm{stat})}_{\pm 1.04\ (\mathrm{tot})}$	$6.17^{\pm 0.05\ (\mathrm{stat})}_{\pm 0.10\ (\mathrm{tot})}$	$0.194^{\pm 0.010\ (\mathrm{stat})}_{\pm 0.020\ (\mathrm{tot})}$	$\frac{1.92\ (\mathrm{stat})}{0.46\ (\mathrm{tot})}$	16

Table 10.5: Parameters and χ^2/ndf of the Tsallis function on the combined ω spectrum in Fig. 10.20 (left), defined by Eq. 3.48. The given statistical uncertainties are acquired by excluding the systematic uncertainties of the data points in the parametrization procedure.

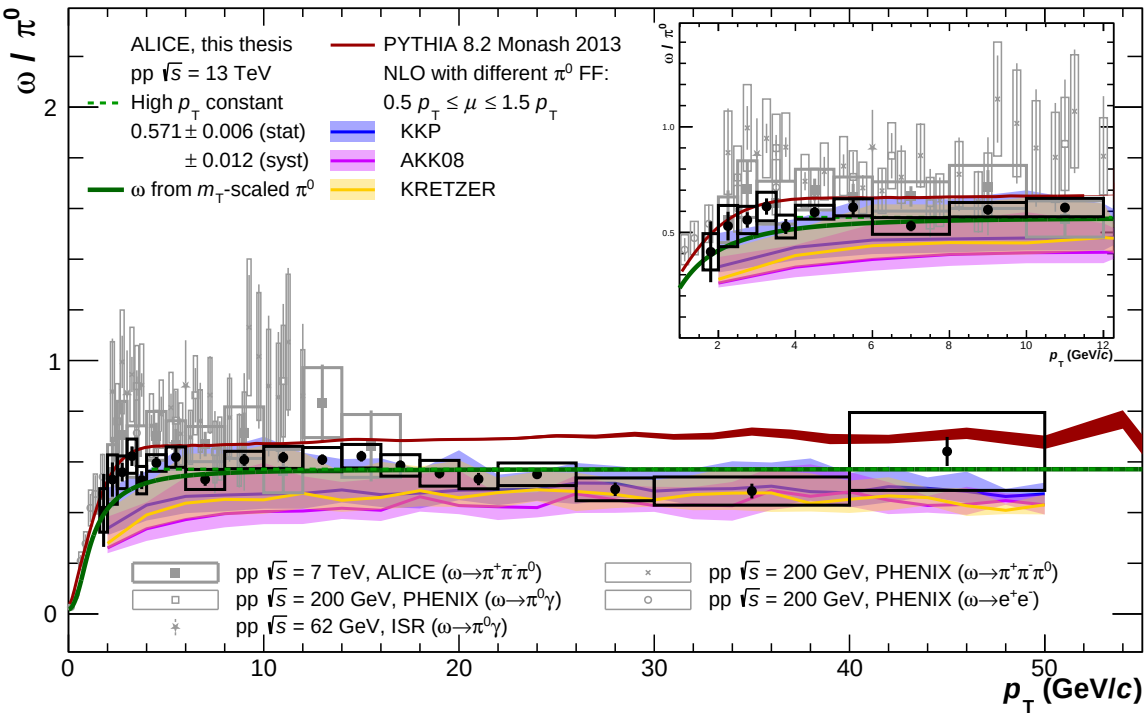

Figure 10.21: ω/π^0 ratio in dependence of p_{T} for $\sqrt{s} = 13$ TeV in comparison to various measurements with a center of mass energy range of $\sqrt{s} = 62$ GeV- 7 TeV [104][105][106][107][97].

However, the ratio at high p_{T} is found to be consistent with a constant within the uncertainties. By parametrizing the ratio above $4\,\mathrm{GeV}/c$ with a constant, a constant value of $C^{\omega/\pi^0} = 0.571 \pm 0.006$ (stat.) ± 0.012 (syst.) has been determined. This is the most precise value of C^{ω/π^0} up to this date. The PYTHIA 8.2 simulation is in good agreement with the ω/π^0 ratio for low p_{T}, while it is overestimating the ratio for $p_{\mathrm{T}} > 15\,\mathrm{GeV}/c$. In comparison to the individual cross sections, where an overestimation of 50 % was observed, the ω/π^0 ratio is described significantly better by this simulation. In addition to the PYTHIA 8.2 simulation, the ω/π^0 ratio is compared to different NLO calculations. These NLO calculations are using the same model, as the NLO calculation for the invariant ω cross sections, while the different NLO calculations are using different FFs for the calculation of the π^0 cross section: KKP[108], AKK08[109] and KRETZER[110]. The different bands are representing the variations of the factorization scale μ from $\mu = p_{\mathrm{T}}$ to $0.5p_{\mathrm{T}} < \mu < 1.5p_{\mathrm{T}}$. While all NLO calculations are describing the ω/π^0 ratio well within uncertainties, KKP shows the best agreement. At last, the ω/π^0 ratio is compared to the m_{T} scaled distribution, shown as a solid green line. As explained in Sec. 9, the m_{T} scaled distribution is obtained with the help of Eq. 9.8 using C^{ω/π^0}. The m_{T} scaled distribution is able to describe the ω/π^0 ratio over nearly the whole p_{T} range, while slightly underestimating the data for low p_{T}, giving the

possibility of reasonable estimations of the ω production cross section with help of the m_{T} scaled distribution.

11 Summary

This thesis presents the measurement of the cross section of π^0, η and ω meson production in pp collisions at $\sqrt{s} = 13$ TeV with the ALICE experiment, recorded from 2016 to 2018 during Run 2 of LHC operation. The cross sections of π^0 and η meson production are measured using their decay into two photons. Photons can be measured via two fundamentally different methods in ALICE: With the help of the calorimeters or with help of the Photon Conversion Method (PCM). While photons are directly measured with help of the calorimeters EMCal (including DCal) or PHOS, with help of PCM, tracks of e^+ and e^- particles originating from photon conversions in the inner detector material are measured using the ITS and TPC. Two different reconstruction methods are used for the dedicated π^0 and η meson cross section measurement during this work: PHOS and PCM-PHOS. For the PHOS method, both decay photons are directly measured with help of the PHOS detector, while for the PCM-PHOS method one decay photon is measured with help of the PHOS calorimeter and the second decay photon is measured with help of PCM. The final implementation of the PHOS trigger was performed in close collaboration with Adrian Florin Mechler[1], while the basic requirements for this implementation were provided in the course of this work. In addition to that, the estimation of the systematic uncertainties were also performed in collaboration with Adrian Florin Mechler after the trigger was implemented. Using the MB dataset, the π^0 meson is measured in a momentum range of $0.7\,\mathrm{GeV}/c < p_\mathrm{T} < 10\,\mathrm{GeV}/c$ with PHOS and $0.5\,\mathrm{GeV}/c < p_\mathrm{T} < 10\,\mathrm{GeV}/c$ with PCM-PHOS, while the η meson is measured in a momentum range of $2.5\,\mathrm{GeV}/c < p_\mathrm{T} < 10\,\mathrm{GeV}/c$ with PHOS and $1\,\mathrm{GeV}/c < p_\mathrm{T} < 10\,\mathrm{GeV}/c$ with PCM-PHOS. The implementation of the PHOS trigger increases this range to up to $p_\mathrm{T} = 35\,\mathrm{GeV}/c$ for the π^0 meson and $p_\mathrm{T} = 30\,\mathrm{GeV}/c$ for the η meson.

Within the ALICE collaboration, the π^0 and η meson cross section were measured with additional reconstruction methods and all available measurements were combined, including the PHOS and PCM-PHOS measurement provided in this work, to one spectrum. The combination has been performed in close collaboration with the "Soft Photons and Neutral Mesons Physics Analysis Group" within the ALICE collaboration. The spectra of the different reconstruction methods align within uncertainties and are parametrized with a TCM function,

[1] Institut für Kernphysik, Universität Frankfurt, Frankfurt, Germany

which is able to describe the data over the whole p_{T} range. The combined invariant cross sections cover a momentum range of $0.2\,\mathrm{GeV}/c < p_{\mathrm{T}} < 200\,\mathrm{GeV}/c$ for the π^0 meson and $0.4\,\mathrm{GeV}/c < p_{\mathrm{T}} < 50\,\mathrm{GeV}/c$ for the η meson. The cross sections are compared to the corresponding PYTHIA 8.2 simulations as well as NLO calculations using the PDFs CT18 [85] and CT14 [86] with the two FFs NNFF1.0 [87] and DSS14 [88] for the π^0 meson and a NLO calculation using the CT18 PDF with the AESSS FF for the η meson. The PYTHIA 8.2 simulation, using the Monash 2013 tune, is overestimating the π^0 meson production for low p_{T} by up to 50 %, while also the shape of the data is not reproduced by the PYTHIA simulation. A similar behavior has already been observed for charged pions [89]. For the η meson, PYTHIA also significantly overestimates the measured data at low p_{T}, while its shape is also not well described. The predicted cross section is getting closer to the measured distribution until it is crossing with the measurement at $p_{\mathrm{T}} \approx 15\,\mathrm{GeV}/c$. The NLO calculations using the PDF CT14 with the FF DSS14 for the π^0 meson and the PDF CT18 with the FF AESSS for the η meson are overestimating the measured spectra. A similar overestimation could be observed in previous measurements at LHC energies [90] for NLO calculations, which use the FF DSS14 for the π^0 meson and the PDF CT18 with the FF AESSS for the η meson. The NLO calculation, using the PDF CT18 with the FF NNFF1.0 for the π^0 is describing the spectrum within uncertainties. The good agreement of the NLO calculation, using the PDF CT18 with the FF NNFF1.0 is also been observed in [90]. As in [90], only the FF changes from DSS14 to NNFF1.0, while the PDF remains unchanged, the improvement for the data description by the use of the more recent NNFF1.0 FF can be observed. This is interesting, as NNFF1.0 is using no LHC data and has not been created for neutral pions, while both is the case for DSS14. This might indicate benefits of using novel fitting approaches, which make use of neural networks to determine fragmentation functions, as done for NNFF1.0

The combined η/π^0 ratio, that includes the PHOS and PCM-PHOS measurement provided in this work, is compared to the PYTHIA calculation and predictions from m_{T} scaling, while it can be seen that the ratio in data for $p_{\mathrm{T}} < 4\,\mathrm{GeV}/c$ is significantly lower than the distribution, that is expected from m_{T} scaling. A similar behavior has already been measured by [93][94][95][96] and can be explained by a large amount of feed-down (π^0 mesons from decays of heavy particles) to the π^0 distribution at low p_{T}. Furthermore, the PYTHIA prediction is underestimating the measured ratio for high p_{T}. A comparison to previous measurements shows a good agreement within their uncertainties, while the available p_{T} range is extended to up to $50\,\mathrm{GeV}/c$.

The ω meson measurement is using the ω decay into three pions $\omega \to \pi^+\pi^-\pi^0$. The charged pions π^+ and π^- are measured directly with help of the tracking detectors ITS and TPC. In contrast to the dedicated π^0 production cross section measurement, π^0 mesons used for the ω

meson reconstruction are reconstructed themselves with help of the EMCal (including DCal) and PHOS calorimeters, as well as with help of PCM and a combination of these calorimeters with PCM. Hence, five different reconstruction methods are used for the ω reconstruction in total, while each reconstruction method has its own benefits. In comparison to the other reconstruction methods, PCM offers a good resolution and enables photon measurements down to $p_{\mathrm{T}} = 1.6\,\mathrm{GeV}/c$. However, the momentum range of the ω meson reconstruction is limited by the low photon conversion probability in the inner detector material. Calorimeters on the other hand can provide high p_{T} photon triggers, which can enhance the momentum coverage of the measurement significantly. In addition to that, different reconstruction methods provide important cross-checks between each other and all reconstruction methods agree with each other within the statistical and systematic uncertainties.

By combining the spectra obtained with different reconstruction methods to one combined spectrum, the benefits of the different methods are utilized. The resulting invariant cross section covers an unprecedented momentum range of $1.6\,\mathrm{GeV}/c < p_{\mathrm{T}} < 50\,\mathrm{GeV}/c$ with a total uncertainty of approximately 10 % for the majority of this momentum range. With 3.1 % being the lowest systematic uncertainty and 5.8 % for the lowest statistical uncertainty for certain p_{T} intervals, the uncertainties are reduced by a factor of two, compared to the previous ω cross section measurement performed at $\sqrt{s} = 7$ TeV [97] by ALICE. In addition to that, compared to the measurement at $\sqrt{s} = 7$ TeV, the ω meson cross section shown in this thesis extends the momentum range by more than $30\,\mathrm{GeV}/c$. The uncertainty is predominantly driven by the systematic uncertainty, whose largest contribution is coming from the signal extraction. The combined spectrum is parametrized with a Tsallis function [19], which is in agreement with the measured data within statistical and systematic uncertainties. The cross section is compared to a PYTHIA 8.2 simulation, which is overestimating the measurement of the cross section of the ω meson by up to 50 %. As already mentioned, the π^0 meson cross section measurement in $\sqrt{s} = 13$ TeV, performed in this work, and the measurement of the charged pion production cross section [89] show a similar disagreement with PYTHIA. This gives the indication, that the Monash 2013 tune may be insufficient to describe the light meson production at the unprecedented transverse momenta and collision energies, that have recently become accessible at the LHC. However, the NLO calculation provided by [103] uses a broken SU(3) model approach for the ω fragmentation and shows a good agreement with the data.

The ω/π^0 ratio is calculated using the combined ω and π^0 cross sections. Analogously to the measurement of the ω meson cross section, the ω/π^0 ratio covers a momentum range of $1.6\,\mathrm{GeV}/c < p_{\mathrm{T}} < 50\,\mathrm{GeV}/c$. A comparison to previous measurements shows an agreement with the previous measurements within the statistical and systematic uncertainties, while

the momentum range is extended by over 30 GeV/c. However, the ω/π^0 ratio is showing a tendency for lower values in comparison, while a slight hint of lower values for higher collision energies or precision is observed. The PYTHIA 8.2 simulation is in good agreement with the ω/π^0 ratio for low p_{T}, while it is overestimating the ratio for $p_{\mathrm{T}} > 15\,\mathrm{GeV}/c$. PYTHIA is in significantly better agreement for the ω/π^0 ratio, compared to the separate meson measurements. Furthermore, the ω/π^0 measurement is compared to different NLO calculations with the measured spectrum using the same model, as the NLO calculation for the invariant ω cross sections but different π^0 fragmentation functions. All compared NLO calculations are showing a good agreement with the measured Spectrum, while the π^0 FF KKP, describes the measured cross section best. A slight decrease of the ω/π^0 ratio for high p_{T}, which is found to be consistent with a constant within the uncertainties is observed. The high p_{T} constant fit provides a value of $C^{\omega/\pi^0} = 0.571 \pm 0.006$ (stat.) ± 0.012 (syst.), which is the most precise value of C^{ω/π^0} up to this date. The m_{T} scaled distribution describes the ω/π^0 ratio over nearly the whole p_{T} range, while slightly underestimating the data for low p_{T}. Hence, reasonable estimations of the ω production cross section can be given over the whole p_{T} range. This observation is in line with the previous ω cross section measurement performed at $\sqrt{s} = 7$ TeV, where the m_{T} scaled distribution was able to describe the ω/π^0 ratio over whole p_{T} range up to 17 GeV/c.

12 Zusammenfassung

In dieser Arbeit wird die Messung des Wirkungsquerschnitts der π^0-, η- und ω-Meson Produktion in pp-Kollisionen bei $\sqrt{s} = 13$ TeV mit dem ALICE-Experiment vorgestellt, dessen Daten zwischen 2016 und 2018 während Run 2 des LHC-Betriebs aufgenommen wurden. Die Wirkungsquerschnitte der π^0- und η-Meson Produktionen werden durch ihren Zerfall in zwei Photonen gemessen. Photonen können mit zwei grundlegenden Methoden in ALICE gemessen werden: Mit Hilfe der Kalorimeter oder mit Hilfe der Photon Conversion Method (PCM). Während Photonen direkt mit Hilfe der Kalorimeter EMCal (einschließlich DCal) oder PHOS gemessen werden, werden mit Hilfe von PCM die Spuren von e^+- und e^--Teilchen, die durch Photonenumwandlungen im inneren Detektormaterial entstehen, gemessen indem dazu ITS und TPC verwendet werden . Für die spezifische Messung des Wirkungsquerschnitts der π^0- und η- Meson Produktion wurden zwei verschiedene Rekonstruktionsmethoden verwendet: PHOS und PCM-PHOS. Bei der PHOS-Methode werden beide Zerfallsphotonen direkt mit Hilfe des PHOS-Detektors gemessen, während bei der PCM-PHOS-Methode ein Zerfallsphoton mit Hilfe des PHOS-Kalorimeters und das zweite Zerfallsphoton mit Hilfe von PCM gemessen wird. Die endgültige Implementierung des PHOS-Triggers wurde in Zusammenarbeit mit Adrian Florin Mechler[1]durchgeführt, während die grundlegenden Anforderungen für diese Implementierung durch diese Arbeit bereitgestellt wurden. Darüber hinaus wurde die Abschätzung der systematischen Unsicherheiten nach der Implementierung des Triggers ebenfalls in Zusammenarbeit mit Adrian Florin Mechler durchgeführt. Mit dem MB-Datensatz wurde das π^0-Meson in einem Impulsbereich von $0{,}5\,\mathrm{GeV}/c < p_\mathrm{T} < 10\,\mathrm{GeV}/c$ gemessen, während das η-Meson in einem Impulsbereich von $1\,\mathrm{GeV}/c < p_\mathrm{T} < 10\,\mathrm{GeV}/c$ gemessen wurde. Die Implementierung des PHOS-Triggers erweitert diesen Bereich auf bis zu $35\,\mathrm{GeV}/c$ für das π^0-Meson und $30\,\mathrm{GeV}/c$ für das η-Meson.

Innerhalb der ALICE-Kollaboration wurde der π^0- und η-Meson Wirkungsquerschnitt mit zusätzlichen Rekonstruktionsmethoden gemessen und alle verfügbaren Messungen, einschließlich der PHOS- und PCM-PHOS-Messung aus dieser Arbeit, zu einem Spektrum zusammengefasst. Die Kombination wurde in enger Zusammenarbeit mit der „Soft Photons and Neutral Mesons Physics Analysis Group“ innerhalb der ALICE Kollaboration durchgeführt.

[1]Institut für Kernphysik, Universität Frankfurt, Frankfurt, Germany

Die Spektren der verschiedenen Rekonstruktionsmethoden stimmen innerhalb der Unsicherheiten überein und werden mit einer TCM-Funktion parametrisiert, welche die Daten über den gesamten p_{T}-Bereich beschreiben kann. Die kombinierten invarianten Wirkungsquerschnitte decken einen Impulsbereich von $0{,}2\,\mathrm{GeV}/c < p_{\mathrm{T}} < 200\,\mathrm{GeV}/c$ für das π^0-Meson und $0{,}4\,\mathrm{GeV}/c < p_{\mathrm{T}} < 50\,\mathrm{GeV}/c$ für das η-Meson ab. Die Wirkungsquerschnitte werden mit den entsprechenden PYTHIA 8.2-Simulationen, die den Monash 2013 Tune verwenden, sowie mit NLO-Rechnungen, die die PDFs CT18 [85] und CT14 [86] mit den beiden FFs NNFF1 [87] und DSS14 [88] für das π^0-Meson nutzen und mit der NLO-Rechnung, die die PDF CT18 mit der FF AESSS für das η-Meson nutzt verglichen. Die PYTHIA 8.2-Simulation, überschätzt die π^0-Meson Produktion für niedriges p_{T} um bis zu 50 %, während auch die Form der Daten durch die PYTHIA-Simulation nicht reproduziert wird. Ein ähnliche Abweichung konnte bereits bei geladenen Pionen beobachtet werden [89]. Für das η-Meson überschätzt PYTHIA die gemessenen Werte ebenfalls bei niedrigem p_{T} erheblich, während auch die Form nicht gut beschrieben wird. Die Simulation nähert sich der gemessenen Verteilung an, bis sie sich bei $p_{\mathrm{T}} \approx 15\,\mathrm{GeV}/c$ mit der Messung kreuzt. Die NLO-Berechnungen, die die PDF CT14 mit der FF DSS14 für das π^0-Meson und die PDF CT18 mit der FF AESSS für das η-Meson nutzen, überschätzen die gemessenen Spektren. In bisherigen Messungen bei LHC Energien [90] konnte bereits eine ähnliche Überschätzung von NLO-Rechnungen beobachtet, welche die FF DSS14 für das π^0-Meson und die PDF CT18 mit der FF AESSS für das η-Meson nutzen. Die NLO-Berechnung, die die PDF CT18 mit der FF NNFF1.0 für das π^0-Meson nutzt, beschreibt das Spektrum innerhalb der Unsicherheiten. Die gute Übereinstimming der NLO-Rechnung, die die PDF CT18 mit der FF NNFF1.0 nutzt, konnte ebenfalls bereits in [90] beobachtet werden. Da sich in [90] lediglich die FF von DSS14 zu NNFF1.0 verändert, während die PDF unverändert bleibt, kann hier die Verbesserung der Datenbeschreibung durch die Verwendung der neueren NNFF1.0 FF beobachtet werden. Dies ist interessant, da NNFF1.0 keine LHC-Daten verwendet und nicht für neutrale Pionen erstellt wurde, während beides bei DSS14 der Fall ist. Dies könnte auf die Vorteile neuartiger Fitting-Ansätze hindeuten, bei denen neuronale Netze zur Bestimmung von Fragmentierungsfunktionen verwendet werden, wie dies bei NNFF1.0 der Fall ist.

Das kombinierte η/π^0-Verhältnis, das auch die in dieser Arbeit durchgeführten Messungen von PHOS und PCM-PHOS umfasst, wird mit der PYTHIA-Berechnung und der m_{T}-Skalierung verglichen, wobei zu erkennen ist, dass das Verhältnis in den Daten für $p_{\mathrm{T}} < 4\,\mathrm{GeV}/c$ signifikant niedriger ist als die Verteilung, die von der m_{T}-Skalierung erwartet wird. Eine ähnliche Beobachtung konnte bereits in den bisherigen Messungen [93][94][95][96] gemacht werden, was durch einen hohen Anteil an feed-down (π^0-Mesonen aus Zerfällen schwerer Teilchen) zu niedrigen p_{T} der π^0-Verteilung zu erklären ist. Außerdem unterschreitet PYTHIA das

gemessene Verhältnis bei hohem p_{T}. Ein Vergleich mit früheren Messungen zeigt eine gute Übereinstimmung innerhalb ihrer Unsicherheiten, während der verfügbare p_{T}-Bereich auf bis zu $50\,\mathrm{GeV}/c$ erweitert wird.

Die Messung des ω-Mesons erfolgt über seinen Zerfall in drei Pionen $\omega \rightarrow \pi^+\pi^-\pi^0$. Die geladenen Pionen π^+ und π^- werden direkt mit Hilfe der Spurdetektoren ITS und TPC gemessen. Im Gegensatz zur dedizierten π^0-Messung werden π^0-Mesonen, die für die ω-Rekonstruktion verwendet werden, mit den Kalorimetern EMCal (einschließlich DCal) und PHOS sowie mit PCM und einer Kombination von diesen Kalorimetern und PCM rekonstruiert. Insgesamt wurden fünf verschiedene Rekonstruktionsmethoden für die ω-Rekonstruktion verwendet, wobei jede Rekonstruktionsmethode ihre eigenen Vorteile hat. Im Vergleich zu den anderen Rekonstruktionsmethoden bietet PCM eine gute Auflösung und ermöglicht Photonenmessungen bis zu niedrigen Impulsen von $p_{\mathrm{T}} = 1{,}6\,\mathrm{GeV}/c$. Allerdings ist der Impulsbereich der ω-Rekonstruktion durch die geringe Wahrscheinlichkeit von Photonenumwandlungen im inneren Detektormaterial begrenzt. Kalorimeter hingegen können Trigger bereitstellen, die den Impulsbereich der Messung erheblich zu hohen p_{T} erweitern können. Darüber hinaus dienen die verschiedenen Rekonstruktionsmethoden als wichtige Kontrollmessungen untereinander und alle Rekonstruktionsmethoden stimmen innerhalb der statistischen und systematischen Unsicherheiten miteinander überein.

Durch die Kombination der verschiedenen Rekonstruktionsmethoden zu einem kombinierten Spektrum werden die Vorteile der verschiedenen Methoden ausgenutzt.
Der resultierende invariante Wirkungsquerschnitt deckt einen beispiellosen Impulsbereich von $1{,}6\,\mathrm{GeV}/c < p_{\mathrm{T}} < 50\,\mathrm{GeV}/c$ mit einer Gesamtunsicherheit von etwa 10 % für den Großteil dieses Impulsbereichs ab. Mit 3,1 % als niedrigste systematische Unsicherheit und 5,8 % als niedrigste statistische Unsicherheit in gewissen p_{T}-Intervallen, sind die Unsicherheiten im Vergleich zu der veröffentlichten ω-Messung in $\sqrt{s} = 7$ TeV [97] von ALICE um einen Faktor zwei reduziert. Desweiteren wird im Vergleich von der ω-Messung in $\sqrt{s} = 7$ TeV zu der Messung des ω Wirkungsquerschnitts in dieser Arbeit der Impulsbereich um über $30\,\mathrm{GeV}/c$ erweitert. Die Unsicherheit wird hauptsächlich durch die systematische Unsicherheit bestimmt, deren größter Beitrag durch die Signalextraktion gegeben ist. Das kombinierte Spektrum wird mit einer Tsallis-Funktion [19] parametrisiert, die innerhalb der statistischen und systematischen Unsicherheiten mit der Messung übereinstimmt. Der Wirkungsquerschnitt wird mit einer PYTHIA 8.2-Simulation verglichen, die die Messung des ω-Mesons um bis zu 50 % überschätzt. Wie bereits beschrieben zeigen die Messung des Wirkungsquerschnitts von π^0-Mesonen in $\sqrt{s} = 13$ TeV, welcher in dieser Arbeit gemessen wurde, und die Messung von geladenen Pionen [89] einen ähnlichen Widerspruch zu PYTHIA. Dies gibt einen Hinweis darauf, dass der Monash 2013 Tune unzureichend ist um die leichte Mesonen Produktion in

den beispiellosen Transversalimpuls und Kollisionsenergie Bereichen zu beschreiben, die seit kurzem am LHC erreichbar sind. Die NLO-Berechnung, die von [103] bereitgestellt wird, verwendet einen gebrochenen SU(3)-Modellansatz für die ω-Fragmentierung und zeigt eine gute Übereinstimmung mit den Daten.

Das ω/π^0-Verhältnis wurde auf den kombinierten ω- und π^0- Wirkungsquerschnitten berechnet. Analog zur Messung des ω-Meson Wirkungsquerschnitts deckt das ω/π^0-Verhältnis einen Impulsbereich von $1{,}6\,\mathrm{GeV}/c < p_\mathrm{T} < 50\,\mathrm{GeV}/c$ ab. Ein Vergleich mit früheren Messungen zeigt eine Übereinstimmung innerhalb der statistischen und systematischen Unsicherheiten, während der Impulsbereich um über $30\,\mathrm{GeV}/c$ zu hohen p_T erweitert wird. Das ω/π^0-Verhältnis zeigt im Vergleich jedoch eine Tendenz zu niedrigeren Werten, während ein leichter Hinweis auf geringere Werte für höhere Kollisionsenergien oder bessere Messgenauigkeiten zu erkennen ist. Die PYTHIA 8.2-Simulation stimmt gut mit dem ω/π^0-Verhältnis für niedrige p_T überein, während sie das Verhältnis für $p_\mathrm{T} > 15\,\mathrm{GeV}/c$ überschätzt. PYTHIA stimmt dabei mit dem ω/π^0-Verhältnis signifikant besser überein als mit den einzelnen Mesonen Messungen. Desweiteren wird das ω/π^0-Verhältnis mit verschiedenen NLO-Rechnungen verglichen, die das gleiche Modell wie die NLO-Rechnung für den invarianten ω Wirkungsquerschnitt, nutzen aber unterschiedliche π^0-Fragmentationsfunktionen. Alle verglichenen NLO-Rechnungen zeigen eine gute Übereinstimmung mit dem gemessenen Spektrum, während die FF KKP die Messung am besten beschreibt. Eine geringe Abnahme des ω/π^0-Verhältnisses, welche mit einer Konstante innerhalb der Unsicherheiten übereinstimmt, kann für hohe p_T beobachtet werden. Die Parametrisierung der Konstante für hohe p_T ergibt einen Wert von $C^{\omega/\pi^0} = 0{,}571 \pm 0{,}006\ (\mathrm{stat.})\ \pm 0{,}012\ (\mathrm{syst.})$, was der bisher genaueste Wert für C^{ω/π^0} ist. Die m_T-skalierte Verteilung beschreibt das ω/π^0-Verhältnis über fast den gesamten p_T-Bereich, unterschätzt aber die Daten für niedrige p_T-Werte leicht. Daher können sinnvolle Schätzungen des Wirkungsquerschnitts der ω-Produktion über den gesamten p_T-Bereich gegeben werden. Diese Beobachtung steht im Einklang mit der früheren ω-Wirkungsquerschnitt Messung, die bei $\sqrt{s} = 7$ TeV durchgeführt wurde, wo die m_T-skalierte Verteilung das ω/π^0-Verhältnis über den gesamten p_T-Bereich bis zu $17\,\mathrm{GeV}/c$ beschreiben konnte.

13 Lebenslauf

Name:	Jens Robert Lühder
Geburtsdatum:	30.04.1988
Staatsangehörigkeit:	Deutsch
Eltern:	Martin Robert Lühder und Andrea Lühder (geb. Ehrenfeld)

Schulausbildung

06/2007	Allgemeine Hochschulreife
08/2005 – 06/2007	Wilhelm-Hittorf-Gymnasium, Münster
08/1998 – 06/2005	Joseph-Haydn-Gymnasium, Senden
08/1994 – 06/1998	Katholische Grundschule Marienschule, Senden

Zivildienst

04/2008 – 10/2008	Alexianer Werkstätten GmbH, Münster

Studium

Seit 11/2016	Promotionsstudium an der WWU Münster
10/2012 – 09/2016	M.Sc. Physik, WWU Münster, Titel der Abschlussarbeit: Optimization of the Resolution of a Small-Animal-PET-Camera
10/2007 – 09/2012	B.Sc. Physik, WWU Münster, Titel der Abschlussarbeit: Umrüstung eines automatischen Scanning-Mikroskops auf eine SPS-Steuerung

14 Danksagung

Ich möchte mich an dieser Stelle gerne bei allen bedanken, die mir im Laufe dieser Arbeit zur Seite standen. Zuallererst möchte ich Prof. Dr. Anton Andronic und Apl. Prof. Dr. Christian Klein-Bösing für ihre Unterstüzung zu dieser Arbeit danken. Neben der Unterstützung für diese Arbeit haben sie ein so familienfreundliches Arbeitsklima in der Arbeitsgruppe geschaffen, dass während meiner Zeit in dieser Arbeitsgruppe mein Sohn Tom geboren wurde. Desweiteren möchte ich insbesondere meiner Frau Kristina Lühder danken, die mich vom Beginn meines Physik Studiums an bis zum Ende dieser Arbeit begleitet hat. Für unseren regelmäßigen Austausch und unsere zahlreichen produktiven Diskussionen möchte ich außerdem Florian Jonas, Joshua König, Adrian Mechler, Ana Marin und Edgar Dominguez Rosas danken. Diese Arbeit hat weiterhin maßgeblich von der Unterstützung von Friederike Bock und Daniel Mühlheim profitiert, denen ich hierfür explizit meinen Dank aussprechen möchte. Zu guter Letzt möchte ich mich auch bei der Arbeitsgruppe und bei allen bedanken, die bei unseren regelmäßigen Kaffeerunden bei hitzigen Diskussionen die Stimmung auch in schweren Momenten immer wieder heben konnten.

15 Adjustments

This version has been adjusted, while all adjustments are listed below.

- Curriculum Vitae (CV) removed

A Appendix

A.1 Acronyms and Technical Terms

ADC	Analog-to-Digital Converter
ACORDE	ALICE COsmic Ray DEtector
ALICE	A Large Ion Collider Experiment
AOD	Analysis Object Data
ATLAS	A Toroidal LHC ApparatuS
APD	Avalanche PhotoDiode
BCM	Bad Channel Map
BGratio	Approach to describe the background in an invariant mass analysis by fitting ratio of all reconstructed meson candidates to event mixing background.
BLUE	Best Linear Unbiased Estimate
BR	Branching Ratio
CERN	European Organization for Nuclear Research
CMS	Compact Muon Solenoid experiment
CKM	Cabibbo-Kobayashi-Maskawa
CTP	Central Trigger Processor
DAQ	Data AcQuisition
DCA	Distance of Closest Approach
DCal	Di-jet Calorimeter
DDL	Direct links to the ALICE DAQ
DPG	ALICE Data Preparation Group
eID	electron IDentification

EMCal ElectroMagnetic Calorimeter. This acronym can also mean the method to reconstruct neutral pions is using two photons from the electromagnetic calorimeter

EMC ElectroMagnetic Calorimeter (EMCAL) and Di-jet Calorimeter(DCal). This acronym can also mean the method to reconstruct neutral pions is using two photons from the electromagnetic calorimeter

mEMC Purity based analysis where merged ElectroMagnetic Calorimeter (EMCal) and Di-jet Calorimeter(DCal) clusters are used

PCM-EMCal Photon Conversion Method - ElectroMagnetic Calorimeter

PCM-PHOS Photon Conversion Method - PHOton Spectrometer

ESD Event Summary Data

EGA EMCal L1, following EMCal L0

EGA2 Like EGA, with a lower threshold

EG1 Acronym for EGA

EG2 Acronym for EGA2

FIFO First In First Out

FMD Forward Multiplicity Detector

FMD1 Sub-detector of FMD

FMD2 Sub-detector of FMD

FMD3 Sub-detector of FMD

FF Fragmentation Function

HIJING Heavy Ion Jet Interaction Generator

HLT High Level Trigger

HMPID High Momentum Particle Identification Detector

ITS Inner Tracking System

INT1 Acronym for V0OR

INT7 Acronym for V0AND

JJMC Jet-Jet Monte Carlo simulation

lowJJMC γ enhanced jet-jet MC simulation with minimum energy threshold of 3.5 GeV

highJJMC	γ enhanced jet-jet MC simulation with minimum energy threshold of 7 GeV
L0	Level-0
L1	Level-1
L2	Level-2
LCG	LHC Computing Grid
LEGO	Lightweight Environment for Grid Operations
LEP	Large Electron Positron Collider
LHC	Large Hadron Collider
LHCb	LHC beauty experiment
LHCf	Large Hadron Collider forward
CP	Charge Parity
LQ1D	1 dimensional likelihood (total integreated charge)
LQ2D	2 dimensional likelihood (charge + position)
LQ3D	3 dimensional likelihood (charge + position)
LQ7D	7 dimensional likelihood (charge + position)
LINAC2	LINear ACcelerator
LQCD	Lattice QCD
MB	Minimum Bias
MBand	Acronym for V0AND
MC	Monte Carlo simulation
MCH	Muon chambers
MoEDAL	Monopole and Exotics Detector at the LHC
MIP	Minimum Ionizing Particle
MRPC	Multigap Resistive Plate Chamber
MTR	Muon Trigger chambeR
MWPC	MultiWire Proportional Chamber
NLO	Next-to-Leading Order
nPDF	nuclear Parton Distribution Function
PDF	Parton Distribution Function

PHOS	PHOton Spectrometer. This acronym can also mean the method to reconstruct neutral pions is using two photons from the photon spectrometer
PHI7	PHOS level 0 trigger
PCA	Point of Closest Approach
PCM	Photon Conversion Method
PCM-EMCal	Hybrid of PCM and EMCal
PCM-PHOS	Hybrid of PCM and PHOS.
PDG	Particle Data Group
PDF	Parton Density Function
PHI7	PHOS trigger that requires energy deposit in PHOS and coincidence with INT7
PID	Particle IDentification
PMD	Photon Multiplicity Detector
pQCD	perturbative QCD
PS	Proton Synchrotron
BOOSTER	Proton synchrotron BOOSTER
PSB	Proton Synchrotron Booster
PYTHIA	Monte Carlo event generator for pp-collisions
QA	Quality Assurance
QCD	Quantum ChromoDynamics
QED	Quantum ElectroDynamics
QFT	Quantum Field Theory
QGP	Quark-Gluon Plasma
RMS	Root Mean Square
SDD	Silicon Drift Detector
SM	Standard Model
SPD	Silicon Pixel Detector
SPS	Super Proton Synchrotron
SSD	Silicon Strip Detector

TCM	Two-Component-Model
T0	Timing and trigger Detector
T0A	Sub-detector of T0
T0C	Sub-detector of T0
TOF	Time-Of-Flight detector
TOTEM	TOTal Elastic and diffractive cross section Measurement
TPC	Time Projection Chamber
TR	Transition Radiation
TRD	Transition Radiation Detector
TRF	Trigger Rejection Factor
TRU	Trigger Region Unit
vdM	van der Meer
V^0	Secondary vertex
V0	Triggering and centrality Detector
V0A	Sub-detector of V0
V0C	Sub-detector of V0
V0AND	Minimum bias trigger which requires coincidence of V0A and V0C signals
V0OR	Minimum bias trigger which requires a signal in V0A or V0C
ZDC	Zero Degree Calorimeter
ZEM	Zero degree ElectroMagnetic calorimeter
ZN	Zero degree Neutron calorimeter
ZP	Zero degree Proton calorimeter
SigBG	Distribution of meson signal on top of background distribution
BG	Background

A.2 Charged Pion Selection

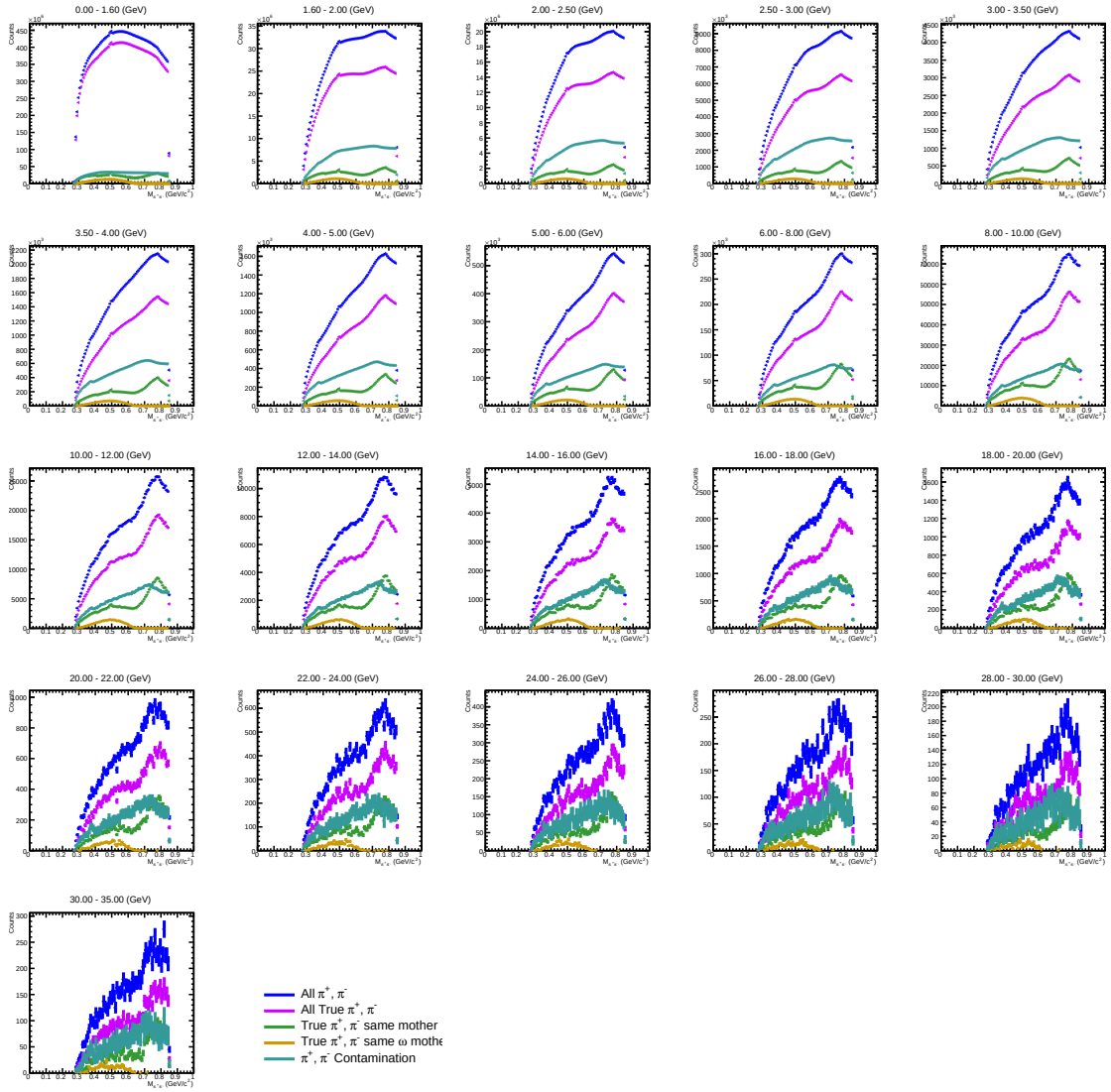

Figure A.1: Different contributions to invariant mass of charged pions for different p_{T}, simulated in MC.

A.3 π^0 and η Reconstruction

A.3.1 Signal Extraction of π^0 Mesons for PHOS

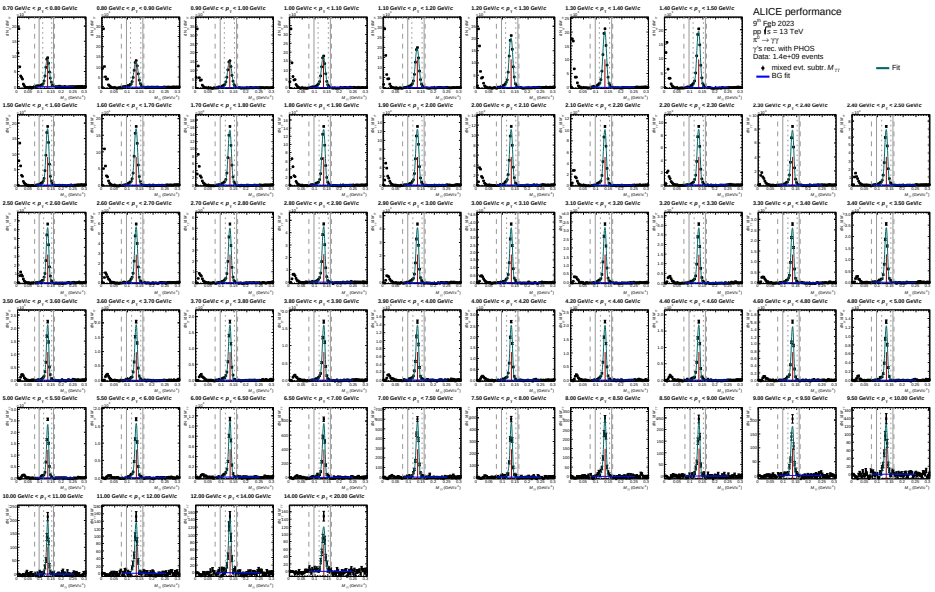

Figure A.2: Parametrization of signal distribution of π^0 meson in data for MB trigger, reconstructed with PHOS.

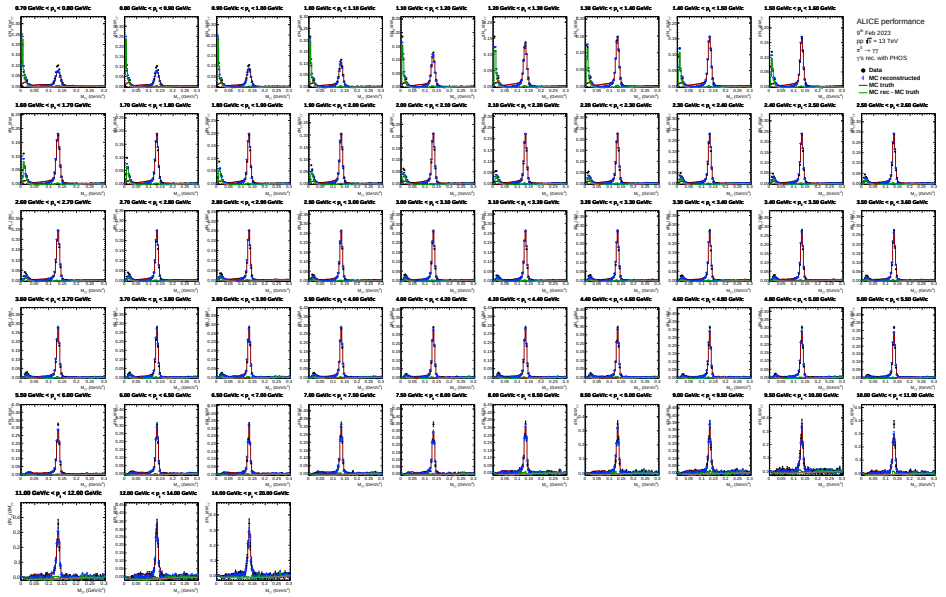

Figure A.3: Comparison of signal shapes in MC of π^0 meson with data for MB trigger, reconstructed with PHOS.

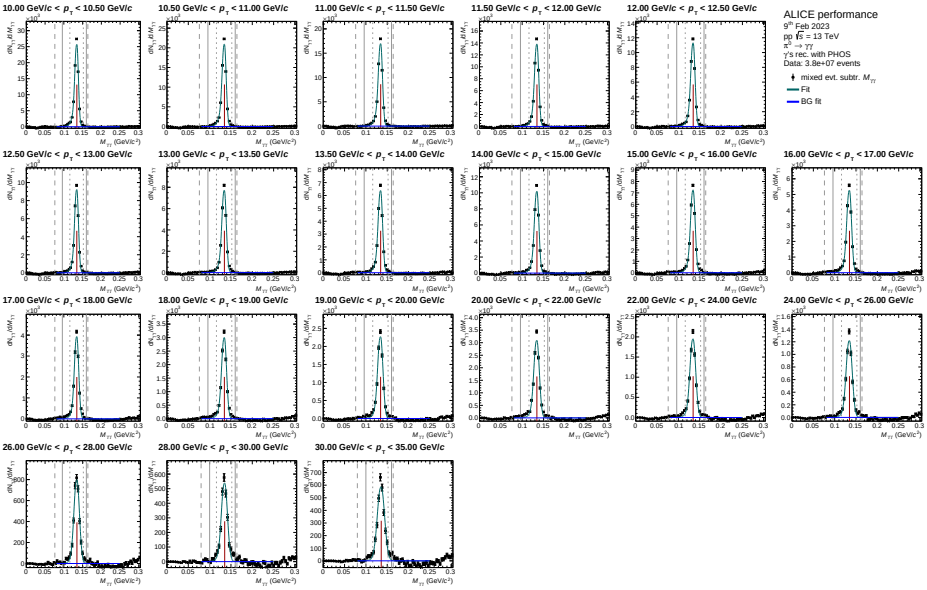

Figure A.4: Parametrization of signal distribution of π^0 meson in data for PHI7 trigger, reconstructed with PHOS.

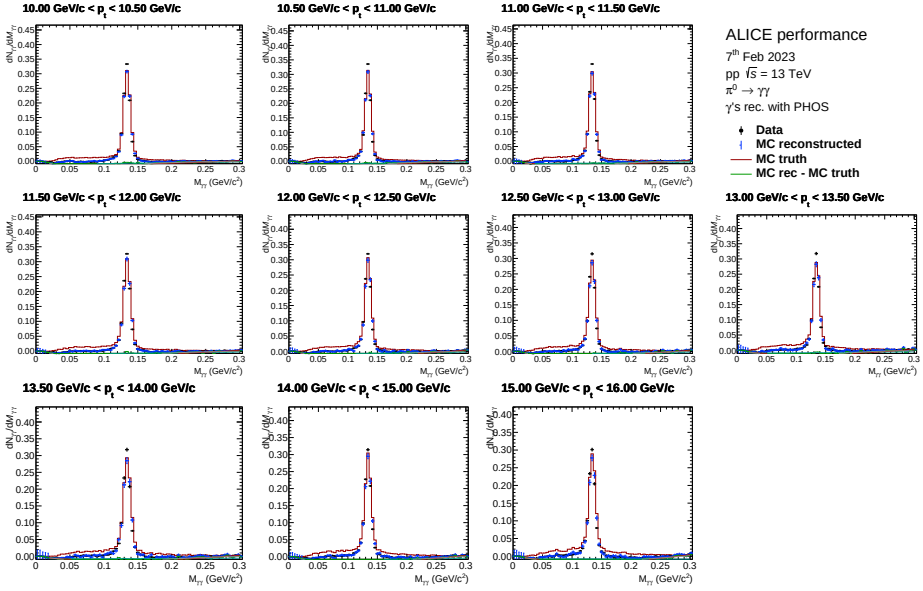

Figure A.5: Comparison of signal shapes in lowJJMC of π^0 meson with data for PHI7 trigger, reconstructed with PHOS.

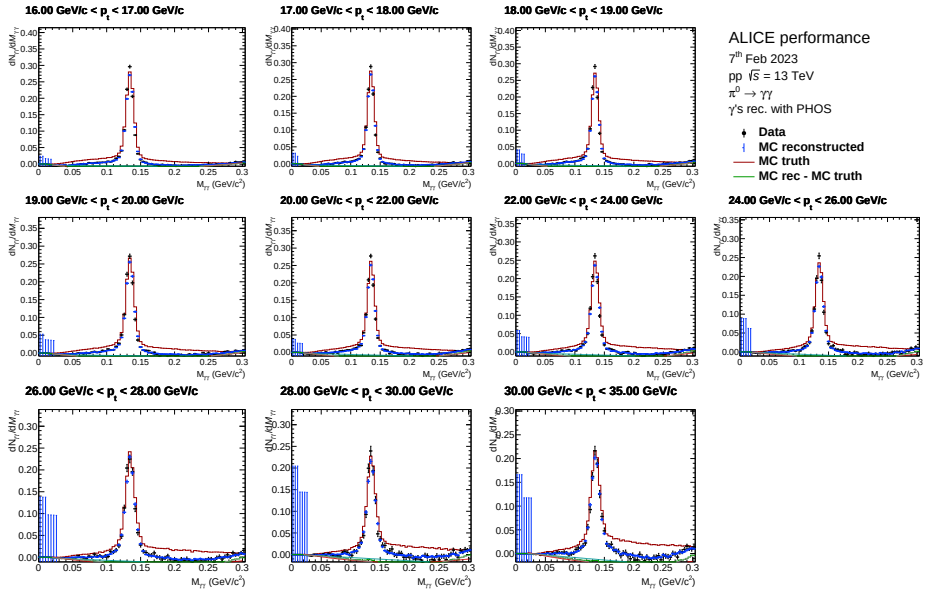

Figure A.6: Comparison of signal shapes in highJJMC of π^0 meson with data for PHI7 trigger, reconstructed with PHOS.

A.3.2 Signal Extraction of π^0 Mesons for PCM-PHOS

Figure A.7: Parametrization of signal distribution of π^0 meson in data for MB trigger, reconstructed with PCM-PHOS.

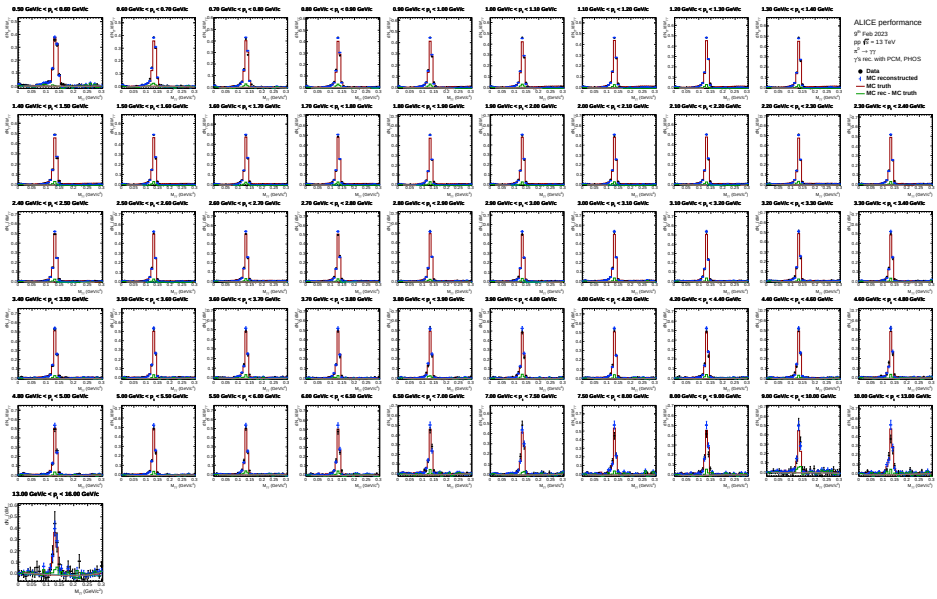

Figure A.8: Comparison of signal shapes in MC of π^0 meson with data for MB trigger, reconstructed with PCM-PHOS.

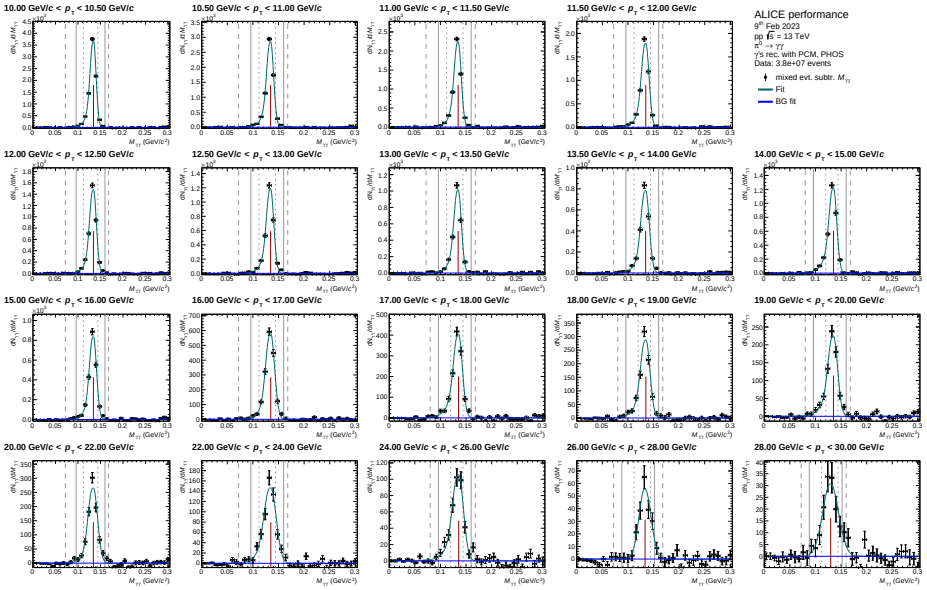

Figure A.9: Parametrization of signal distribution of π^0 meson in data for PHI7 trigger, reconstructed with PCM-PHOS.

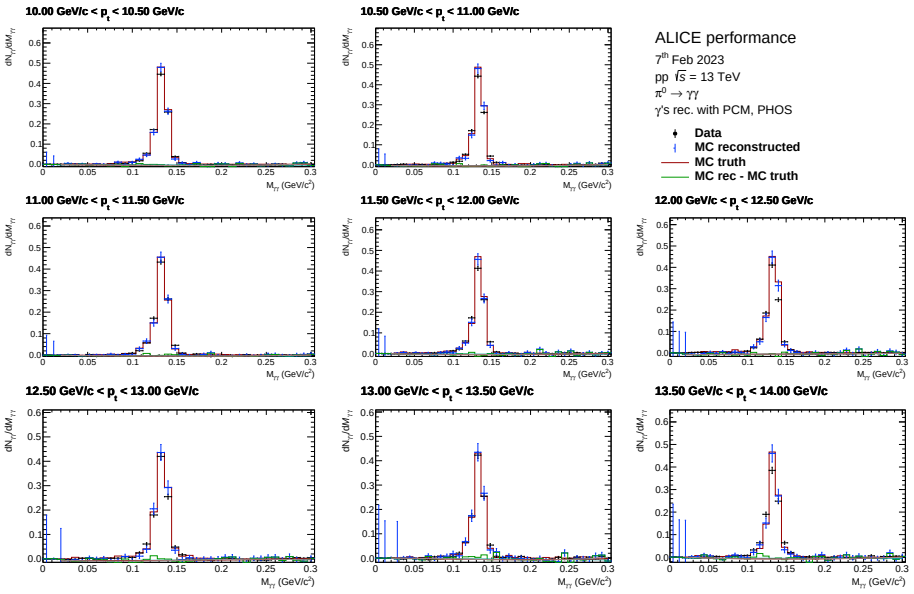

Figure A.10: Comparison of signal shapes in lowJJMC of π^0 meson with data for PHI7 trigger, reconstructed with PCM-PHOS.

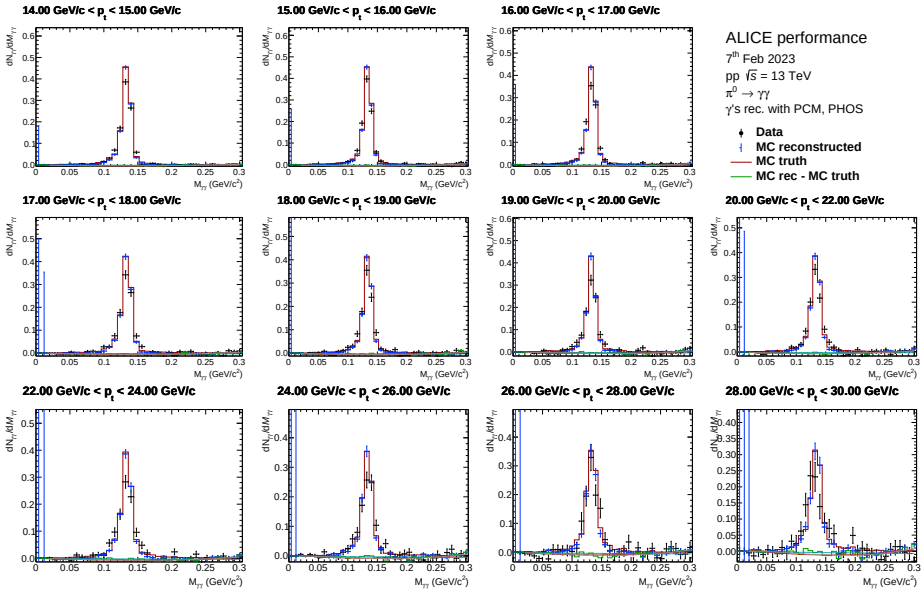

Figure A.11: Comparison of signal shapes in highJJMC of π^0 meson with data for PHI7 trigger, reconstructed with PCM-PHOS.

A.3.3 Signal Extraction of η Mesons for PHOS

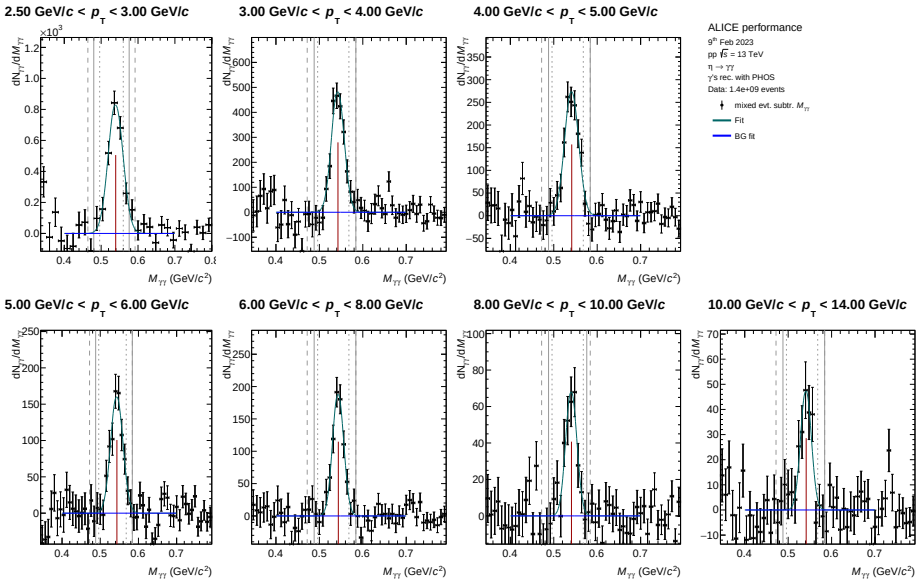

Figure A.12: Parametrization of signal distribution of η meson in data for MB trigger, reconstructed with PHOS.

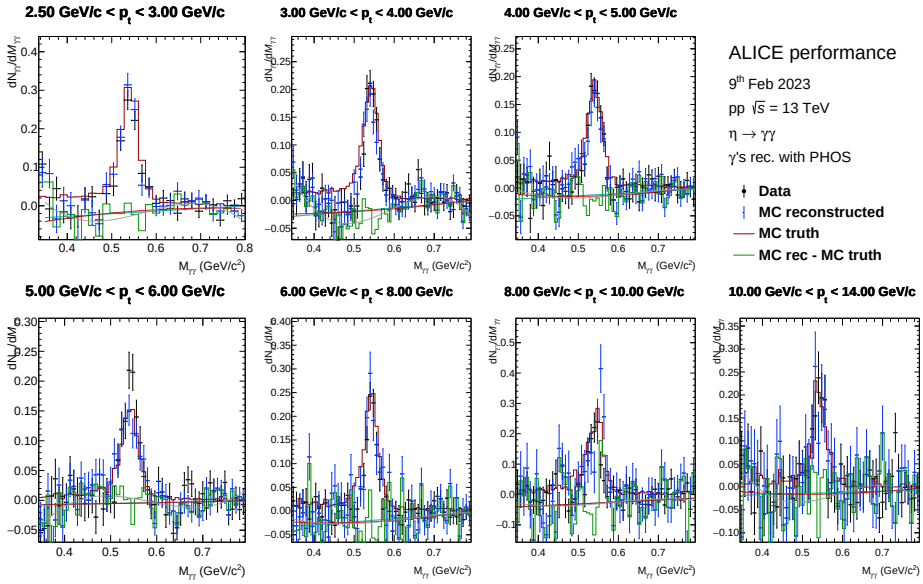

Figure A.13: Comparison of signal shapes in MC of η meson with data for MB trigger, reconstructed with PHOS.

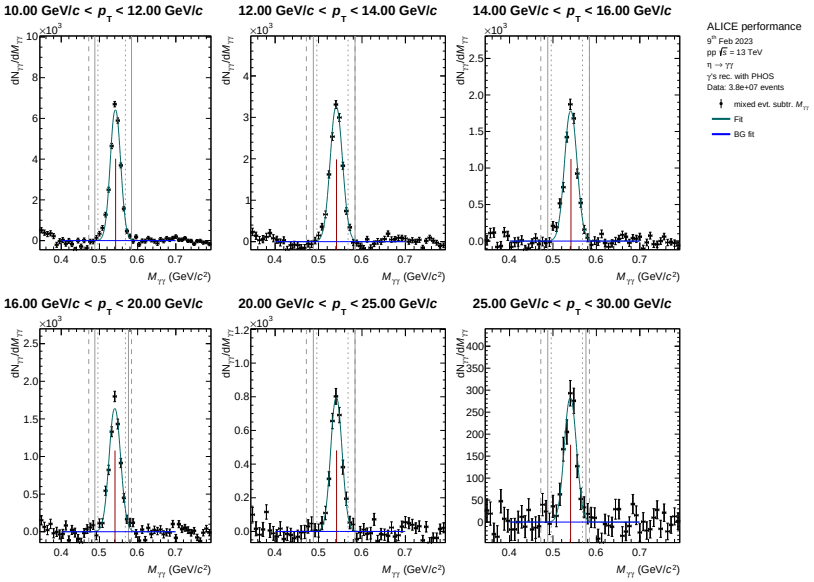

Figure A.14: Parametrization of signal distribution of η meson in data for PHI7 trigger, reconstructed with PHOS.

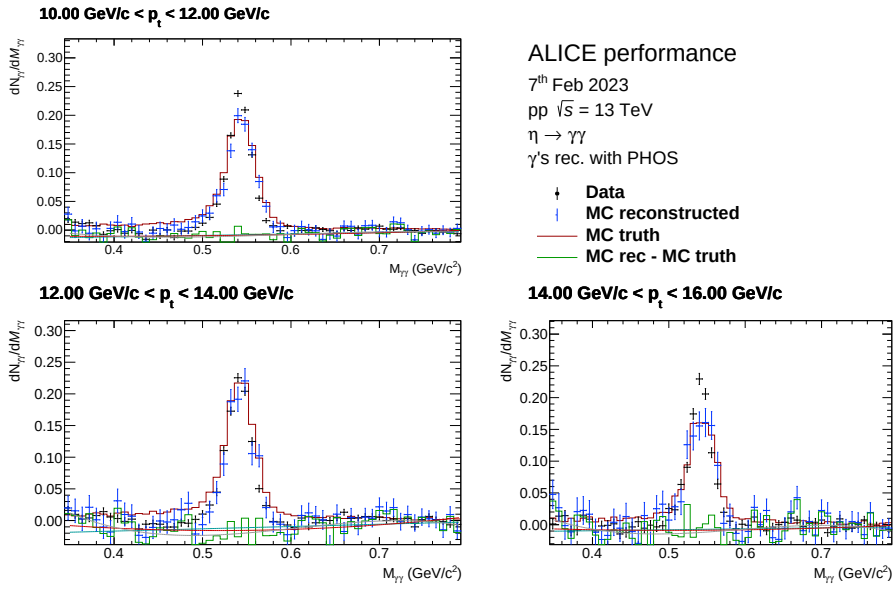

Figure A.15: Comparison of signal shapes in lowJJMC of η meson with data for PHI7 trigger, reconstructed with PHOS.

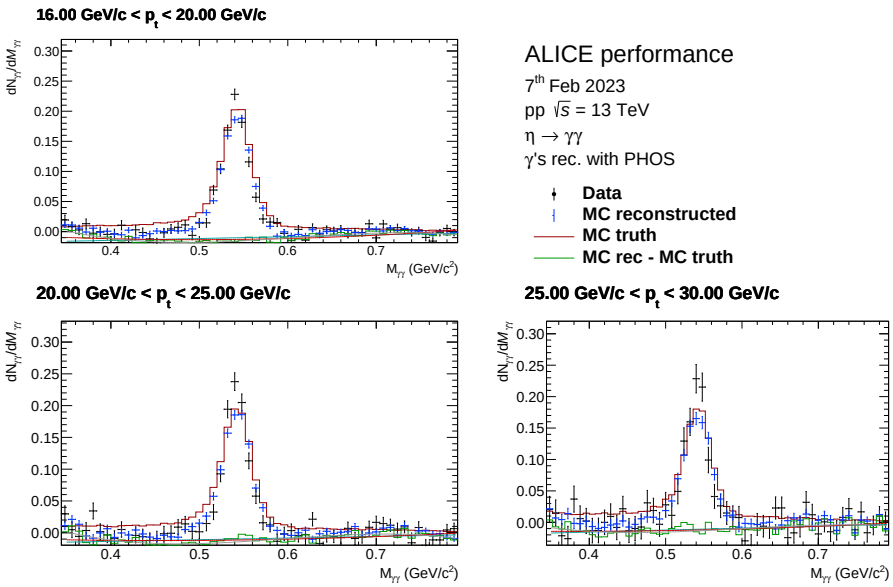

Figure A.16: Comparison of signal shapes in highJJMC of η meson with data for PHI7 trigger, reconstructed with PHOS.

A.3.4 Signal Extraction of η Mesons for PCM-PHOS

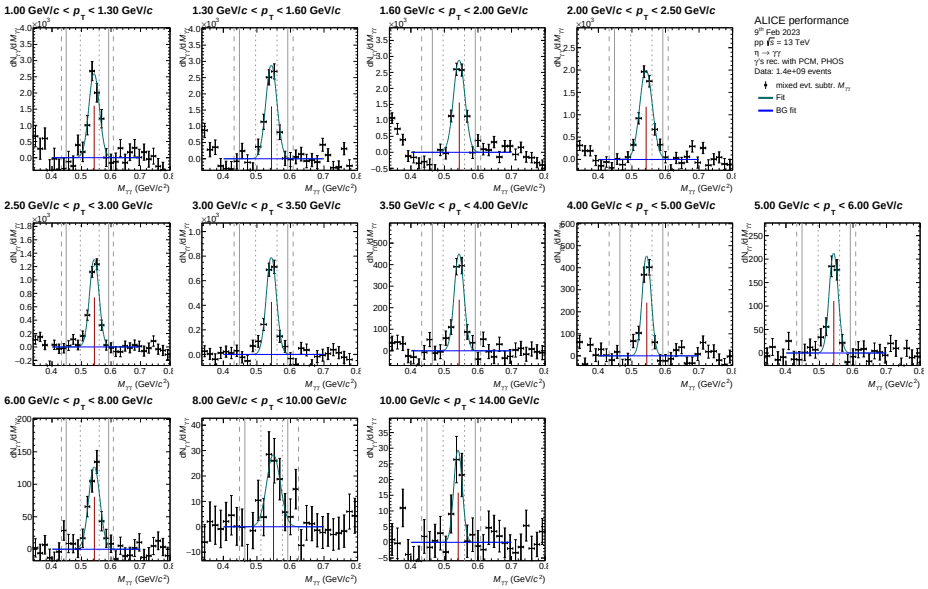

Figure A.17: Parametrization of signal distribution of η meson in data for MB trigger, reconstructed with PCM-PHOS.

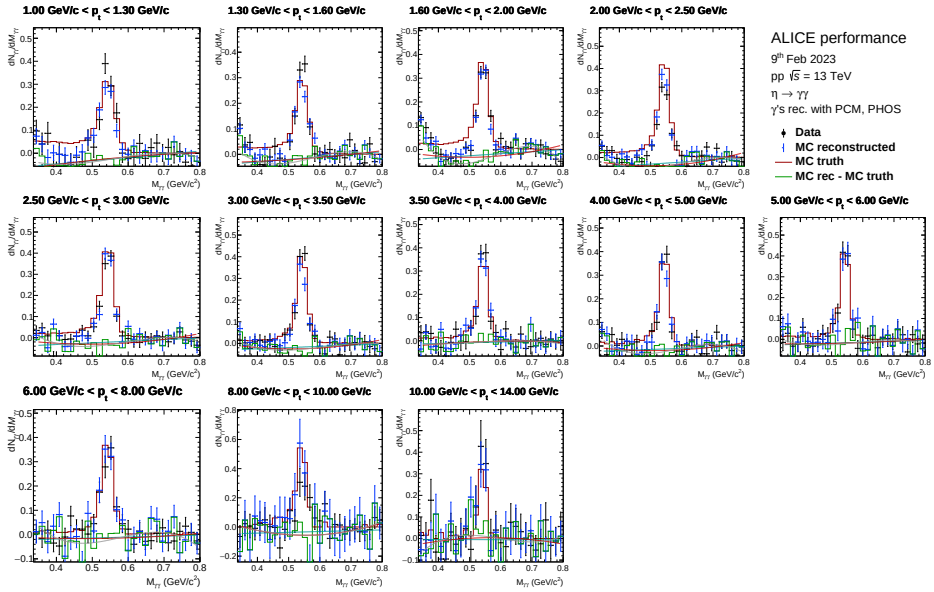

Figure A.18: Comparison of signal shapes in MC of η meson with data for MB trigger, reconstructed with PCM-PHOS.

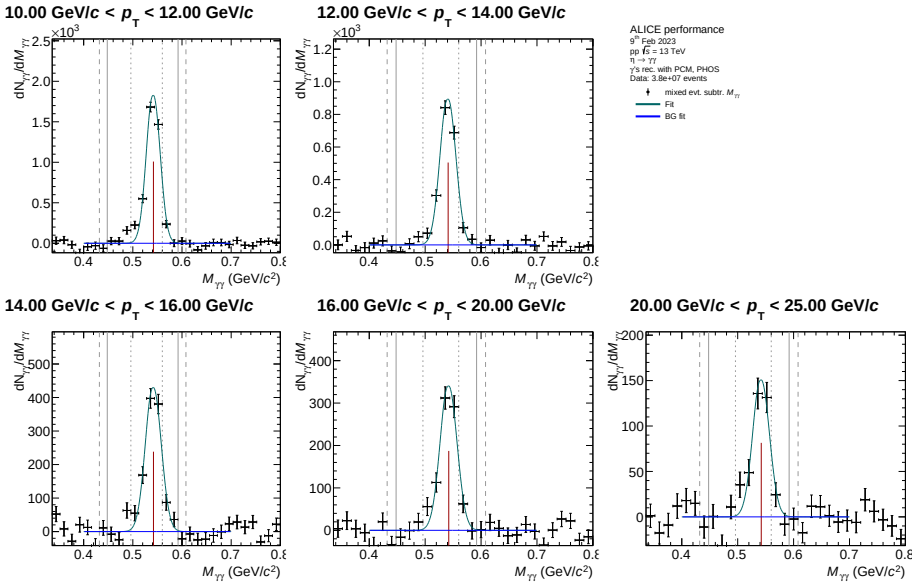

Figure A.19: Parametrization of signal distribution of η meson in data for PHI7 trigger, reconstructed with PCM-PHOS.

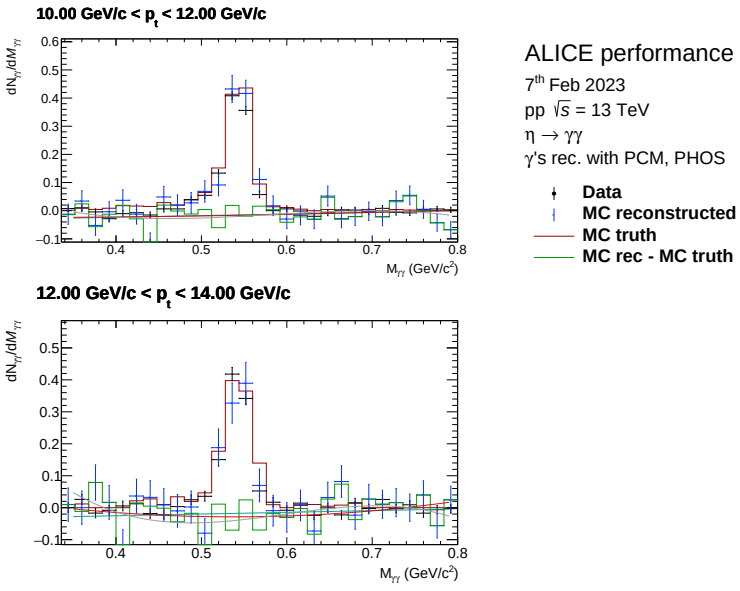

Figure A.20: Comparison of signal shapes in lowJJMC of η meson with data for PHI7 trigger, reconstructed with PCM-PHOS.

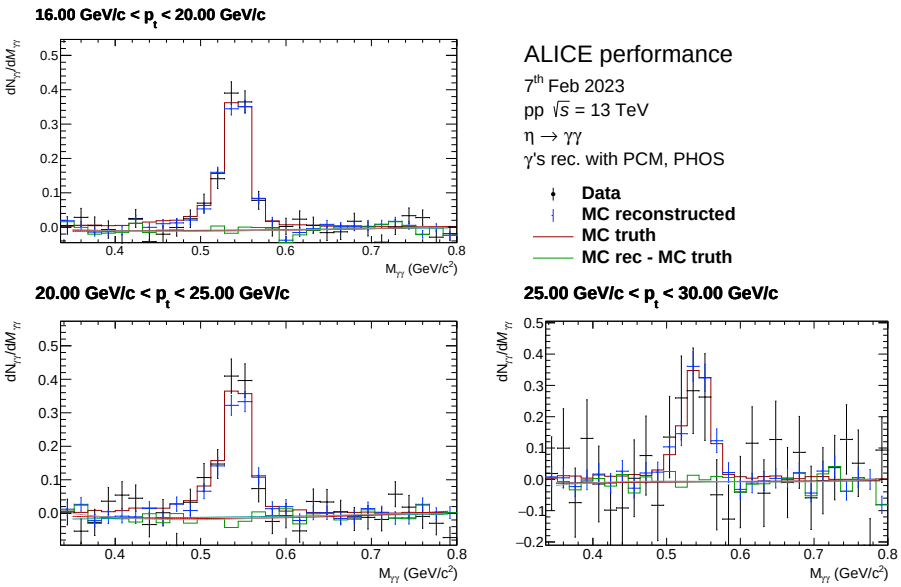

Figure A.21: Comparison of signal shapes in highJJMC of η meson with data for PHI7 trigger, reconstructed with PCM-PHOS.

A.4 ω Meson Reconstruction

A.4.1 Background Description Method Studies for ω Mesons

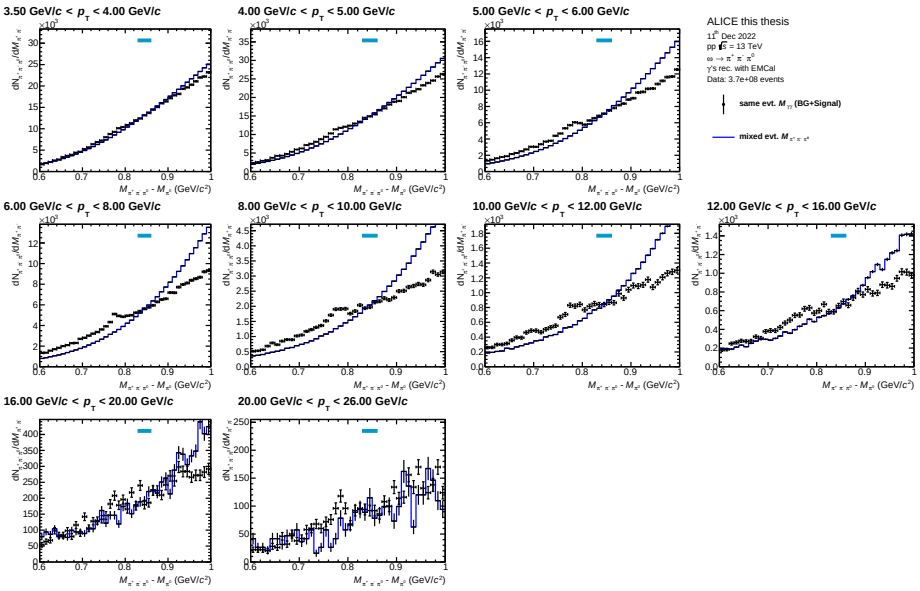

Figure A.22: SigBG of ω mesons compared to event-mixing BG in data for MB trigger, reconstructed with EMCal.

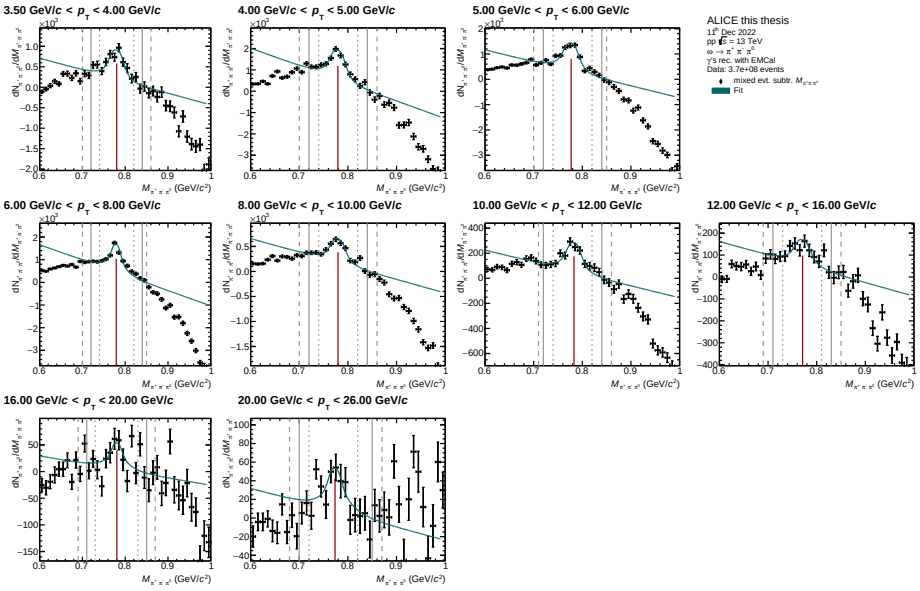

Figure A.23: Signal distribution of ω mesons in data for MB trigger, reconstructed with EMCal. The BG has been described by event-mixing.

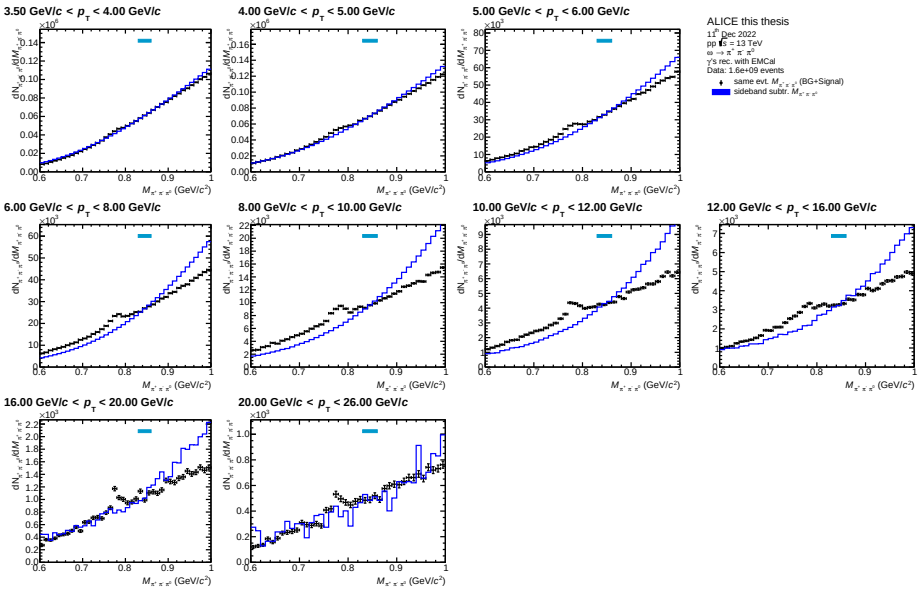

Figure A.24: SigBG of ω mesons compared to sideband-mixing BG in data for MB trigger, reconstructed with EMCal.

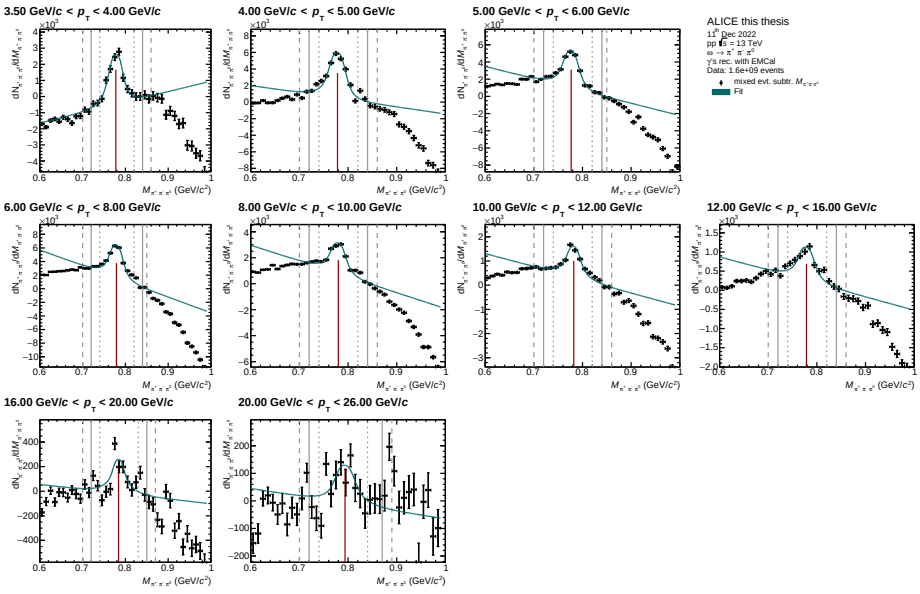

Figure A.25: Signal distribution of ω mesons in data for MB trigger, reconstructed with EMCal. The BG has been described by sideband-mixing.

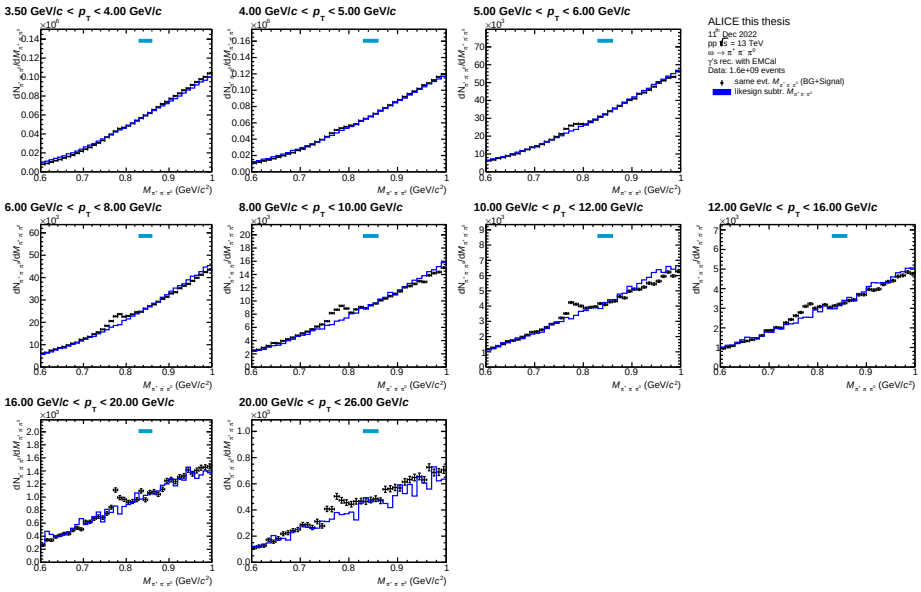

Figure A.26: SigBG of ω mesons compared to likesign-mixing BG in data for MB trigger, reconstructed with EMCal.

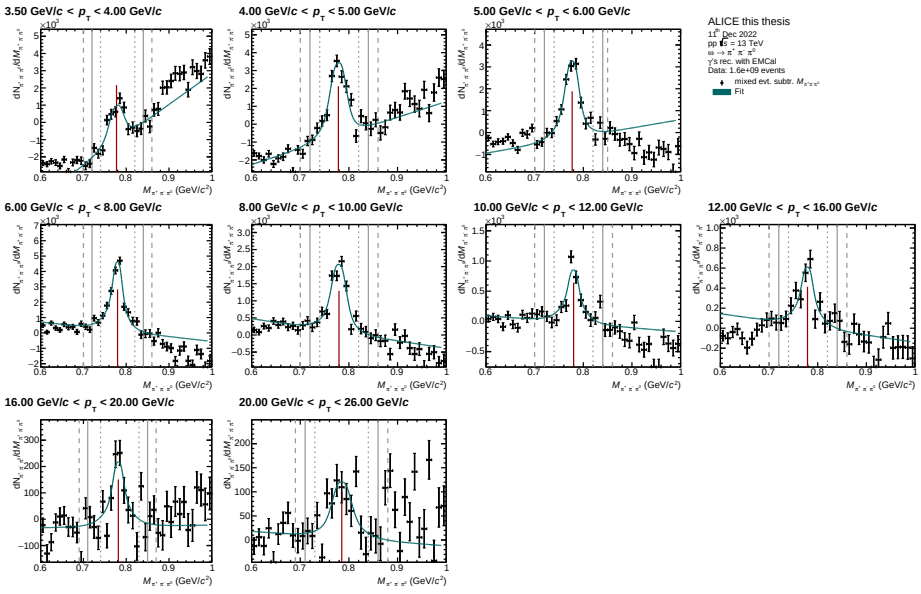

Figure A.27: Signal distribution of ω mesons in data for MB trigger, reconstructed with EMCal. The BG has been described by likesign-mixing.

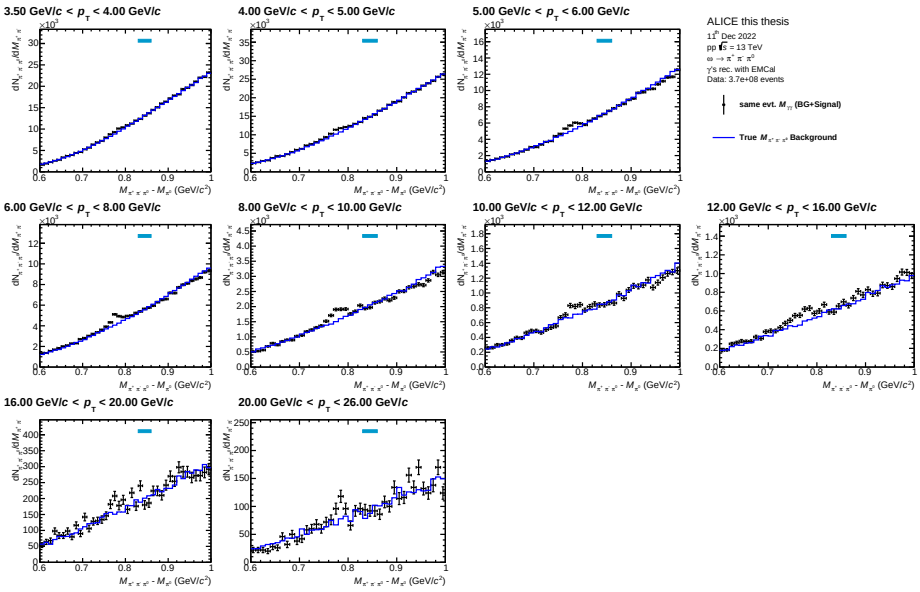

Figure A.28: SigBG of ω mesons compared to true MC BG in data for MB trigger, reconstructed with EMCal.

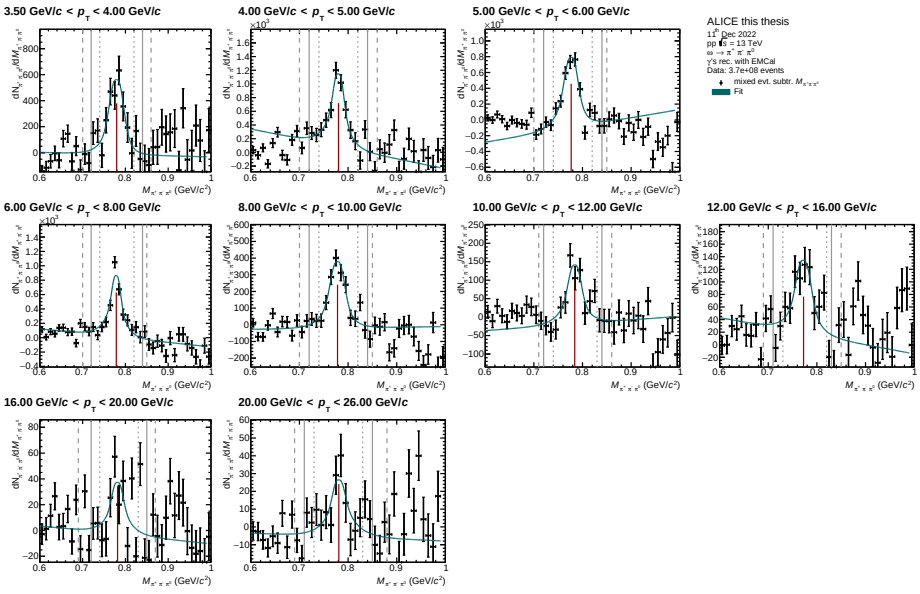

Figure A.29: Signal distribution of ω mesons in data for MB trigger, reconstructed with EMCal. The BG has been described by true MC.

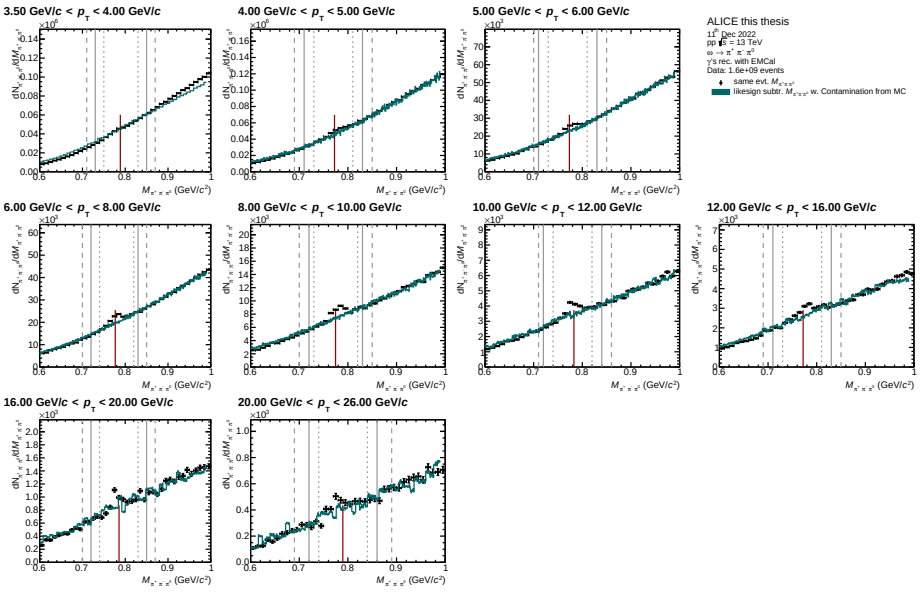

Figure A.30: SigBG of ω mesons compared to event-mixing and the contamination extracted from MC in data for MB trigger, reconstructed with EMCal.

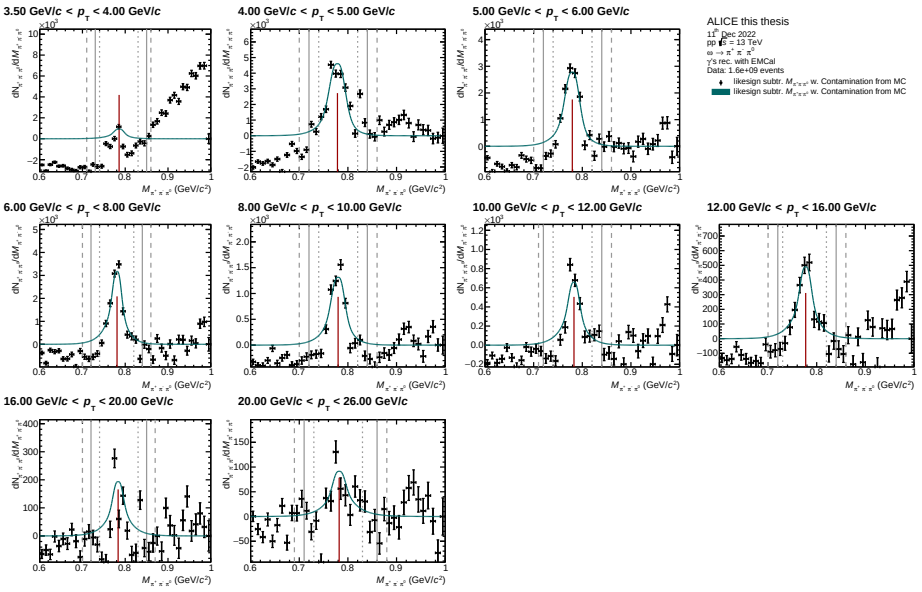

Figure A.31: Signal distribution of ω mesons in data for MB trigger, reconstructed with EMCal. The BG has been described by event-mixing and the contamination extracted from MC.

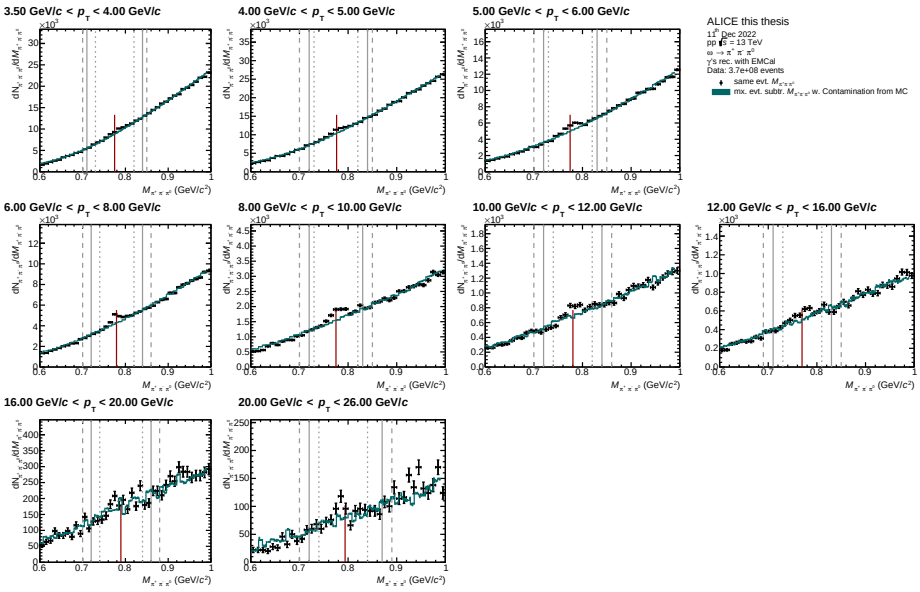

Figure A.32: SigBG of ω mesons compared to likesign-mixing and the contamination extracted from MC in data for MB trigger, reconstructed with EMCal.

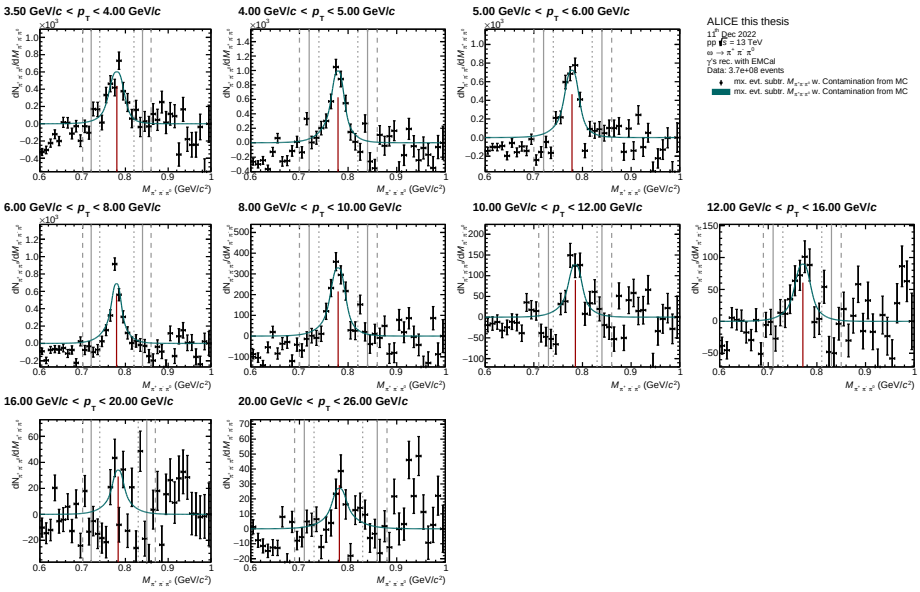

Figure A.33: Signal distribution of ω mesons in data for MB trigger, reconstructed with EMCal. The BG has been described by likesign-mixing and the contamination extracted from MC.

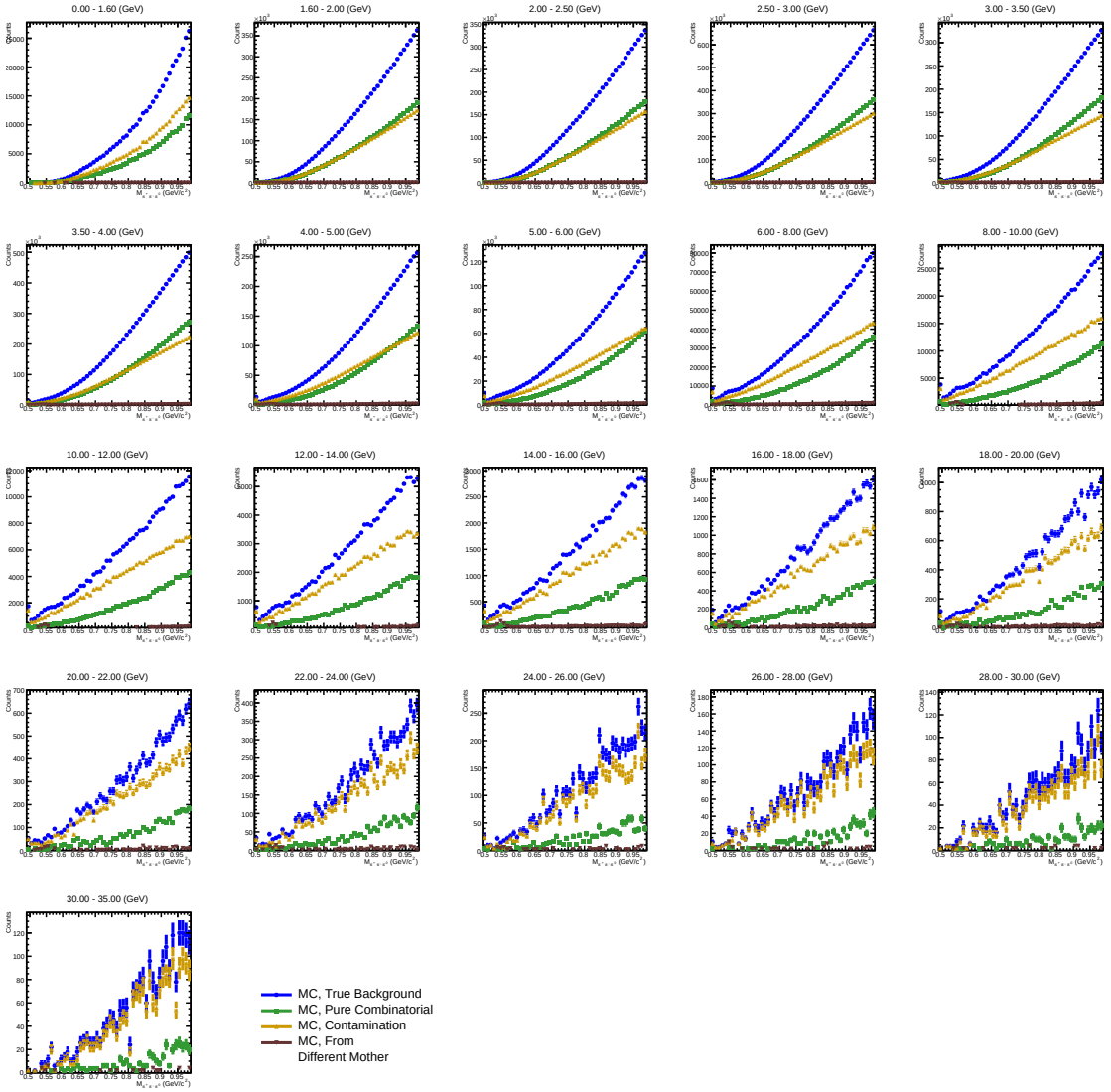

Figure A.34: Different contributions to ω meson background for different p_{T} intervals in EMCal for MC, using the MB trigger. The blue distribution is acquired by subtracting all validated ω mesons from the SigBG distribution. The blue distribution is split in three categories: The green distribution consists of ω candidates originating from uncorrelated pions, the combinatorial background. In the orange distribution at least one pion is not the identified pion, the contamination background. The brown distribution originates from the same mother meson, which is not the ω meson.

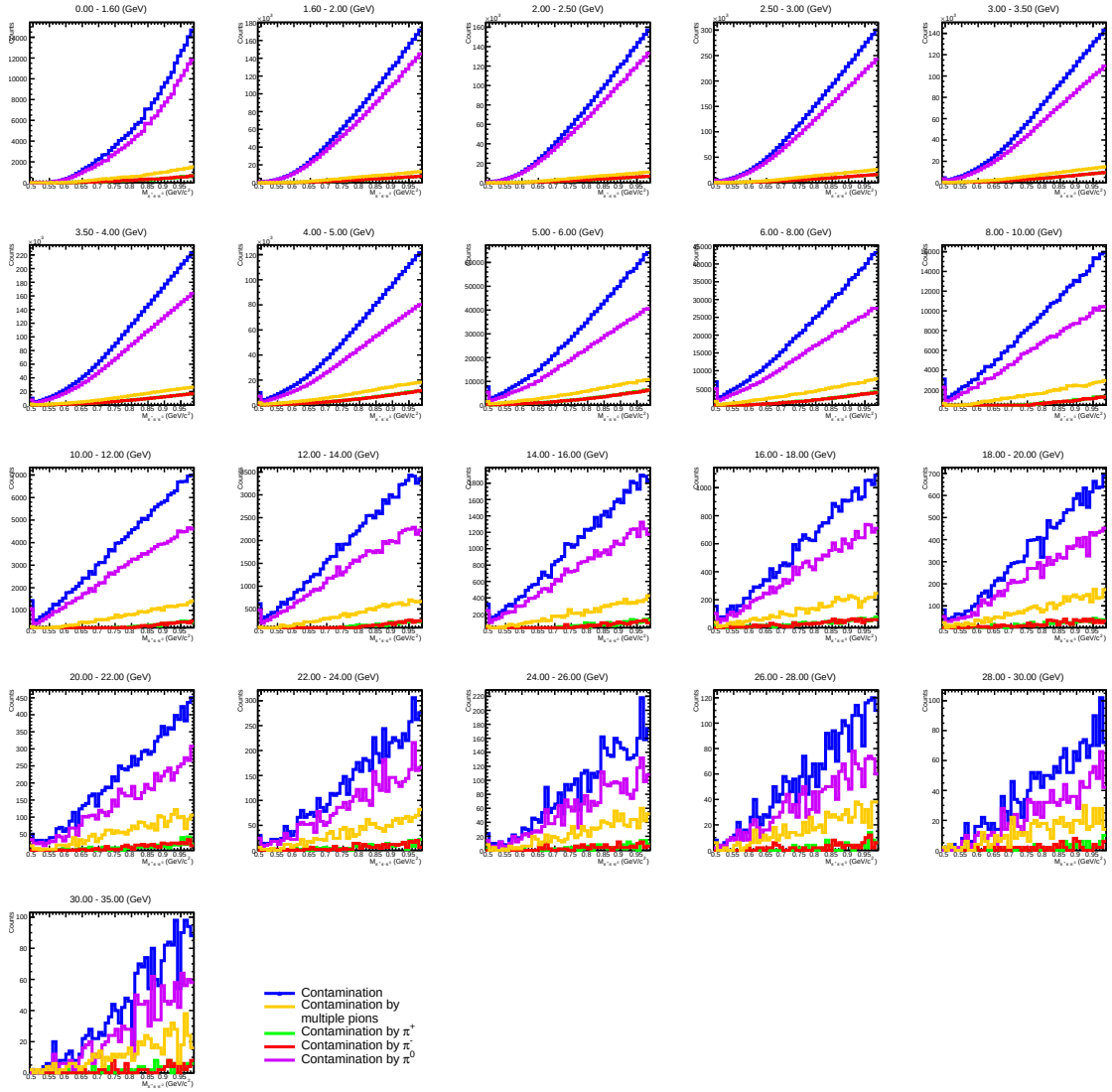

Figure A.35: Different contributions to ω meson contamination background for different p_{T} intervals in EMCal for MC, using the MB trigger. The blue distribution shows the total contamination background. The purple distribution shows the contamination contribution caused by neutral pions. This contribution is generating the majority of the total contamination background. The green and red distributions shows the contamination contribution caused by charged pions. The orange distribution is describing cases, in which more than one pion is falsely identified.

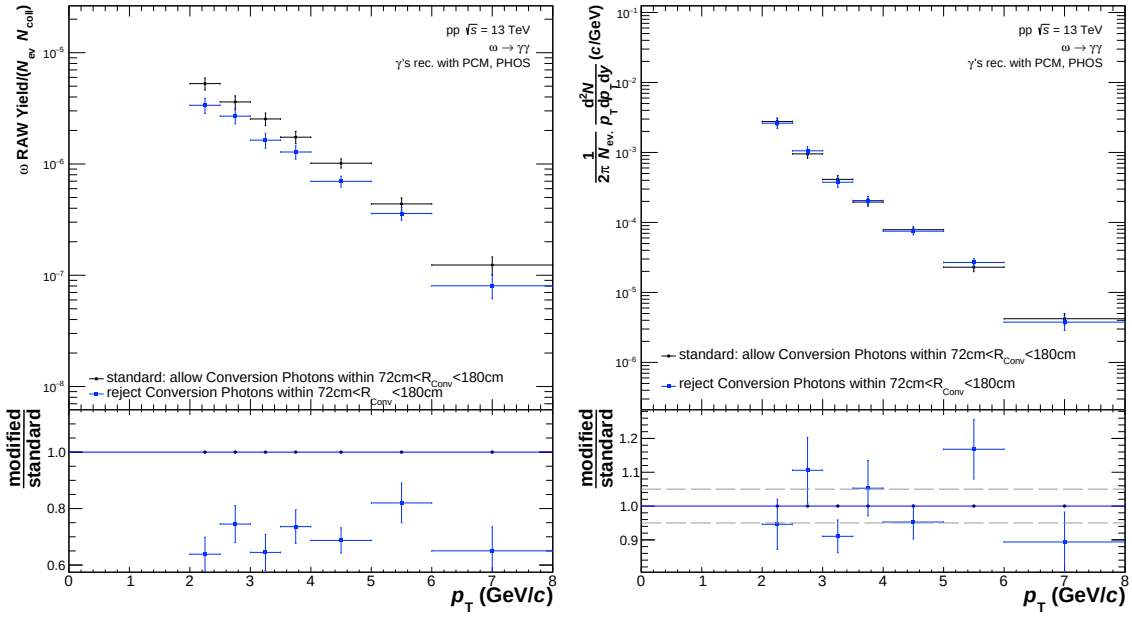

Figure A.36: Comparison of different raw yields (left) and corrected yields (right) for ω meson, reconstructed with PCM-PHOS, using the MB trigger. The plots compare extracted yields with and without using conversion photons, which converted within 72 cm $< R_{\mathrm{conv}} <$ 180 cm.

A.4.2 Signal Extraction of ω Mesons

Signal Extraction of ω Mesons for PCM

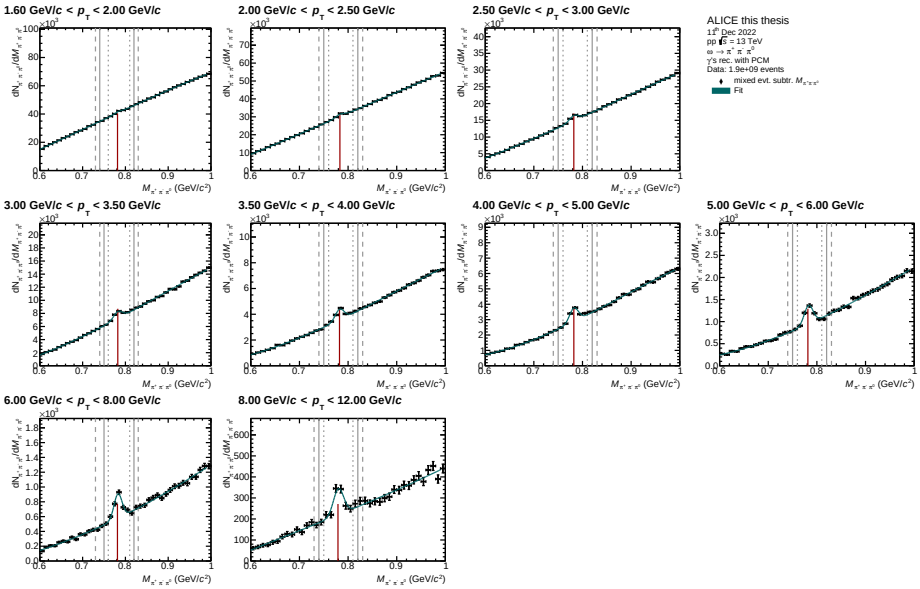

Figure A.37: Background parametrization of SigBG of ω meson in data for MB trigger, reconstructed with PCM.

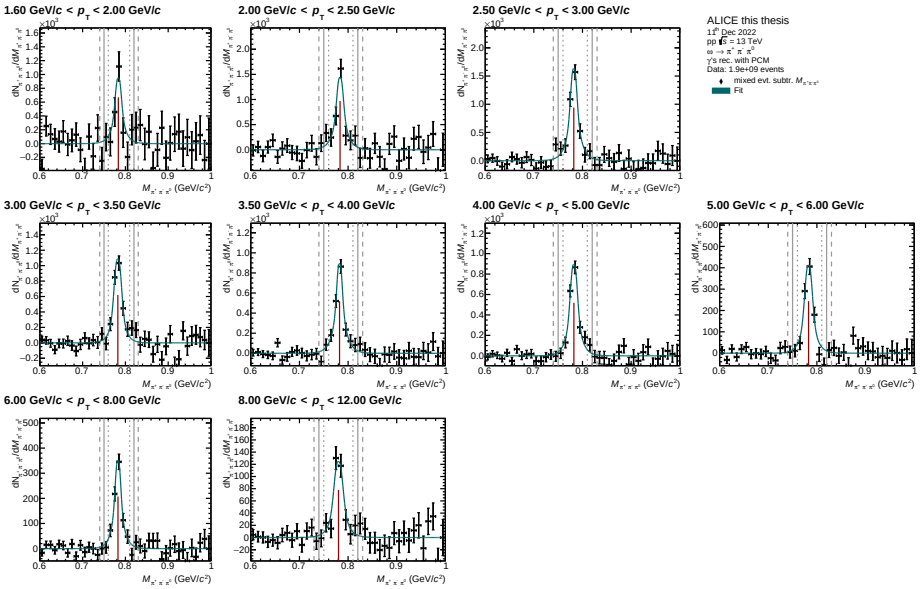

Figure A.38: Parametrization of signal distribution of ω meson in data for MB trigger, reconstructed with PCM.

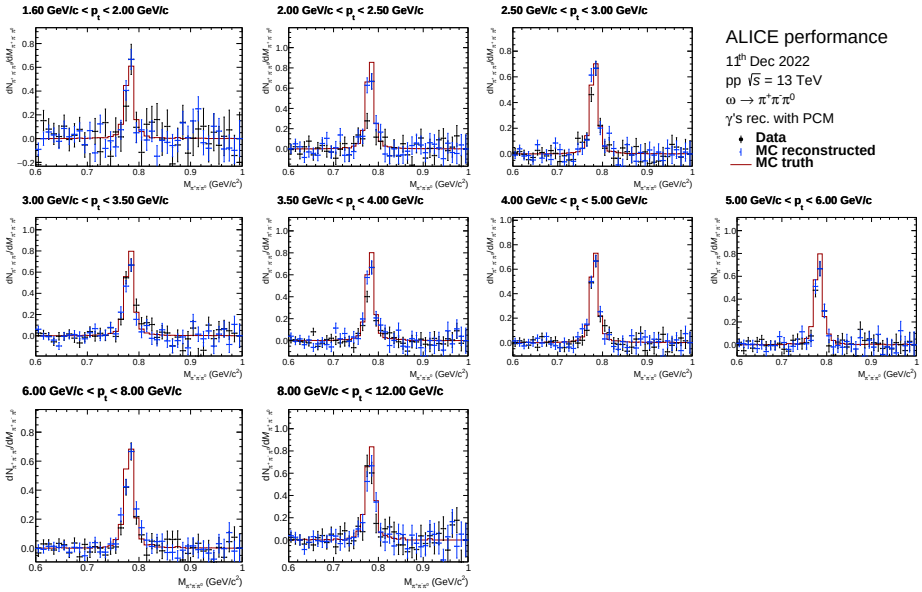

Figure A.39: Comparison of signal shapes in MC of ω meson with data for MB trigger, reconstructed with PCM.

Signal Extraction of ω Mesons for EMCal

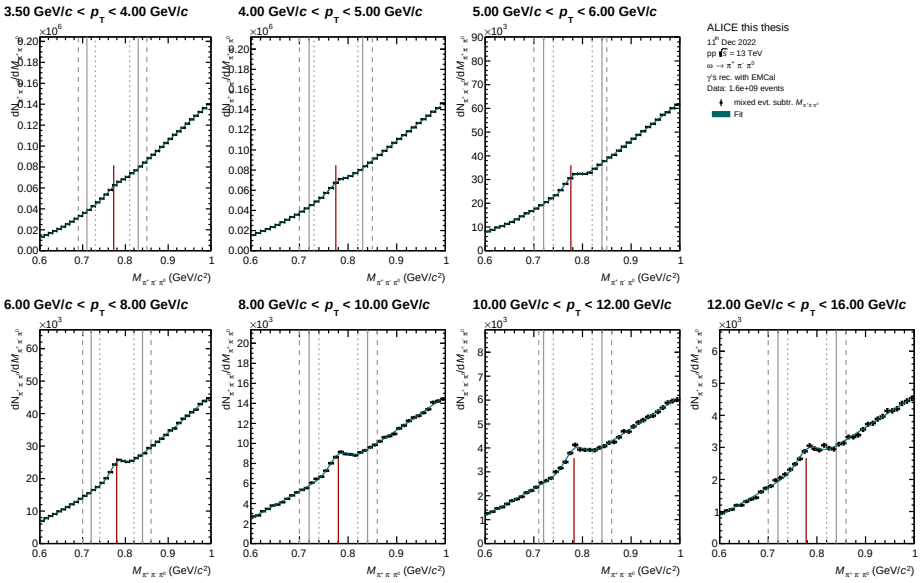

Figure A.40: Background parametrization of SigBG of ω meson in data for MB trigger, reconstructed with EMCal.

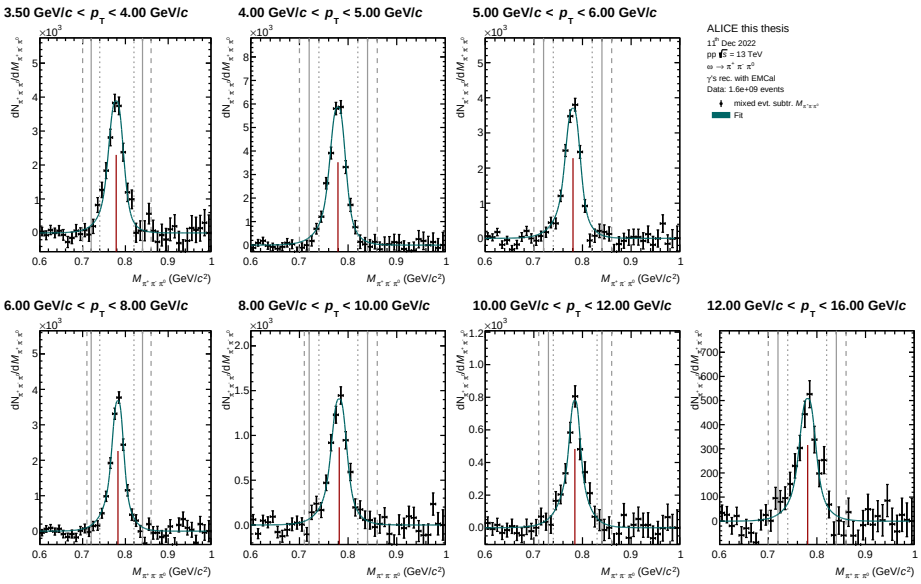

Figure A.41: Parametrization of signal distribution of ω meson in data for MB trigger, reconstructed with EMCal.

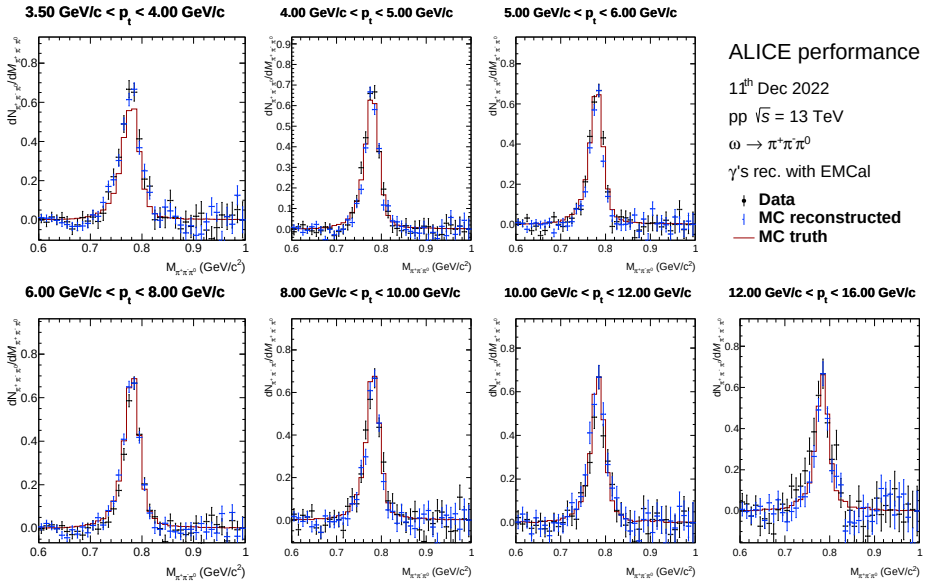

Figure A.42: Comparison of signal shapes in MC of ω meson with data for MB trigger, reconstructed with EMCal.

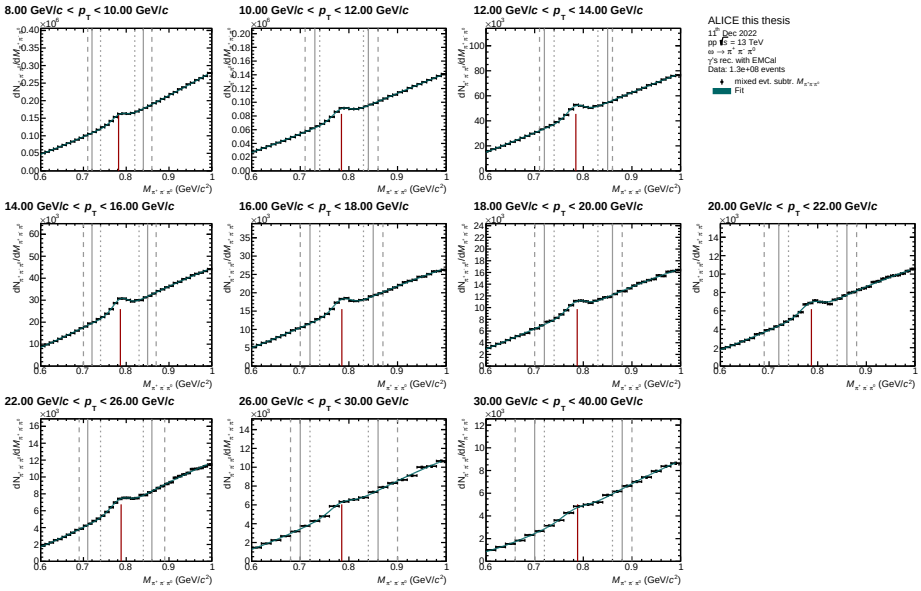

Figure A.43: Background parametrization of SigBG of ω meson in data for EG2 trigger, reconstructed with EMCal.

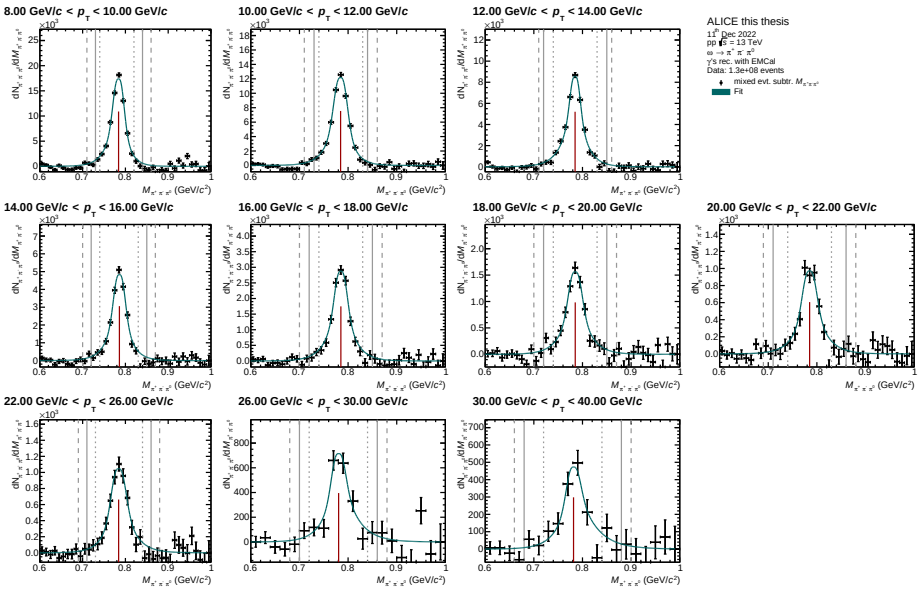

Figure A.44: Parametrization of signal distribution of ω meson in data for EG2 trigger, reconstructed with EMCal.

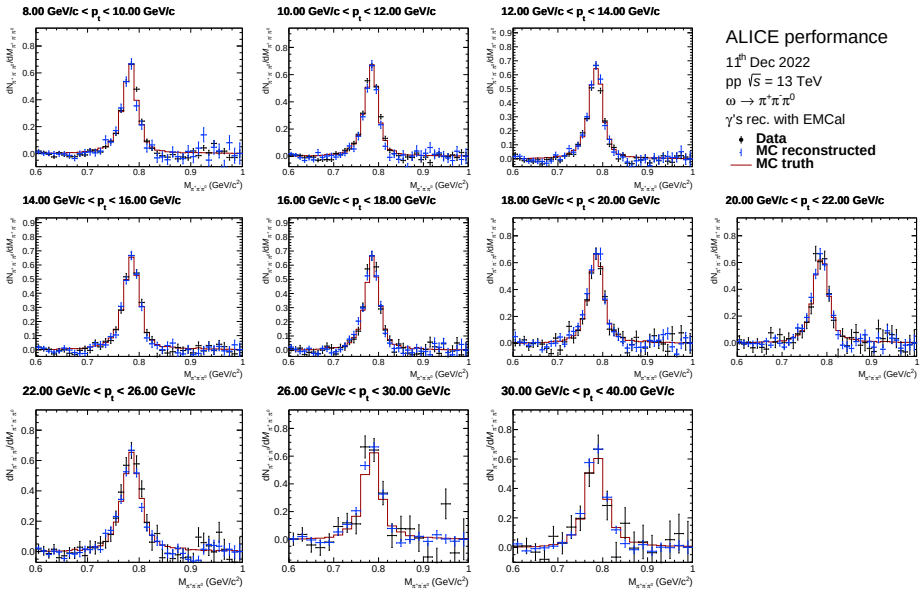

Figure A.45: Comparison of signal shapes in MC of ω meson with data for EG2 trigger, reconstructed with EMCal.

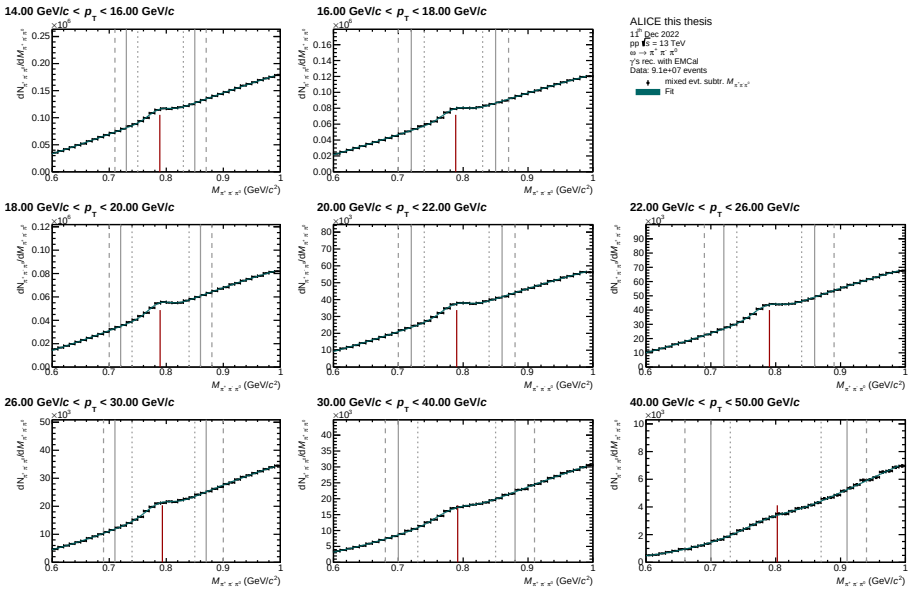

Figure A.46: Background parametrization of SigBG of ω meson in data for EG1 trigger, reconstructed with EMCal.

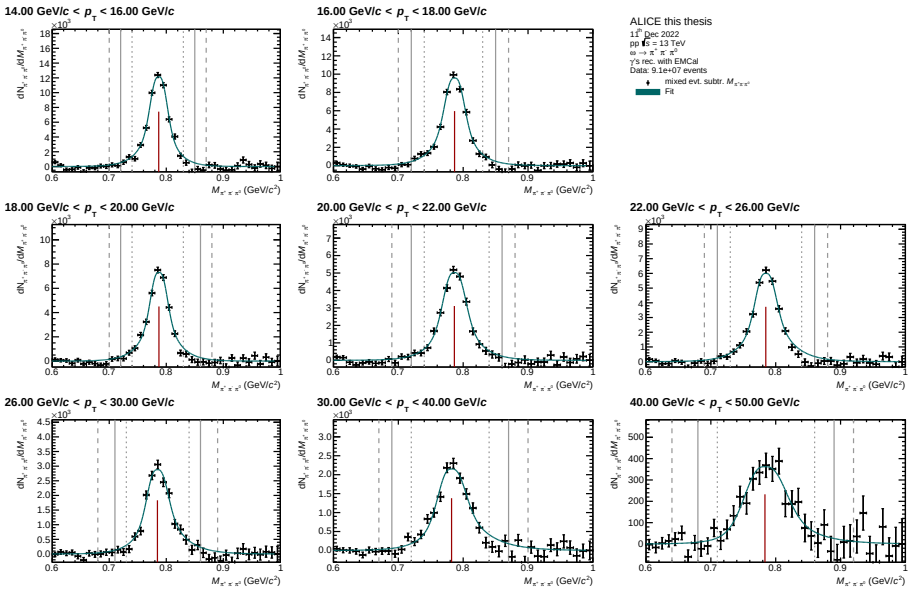

Figure A.47: Parametrization of signal distribution of ω meson in data for EG1 trigger, reconstructed with EMCal.

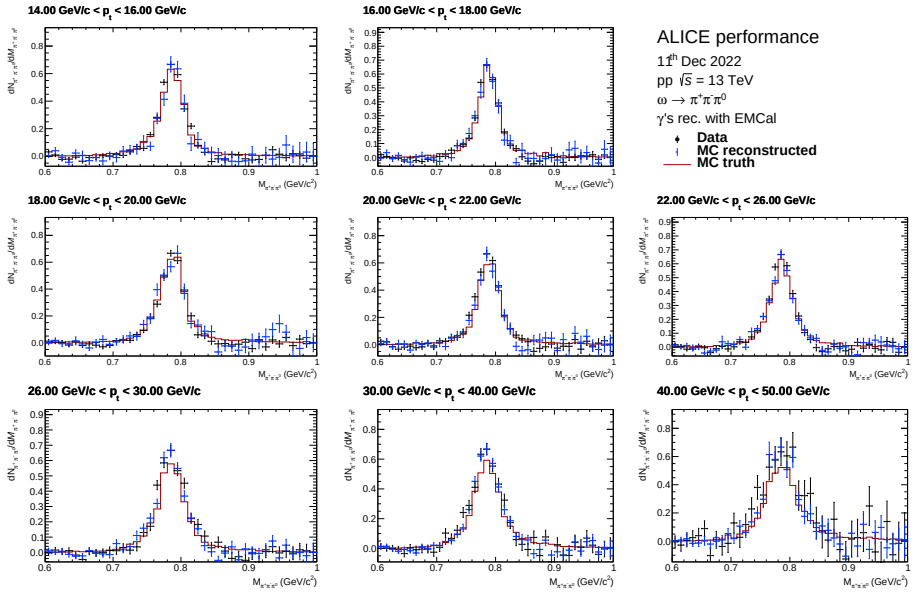

Figure A.48: Comparison of signal shapes in MC of ω meson with data for EG1 trigger, reconstructed with EMCal.

Signal Extraction of ω Mesons for PCM-EMCal

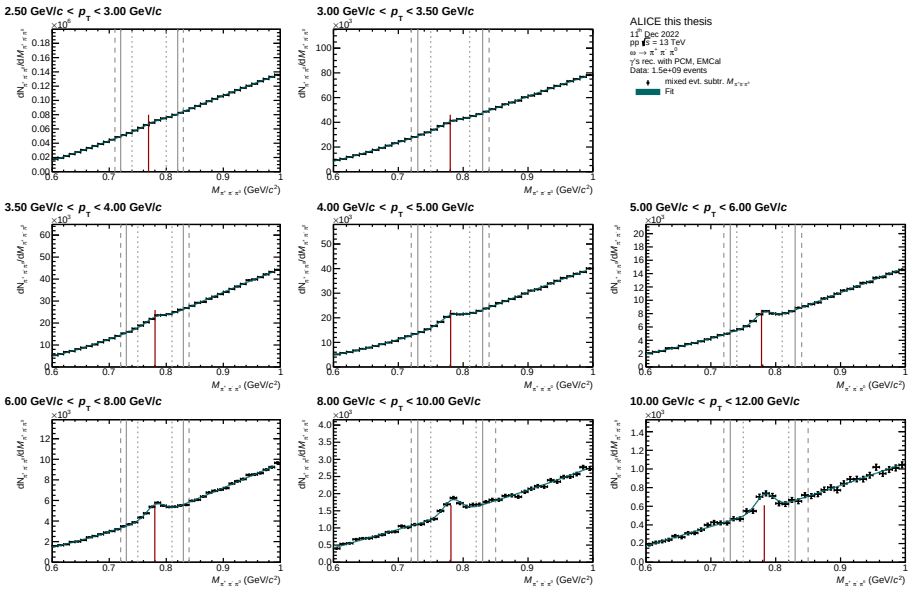

Figure A.49: Background parametrization of SigBG of ω meson in data for MB trigger, reconstructed with PCM-EMCal.

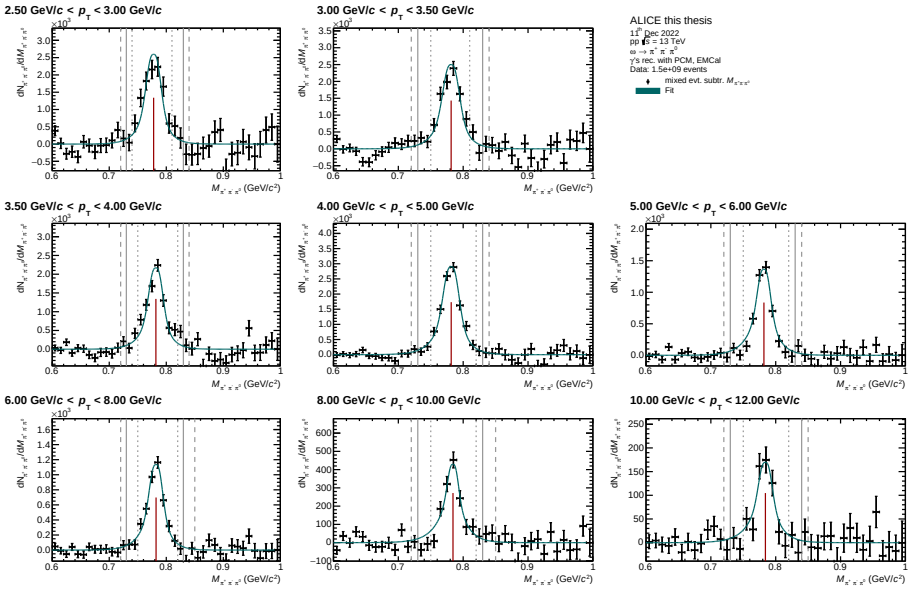

Figure A.50: Parametrization of signal distribution of ω meson in data for MB trigger, reconstructed with PCM-EMCal.

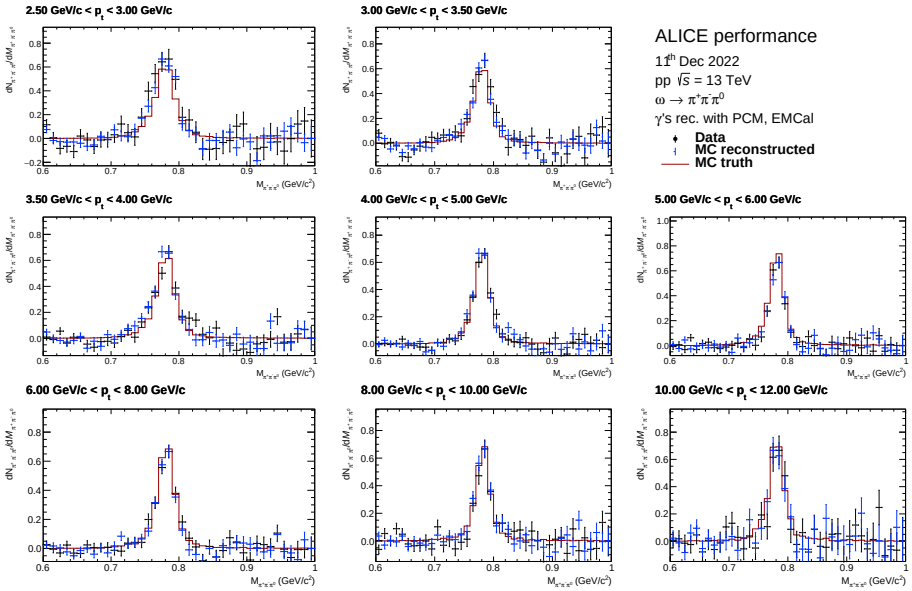

Figure A.51: Comparison of signal shapes in MC of ω meson with data for MB trigger, reconstructed with PCM-EMCal.

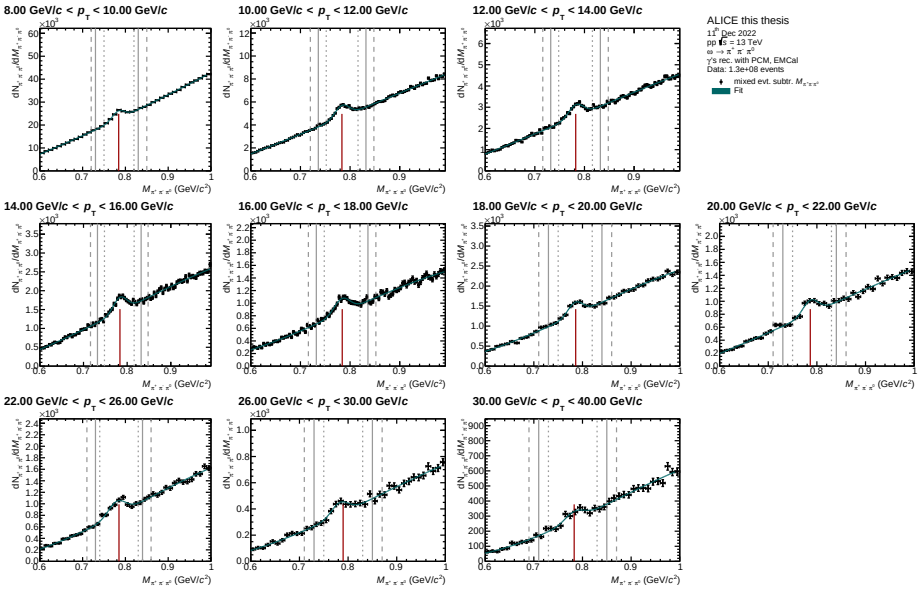

Figure A.52: Background parametrization of SigBG of ω meson in data for EG2 trigger, reconstructed with PCM-EMCal.

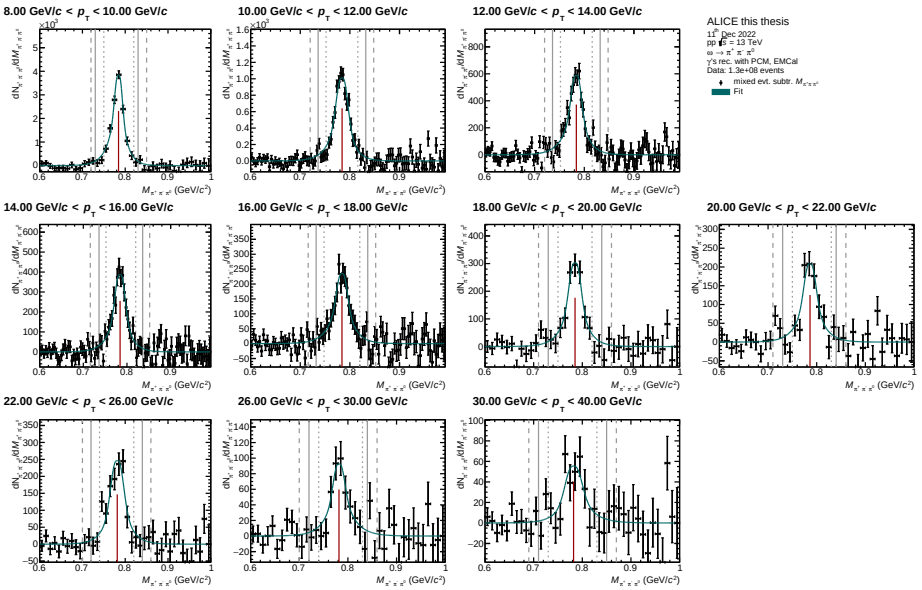

Figure A.53: Parametrization of signal distribution of ω meson in data for EG2 trigger, reconstructed with PCM-EMCal.

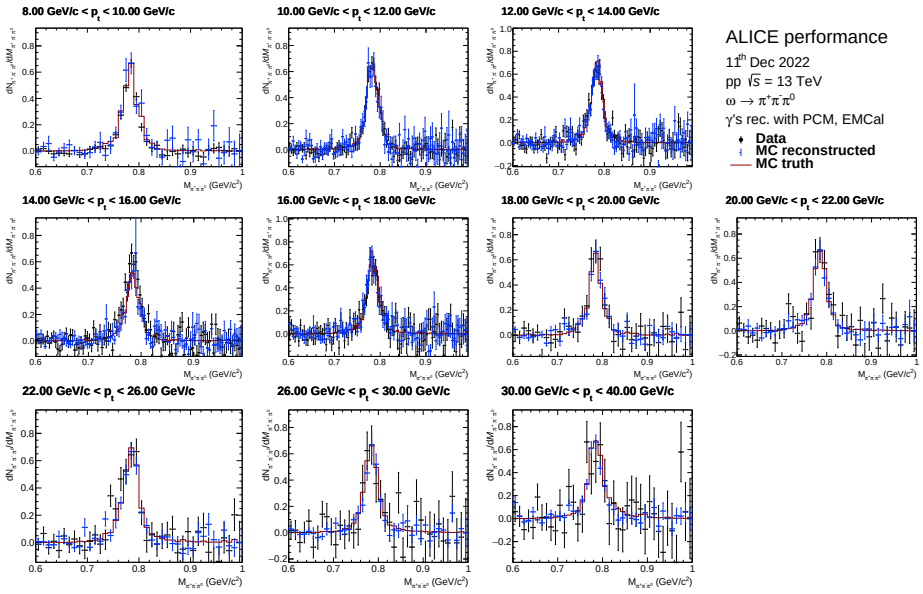

Figure A.54: Comparison of signal shapes in MC of ω meson with data for EG2 trigger, reconstructed with PCM-EMCal.

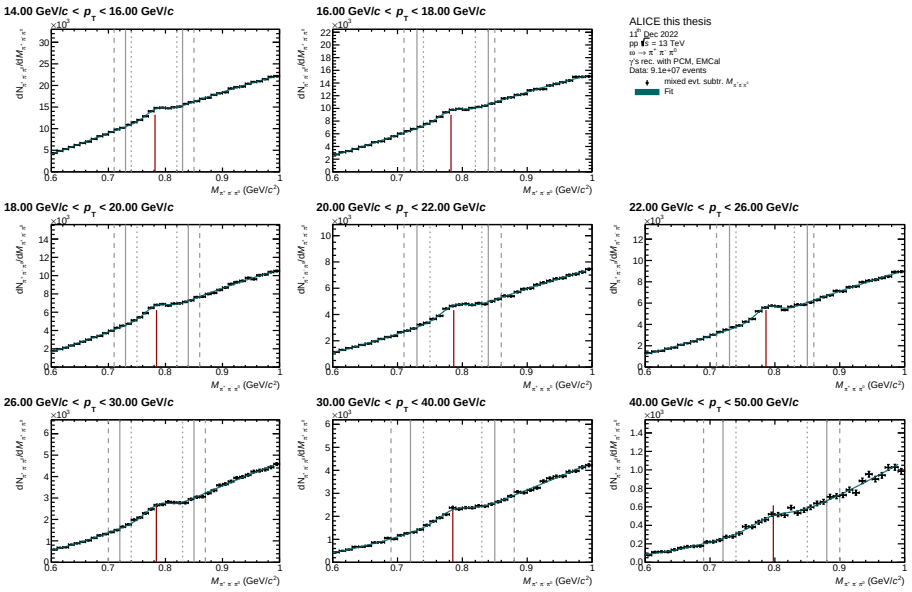

Figure A.55: Background parametrization of SigBG of ω meson in data for EG1 trigger, reconstructed with PCM-EMCal.

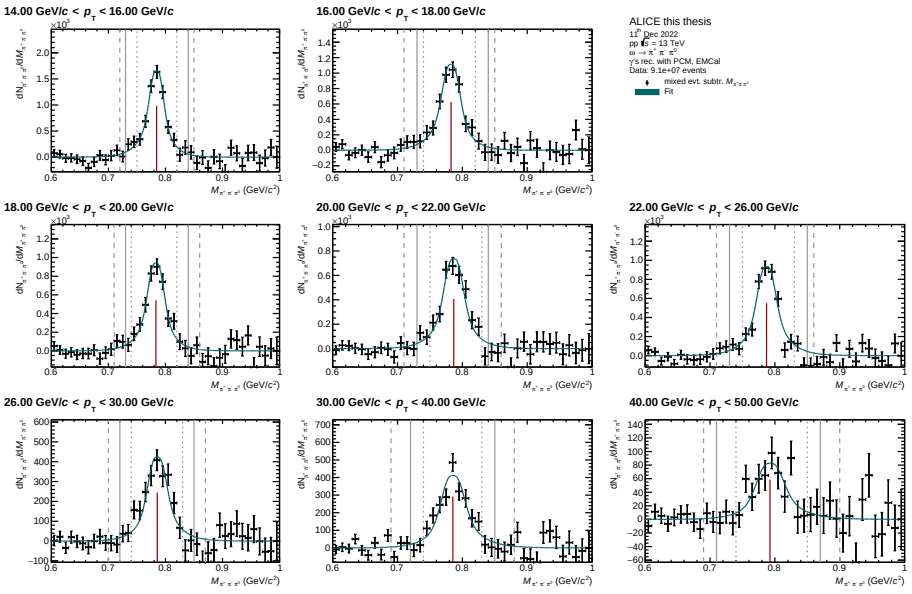

Figure A.56: Parametrization of signal distribution of ω meson in data for EG1 trigger, reconstructed with PCM-EMCal.

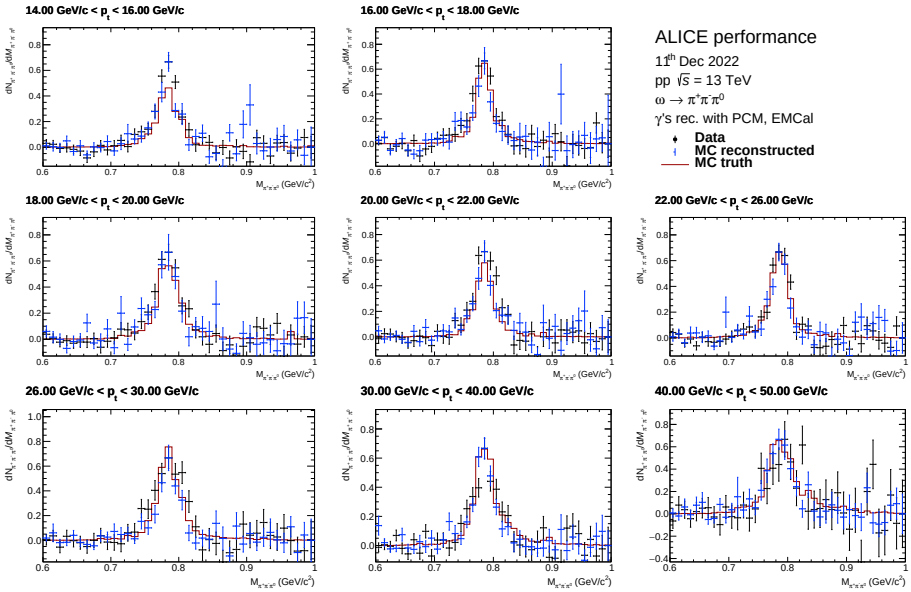

Figure A.57: Comparison of signal shapes in MC of ω meson with data for EG1 trigger, reconstructed with PCM-EMCal.

Signal Extraction of ω Mesons for PHOS

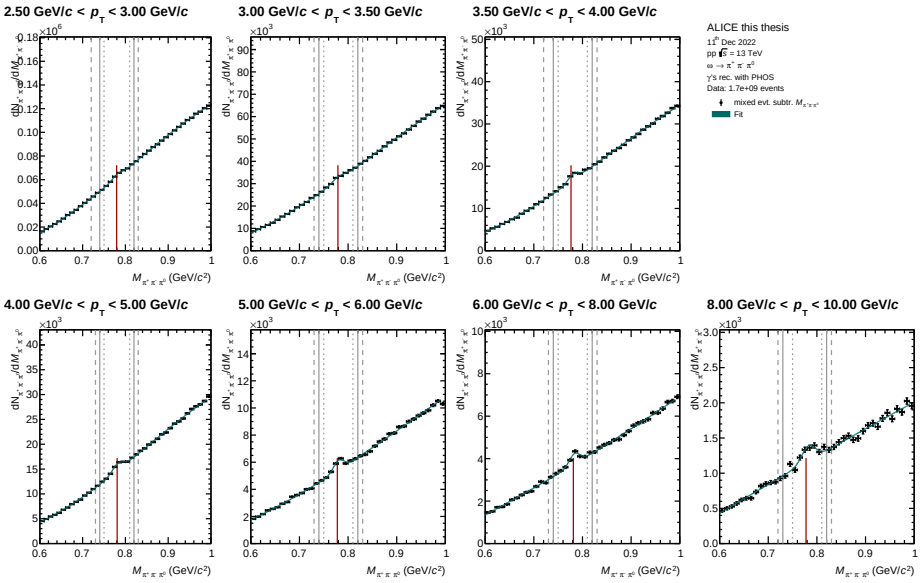

Figure A.58: Background parametrization of SigBG of ω meson in data for MB trigger, reconstructed with PHOS.

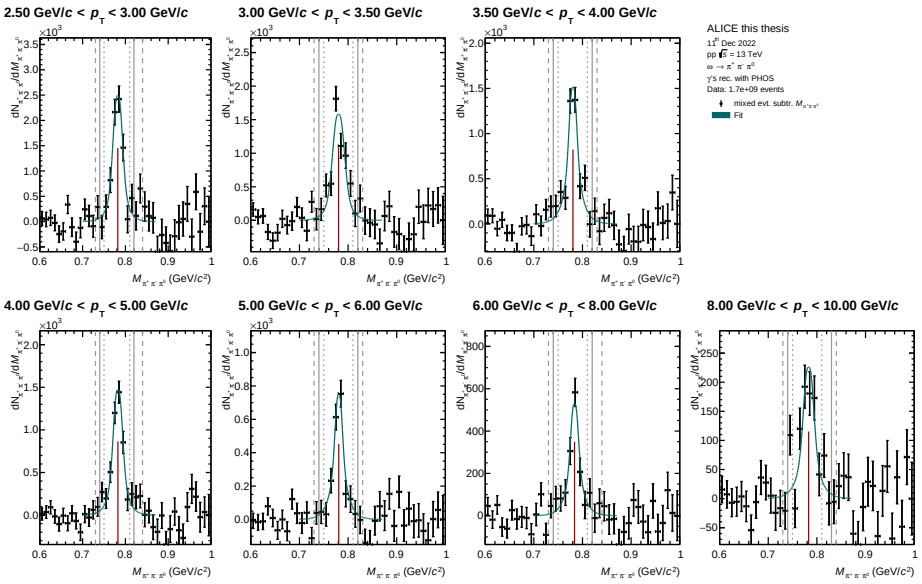

Figure A.59: Parametrization of signal distribution of ω meson in data for MB trigger, reconstructed with PHOS.

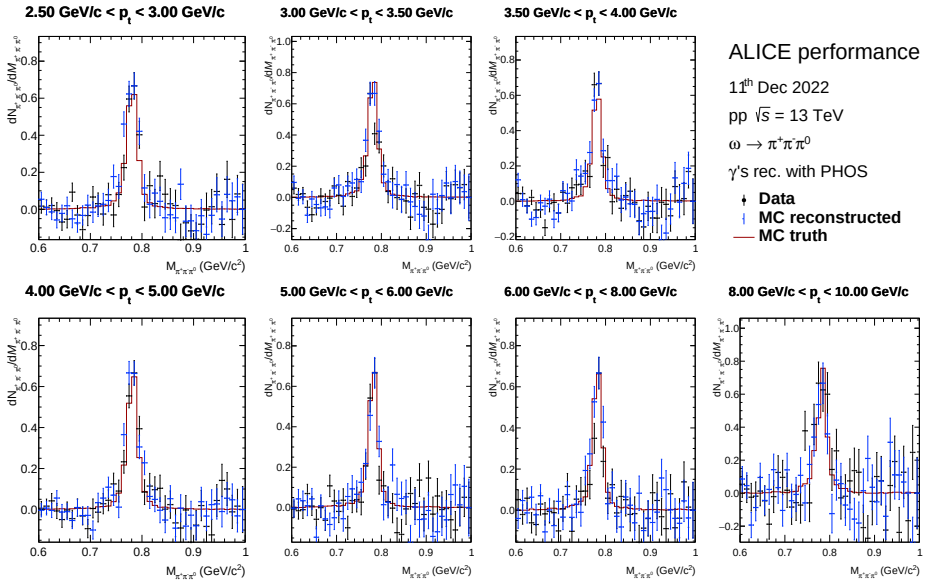

Figure A.60: Comparison of signal shapes in MC of ω meson with data for MB trigger, reconstructed with PHOS.

Signal Extraction of ω Mesons for PCM-PHOS

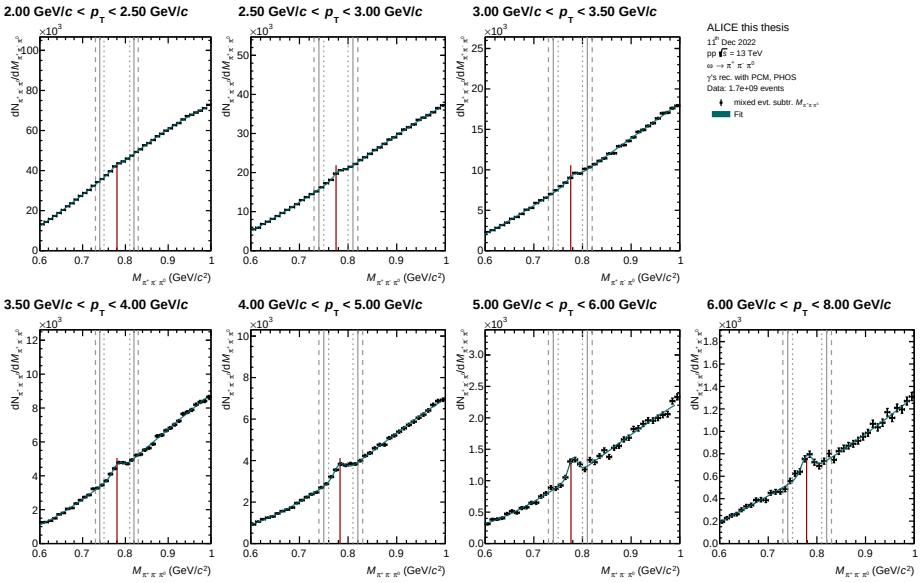

Figure A.61: Background parametrization of SigBG of ω meson in data for MB trigger, reconstructed with PCM-PHOS.

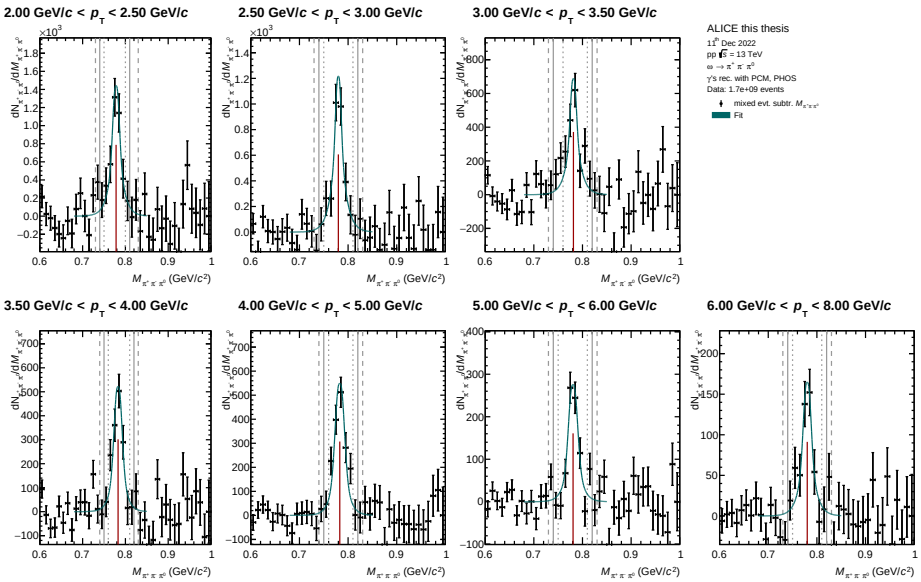

Figure A.62: Parametrization of signal distribution of ω meson in data for MB trigger, reconstructed with PCM-PHOS.

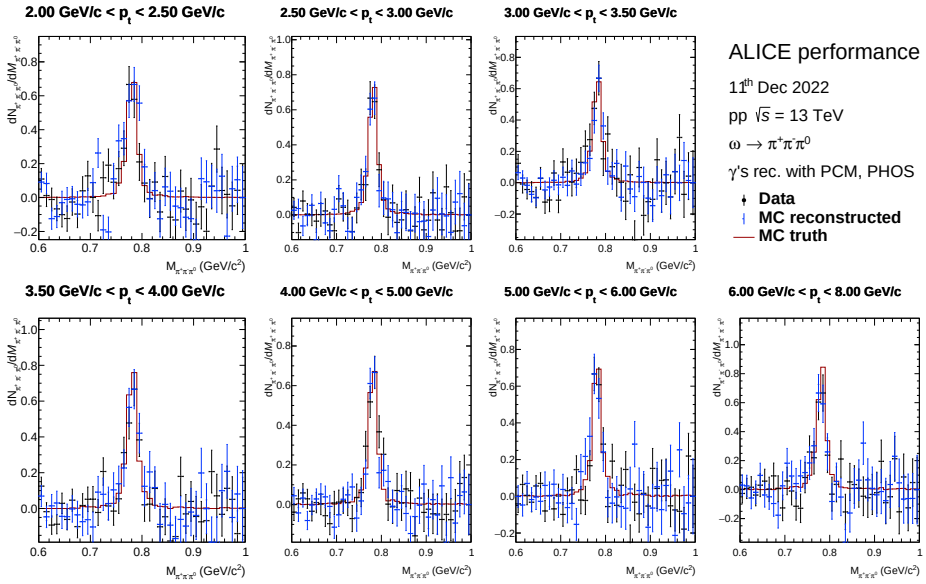

Figure A.63: Comparison of signal shapes in MC of ω meson with data for MB trigger, reconstructed with PCM-PHOS.

A.4.3 Comparison of ω Meson Efficiencies

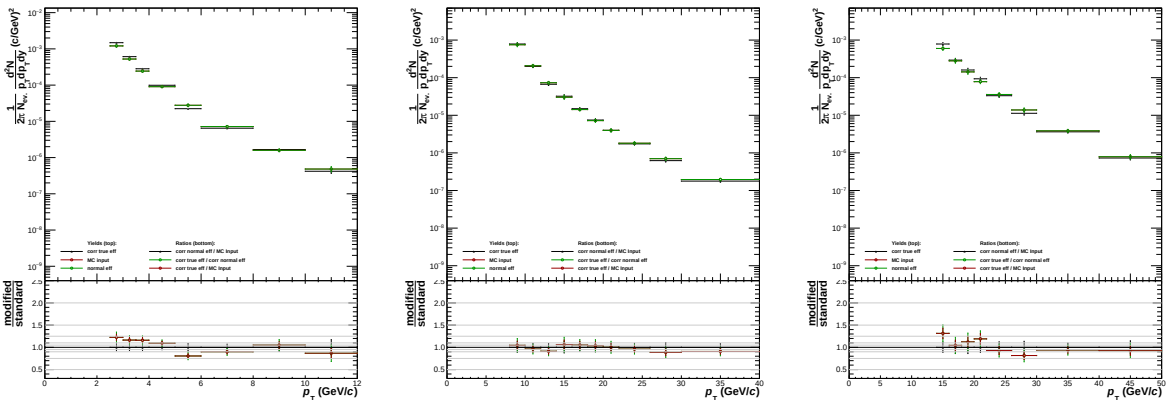

Figure A.64: Comparison of corrected yields corrected with different efficiencies for different triggers EMCal. The green distribution is using the reconstruction efficiency, while the black distribution is using the true efficiency. The red distribution is only shown to ensure, that the reconstruction efficiency calculated properly. It is using the MC input spectrum and has to be the same as the green distribution by construction. From left to right, the used triggers are MB,EG2 and EG1.

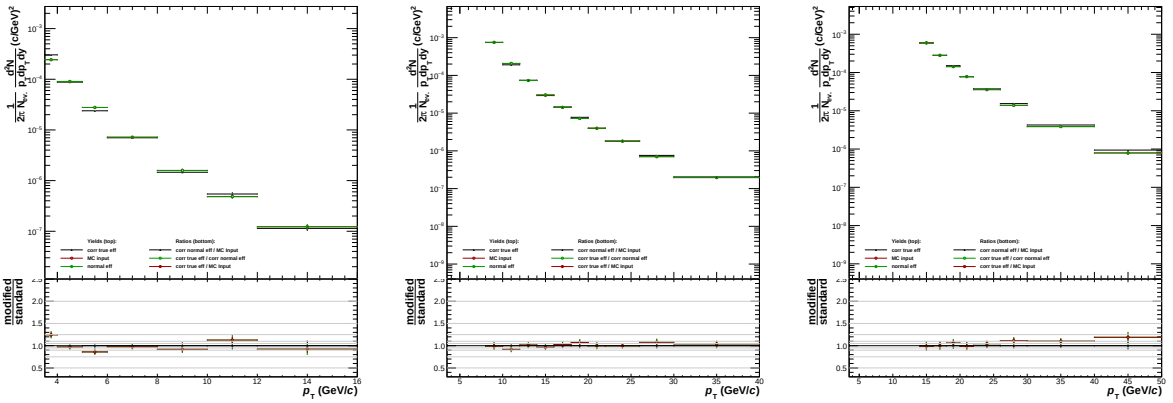

Figure A.65: Comparison of corrected yields corrected with different efficiencies for different triggers PCM-EMCal. The green distribution is using the reconstruction efficiency, while the black distribution is using the true efficiency. The red distribution is only shown to ensure, that the reconstruction efficiency calculated properly. It is using the MC input spectrum and has to be the same as the green distribution by construction. From left to right, the used triggers are MB,EG2 and EG1.

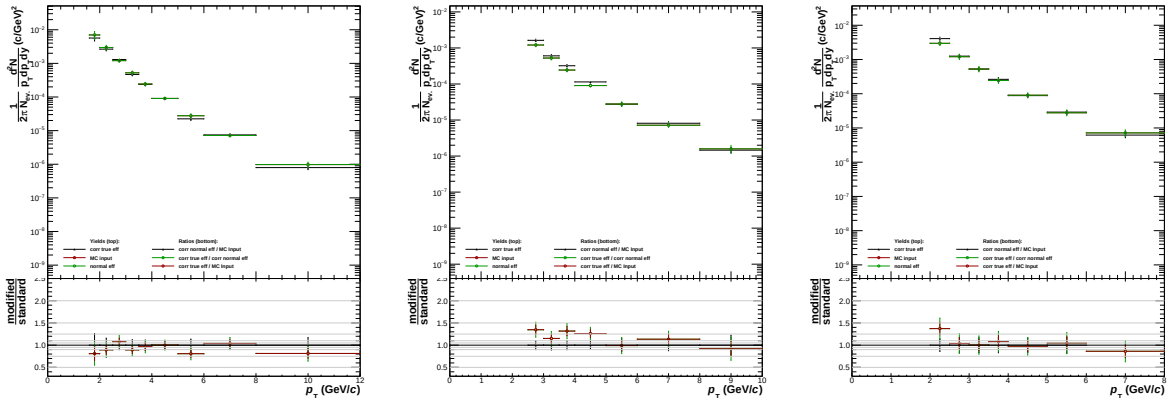

Figure A.66: Comparison of corrected yields corrected with different efficiencies for PCM (left), PHOS (middle) and PCM-PHOS (right). The green distribution is using the reconstruction efficiency, while the black distribution is using the true efficiency. The red distribution is only shown to ensure, that the reconstruction efficiency calculated properly. It is using the MC input spectrum and has to be the same as the green distribution by construction.

A.4.4 Systematic Variation of ω Meson Reconstruction

Cut	Standard	Variation 1	Variation 2	Variation 3	Variation 4
ITS Requirement	First or second SPD cluster required	First or second SPD cluster required, min Number of ITS clusters = 3	-	-	-
Clusters	$N_{\text{cls, TPC}} > 80$, $N_{\text{cr. rows, TPC}} > 70$, $R_{\text{cr. rows find. cls, TPC}} < 0.8$, Refit, $F_{\text{shared cls, TPC}} < 0.4$, $N_{\text{shared cls, TPC}} = 10$, $N_{\text{PID cls, TPC}} > 50$	$N_{\text{cls, TPC}} > 80$, $N_{\text{cr. rows, TPC}} > 70$, $R_{\text{cr. rows find. cls, TPC}} < 0.8$, Refit, $F_{\text{shared cls, TPC}} == 0$	$N_{\text{cls, TPC}} > 80$, $N_{\text{cr. rows, TPC}} > 70$, $R_{\text{cr. rows find. cls, TPC}} < 0.8$, Refit, $N_{\text{shared cls, TPC}} = 10$	$N_{\text{cls, TPC}} > 80$, $N_{\text{cr. rows, TPC}} > 70$, $R_{\text{cr. rows find. cls, TPC}} < 0.8$, Refit	-
min p_{T}	$p_{\text{T}} > 0{,}100$ GeV	$p_{\text{T}} > 0{,}075$ GeV	$p_{\text{T}} > 0{,}125$ GeV	$p_{\text{T}} > 0{,}150$ GeV	-
charged pion PID part 1	$-3 < n\sigma < 3$	$-3.5 < n\sigma < 3$	$-3.25 < n\sigma < 3.0$	$-2.75 < n\sigma < 3$	$-2.5 < n\sigma < 3$
charged pion PID part 2		$-3 < n\sigma < 2.5$	$-3 < n\sigma < 2.75$	$-3 < n\sigma < 3.25$	$-3 < n\sigma < 3.5$
charged pion Mass Cut	$M_{\pi^+\pi^-}$ <850 MeV/c^2	$M_{\pi^+\pi^-}$ <875 MeV/c^2	$M_{\pi^+\pi^-}$ <900 MeV/c^2	$M_{\pi^+\pi^-}$ <1000 MeV/c^2	-

Table A.1: Overview of variations used for systematic uncertainty estimation of the charged pion cuts.

Cut	Standard	Variation 1	Variation 2	Variation 3	Variation 4
Selection Window	-3< σ_{π^0} <3	-2< σ_{π^0} <2	-4< σ_{π^0} <4	-2.5< σ_{π^0} <2.5	-3.5< σ_{π^0} <3.5
α	no cut	$\alpha < 0.75$	$\alpha < 0.8$	$\alpha < 0.85$	-
$p_{T,\text{max}}$ (only EMCAL EG1, EG2)	25 GeV/c	20 GeV/c	no cut	-	-

Table A.2: Overview of variations used for systematic uncertainty estimation of the neutral pion cuts.

Quantity	Standard	Cut variation 1	Cut variation 2	Cut variation 3	Cut variation 4	Cut variation 5
fine tuning scheme	Corrected by PCM-EMCal and EMCal	Corrected by EMCal	Corrected by PCM-EMCal	-	-	-
min E_{clus}	0.7 GeV/c	0.6 GeV/c	0.8 GeV/c	-	-	-
min N_{cells}	≥ 1	≥ 2 Corrected by EMCal	≥ 2 Corrected by PCM-EMCal	-	-	-
t_{clus}	$-20 < t_{\mathrm{clus}} < 25$ ns	$-30 < t_{\mathrm{clus}} < 35$ ns	$-12.5 < t_{\mathrm{clus}} < 13$ ns	$-50 < t_{\mathrm{clus}} < 50$ ns	$-20 < t_{\mathrm{clus}} < 30$ ns	-
min M_{02}	$0.10 < M_{02} < 0.70$	$0.10 < M_{02} < 0.50$	$0.10 < M_{02} < 1.0$	-	-	-
cluster–track-matching						
- $\lvert\Delta\eta\rvert <$	$0.010 + (p_{\mathrm{T}} + 4.07)^{-2.5}$	$0.010 + (p_{\mathrm{T}} + 4.07)^{-2.5}$	$0.010 + (p_{\mathrm{T}} + 4.07)^{-2.5}$	$0.010 + (p_{\mathrm{T}} + 4.07)^{-2.5}$	$0.010 + (p_{\mathrm{T}} + 4.37)^{-2.5}$	$0.010 + (p_{\mathrm{T}} + 3.82)^{-2.5}$
- $\lvert\Delta\phi\rvert <$	$0.015 + (p_{\mathrm{T}} + 3.65)^{-2}$	$0.015 + (p_{\mathrm{T}} + 3.65)^{-2}$	$0.015 + (p_{\mathrm{T}} + 3.65)^{-2}$	$0.015 + (p_{\mathrm{T}} + 3.65)^{-2}$	$0.015 + (p_{\mathrm{T}} + 3.78)^{-2}$	$0.015 + (p_{\mathrm{T}} + 3.54)^{-2}$
- $E/p <$	1.75	2.0	1.50	none	1.75	1.75

Table A.3: Overview of variations used for systematic uncertainty estimation of the cluster reconstruction cuts for EMCal and PCM-EMCal.

Quantity	Standard	Cut variation 1	Cut variation 2	Cut variation 3	Cut variation 4	Cut variation 5
fine tuning scheme	Corrected by PHOS and PCM-PHOS	Corrected by PHOS	Corrected by PCM-PHOS	-	-	-
min E_{clus}	0.3 GeV/c	0.2 GeV/c	0.4 GeV/c	-	-	-
min N_{cells}	≥ 2 for E> 1GeV	≥ 2	≥ 3 for E> 1GeV	≥ 1	-	-
t_{clus}	$-30 < t_{\mathrm{clus}} < 30$ ns with Timing Efficiency from PHI7	$-30 < t_{\mathrm{clus}} < 35$ ns with Timing Efficiency Low p_T from MB	$-25 < t_{\mathrm{clus}} < 25$ ns with Timing Efficiency	-	-	-
min M_{02}	$0.10 < M_{02} < 1000$ for E> 1GeV	$0.20 < M_{02} < 1000$ E> 1GeV	$0.10 < M_{02} < 2.5$ E> 1GeV	-	-	-
cluster–track-matching - $\lvert\Delta\eta\rvert$ - $\lvert\Delta\phi\rvert$	 < 0.002 $-0.08 < \lvert\Delta\phi\rvert < 0.08$	TM Off	 < 0.005 $-0.03 < \lvert\Delta\phi\rvert < 0.03$	 $< 0.005 + (p_{\mathrm{T}} + 2.81)^{-3}$ $< 0.002 + (p_{\mathrm{T}} + 3.52)^{-3}$	 $< 0.005 + (p_{\mathrm{T}} + 1.63)^{-2.3}$ $< 0.005 + (p_{\mathrm{T}} + 5.87)^{-2.5}$	-

Table A.4: Overview of variations used for systematic uncertainty estimation of the cluster reconstruction cuts for PHOS and PCM-PHOS

Cut	Standard	Variation 1	Variation 2	Variation 3	Variation 4	Variation 5
min. track p_{T}	50 MeV	75 MeV	100 MeV	-	-	-
electron PID	$-3 < n\sigma < 4$	$-4 < n\sigma < 5$	$-2.5 < n\sigma < 4$	-	-	-
pion rejection	$n\sigma > 1$	$n\sigma > 0$	$n\sigma > 2$	-	-	-
q_T cut part 1	$q_{\mathrm{T}} < q_{\mathrm{T,max}} \cdot\sqrt{1-\alpha^2/\alpha^2_{\mathrm{max}}}$ with $\alpha_{\mathrm{max}} = 0.95$ and $q_{\mathrm{T,\,max}} = 0.125 \cdot p_{\mathrm{T}}$ (GeV), limited by $q_{\mathrm{T,\,max}}$ = 50.0 MeV	q_T <0.05 Gev/c, α <0.95	q_T <0.05 Gev/c	q_T <0.06 Gev/c α <0.95	q_T <0.03 Gev/c α <0.95	$q_{\mathrm{T}} < q_{\mathrm{T,max}} \cdot\sqrt{1-\alpha^2/\alpha^2_{\mathrm{max}}}$ with $\alpha_{\mathrm{max}} = 0.95$ and $q_{\mathrm{T,\,max}} = 0.125 \cdot p_{\mathrm{T}}$ (GeV), limited by $q_{\mathrm{T,\,max}}$ = 1.0 GeV
q_T cut part 2	-	$q_{\mathrm{T}} < q_{\mathrm{T,max}} \cdot\sqrt{1-\alpha^2/\alpha^2_{\mathrm{max}}}$ with $\alpha_{\mathrm{max}} = 0.95$ and $q_{\mathrm{T,\,max}} = 0.110 \cdot p_{\mathrm{T}}$ (GeV), limited by $q_{\mathrm{T,\,max}}$ = 40.0 MeV	$q_{\mathrm{T}} < q_{\mathrm{T,max}} \cdot\sqrt{1-\alpha^2/\alpha^2_{\mathrm{max}}}$ with $\alpha_{\mathrm{max}} = 0.95$ and $q_{\mathrm{T,\,max}} = 0.140 \cdot p_{\mathrm{T}}$ (GeV), limited by $q_{\mathrm{T,\,max}}$ = 60.0 MeV	$q_{\mathrm{T}} < q_{\mathrm{T,max}} \cdot\sqrt{1-\alpha^2/\alpha^2_{\mathrm{max}}}$ with $\alpha_{\mathrm{max}} = 0.95$ and $q_{\mathrm{T,\,max}} = 0.110 \cdot p_{\mathrm{T}}$ (GeV), limited by $q_{\mathrm{T,\,max}}$ = 40.0 MeV	$q_{\mathrm{T}} < q_{\mathrm{T,max}} \cdot\sqrt{1-\alpha^2/\alpha^2_{\mathrm{max}}}$ with $\alpha_{\mathrm{max}} = 0.95$ and $q_{\mathrm{T,\,max}} = 0.140 \cdot p_{\mathrm{T}}$ (GeV), limited by $q_{\mathrm{T,\,max}}$ = 60.0 MeV	$q_{\mathrm{T}} < q_{\mathrm{T,max}} \cdot\sqrt{1-\alpha^2/\alpha^2_{\mathrm{max}}}$ with $\alpha_{\mathrm{max}} = 0.95$ and $q_{\mathrm{T,\,max}} = 0.160 \cdot p_{\mathrm{T}}$ (GeV), limited by $q_{\mathrm{T,\,max}}$ = 32.0 MeV
ψ_{pair} and χ^2_γ/ndf part 1	$\lvert\psi_{\mathrm{pair}}\rvert < 0.18, \cdot\exp\left(-0.055 \cdot \chi^2_\gamma\right)$, χ^2_γ/ndf< 50	$\lvert\psi_{\mathrm{pair}}\rvert < 0.3$, χ^2_γ/ndf < 1000000	$\lvert\psi_{\mathrm{pair}}\rvert < 0.3$, χ^2_γ/ndf < 50	$\lvert\psi_{\mathrm{pair}}\rvert < 0.3$, χ^2_γ/ndf < 5	$\lvert\psi_{\mathrm{pair}}\rvert < 0.3$, χ^2_γ/ndf < 20	$\lvert\psi_{\mathrm{pair}}\rvert < 0.2$, χ^2_γ/ndf < 45
ψ_{pair} and χ^2_γ/ndf part 2	-	$\lvert\psi_{\mathrm{pair}}\rvert < 0.35$, $\cdot\exp\left(-0.065 \cdot \chi^2_\gamma\right)$,χ^2_γ/ndf < 50	$\lvert\psi_{\mathrm{pair}}\rvert < 0.3$, ,$\chi^2_\gamma$/ndf < 45	$\lvert\psi_{\mathrm{pair}}\rvert < 0.3$, $\cdot\exp\left(-0.065 \cdot \chi^2_\gamma\right)$,χ^2_γ/ndf < 50	$\lvert\psi_{\mathrm{pair}}\rvert < 0.3$, $\cdot\exp\left(-0.055 \cdot \chi^2_\gamma\right)$,χ^2_γ/ndf < 50	$\lvert\psi_{\mathrm{pair}}\rvert < 0.35$, χ^2_γ/ndf < 55
ψ_{pair} and χ^2_γ/ndf part 3	-	$\lvert\psi_{\mathrm{pair}}\rvert < 0.05$, χ^2_γ/ndf < 1000000	$\lvert\psi_{\mathrm{pair}}\rvert < 0.20$, χ^2_γ/ndf < 55	-	-	-

Table A.5: Overview of variations used for systematic uncertainty estimation of the conversion photon cuts.

Cut	Standard	Variation 1	Variation 2	Variation 3	Variation 4
Integration range	3σ	2σ	4σ	3σ	3σ
Fit range	$0.6 - 0{,}99\,\mathrm{GeV}$	$0.6 - 0{,}95\,\mathrm{GeV}$	$0.65 - 0{,}95\,\mathrm{GeV}$	$0.6 - 0{,}99\,\mathrm{GeV}$	$0.6 - 0{,}99\,\mathrm{GeV}$
background description	Gaussian with an additional polynomial of 3rd order and subtracting the polynomial part	Gaussian with an additional polynomial of 3rd order and subtracting the polynomial part	Gaussian with an additional polynomial of 3rd order and subtracting the polynomial part	Gaussian with an additional polynomial of 3rd order and subtracting the polynomial part	Gaussian with an additional polynomial of 4th order and subtracting the polynomial part
Efficiency for Yield Correction	Yield corrected by reconstruction efficiency	Yield corrected by reconstruction efficiency	Yield corrected by reconstruction efficiency	Yield corrected by validated or true efficiency	Yield corrected by reconstruction efficiency

Cut	Variation 5	Variation 6	Variation 6	Variation 7	
Integration range	3σ	3σ	3σ	3σ	
Fit range	$0.6 - 0{,}95\,\mathrm{GeV}$	$0.65 - 0{,}95\,\mathrm{GeV}$	$0.6 - 0{,}99\,\mathrm{GeV}$	$0.6 - 0{,}99\,\mathrm{GeV}$	
background description	Gaussian with an additional polynomial of 3rd order and subtracting the polynomial part	Gaussian with an additional polynomial of 3rd order and subtracting the polynomial part	Gaussian with exponential tails on both sides with an additional polynomial of 3rd order and subtracting the polynomial part	Gaussian with exponential tails on both sides with an additional polynomial of 4th order and subtracting the polynomial part	
Efficiency for Yield Correction	Yield corrected by reconstruction efficiency	Yield corrected by reconstruction efficiency	Yield corrected by reconstruction efficiency	Yield corrected by reconstruction efficiency	

Table A.6: Overview of variations used for systematic uncertainty estimation for signal extraction.

A.5 List of Good Runs

LHC16d anchored to: LHC17f6

PCM:
252375, 252374, 252371, 252370, 252368, 252336, 252332, 252330, 252326, 252325, 252322, 252319, 252317, 252310, 252271, 252248, 252235

LHC16e anchored to: LHC17f9

PCM:
252858, 252867, 253437, 253478, 253481, 253482, 253488, 253517, 253529, 253530, 253563, 253589, 253591
PHOS:
253478, 253481, 253482, 253488, 253517, 253529, 253530, 253589, 253591
PHOS Trigger:
253478, 253481, 253482, 253488, 253517, 253529, 253530, 253589, 253591

LHC16g anchored to: LHC17d17

PCM:
254128, 254147, 254148, 254149, 254174, 254175, 254178, 254193, 254199, 254204, 254205, 254293, 254302, 254303, 254304, 254330, 254331, 254332
EMCal:
254128, 254147, 254148, 254149, 254174, 254199, 254204, 254205, 254293, 254302, 254303, 254304, 254330, 254331, 254332
PCM-EMCal:
254128, 254147, 254148, 254149, 254174, 254199, 254204, 254205, 254293, 254302, 254303, 254304, 254330, 254331, 254332
PHOS:
254332, 254331, 254330, 254304, 254303, 254302, 254293, 254205, 254204, 254199, 254193, 254178, 254175, 254174, 254149, 254147, 254128
PHOS Trigger:
254332, 254331, 254330, 254304, 254303, 254302, 254293, 254205, 254204, 254199, 254193, 254178, 254175, 254174, 254149, 254147, 254128

LHC16h anchored to: LHC17f5

PCM:
255469, 255467, 255466, 255465, 255463, 255447, 255442, 255440, 255421, 255420, 255419, 255418, 255415, 255407, 255402, 255398, 255352, 255351, 255350, 255283, 255280, 255276, 255275, 255256, 255255, 255253, 255252, 255251, 255249, 255248, 255247, 255242, 255240, 255177, 255176, 255174, 255173, 255171, 255167, 255162, 255159, 255154, 255111, 255091, 255086, 255085, 255082, 255079, 254654, 254653, 254652, 254651, 254649, 254648, 254646, 254644, 254640, 254632, 254630, 254629, 254621, 254608, 254606, 254604
EMCal:
254604, 254606, 254608, 254621, 254629, 254630, 254632, 254640, 254644, 254646, 254648, 254649, 254651, 254652, 254653, 254654, 255248, 255249, 255251, 255252, 255253, 255255, 255256, 255275, 255276, 255350, 255351, 255352, 255418, 255419, 255420, 255421, 255440, 255463, 255465, 255466, 255467
PCM-EMCal:
254604, 254606, 254621, 254629, 254630, 254632, 254640, 254644, 254646, 254648, 254649, 254651, 254652, 254653, 254654, 255249, 255251, 255252, 255253, 255255, 255256, 255275, 255276, 255350, 255351, 255352, 255418, 255419, 255420, 255421, 255463, 255465, 255466, 255467
PHOS:
254604, 254606, 254621, 254629, 254630, 254632, 254640, 254644, 254646, 254648, 254649, 254651, 254652, 254653, 254654, 254983, 254984, 255079, 255082, 255085, 255086, 255091, 255111, 255154, 255159, 255162, 255167, 255171, 255173, 255174, 255176, 255177, 255180, 255181, 255182, 255240, 255242, 255247, 255248, 255249, 255251, 255252, 255253, 255255, 255256, 255275, 255276, 255280, 255283, 255350, 255351, 255352, 255398, 255402, 255407, 255415, 255418, 255419, 255420, 255421, 255440, 255442, 255447, 255463, 255465, 255466, 255467
PHOS Trigger:
254604, 254606, 254621, 254629, 254630, 254632, 254640, 254644, 254646, 254648, 254649, 254651, 254652, 254653, 254654, 254983, 254984, 255079, 255082, 255085, 255086, 255091, 255111, 255154, 255159, 255162, 255167, 255171, 255173, 255174, 255176, 255177, 255180, 255181, 255182, 255240, 255242, 255247, 255248, 255249, 255251, 255252, 255253, 255255, 255256, 255275, 255276, 255280, 255283, 255350, 255351, 255352, 255398, 255402, 255407, 255415, 255418, 255419, 255420, 255421, 255440, 255442, 255447, 255463, 255465, 255466, 255467

LHC16i anchored to: LHC17d3

PCM:
255539, 255540, 255541, 255542, 255543, 255577, 255582, 255583, 255591, 255592, 255614, 255615, 255616, 255617, 255618
EMCal Trigger:
255539, 255540, 255541, 255542, 255543, 255577, 255582, 255583, 255591, 255592, 255614, 255615, 255616, 255617, 255618
EMCal:
255539, 255540, 255541, 255542, 255543, 255577, 255582, 255583, 255591, 255592, 255614, 255615, 255616, 255617, 255618
PCM-EMCal:
255539, 255540, 255541, 255542, 255543, 255577, 255582, 255583, 255591, 255592, 255614, 255615, 255616, 255617, 255618
PHOS:
255539, 255540, 255541, 255542, 255543, 255577, 255582, 255583, 255591, 255614, 255615, 255616, 255617, 255618
PHOS Trigger:
255539, 255540, 255541, 255542, 255543, 255577, 255582, 255583, 255591, 255614, 255615, 255616, 255617, 255618

LHC16j anchored to: LHC17e5

PCM:
256204, 256207, 256210, 256212, 256213, 256215, 256219, 256222, 256223, 256225, 256227, 256228, 256231, 256281, 256282, 256283, 256284, 256287, 256289, 256290, 256292, 256295, 256297, 256298, 256299, 256302, 256307, 256309, 256311, 256356, 256357, 256361, 256362, 256363, 256364, 256365, 256366, 256368, 256371, 256372, 256373, 256415, 256417, 256418, 256420
EMCal Trigger:
256207, 256231, 256281, 256282, 256283, 256284, 256289, 256290, 256292, 256295, 256297, 256298, 256299, 256302, 256307, 256309, 256311, 256356, 256357, 256361, 256362, 256364, 256365, 256366, 256371, 256372, 256373, 256415, 256417, 256418, 256420
EMCal:
256207, 256223, 256225, 256231, 256281, 256282, 256283, 256284, 256289, 256290, 256292, 256295, 256297, 256298, 256299, 256302, 256307, 256309, 256311, 256356, 256357, 256361, 256362, 256363, 256364, 256365, 256366, 256371, 256372, 256373, 256415, 256417, 256418, 256420
PCM-EMCal:
256207, 256223, 256225, 256231, 256281, 256282, 256283, 256284, 256289, 256290, 256292, 256295, 256297, 256298, 256299, 256302, 256307, 256309, 256311, 256356, 256357, 256361, 256362, 256364, 256365, 256366, 256371, 256372, 256373, 256415, 256417, 256418, 256420
PHOS:
256219, 256223, 256227, 256228, 256231, 256281, 256282, 256283, 256284, 256287, 256289, 256290, 256292, 256297, 256299, 256302, 256307, 256309, 256311, 256356, 256361, 256362, 256363, 256364, 256365, 256366, 256368, 256371, 256372, 256415, 256417, 256418
PHOS Trigger:
256219, 256223, 256227, 256228, 256231, 256281, 256282, 256283, 256284, 256287, 256289, 256290, 256292, 256297, 256299, 256302, 256307, 256309, 256311, 256356, 256361, 256362, 256363, 256364, 256365, 256366, 256368, 256371, 256372, 256415, 256417, 256418

LHC16k anchored to: LHC18f1

PCM:
258537, 258499, 258477, 258456, 258454, 258452, 258426, 258393, 258391, 258359, 258336, 258332, 258307, 258306, 258303, 258302, 258301, 258299, 258278, 258274, 258273, 258271, 258270, 258258, 258257, 258256, 258204, 258203, 258202, 258198, 258197, 258178, 258117, 258114, 258113, 258109, 258108, 258107, 258063, 258062, 258060, 258059, 258053, 258049, 258048, 258045, 258042, 258041, 258039, 258019, 258017, 258014, 258012, 258008, 258003, 257992, 257989, 257986, 257979, 257963, 257960, 257958, 257957, 257939, 257937, 257936, 257932, 257912, 257901, 257893, 257855, 257853, 257851, 257850, 257804, 257803, 257800, 257799, 257798, 257797, 257773, 257765, 257757, 257754, 257737, 257735, 257734, 257733, 257727, 257725, 257724, 257697, 257694, 257692, 257691, 257689, 257688, 257687, 257685, 257684, 257682, 257644, 257642, 257636, 257635, 257632, 257630, 257606, 257605, 257604, 257595, 257594, 257592, 257590, 257588, 257587, 257566, 257562, 257561, 257560, 257541, 257540, 257539, 257537, 257531, 257530, 257492, 257491, 257490, 257488, 257487, 257474, 257468, 257457, 257433, 257364, 257358, 257330, 257322, 257320, 257318, 257260, 257224, 257209, 257206, 257204, 257145, 257144, 257142, 257141, 257140, 257139, 257138, 257137, 257136, 257100, 257095, 257092, 257086, 257084, 257083, 257082, 257080, 257077, 257071, 257026, 257021, 257012, 256944, 256942, 256941
EMCal Trigger:
258537, 258499, 258498, 258477, 258456, 258454, 258426, 258393, 258388, 258387, 258359, 258336, 258299, 258280, 258278, 258274, 258273, 258271, 258270, 258258, 258257, 258256, 258204, 258203, 258202, 258198, 258197, 258178, 258117, 258114, 258113, 258109, 258108, 258107, 258063, 258062, 258059, 258049, 258048, 258045, 258042, 258019, 258017, 258014, 258012, 257963, 257960, 257958, 257957, 257939, 257937, 257936, 257893, 257855, 257850, 257803, 257800, 257799, 257798, 257797, 257773, 257765, 257754, 257737, 257735, 257734, 257733, 257724, 257697, 257694, 257692, 257691, 257689, 257687, 257682, 257642, 257606, 257605, 257594, 257590, 257587, 257566, 257562, 257561, 257560, 257541, 257540, 257539, 257537, 257531, 257530, 257492, 257491, 257490, 257487, 257474, 257457, 257260, 257224, 257209, 257206, 257204, 257145, 257144, 257142, 257141, 257140, 257139, 257138, 257137, 257136, 257100, 257092, 257084, 257083, 257082, 257080, 257077, 257026, 257021, 257012, 257011, 256944, 256942, 256941, 256697, 256695, 256694, 256691, 256684, 256681, 256677, 256676, 256658, 256620, 256619, 256591, 256589, 256567, 256565, 256564, 256562, 256561, 256560, 256556, 256554, 256552, 256514, 256512, 256510, 256506, 256504
EMCal:
256504, 256506, 256510, 256512, 256552, 256554, 256556, 256560, 256561, 256562, 256564, 256565, 256567, 256589, 256619, 256620, 256658, 256676, 256677, 256681, 256684, 256691, 256694, 256695, 256697, 256941, 256942, 256944, 257012, 257021, 257026, 257071,

257077, 257080, 257082, 257083, 257084, 257092, 257100, 257136, 257137, 257138, 257139, 257140, 257141, 257142, 257144, 257145, 257204, 257206, 257209, 257224, 257260, 257318, 257320, 257322, 257364, 257433, 257457, 257474, 257487, 257490, 257491, 257492, 257530, 257531, 257537, 257539, 257540, 257541, 257560, 257561, 257562, 257566, 257587, 257590, 257594, 257605, 257606, 257630, 257642, 257682, 257684, 257687, 257688, 257689, 257691, 257692, 257694, 257697, 257724, 257725, 257733, 257734, 257735, 257737, 257754, 257765, 257773, 257797, 257798, 257799, 257800, 257803, 257804, 257850, 257853, 257855, 257893, 257936, 257937, 257939, 257957, 257958, 257960, 257963, 257979, 258012, 258014, 258017, 258019, 258039, 258041, 258042, 258045, 258048, 258049, 258059, 258060, 258062, 258063, 258107, 258108, 258109, 258113, 258114, 258117, 258178, 258197, 258198, 258202, 258203, 258204, 258256, 258257, 258258, 258270, 258271, 258273, 258274, 258278, 258299, 258336, 258359, 258393, 258426, 258454, 258456, 258477, 258499, 258537

PCM-EMCal:

258537, 258499, 258477, 258456, 258454, 258426, 258393, 258359, 258336, 258299, 258278, 258274, 258273, 258271, 258270, 258258, 258257, 258256, 258204, 258203, 258202, 258198, 258197, 258178, 258117, 258114, 258113, 258109, 258108, 258107, 258063, 258062, 258059, 258049, 258048, 258045, 258042, 258019, 258017, 258014, 258012, 257963, 257960, 257958, 257957, 257939, 257937, 257936, 257893, 257855, 257850, 257803, 257800, 257799, 257798, 257797, 257773, 257765, 257754, 257737, 257735, 257734, 257733, 257724, 257697, 257694, 257692, 257691, 257689, 257687, 257682, 257642, 257606, 257605, 257594, 257590, 257587, 257566, 257562, 257561, 257560, 257541, 257540, 257539, 257537, 257531, 257530, 257492, 257491, 257490, 257487, 257474, 257457, 257433, 257364, 257322, 257320, 257318, 257260, 257224, 257209, 257206, 257204, 257145, 257144, 257142, 257141, 257140, 257139, 257138, 257137, 257136, 257100, 257092, 257084, 257083, 257082, 257080, 257077, 257026, 257021, 257012, 256944, 256942, 256941, 256697, 256695, 256694, 256691, 256684, 256681, 256677, 256676, 256658, 256620, 256619, 256589, 256567, 256565, 256564, 256562, 256561, 256560, 256556, 256554, 256552, 256512, 256510, 256506, 256504

PHOS:

258537, 258499, 258477, 258456, 258454, 258452, 258393, 258391, 258387, 258359, 258336, 258332, 258307, 258306, 258303, 258302, 258301, 258299, 258278, 258274, 258273, 258271, 258270, 258258, 258257, 258256, 258204, 258203, 258202, 258198, 258197, 258178, 258117, 258114, 258113, 258109, 258108, 258107, 258063, 258062, 258060, 258059, 258053, 258049, 258045, 258041, 258039, 258019, 258008, 258003, 257992, 257989, 257986, 257979, 257963, 257960, 257957, 257939, 257937, 257936, 257855, 257853, 257851, 257850, 257804, 257803, 257800, 257799, 257798, 257797, 257773, 257765, 257757, 257754, 257737, 257735, 257734, 257733, 257727, 257725, 257724, 257697, 257692, 257691, 257689, 257688, 257687, 257685, 257684, 257682, 257644, 257642, 257636, 257635, 257632, 257630, 257606, 257605, 257604, 257601, 257595, 257594, 257592, 257590, 257588, 257587, 257566, 257562, 257561, 257560, 257541, 257540, 257539, 257537, 257531, 257530, 257491, 257490, 257488, 257487, 257433, 257364, 257358, 257260, 257224, 257209, 257206, 257204, 257144, 257141, 257139, 257138, 257137, 257136, 257100, 257095, 257092, 257086, 257084, 257082, 257080, 257077, 257028, 257026, 257021, 257012, 257011, 256944, 256942, 256941

PHOS Trigger:

258537, 258499, 258477, 258456, 258454, 258452, 258393, 258391, 258387, 258359, 258336, 258332, 258307, 258306, 258303, 258302, 258301, 258299, 258278, 258274, 258273, 258271, 258270, 258258, 258257, 258256, 258204, 258203, 258202, 258198, 258197, 258178, 258117, 258114, 258113, 258109, 258108, 258107, 258063, 258062, 258060, 258059, 258053, 258049, 258045, 258041, 258039, 258019, 258008, 258003, 257992, 257989, 257986, 257979, 257963, 257960, 257957, 257939, 257937, 257936, 257892, 257855, 257853, 257851, 257850, 257804, 257803, 257800, 257799, 257798, 257797, 257773, 257765, 257757, 257754, 257737, 257735, 257734, 257733, 257727, 257725, 257724, 257697, 257692, 257691, 257689, 257688, 257687, 257685, 257684, 257682, 257644, 257642, 257636, 257635, 257632, 257630, 257606, 257605, 257604, 257601, 257595, 257594, 257592, 257590, 257588, 257587, 257566, 257562, 257561, 257560, 257541, 257540, 257539, 257537, 257531, 257530, 257491, 257490, 257488, 257487, 257433, 257364, 257358, 257260, 257224, 257209, 257206, 257204, 257144, 257141, 257139, 257138, 257137, 257136, 257100, 257095, 257092, 257086, 257084, 257082, 257080, 257077, 257028, 257026, 257021, 257012, 257011, 256944, 256942, 256941

LHC16l anchored to: LHC18d8

PCM:

259888, 259868, 259867, 259866, 259860, 259842, 259841, 259822, 259789, 259788, 259781, 259756, 259752, 259751, 259750, 259748, 259747, 259477, 259473, 259396, 259395, 259394, 259389, 259388, 259382, 259381, 259378, 259342, 259341, 259340, 259339, 259336, 259334, 259307, 259305, 259303, 259302, 259274, 259273, 259272, 259271, 259270, 259269, 259264, 259263, 259261, 259257, 259204, 259164, 259162, 259118, 259117, 259099, 259096, 259091, 259090, 259088, 259086, 258964, 258962

EMCal:

258962, 258964, 259088, 259090, 259091, 259096, 259099, 259117, 259118, 259164, 259204, 259257, 259263, 259269, 259270, 259271, 259272, 259273, 259274, 259302, 259305, 259307, 259334, 259336, 259339, 259340, 259341, 259342, 259378, 259382, 259388, 259389, 259394, 259395, 259396, 259473, 259477, 259649, 259650, 259668, 259697, 259703, 259704, 259711, 259747, 259748, 259750, 259751, 259752, 259756, 259781, 259788, 259822, 259841, 259842, 259860, 259866, 259867, 259868, 259888

PCM-EMCal:

258962, 258964, 259088, 259090, 259091, 259096, 259099, 259117, 259118, 259164, 259204, 259257, 259263, 259269, 259270, 259271, 259272, 259273, 259274, 259302, 259305, 259307, 259334, 259336, 259339, 259340, 259341, 259342, 259378, 259382, 259388, 259389, 259394, 259395, 259396, 259473, 259477, 259649, 259650, 259668, 259697, 259703, 259704, 259711, 259747, 259748, 259750, 259751, 259752, 259756, 259781, 259788, 259822, 259841, 259842, 259860, 259866, 259867, 259868, 259888

PHOS:

258962, 258964, 259088, 259090, 259091, 259096, 259099, 259117, 259162, 259164, 259204, 259257, 259261, 259263, 259264, 259269, 259270, 259271, 259272, 259273, 259274, 259302, 259303, 259305, 259307, 259334, 259336, 259339, 259340, 259341, 259342, 259378, 259382, 259388, 259389, 259394, 259395, 259396, 259473, 259477, 259747, 259748, 259750, 259751, 259752, 259756, 259788, 259789, 259822, 259841, 259842, 259860, 259866, 259867, 259868, 259888

PHOS Trigger:

258962, 258964, 259088, 259090, 259091, 259096, 259099, 259117, 259162, 259164, 259204, 259257, 259261, 259263, 259264, 259269, 259270, 259271, 259272, 259273, 259274, 259302, 259303, 259305, 259307, 259334, 259336, 259339, 259340, 259341, 259342, 259378,

259382, 259388, 259389, 259394, 259395, 259396, 259473, 259477, 259747, 259748, 259750, 259751, 259752, 259756, 259788, 259789, 259822, 259841, 259842, 259860, 259866, 259867, 259868, 259888

LHC16o anchored to: LHC17d16

PCM:

262450, 262451, 262487, 262489, 262490, 262492, 262528, 262532, 262533, 262537, 262563, 262567, 262568, 262569, 262570, 262571, 262572, 262574, 262578, 262583, 262593, 262594, 262624, 262628, 262632, 262635, 262705, 262706, 262708, 262713, 262717, 262719, 262723, 262725, 262727, 262760, 262768, 262776, 262777, 262778, 262841, 262842, 262844, 262847, 262849, 262853, 262855, 262858, 263332, 263487, 263490, 263496, 263497, 263529, 263647, 263652, 263653, 263654, 263657, 263662, 263663, 263682, 263689, 263690, 263691, 263737, 263738, 263739, 263741, 263743, 263744, 263784, 263785, 263786, 263787, 263790, 263792, 263793, 263803, 263810, 263861, 263863, 263866, 263905, 263916, 263917, 263920, 263977, 263978, 263979, 263981, 263984, 263985, 264033, 264035

EMCal Trigger:

264035, 264033, 263985, 263984, 263981, 263979, 263978, 263977, 263923, 263917, 263916, 263905, 263866, 263863, 263861, 263803, 263793, 263792, 263790, 263786, 263785, 263784, 263744, 263743, 263741, 263739, 263738, 263737, 263691, 263690, 263689, 263682, 263663, 263662, 263657, 263654, 263653, 263652, 262778, 262777, 262776, 262768, 262760, 262727, 262719, 262717, 262713, 262708, 262706, 262705, 262635, 262632, 262628, 262624, 262594, 262593, 262583, 262574, 262572, 262571, 262570, 262569, 262567, 262563, 262533, 262532, 262492, 262451, 262450

EMCal:

262450, 262451, 262492, 262528, 262532, 262533, 262563, 262567, 262569, 262570, 262571, 262572, 262574, 262583, 262593, 262594, 262624, 262628, 262632, 262635, 262705, 262706, 262708, 262713, 262717, 262719, 262723, 262727, 262760, 262768, 262776, 262777, 262778, 262841, 262844, 262849, 262853, 262858, 263332, 263487, 263496, 263529, 263647, 263652, 263653, 263654, 263657, 263662, 263663, 263682, 263689, 263690, 263691, 263737, 263738, 263739, 263741, 263743, 263744, 263784, 263785, 263786, 263787, 263790, 263792, 263793, 263803, 263861, 263863, 263866, 263905, 263916, 263917, 263977, 263978, 263979, 263981, 263984, 263985, 264033, 264035

PCM-EMCal:

264035, 264033, 263985, 263984, 263981, 263979, 263978, 263977, 263917, 263916, 263905, 263866, 263863, 263861, 263803, 263793, 263792, 263790, 263787, 263786, 263785, 263784, 263744, 263743, 263741, 263739, 263738, 263737, 263691, 263690, 263689, 263682, 263663, 263662, 263657, 263654, 263653, 263652, 263496, 263487, 263332, 262858, 262853, 262849, 262844, 262841, 262778, 262777, 262776, 262768, 262760, 262727, 262719, 262717, 262713, 262708, 262706, 262705, 262635, 262632, 262628, 262624, 262594, 262593, 262583, 262574, 262572, 262571, 262570, 262569, 262567, 262563, 262533, 262532, 262492, 262451, 262450

PHOS:

262424, 262425, 262426, 262428, 262705, 262706, 262708, 262713, 262717, 262723, 262725, 262727, 262760, 262768, 262776, 262777, 262778, 262841, 262842, 262844, 262847, 262849, 262853, 262855, 262858, 263331, 263332, 263487, 263490, 263496, 263497, 263529, 263647, 263652, 263654, 263657, 263662, 263663, 263682, 263690, 263691, 263737, 263738, 263739, 263741, 263743, 263744, 263784, 263785, 263786, 263787, 263790, 263792, 263803, 263810, 263863, 263866, 263905, 263916, 263917, 263920, 263923, 263977, 263978, 263981, 263984, 263985, 264033, 264035

PHOS Trigger:

262424, 262425, 262426, 262428, 262705, 262706, 262708, 262713, 262717, 262723, 262725, 262727, 262760, 262768, 262776, 262777, 262778, 262841, 262842, 262844, 262847, 262849, 262853, 262855, 262858, 263331, 263332, 263487, 263490, 263496, 263497, 263529, 263647, 263652, 263654, 263657, 263662, 263663, 263682, 263690, 263691, 263737, 263738, 263739, 263741, 263743, 263744, 263784, 263785, 263786, 263787, 263790, 263792, 263803, 263810, 263863, 263866, 263905, 263916, 263917, 263920, 263923, 263977, 263978, 263981, 263984, 263985, 264033, 264035

LHC16p anchored to: LHC17d18

PCM:

264076, 264078, 264082, 264085, 264086, 264109, 264110, 264129, 264137, 264138, 264139, 264164, 264188, 264190, 264194, 264197, 264198, 264232, 264233, 264235, 264238, 264259, 264260, 264261, 264262, 264264, 264265, 264266, 264267, 264273, 264277, 264279, 264281, 264305, 264306, 264312, 264336, 264341, 264345, 264346, 264347

EMCal Trigger:

264347, 264346, 264345, 264336, 264312, 264306, 264305, 264281, 264279, 264277, 264267, 264266, 264265, 264264, 264262, 264261, 264260, 264259, 264238, 264235, 264233, 264232, 264198, 264197, 264190, 264188, 264168, 264164, 264139, 264138, 264137, 264129, 264110, 264109, 264086, 264085, 264082, 264078, 264076

EMCal:

264347, 264346, 264345, 264336, 264312, 264306, 264305, 264281, 264279, 264277, 264267, 264266, 264265, 264264, 264262, 264261, 264260, 264259, 264238, 264235, 264233, 264232, 264198, 264197, 264190, 264188, 264168, 264164, 264139, 264138, 264137, 264129, 264110, 264109, 264086, 264085, 264082, 264078, 264076

PCM-EMCal:

264347, 264346, 264345, 264336, 264312, 264306, 264305, 264281, 264279, 264277, 264267, 264266, 264265, 264264, 264262, 264261, 264260, 264259, 264238, 264235, 264233, 264232, 264198, 264197, 264190, 264188, 264164, 264139, 264138, 264137, 264129, 264110, 264109, 264086, 264085, 264082, 264078, 264076

PHOS:

264076, 264078, 264082, 264085, 264086, 264109, 264110, 264129, 264137, 264138, 264139, 264164, 264168, 264188, 264190, 264194, 264197, 264198, 264232, 264233, 264235, 264238, 264259, 264260, 264261, 264262, 264264, 264265, 264266, 264267, 264277, 264279, 264281, 264305, 264306, 264312, 264336, 264341, 264345, 264346, 264347

PHOS Trigger:
264078, 264082, 264085, 264086, 264110, 264129, 264137, 264138, 264164, 264168, 264190, 264194, 264197, 264198, 264232, 264233, 264235, 264238, 264259, 264260, 264261, 264262, 264264, 264265, 264266, 264267, 264277, 264279, 264281, 264305, 264306, 264312, 264336, 264341, 264346, 264347

LHC17c anchored to: LHC18d3

PCM:
270581, 270661, 270663, 270665, 270667
EMCal:
270661, 270663, 270665
PCM-EMCal:
270661, 270663, 270665
PHOS:
270581, 270661, 270663, 270665, 270667
PHOS Trigger:
270581, 270661, 270663, 270665, 270667

LHC17e anchored to: LHC17h1

PCM:
270822, 270824, 270827, 270828, 270830
PHOS:
270830, 270828, 270827, 270822
PHOS Trigger:
270822, 270824, 270827, 270828, 270830

LHC17f anchored to: LHC18d3

PCM:
270854, 270855, 270856, 270861, 270865
PHOS:
270854, 270855, 270856, 270861, 270865
PHOS Trigger:
270854, 270855, 270856, 270861, 270865

LHC17h anchored to: LHC18c12

PCM:
273103, 273100, 273099, 273077, 273010, 273009, 272985, 272983, 272976, 272949, 272947, 272939, 272935, 272934, 272933, 272932, 272905, 272903, 272880, 272873, 272871, 272870, 272836, 272834, 272833, 272829, 272828, 272784, 272783, 272782, 272764, 272763, 272760, 272749, 272747, 272712, 272691, 272690, 272620, 272610, 272608, 272607, 272585, 272577, 272575, 272574, 272521, 272468, 272466, 272463, 272462, 272461, 272413, 272411, 272400, 272399, 272395, 272394, 272389, 272388, 272360, 272359, 272340, 272335, 272194, 272156, 272155, 272154, 272153, 272152, 272151, 272123, 272101, 272100, 272076, 272042, 272040, 272039, 272038, 272036, 272020, 272018, 271886, 271880, 271874, 271873, 271871, 271870
EMCal Trigger:
272076, 272100, 272101, 272123, 272151, 272152, 272153, 272154, 272155, 272156, 272194, 272335, 272340, 272359, 272360, 272388, 272389, 272394, 272395, 272399, 272400, 272411, 272413, 272414, 272417, 272461, 272462, 272463, 272466, 272468, 272469, 272521, 272574, 272575, 272585, 272607, 272608, 272610, 272620, 272690, 272691, 272692, 272712, 272746, 272747, 272749, 272760, 272762, 272763, 272764, 272782, 272783, 272828, 272903, 272905, 272932, 272933, 272934, 272947, 272949, 273009, 273077, 273099, 273100
EMCal:
271870, 271871, 271873, 271874, 271880, 271886, 272018, 272020, 272076, 272100, 272101, 272123, 272151, 272152, 272153, 272154, 272155, 272156, 272194, 272335, 272340, 272359, 272360, 272388, 272389, 272394, 272395, 272399, 272400, 272411, 272413, 272461, 272462, 272463, 272466, 272468, 272521, 272574, 272575, 272585, 272607, 272608, 272610, 272620, 272690, 272691, 272712, 272747, 272749, 272760, 272763, 272764, 272782, 272783, 272784, 272828, 272903, 272905, 272932, 272933, 272934, 272935, 272947, 272949, 273009, 273077, 273099, 273100, 272949, 273009, 273077, 273099, 273100
PCM-EMCal:
271868, 271870, 271871, 271873, 271874, 271880, 271881, 271886, 272018, 272020, 272076, 272100, 272101, 272123, 272151, 272152, 272153, 272154, 272155, 272156, 272194, 272335, 272340, 272359, 272360, 272388, 272389, 272394, 272395, 272399, 272400, 272411, 272413, 272414, 272417, 272461, 272462, 272463, 272466, 272468, 272469, 272521, 272574, 272575, 272585, 272607, 272608, 272610, 272620, 272690, 272691, 272692, 272712, 272746, 272747, 272749, 272760, 272762, 272763, 272764, 272782, 272783, 272784, 272828,

272903, 272905, 272932, 272933, 272934, 272947, 272949, 273009, 273077, 273099, 273100

PHOS:

273103, 273100, 273099, 273077, 273010, 273009, 272985, 272983, 272976, 272949, 272947, 272939, 272935, 272934, 272933, 272932, 272905, 272903, 272880, 272873, 272871, 272870, 272836, 272834, 272833, 272829, 272828, 272784, 272783, 272782, 272764, 272763, 272760, 272749, 272747, 272712, 272691, 272690, 272620, 272610, 272608, 272607, 272585, 272577, 272575, 272574, 272521, 272468, 272466, 272463, 272462, 272461, 272413, 272411, 272400, 272399, 272395, 272394, 272389, 272388, 272360, 272359, 272340, 272335, 272194, 272156, 272155, 272154, 272153, 272152, 272151, 272123, 272101, 272100, 272076, 272042, 272040, 272039, 272038, 272036, 272020, 272018, 271886, 271880, 271874, 271873, 271871, 271870

PHOS Trigger:

273103, 273100, 273099, 273077, 273010, 273009, 272985, 272983, 272976, 272949, 272947, 272939, 272935, 272934, 272933, 272932, 272905, 272903, 272880, 272873, 272871, 272870, 272836, 272834, 272833, 272829, 272828, 272784, 272783, 272782, 272764, 272763, 272760, 272749, 272747, 272712, 272691, 272690, 272620, 272610, 272608, 272607, 272585, 272577, 272575, 272574, 272521, 272468, 272466, 272463, 272462, 272461, 272413, 272411, 272400, 272399, 272395, 272394, 272389, 272388, 272360, 272359, 272340, 272335, 272194, 272156, 272155, 272154, 272153, 272152, 272151, 272123, 272101, 272100, 272076, 272042, 272040, 272039, 272038, 272036, 272020, 272018, 271886, 271880, 271874, 271873, 271871, 271870

LHC17i anchored to: LHC17k4

PCM:

273591, 273592, 273593, 273653, 273654, 273687, 273689, 273690, 273695, 273709, 273711, 273719, 273824, 273825, 273885, 273886, 273887, 273889, 273918, 273942, 273943, 273946, 273985, 273986, 274058, 274064, 274092, 274125, 274147, 274148, 274174, 274212, 274232, 274258, 274259, 274263, 274264, 274266, 274268, 274269, 274270, 274271, 274276, 274278, 274280, 274281, 274283, 274329, 274351, 274352, 274360, 274363, 274364, 274385, 274386, 274387, 274388, 274389, 274390, 274442

EMCal Trigger:

273824, 273825, 273885, 273886, 273887, 273889, 273918, 273942, 273943, 273946, 273985, 273986, 274063, 274064, 274092, 274125, 274147, 274148, 274174, 274212, 274232, 274258, 274259, 274263, 274264, 274269, 274270, 274271, 274278, 274280, 274281, 274283, 274329, 274351, 274352, 274355, 274363, 274364, 274442

EMCal:

273591, 273592, 273593, 273653, 273654, 273687, 273689, 273690, 273695, 273709, 273711, 273719, 273824, 273825, 273885, 273886, 273887, 273889, 273918, 273942, 273943, 273946, 273985, 273986, 274063, 274064, 274092, 274125, 274147, 274148, 274174, 274212, 274232, 274258, 274259, 274263, 274264, 274269, 274270, 274271, 274278, 274280, 274281, 274283, 274329, 274351, 274352, 274355, 274363, 274364, 274385, 274386, 274387, 274388, 274389, 274390, 274442

PCM-EMCal:

273591, 273592, 273593, 273653, 273654, 273687, 273689, 273690, 273695, 273709, 273711, 273719, 273824, 273825, 273885, 273886, 273887, 273889, 273918, 273942, 273943, 273946, 273985, 273986, 274064, 274092, 274125, 274147, 274148, 274174, 274212, 274232, 274258, 274259, 274263, 274264, 274269, 274270, 274271, 274278, 274280, 274281, 274283, 274329, 274351, 274352, 274363, 274364, 274385, 274386, 274387, 274388, 274389, 274390, 274442

PHOS:

273824, 273825, 273885, 273886, 273887, 273889, 273918, 273942, 273943, 273946, 273985, 273986, 274058, 274064, 274092, 274094, 274125, 274147, 274148, 274174, 274212, 274232, 274258, 274259, 274263, 274264, 274266, 274268, 274269, 274270, 274271, 274276, 274278, 274280, 274281, 274283, 274329, 274351, 274352, 274360, 274363, 274364, 274385, 274386, 274387, 274388, 274389, 274390, 274442

PHOS Trigger:

273824, 273825, 273885, 273886, 273887, 273889, 273918, 273942, 273943, 273946, 273985, 273986, 274058, 274064, 274092, 274094, 274125, 274147, 274148, 274174, 274212, 274232, 274258, 274259, 274263, 274264, 274266, 274268, 274269, 274270, 274271, 274276, 274278, 274280, 274281, 274283, 274329, 274351, 274352, 274360, 274363, 274364, 274385, 274386, 274387, 274388, 274389, 274390, 274442

LHC17j anchored to: LHC17h11

PCM:

274593, 274594, 274595, 274596, 274601, 274653, 274657, 274667, 274669, 274671

EMCal Trigger:

274593, 274595, 274596, 274601, 274653, 274657, 274667, 274669, 274671

EMCal:

274593, 274595, 274596, 274601, 274653, 274657, 274667, 274669, 274671

PCM-EMCal:

274593, 274595, 274596, 274601, 274653, 274657, 274667, 274669, 274671

PHOS:

274593, 274594, 274595, 274596, 274601, 274653, 274657, 274667, 274669, 274671

PHOS Trigger:

274593, 274594, 274595, 274596, 274601, 274653, 274657, 274667, 274669, 274671

LHC17k anchored to: LHC18c13

PCM:

276508, 276507, 276506, 276462, 276439, 276438, 276437, 276435, 276351, 276348, 276312, 276307, 276302, 276297, 276294, 276292, 276291, 276290, 276259, 276257, 276230, 276205, 276178, 276177, 276170, 276169, 276166, 276145, 276140, 276135, 276104, 276102, 276099, 276098, 276097, 276045, 276041, 276040, 276020, 276019, 276017, 276013, 276012, 275925, 275924, 275847, 275664, 275661, 275657, 275650, 275648, 275647, 275624, 275623, 275622, 275621, 275617, 275612, 275559, 275558, 275515, 275472, 275471, 275467, 275459, 275457, 275456, 275453, 275452, 275448, 275443, 275406, 275404, 275401, 275395, 275394, 275372, 275369, 275361, 275360, 275333, 275332, 275328, 275326, 275324, 275322, 275314, 275283, 275247, 275246, 275245, 275239, 275188, 275184, 275180, 275177, 275174, 275173, 275151, 275150, 275149, 275076, 275075, 275073, 275068, 275067, 274979, 274978, 274886, 274882, 274878, 274877, 274822, 274821, 274817, 274815, 274811, 274807, 274806, 274803, 274802, 274801, 274708

EMCal Trigger:

274708, 274801, 274802, 274806, 274815, 274821, 274822, 274877, 274878, 274882, 275067, 275068, 275073, 275075, 275076, 275149, 275150, 275151, 275173, 275174, 275177, 275239, 275245, 275246, 275247, 275283, 275314, 275324, 275326, 275328, 275332, 275360, 275361, 275369, 275372, 275401, 275406, 275448, 275452, 275453, 275456, 275457, 275471, 275472, 275515, 275558, 275559, 275612, 275621, 275622, 275623, 275624, 275648, 275661, 275664, 276097, 276098, 276102, 276104, 276135, 276140, 276145, 276166, 276169, 276170, 276178, 276205, 276230, 276257, 276259, 276290, 276292, 276294, 276302, 276348, 276351, 276435, 276437, 276438, 276439, 276462, 276506, 276507, 276508

EMCal:

274690, 274708, 274801, 274802, 274806, 274815, 274821, 274822, 274877, 274878, 274882, 275067, 275068, 275073, 275075, 275076, 275149, 275150, 275151, 275173, 275174, 275177, 275239, 275245, 275246, 275247, 275283, 275314, 275324, 275326, 275328, 275332, 275360, 275361, 275369, 275372, 275401, 275406, 275443, 275448, 275452, 275453, 275456, 275457, 275471, 275472, 275515, 275558, 275559, 275612, 275621, 275622, 275623, 275624, 275648, 275661, 275664, 275847, 276097, 276098, 276102, 276104, 276135, 276140, 276145, 276166, 276169, 276170, 276178, 276205, 276230, 276257, 276259, 276290, 276292, 276294, 276302, 276348, 276351, 276435, 276437, 276438, 276439, 276462, 276506, 276507, 276508

PCM-EMCal:

274690, 274708, 274801, 274802, 274806, 274815, 274821, 274822, 274877, 274878, 274882, 275067, 275068, 275073, 275075, 275076, 275149, 275150, 275151, 275173, 275174, 275177, 275239, 275245, 275246, 275247, 275283, 275314, 275324, 275326, 275328, 275332, 275360, 275361, 275369, 275372, 275401, 275406, 275443, 275448, 275452, 275453, 275456, 275457, 275471, 275472, 275515, 275558, 275559, 275612, 275621, 275622, 275623, 275624, 275648, 275661, 275664, 275847, 276097, 276098, 276102, 276104, 276135, 276140, 276145, 276166, 276169, 276170, 276178, 276205, 276230, 276257, 276259, 276290, 276292, 276294, 276302, 276348, 276351, 276435, 276437, 276438, 276439, 276462, 276506, 276507, 276508

PHOS:

274801, 274802, 274803, 274806, 274807, 274811, 274815, 274817, 274821, 274822, 274877, 274878, 274882, 274886, 274978, 274979, 275067, 275068, 275073, 275075, 275076, 275149, 275150, 275151, 275173, 275174, 275177, 275180, 275184, 275188, 275239, 275245, 275246, 275247, 275283, 275314, 275322, 275324, 275326, 275328, 275332, 275333, 275360, 275361, 275369, 275372, 275394, 275395, 275401, 275404, 275406, 275443, 275448, 275452, 275453, 275456, 275457, 275459, 275467, 275471, 275472, 275515, 275558, 275559, 275612, 275617, 275621, 275622, 275623, 275624, 275647, 275648, 275650, 275657, 275661, 275664, 275847, 275924, 275925, 276012, 276013, 276017, 276019, 276020, 276040, 276041, 276045, 276097, 276098, 276099, 276102, 276104, 276135, 276140, 276145, 276166, 276169, 276170, 276177, 276178, 276205, 276230, 276257, 276259, 276290, 276291, 276292, 276294, 276297, 276302, 276307, 276312, 276348, 276351, 276435, 276437, 276438, 276439, 276462, 276506, 276507, 276508

PHOS Trigger:

274801, 274802, 274803, 274806, 274807, 274811, 274815, 274817, 274821, 274822, 274877, 274878, 274882, 274886, 274978, 274979, 275067, 275068, 275073, 275075, 275076, 275149, 275150, 275151, 275173, 275174, 275177, 275180, 275184, 275188, 275239, 275245, 275246, 275247, 275283, 275314, 275322, 275324, 275326, 275328, 275332, 275333, 275360, 275361, 275369, 275372, 275394, 275395, 275401, 275404, 275406, 275443, 275448, 275452, 275453, 275456, 275457, 275459, 275467, 275471, 275472, 275515, 275558, 275559, 275612, 275617, 275621, 275622, 275623, 275624, 275647, 275648, 275650, 275657, 275661, 275664, 275847, 275924, 275925, 276012, 276013, 276017, 276019, 276020, 276040, 276041, 276045, 276097, 276098, 276099, 276102, 276104, 276135, 276140, 276145, 276166, 276169, 276170, 276177, 276178, 276205, 276230, 276257, 276259, 276290, 276291, 276292, 276294, 276297, 276302, 276307, 276312, 276348, 276351, 276435, 276437, 276438, 276439, 276462, 276506, 276507, 276508

LHC17l anchored to: LHC18a8

PCM:

276551, 276552, 276553, 276556, 276557, 276608, 276644, 276670, 276671, 276672, 276674, 276675, 276762, 276916, 276917, 276920, 276967, 276969, 276970, 276971, 276972, 277015, 277016, 277017, 277037, 277073, 277076, 277079, 277082, 277087, 277091, 277117, 277121, 277155, 277180, 277181, 277182, 277183, 277184, 277188, 277189, 277193, 277194, 277196, 277197, 277256, 277257, 277262, 277293, 277310, 277312, 277314, 277360, 277383, 277384, 277385, 277386, 277389, 277416, 277417, 277418, 277472, 277473, 277476, 277477, 277478, 277479, 277530, 277531, 277534, 277536, 277537, 277574, 277575, 277576, 277577, 277721, 277722, 277723, 277725, 277745, 277746, 277747, 277749, 277794, 277795, 277799, 277800, 277801, 277802, 277805, 277834, 277836, 277841, 277842, 277845, 277847, 277848, 277870, 277876, 277897, 277898, 277899, 277900, 277901, 277903, 277904, 277907, 277930, 277952, 277987, 277989, 277991, 277996, 278121, 278122, 278123, 278126, 278127, 278158, 278163, 278164, 278165, 278166, 278167, 278189, 278191, 278215, 278216

EMCal Trigger:

276552, 276553, 276556, 276557, 276608, 276669, 276670, 276671, 276672, 276674, 276675, 276762, 276916, 276917, 276920, 276970, 276971, 276972, 277015, 277016, 277017, 277037, 277073, 277076, 277079, 277087, 277091, 277121, 277155, 277180, 277181, 277182, 277183, 277188, 277189, 277193, 277194, 277196, 277197, 277256, 277257, 277262, 277293, 277310, 277312, 277314, 277360, 277383, 277384, 277385, 277389, 277472, 277473, 277476, 277477, 277478, 277479, 277530, 277536, 277537, 277574, 277575, 277576, 277577,

277721, 277722, 277723, 277725, 277745, 277746, 277747, 277749, 277794, 277799, 277800, 277801, 277802, 277834, 277842, 277845, 277847, 277848, 277876, 277897, 277898, 277899, 277900, 277901, 277903, 277907, 277930, 277952, 277987, 277988, 277989, 277996, 278121, 278122, 278126, 278127, 278158, 278163, 278164, 278165, 278166, 278167, 278189, 278191, 278215

EMCal:

276551, 276552, 276553, 276556, 276557, 276608, 276644, 276670, 276671, 276672, 276674, 276675, 276762, 276916, 276917, 276920, 276967, 276969, 276970, 276971, 276972, 277015, 277016, 277017, 277037, 277073, 277076, 277079, 277087, 277091, 277121, 277155, 277180, 277181, 277182, 277183, 277188, 277189, 277193, 277194, 277196, 277197, 277256, 277257, 277262, 277293, 277310, 277312, 277314, 277360, 277383, 277384, 277385, 277389, 277416, 277417, 277418, 277472, 277473, 277476, 277477, 277478, 277479, 277530, 277531, 277534, 277536, 277537, 277574, 277575, 277576, 277577, 277721, 277722, 277723, 277725, 277745, 277746, 277747, 277749, 277794, 277799, 277800, 277801, 277802, 277834, 277841, 277842, 277845, 277847, 277848, 277876, 277897, 277898, 277899, 277900, 277901, 277903, 277907, 277930, 277952, 277987, 277989, 277996, 278121, 278122, 278126, 278127, 278158, 278163, 278164, 278165, 278166, 278167, 278189, 278191, 278215, 278216

PCM-EMCal:

276552, 276553, 276556, 276557, 276608, 276644, 276669, 276670, 276671, 276672, 276674, 276675, 276762, 276916, 276917, 276920, 276967, 276969, 276970, 276971, 276972, 277015, 277016, 277017, 277037, 277073, 277076, 277079, 277087, 277091, 277121, 277155, 277180, 277181, 277182, 277183, 277188, 277189, 277193, 277194, 277196, 277197, 277256, 277257, 277262, 277293, 277310, 277312, 277314, 277360, 277383, 277384, 277385, 277389, 277416, 277417, 277418, 277470, 277472, 277473, 277476, 277477, 277478, 277479, 277530, 277531, 277534, 277536, 277537, 277574, 277575, 277576, 277577, 277721, 277722, 277723, 277725, 277745, 277746, 277747, 277749, 277794, 277799, 277800, 277801, 277802, 277834, 277841, 277842, 277845, 277847, 277848, 277876, 277897, 277898, 277899, 277900, 277901, 277903, 277907, 277930, 277952, 277987, 277988, 277989, 277996, 278121, 278122, 278126, 278127, 278158, 278163, 278164, 278165, 278166, 278167, 278189, 278191, 278215, 278216

PHOS:

276551, 276552, 276553, 276556, 276557, 276608, 276644, 276670, 276671, 276672, 276674, 276675, 276762, 276916, 276917, 276920, 276967, 276969, 276970, 276971, 276972, 277015, 277016, 277017, 277037, 277073, 277076, 277079, 277082, 277087, 277091, 277117, 277121, 277155, 277180, 277181, 277182, 277183, 277184, 277188, 277189, 277193, 277194, 277196, 277197, 277256, 277257, 277262, 277293, 277310, 277312, 277314, 277360, 277383, 277384, 277385, 277386, 277389, 277416, 277417, 277418, 277472, 277473, 277476, 277477, 277478, 277479, 277530, 277531, 277536, 277537, 277574, 277575, 277576, 277577, 277721, 277722, 277723, 277725, 277745, 277746, 277747, 277749, 277794, 277795, 277799, 277800, 277801, 277802, 277805, 277834, 277836, 277841, 277842, 277845, 277847, 277848, 277870, 277876, 277897, 277898, 277899, 277900, 277901, 277903, 277904, 277907, 277930, 277952, 277987, 277989, 277991, 277996, 278121, 278122, 278123, 278126, 278127, 278158, 278163, 278164, 278165, 278166, 278167, 278189, 278191, 278215, 278216

PHOS Trigger:

276551, 276552, 276553, 276556, 276557, 276608, 276644, 276670, 276671, 276672, 276674, 276675, 276762, 276916, 276917, 276920, 276967, 276969, 276970, 276971, 276972, 277015, 277016, 277017, 277037, 277073, 277076, 277079, 277082, 277087, 277091, 277117, 277121, 277155, 277180, 277181, 277182, 277183, 277184, 277188, 277189, 277193, 277194, 277196, 277197, 277256, 277257, 277262, 277293, 277310, 277312, 277314, 277360, 277383, 277384, 277385, 277386, 277389, 277416, 277417, 277418, 277472, 277473, 277476, 277477, 277478, 277479, 277530, 277531, 277536, 277537, 277574, 277575, 277576, 277577, 277721, 277722, 277723, 277725, 277745, 277746, 277747, 277749, 277794, 277795, 277799, 277800, 277801, 277802, 277805, 277834, 277836, 277841, 277842, 277845, 277847, 277848, 277870, 277876, 277897, 277898, 277899, 277900, 277901, 277903, 277904, 277907, 277930, 277952, 277987, 277989, 277991, 277996, 278121, 278122, 278123, 278126, 278127, 278158, 278163, 278164, 278165, 278166, 278167, 278189, 278191, 278215, 278216

LHC17m anchored to: LHC17l5

PCM:

280140, 280135, 280134, 280131, 280126, 280118, 280114, 280111, 280108, 280107, 280066, 280052, 280051, 279879, 279855, 279854, 279853, 279830, 279827, 279826, 279773, 279749, 279747, 279719, 279718, 279715, 279689, 279688, 279687, 279684, 279683, 279682, 279679, 279677, 279676, 279642, 279641, 279632, 279630, 279559, 279550, 279491, 279488, 279487, 279483, 279441, 279439, 279435, 279410, 279391, 279355, 279354, 279349, 279348, 279344, 279342, 279312, 279310, 279309, 279274, 279273, 279270, 279268, 279267, 279265, 279264, 279242, 279238, 279235, 279234, 279232, 279208, 279207, 279201, 279199, 279157, 279155, 279130, 279123, 279122, 279118, 279117, 279107, 279106, 279075, 279074, 279073, 279069, 279068, 279044, 279043, 279041, 279036, 279035, 279008, 279007, 279005, 279000, 278999, 278964, 278963, 278960, 278959, 278941, 278939, 278936, 278915, 278914

EMCal Trigger:

279005, 279008, 279035, 279036, 279041, 279043, 279044, 279068, 279069, 279073, 279074, 279075, 279106, 279107, 279117, 279118, 279122, 279123, 279130, 279155, 279157, 279199, 279201, 279207, 279208, 279232, 279234, 279235, 279242, 279264, 279265, 279268, 279270, 279273, 279274, 279309, 279310, 279312, 279342, 279344, 279348, 279355, 279391, 279410, 279439, 279441, 279483, 279487, 279491, 279550, 279559, 279632, 279641, 279642, 279676, 279677, 279682, 279687, 279688, 279689, 279718, 279719, 279747, 279749, 279773, 279826, 279853, 279855, 280051, 280052, 280066, 280107, 280108, 280111, 280114, 280126, 280131, 280134, 280140

EMCal:

278915, 278936, 278939, 278941, 278959, 278960, 278963, 278964, 278999, 279000, 279005, 279007, 279008, 279035, 279036, 279041, 279043, 279044, 279068, 279069, 279073, 279074, 279075, 279106, 279107, 279117, 279118, 279122, 279123, 279130, 279155, 279157, 279199, 279201, 279207, 279208, 279232, 279234, 279235, 279242, 279264, 279265, 279268, 279270, 279273, 279274, 279309, 279310, 279312, 279342, 279344, 279348, 279354, 279355, 279391, 279410, 279439, 279441, 279483, 279487, 279488, 279491, 279550, 279559, 279630, 279632, 279641, 279642, 279676, 279677, 279682, 279683, 279687, 279688, 279689, 279718, 279719, 279747, 279749, 279773, 279826, 279830, 279853, 279855, 280051, 280052, 280066, 280107, 280108, 280111, 280114, 280126, 280131, 280134, 280140

PCM-EMCal:

278915, 278936, 278939, 278941, 278959, 278960, 278963, 278964, 278999, 279000, 279005, 279007, 279008, 279035, 279036, 279041, 279043, 279044, 279068, 279069, 279073, 279074, 279075, 279106, 279107, 279117, 279118, 279122, 279123, 279130, 279155, 279157, 279199, 279201, 279207, 279208, 279232, 279234, 279235, 279242, 279264, 279265, 279268, 279270, 279273, 279274, 279309, 279310, 279312, 279342, 279344, 279348, 279354, 279355, 279391, 279410, 279439, 279441, 279483, 279487, 279488, 279491, 279550, 279559,

279630, 279632, 279641, 279642, 279676, 279677, 279682, 279683, 279687, 279688, 279689, 279718, 279719, 279747, 279749, 279773, 279826, 279830, 279853, 279855, 280051, 280052, 280066, 280107, 280108, 280111, 280114, 280126, 280131, 280134, 280140

PHOS:

279234, 279235, 279238, 279242, 279264, 279265, 279267, 279268, 279270, 279273, 279274, 279309, 279310, 279312, 279342, 279344, 279348, 279349, 279354, 279355, 279391, 279410, 279435, 279439, 279441, 279483, 279487, 279488, 279491, 279550, 279559, 279630, 279632, 279641, 279642, 279676, 279677, 279679, 279682, 279683, 279684, 279687, 279688, 279689, 279715, 279718, 279719, 279747, 279749, 279773, 279826, 279827, 279830, 279853, 279854, 279855, 279879, 280051, 280052, 280066, 280107, 280108, 280111, 280114, 280118, 280126, 280131, 280134, 280135, 280140

PHOS Trigger:

279234, 279235, 279238, 279242, 279264, 279265, 279267, 279268, 279270, 279273, 279274, 279309, 279310, 279312, 279342, 279348, 279349, 279354, 279355, 279391, 279410, 279435, 279439, 279441, 279483, 279487, 279488, 279491, 279550, 279559, 279630, 279632, 279641, 279642, 279676, 279679, 279682, 279683, 279684, 279687, 279688, 279689, 279715, 279718, 279719, 279747, 279749, 279773, 279826, 279827, 279830, 279853, 279854, 279855, 279879, 280051, 280052, 280066, 280107, 280108, 280111, 280114, 280118, 280126, 280131, 280134, 280135, 280140

LHC17o anchored to: LHC18a9

PCM:

280282, 280283, 280284, 280285, 280286, 280290, 280310, 280312, 280348, 280349, 280350, 280351, 280374, 280375, 280403, 280405, 280406, 280412, 280413, 280415, 280419, 280443, 280445, 280446, 280447, 280448, 280490, 280499, 280518, 280519, 280546, 280547, 280550, 280551, 280574, 280575, 280576, 280581, 280583, 280613, 280634, 280636, 280637, 280639, 280645, 280647, 280671, 280679, 280681, 280705, 280706, 280729, 280753, 280754, 280755, 280756, 280757, 280761, 280762, 280763, 280764, 280765, 280766, 280767, 280768, 280786, 280787, 280792, 280793, 280842, 280844, 280845, 280847, 280848, 280849, 280854, 280856, 280880, 280881, 280890, 280897, 280936, 280940, 280943, 280947, 280990, 280994, 280996, 280997, 280998, 280999, 281032, 281033, 281035, 281036, 281060, 281061, 281062, 281080, 281081, 281179, 281180, 281181, 281189, 281190, 281191, 281212, 281213, 281240, 281241, 281242, 281243, 281244, 281271, 281273, 281275, 281277, 281301, 281321, 281415, 281441, 281443, 281444, 281446, 281449, 281450, 281475, 281477, 281509, 281511, 281557, 281562, 281563, 281568, 281569, 281574, 281583, 281592, 281633, 281892, 281893, 281894, 281895, 281915, 281916, 281918, 281920, 281928, 281931, 281932, 281939, 281940, 281953, 281956, 281961

EMCal Trigger:

280282, 280283, 280284, 280285, 280286, 280348, 280349, 280350, 280351, 280352, 280374, 280375, 280403, 280412, 280413, 280415, 280419, 280518, 280519, 280546, 280547, 280550, 280551, 280574, 280576, 280581, 280583, 280613, 280634, 280636, 280637, 280647, 280648, 280650, 280671, 280673, 280676, 280679, 280705, 280706, 280729, 280753, 280754, 280755, 280756, 280757, 280761, 280762, 280763, 280764, 280765, 280766, 280767, 280768, 280786, 280787, 280793, 280842, 280844, 280845, 280847, 280848, 280849, 280854, 280856, 280880, 280881, 280897, 280936, 280943, 280947, 280994, 280996, 280997, 280998, 280999, 281032, 281033, 281035, 281036, 281060, 281061, 281062, 281080, 281081, 281179, 281180, 281181, 281189, 281190, 281191, 281212, 281213, 281240, 281241, 281242, 281243, 281244, 281271, 281273, 281275, 281277, 281301, 281321, 281415, 281443, 281444, 281446, 281449, 281450, 281563, 281568, 281569, 281574, 281580, 281705, 281706, 281707, 281713, 281750, 281751, 281753, 281892, 281893, 281894, 281895, 281915, 281916, 281918, 281920, 281928, 281931, 281932, 281939, 281961

EMCal:

280282, 280283, 280284, 280285, 280286, 280348, 280349, 280350, 280351, 280352, 280374, 280375, 280403, 280412, 280413, 280415, 280419, 280499, 280518, 280519, 280546, 280547, 280550, 280551, 280574, 280575, 280576, 280581, 280583, 280613, 280634, 280636, 280637, 280647, 280648, 280650, 280671, 280673, 280676, 280679, 280705, 280706, 280729, 280753, 280754, 280755, 280756, 280757, 280761, 280762, 280763, 280764, 280765, 280766, 280767, 280768, 280786, 280787, 280792, 280793, 280842, 280844, 280845, 280847, 280848, 280849, 280854, 280856, 280880, 280881, 280897, 280936, 280943, 280947, 280994, 280996, 280997, 280998, 280999, 281032, 281033, 281035, 281036, 281060, 281061, 281062, 281080, 281081, 281179, 281180, 281181, 281189, 281190, 281191, 281212, 281213, 281240, 281241, 281242, 281243, 281244, 281271, 281273, 281275, 281277, 281301, 281321, 281415, 281441, 281443, 281444, 281446, 281449, 281450, 281475, 281557, 281563, 281568, 281569, 281574, 281580, 281581, 281583, 281592, 281633, 281705, 281706, 281707, 281713, 281750, 281751, 281753, 281754, 281892, 281893, 281894, 281895, 281915, 281916, 281918, 281920, 281928, 281931, 281932, 281939, 281940, 281961

PCM-EMCal:

280282, 280283, 280284, 280285, 280286, 280348, 280349, 280350, 280351, 280374, 280375, 280403, 280412, 280413, 280415, 280419, 280499, 280518, 280519, 280546, 280547, 280550, 280551, 280574, 280575, 280576, 280581, 280583, 280613, 280634, 280636, 280637, 280647, 280671, 280679, 280705, 280706, 280729, 280753, 280754, 280755, 280756, 280757, 280761, 280762, 280763, 280764, 280765, 280766, 280767, 280768, 280786, 280787, 280792, 280793, 280842, 280844, 280845, 280847, 280848, 280849, 280854, 280856, 280880, 280881, 280897, 280936, 280943, 280947, 280994, 280996, 280997, 280998, 280999, 281032, 281033, 281035, 281036, 281060, 281061, 281062, 281080, 281081, 281179, 281180, 281181, 281189, 281190, 281191, 281212, 281213, 281240, 281241, 281242, 281243, 281244, 281271, 281273, 281275, 281277, 281301, 281321, 281415, 281441, 281443, 281444, 281446, 281449, 281450, 281475, 281557, 281563, 281568, 281569, 281574, 281583, 281592, 281633, 281892, 281893, 281894, 281895, 281915, 281916, 281918, 281920, 281928, 281931, 281932, 281939, 281940, 281961

PHOS:

280282, 280283, 280284, 280285, 280286, 280290, 280310, 280312, 280348, 280349, 280350, 280351, 280374, 280375, 280403, 280405, 280406, 280412, 280413, 280415, 280419, 280443, 280445, 280446, 280447, 280448, 280490, 280499, 280518, 280519, 280546, 280547, 280551, 280574, 280575, 280576, 280581, 280583, 280613, 280634, 280636, 280637, 280639, 280645, 280647, 280671, 280679, 280681, 280705, 280729, 280753, 280755, 280756, 280757, 280761, 280762, 280763, 280764, 280765, 280766, 280767, 280768, 280786, 280787, 280792, 280793, 280842, 280844, 280845, 280847, 280848, 280849, 280854, 280856, 280880, 280881, 280890, 280897, 280936, 280940, 280943, 280947, 280990, 280994, 280996, 280997, 280998, 280999, 281032, 281033, 281035, 281036, 281060, 281061, 281062, 281080, 281081, 281179, 281180, 281181, 281189, 281190, 281191, 281212, 281213, 281240, 281241, 281242, 281243, 281244, 281271, 281273, 281275, 281277, 281301, 281321, 281415, 281441, 281443, 281444, 281446, 281449, 281450, 281475, 281477, 281509, 281557, 281562, 281563, 281568, 281592, 281633, 281892, 281893, 281894, 281895, 281915, 281916, 281918, 281931, 281932, 281939, 281940, 281953,

281956, 281961

PHOS Trigger:

280282, 280283, 280284, 280285, 280286, 280290, 280310, 280312, 280348, 280349, 280350, 280351, 280374, 280375, 280403, 280405, 280406, 280412, 280413, 280415, 280419, 280443, 280445, 280446, 280447, 280448, 280490, 280499, 280518, 280519, 280546, 280547, 280551, 280574, 280575, 280576, 280581, 280583, 280613, 280634, 280636, 280637, 280639, 280645, 280647, 280671, 280679, 280681, 280705, 280729, 280753, 280755, 280756, 280757, 280761, 280762, 280763, 280765, 280766, 280767, 280768, 280786, 280787, 280792, 280793, 280842, 280844, 280845, 280847, 280848, 280849, 280854, 280856, 280880, 280881, 280890, 280897, 280936, 280940, 280943, 280947, 280990, 280994, 280996, 280997, 280998, 280999, 281032, 281033, 281035, 281036, 281060, 281061, 281062, 281080, 281081, 281179, 281180, 281181, 281189, 281190, 281191, 281212, 281213, 281240, 281241, 281242, 281243, 281244, 281271, 281273, 281275, 281277, 281301, 281321, 281415, 281441, 281443, 281444, 281446, 281449, 281450, 281475, 281477, 281509, 281557, 281562, 281563, 281568, 281592, 281633, 281892, 281893, 281894, 281895, 281915, 281916, 281918, 281931, 281932, 281939, 281940, 281953, 281956, 281961

LHC17r anchored to: LHC18a1

PCM:

282528, 282544, 282545, 282546, 282573, 282575, 282579, 282580, 282606, 282607, 282608, 282609, 282618, 282620, 282622, 282629, 282651, 282653, 282666, 282667, 282668, 282670, 282671, 282673, 282676, 282677, 282700, 282702, 282703, 282704

EMCal Trigger:

282544, 282545, 282546, 282579, 282580, 282606, 282607, 282608, 282609, 282620, 282622, 282651, 282666, 282667, 282670, 282671, 282673, 282676, 282677, 282700, 282702, 282703, 282704

EMCal:

282544, 282545, 282546, 282573, 282579, 282580, 282606, 282607, 282608, 282609, 282618, 282620, 282622, 282629, 282651, 282666, 282667, 282670, 282671, 282673, 282676, 282677, 282700, 282702, 282703, 282704

PCM-EMCal:

282544, 282545, 282546, 282573, 282579, 282580, 282606, 282607, 282608, 282609, 282618, 282620, 282622, 282629, 282651, 282666, 282667, 282670, 282671, 282673, 282676, 282677, 282700, 282702, 282703, 282704

PHOS:

282528, 282544, 282545, 282546, 282573, 282575, 282579, 282580, 282606, 282607, 282608, 282609, 282618, 282620, 282629, 282651, 282653, 282666, 282667, 282668, 282670, 282671, 282676, 282677, 282700, 282702, 282703, 282704

PHOS Trigger:

282528, 282544, 282545, 282546, 282573, 282575, 282579, 282580, 282606, 282607, 282608, 282609, 282618, 282620, 282629, 282651, 282653, 282666, 282667, 282668, 282670, 282671, 282676, 282677, 282700, 282702, 282703, 282704

LHC18b anchored to: LHC18g4

PCM:

285396, 285365, 285364, 285347, 285328, 285327, 285224, 285222, 285203, 285202, 285200, 285165, 285127, 285125, 285108, 285106, 285066, 285065, 285064, 285015, 285014, 285013, 285012, 285011, 285009

EMCal Trigger:

285009, 285011, 285012, 285013, 285014, 285015, 285106, 285108, 285125, 285127, 285165, 285200, 285202, 285203, 285222, 285224, 285327, 285328, 285347, 285364, 285365, 285396

EMCal:

285009, 285011, 285012, 285013, 285014, 285015, 285106, 285108, 285125, 285127, 285165, 285200, 285202, 285203, 285222, 285224, 285327, 285328, 285347, 285364, 285365, 285396

PCM-EMCal:

285009, 285011, 285012, 285013, 285014, 285015, 285106, 285108, 285125, 285127, 285165, 285200, 285202, 285203, 285222, 285224, 285327, 285328, 285347, 285364, 285365, 285396

PHOS:

285396, 285365, 285364, 285347, 285328, 285327, 285222, 285203, 285202, 285200, 285165, 285127, 285125, 285108, 285106, 285066, 285065, 285064, 285015, 285014, 285013, 285012, 285011, 285009

PHOS Trigger:

285396, 285365, 285364, 285347, 285328, 285327, 285222, 285203, 285202, 285200, 285165, 285127, 285125, 285108, 285106, 285066, 285065, 285064, 285015, 285014, 285013, 285012, 285011, 285009

LHC18d anchored to: LHC18g5

PCM:

286350, 286349, 286348, 286345, 286341, 286340, 286337, 286336, 286314, 286313, 286312, 286311, 286310, 286309, 286308, 286289, 286288, 286287, 286284, 286282, 286263, 286261, 286258, 286257, 286255, 286254, 286231, 286230, 286229, 286203, 286202, 286201, 286199, 286198, 286159, 286130, 286129, 286127, 286124, 286064, 286025, 286014, 285980, 285979, 285978

EMCal Trigger:

286014, 286025, 286064, 286124, 286127, 286129, 286130, 286159, 286198, 286201, 286202, 286203, 286229, 286230, 286231, 286254, 286255, 286257, 286258, 286261, 286263, 286282, 286284, 286287, 286288, 286289, 286308, 286309, 286310, 286311, 286313, 286314, 286336, 286337, 286340, 286341, 286345, 286348, 286349, 286350

EMCal:
286014, 286025, 286064, 286124, 286127, 286129, 286130, 286159, 286198, 286201, 286202, 286203, 286229, 286230, 286231, 286254, 286255, 286257, 286258, 286261, 286263, 286282, 286284, 286287, 286288, 286289, 286308, 286309, 286310, 286311, 286313, 286314, 286336, 286337, 286340, 286341, 286345, 286348, 286349, 286350
PCM-EMCal:
286014, 286025, 286064, 286124, 286127, 286129, 286130, 286159, 286198, 286201, 286202, 286203, 286229, 286230, 286231, 286254, 286255, 286257, 286258, 286261, 286263, 286282, 286284, 286287, 286288, 286289, 286308, 286309, 286310, 286311, 286313, 286314, 286336, 286337, 286340, 286341, 286345, 286348, 286349, 286350
PHOS:
285978, 285979, 285980, 286014, 286025, 286027, 286028, 286030, 286064, 286124, 286127, 286129, 286130, 286159, 286198, 286199, 286201, 286202, 286203, 286229, 286230, 286231, 286254, 286255, 286257, 286258, 286261, 286263, 286282, 286284, 286287, 286288, 286289, 286308, 286309, 286310, 286311, 286312, 286313, 286314, 286336, 286337, 286340, 286341, 286345, 286348, 286349, 286350
PHOS Trigger:
286350, 286349, 286348, 286345, 286341, 286340, 286337, 286336, 286314, 286313, 286312, 286311, 286310, 286309, 286308, 286289, 286288, 286287, 286284, 286282, 286263, 286261, 286258, 286257, 286255, 286254, 286231, 286230, 286229, 286203, 286202, 286201, 286199, 286198, 286159, 286130, 286129, 286127, 286124, 286064, 286025, 286014, 285980, 285979, 285978

LHC18e anchored to: LHC18g6

PCM:
286937, 286936, 286933, 286932, 286931, 286930, 286911, 286910, 286908, 286907, 286877, 286876, 286874, 286852, 286850, 286848, 286846, 286810, 286809, 286805, 286801, 286799, 286731, 286695, 286661, 286653, 286633, 286594, 286592, 286591, 286569, 286568, 286567, 286566, 286511, 286509, 286508, 286502, 286501, 286482, 286455, 286454, 286428, 286427, 286426, 286380
EMCal Trigger:
286380, 286426, 286428, 286454, 286455, 286482, 286501, 286502, 286508, 286509, 286511, 286566, 286567, 286568, 286569, 286591, 286592, 286653, 286661, 286695, 286731, 286799, 286801, 286846, 286848, 286850, 286852, 286874, 286876, 286907, 286908, 286910, 286911, 286930, 286931, 286932, 286936, 286937
EMCal:
286380, 286426, 286428, 286454, 286455, 286482, 286501, 286502, 286508, 286509, 286511, 286566, 286567, 286568, 286569, 286591, 286592, 286653, 286661, 286695, 286731, 286799, 286801, 286846, 286848, 286850, 286852, 286874, 286876, 286907, 286908, 286910, 286911, 286930, 286931, 286932, 286936, 286937
PCM-EMCal:
286380, 286426, 286428, 286454, 286455, 286482, 286501, 286502, 286508, 286509, 286511, 286566, 286567, 286568, 286569, 286591, 286592, 286653, 286661, 286695, 286731, 286799, 286801, 286846, 286848, 286850, 286852, 286874, 286876, 286907, 286908, 286910, 286911, 286930, 286931, 286932, 286936, 286937
PHOS:
286380, 286426, 286427, 286428, 286454, 286455, 286482, 286501, 286502, 286508, 286509, 286511, 286566, 286567, 286592, 286907, 286908, 286910, 286911, 286930, 286931, 286932, 286933, 286936, 286937
PHOS Trigger:
286937, 286936, 286933, 286932, 286931, 286930, 286911, 286910, 286908, 286907, 286567, 286566, 286511, 286509, 286508, 286502, 286501, 286482, 286455, 286454, 286428, 286427, 286426, 286380

LHC18f anchored to: LHC18h2

PCM:
287658, 287657, 287656, 287654, 287578, 287576, 287575, 287573, 287524, 287521, 287520, 287518, 287517, 287516, 287513, 287486, 287484, 287481, 287480, 287451, 287413, 287389, 287388, 287387, 287385, 287381, 287380, 287360, 287356, 287355, 287353, 287349, 287347, 287346, 287344, 287343, 287325, 287324, 287323, 287283, 287254, 287251, 287250, 287249, 287248, 287209, 287208, 287204, 287203, 287202, 287201, 287185, 287155, 287137, 287077, 287072, 287071, 287066, 287064, 287063, 287021, 287000
EMCal Trigger:
287000, 287021, 287063, 287064, 287071, 287077, 287137, 287155, 287185, 287201, 287209, 287248, 287249, 287250, 287254, 287283, 287323, 287324, 287325, 287343, 287346, 287347, 287349, 287353, 287355, 287356, 287360, 287380, 287381, 287385, 287387, 287388, 287389, 287413, 287480, 287481, 287484, 287486, 287513, 287516, 287517, 287520, 287521, 287573, 287575, 287576, 287578, 287657, 287783, 287876, 287877, 287883, 287884, 287885, 287911, 287912, 287913, 287915, 287923, 287941, 287975, 287977
EMCal:
287000, 287021, 287063, 287064, 287071, 287077, 287137, 287155, 287185, 287201, 287209, 287248, 287249, 287250, 287254, 287283, 287323, 287324, 287325, 287343, 287346, 287347, 287349, 287353, 287355, 287356, 287360, 287380, 287381, 287385, 287387, 287388, 287389, 287413, 287480, 287481, 287484, 287486, 287513, 287516, 287517, 287520, 287521, 287573, 287575, 287576, 287578, 287657, 287783, 287876, 287877, 287883, 287884, 287885, 287911, 287912, 287913, 287915, 287923, 287941, 287975, 287977
PCM-EMCal:
287000, 287021, 287063, 287064, 287071, 287077, 287137, 287155, 287185, 287201, 287209, 287248, 287249, 287250, 287254, 287283, 287323, 287324, 287325, 287343, 287346, 287347, 287349, 287353, 287355, 287356, 287360, 287380, 287381, 287385, 287387, 287388, 287389, 287413, 287480, 287481, 287484, 287486, 287513, 287516, 287517, 287520, 287521, 287573, 287575, 287576, 287578, 287657, 287783, 287876, 287877, 287883, 287884, 287885, 287911, 287912, 287913, 287915, 287923, 287941, 287975, 287977
PHOS:
287000, 287021, 287063, 287064, 287066, 287071, 287072, 287077, 287137, 287155, 287185, 287201, 287202, 287203, 287204, 287208,

287209, 287248, 287249, 287250, 287251, 287254, 287283, 287323, 287324, 287325, 287343, 287344, 287346, 287347, 287349, 287355, 287356, 287360, 287380, 287387, 287388, 287389, 287413, 287451, 287480, 287481, 287486, 287513, 287516, 287517, 287518, 287520, 287521, 287524, 287573, 287575, 287576, 287578, 287616, 287654, 287656, 287657, 287658, 287783, 287784, 287876, 287877, 287883, 287884, 287885, 287911, 287912, 287913, 287915, 287923, 287941, 287975, 287977

PHOS Trigger:

287658, 287657, 287656, 287654, 287578, 287576, 287575, 287573, 287524, 287521, 287520, 287518, 287517, 287516, 287513, 287486, 287481, 287480, 287451, 287413, 287389, 287388, 287387, 287380, 287360, 287356, 287355, 287349, 287347, 287346, 287344, 287343, 287325, 287324, 287323, 287283, 287254, 287251, 287250, 287249, 287248, 287209, 287208, 287204, 287203, 287202, 287201, 287185, 287155, 287137, 287077, 287072, 287071, 287066, 287064, 287063, 287021, 287000

LHC18g anchored to: LHC18h4

PCM:

288619, 288640, 288642, 288644, 288650, 288687, 288689, 288690, 288743, 288748, 288750

EMCal Trigger:

288619

EMCal:

288619

PCM-EMCal:

288619, 288650

PHOS:

288619, 288640, 288642, 288644, 288650, 288687, 288689, 288690, 288743, 288748, 288750

PHOS Trigger:

288640, 288642, 288644, 288650, 288687, 288689, 288690, 288743, 288748, 288750

LHC18h anchored to: LHC18h4

PCM:

288804, 288806

EMCal Trigger:

288804, 288806

EMCal:

288804, 288806

PCM-EMCal:

288804, 288806

PHOS:

288804, 288806

PHOS Trigger:

288804, 288806

LHC18i anchored to: LHC18h4

PCM:

288861, 288862, 288863, 288864, 288868, 288902, 288903, 288908, 288909

EMCal Trigger:

288861, 288862, 288864, 288868, 288897, 288903, 288908, 288909

EMCal:

288861, 288862, 288864, 288868, 288897, 288903, 288908, 288909

PCM-EMCal:

288861, 288862, 288864, 288868, 288897, 288903, 288908, 288909

PHOS:

288861, 288862, 288863, 288864, 288868, 288897, 288902, 288903, 288908, 288909

PHOS Trigger:

288861, 288862, 288863, 288864, 288868, 288902, 288903, 288908, 288909

LHC18j anchored to: LHC18h4

PCM:

288943

EMCal Trigger:

288943

EMCal:
288943
PCM-EMCal:
288943
PHOS:
288943
PHOS Trigger:
288943

LHC18k anchored to: LHC18h4

PCM:
289165, 289166, 289167, 289169, 289172, 289175, 289176, 289177, 289198, 289199, 289200, 289201
EMCal Trigger:
289165, 289166, 289169, 289172, 289176, 289177, 289198, 289199, 289200, 289201
EMCal:
289165, 289166, 289169, 289172, 289176, 289177, 289198, 289199, 289200, 289201
PCM-EMCal:
289165, 289166, 289169, 289172, 289176, 289177, 289198, 289199, 289200, 289201
PHOS:
289165, 289166, 289167, 289169, 289172, 289175, 289176, 289177, 289198, 289199, 289200, 289201
PHOS Trigger:
289165, 289166, 289167, 289169, 289172, 289176, 289177, 289198, 289199, 289200, 289201

LHC18l anchored to: LHC18j1

PCM:
289971, 289966, 289965, 289943, 289941, 289940, 289935, 289931, 289928, 289884, 289880, 289879, 289857, 289856, 289855, 289854, 289852, 289849, 289830, 289818, 289817, 289816, 289815, 289814, 289811, 289808, 289775, 289757, 289732, 289731, 289729, 289724, 289723, 289721, 289547, 289521, 289494, 289493, 289468, 289466, 289465, 289463, 289462, 289444, 289426, 289374, 289373, 289370, 289369, 289368, 289367, 289366, 289365, 289356, 289355, 289354, 289353, 289309, 289308, 289306, 289303, 289300, 289281, 289280, 289278, 289277, 289276, 289275, 289254, 289253, 289249, 289247, 289243, 289242, 289241, 289240
EMCal Trigger:
289240, 289242, 289243, 289253, 289275, 289276, 289277, 289278, 289280, 289281, 289300, 289303, 289306, 289308, 289309, 289354, 289355, 289356, 289365, 289366, 289367, 289368, 289369, 289370, 289373, 289374, 289426, 289444, 289462, 289463, 289465, 289468, 289493, 289494, 289521, 289547, 289721, 289729, 289731, 289732, 289757, 289775, 289808, 289811, 289815, 289816, 289817, 289818, 289830, 289849, 289854, 289855, 289856, 289857, 289879, 289880, 289884, 289928, 289935, 289940, 289943, 289965, 289966, 289971
EMCal:
289240, 289242, 289243, 289253, 289275, 289276, 289277, 289278, 289280, 289281, 289300, 289303, 289306, 289308, 289309, 289354, 289355, 289356, 289365, 289366, 289367, 289368, 289369, 289370, 289373, 289374, 289426, 289444, 289462, 289463, 289465, 289468, 289493, 289494, 289521, 289547, 289721, 289729, 289731, 289732, 289757, 289775, 289808, 289811, 289815, 289816, 289817, 289818, 289830, 289849, 289854, 289855, 289856, 289857, 289879, 289880, 289884, 289928, 289935, 289940, 289943, 289965, 289966, 289971
PHOS:
289971, 289966, 289965, 289943, 289941, 289940, 289928, 289884, 289880, 289879, 289857, 289856, 289855, 289854, 289852, 289849, 289830, 289818, 289817, 289816, 289815, 289814, 289811, 289808, 289775, 289757, 289732, 289731, 289729, 289724, 289723, 289721, 289666, 289664, 289660, 289659, 289658, 289657, 289625, 289582, 289577, 289576, 289574, 289547, 289521, 289494, 289493, 289468, 289466, 289465, 289463, 289462, 289444, 289426, 289374, 289373, 289370, 289369, 289368, 289367, 289366, 289365, 289356, 289355, 289354, 289353, 289309, 289308, 289306, 289303, 289300, 289281, 289280, 289278, 289277, 289276, 289275, 289254, 289253, 289249, 289247, 289243, 289242, 289241, 289240
PHOS Trigger:
289971, 289966, 289965, 289943, 289941, 289940, 289928, 289884, 289880, 289879, 289857, 289856, 289855, 289854, 289852, 289849, 289830, 289818, 289817, 289816, 289815, 289814, 289811, 289808, 289775, 289757, 289732, 289731, 289729, 289724, 289723, 289721, 289547, 289521, 289494, 289493, 289468, 289466, 289465, 289463, 289462, 289444, 289426, 289374, 289373, 289370, 289369, 289368, 289367, 289366, 289365, 289356, 289355, 289354, 289353, 289309, 289308, 289306, 289303, 289300, 289281, 289280, 289278, 289277, 289276, 289275, 289254, 289253, 289249, 289247, 289243, 289242, 289241, 289240

LHC18m anchored to: LHC18j4

PCM:
292839, 292836, 292834, 292832, 292831, 292811, 292810, 292809, 292804, 292803, 292758, 292754, 292752, 292750, 292748, 292747, 292744, 292739, 292737, 292704, 292701, 292698, 292696, 292695, 292693, 292586, 292584, 292563, 292560, 292559, 292557, 292554, 292553, 292526, 292524, 292523, 292521, 292500, 292497, 292496, 292495, 292461, 292460, 292457, 292456, 292434, 292432, 292430, 292429, 292428, 292406, 292405, 292398, 292397, 292298, 292274, 292273, 292270, 292269, 292265, 292242, 292241, 292240, 292218, 292192, 292168, 292167, 292166, 292164, 292163, 292162, 292161, 292160, 292140, 292115, 292114, 292109, 292108, 292107, 292106,

292081, 292080, 292077, 292075, 292067, 292062, 292061, 292060, 292040, 292012, 291982, 291977, 291976, 291953, 291948, 291946, 291945, 291944, 291943, 291942, 291803, 291796, 291795, 291769, 291768, 291766, 291762, 291760, 291756, 291755, 291729, 291706, 291702, 291698, 291697, 291694, 291692, 291690, 291665, 291661, 291657, 291626, 291624, 291622, 291618, 291615, 291614, 291590, 291485, 291484, 291482, 291481, 291457, 291456, 291453, 291451, 291447, 291446, 291424, 291420, 291419, 291417, 291416, 291402, 291400, 291399, 291397, 291377, 291375, 291363, 291362, 291361, 291360, 291286, 291285, 291284, 291283, 291282, 291266, 291265, 291263, 291262, 291257, 291240, 291209, 291188, 291143, 291116, 291111, 291110, 291101, 291100, 291093, 291069, 291066, 291065, 291041, 291037, 291035, 291006, 291005, 291004, 291003, 291002, 290980, 290979, 290976, 290975, 290974, 290948, 290944, 290943, 290941, 290935, 290932, 290895, 290894, 290892, 290888, 290887, 290886, 290862, 290860, 290853, 290848, 290846, 290843, 290841, 290790, 290787, 290776, 290774, 290769, 290766, 290764, 290721, 290699, 290696, 290692, 290689, 290687, 290665, 290660, 290658, 290645, 290632, 290627, 290615, 290614, 290613, 290612, 290590, 290588, 290553, 290550, 290549, 290544, 290540, 290539, 290538, 290501, 290500, 290499, 290469, 290467, 290459, 290458, 290456, 290428, 290427, 290426, 290425, 290423, 290412, 290411, 290404, 290401, 290399, 290376, 290375, 290374, 290350, 290327, 290324, 290323

EMCal Trigger:

290323, 290324, 290327, 290350, 290374, 290375, 290399, 290401, 290411, 290412, 290425, 290426, 290427, 290428, 290456, 290458, 290459, 290469, 290499, 290500, 290538, 290539, 290540, 290544, 290549, 290550, 290553, 290588, 290590, 290612, 290613, 290614, 290615, 290627, 290632, 290645, 290658, 290660, 290665, 290941, 290943, 290944, 290948, 290974, 290975, 290976, 290979, 290980, 291002, 291003, 291004, 291005, 291035, 291037, 291041, 291065, 291066, 291069, 291093, 291100, 291110, 291111, 291116, 291143, 291188, 291209, 291240, 291257, 291262, 291263, 291265, 291266, 291282, 291283, 291284, 291285, 291286, 291360, 291361, 291362, 291373, 291375, 291377, 291397, 291399, 291402, 291417, 291419, 291420, 291424, 291446, 291447, 291453, 291456, 291457, 291481, 291482, 291484, 291485, 292242, 292397, 292398, 292405, 292406, 292428, 292429, 292430, 292432, 292434, 292456, 292457, 292460, 292461, 292495, 292496, 292497, 292500, 292521, 292523, 292524, 292526, 292553, 292554, 292557, 292559, 292560, 292563, 292584, 292586, 292693, 292695, 292696, 292698, 292701, 292704, 292737, 292739, 292747, 292748, 292750, 292809, 292810, 292811, 292831, 292832, 292836

EMCal:

290323, 290324, 290327, 290350, 290374, 290375, 290376, 290399, 290401, 290411, 290412, 290425, 290426, 290427, 290428, 290456, 290458, 290459, 290469, 290499, 290500, 290538, 290539, 290540, 290544, 290549, 290550, 290553, 290588, 290590, 290612, 290613, 290614, 290615, 290627, 290632, 290645, 290658, 290660, 290665, 290687, 290689, 290692, 290696, 290699, 290721, 290742, 290764, 290766, 290769, 290774, 290787, 290790, 290841, 290843, 290846, 290848, 290860, 290862, 290886, 290887, 290892, 290894, 290895, 290932, 290935, 290941, 290943, 290944, 290948, 290974, 290975, 290976, 290979, 290980, 291002, 291003, 291004, 291005, 291035, 291037, 291041, 291065, 291066, 291069, 291093, 291100, 291110, 291111, 291116, 291143, 291188, 291209, 291240, 291257, 291262, 291263, 291265, 291266, 291282, 291283, 291284, 291285, 291286, 291360, 291361, 291362, 291373, 291375, 291377, 291397, 291399, 291402, 291417, 291419, 291420, 291424, 291446, 291447, 291453, 291456, 291457, 291481, 291482, 291484, 291485, 291614, 291615, 291618, 291622, 291624, 291626, 291657, 291661, 291665, 291690, 291692, 291694, 291698, 291706, 291729, 291755, 291756, 291760, 291768, 291795, 291796, 291803, 291942, 291943, 291944, 291945, 291946, 291948, 291953, 291976, 291977, 291982, 292012, 292040, 292060, 292061, 292062, 292067, 292075, 292080, 292081, 292106, 292107, 292108, 292109, 292114, 292115, 292140, 292160, 292161, 292162, 292163, 292164, 292166, 292167, 292168, 292192, 292218, 292240, 292242, 292265, 292270, 292273, 292274, 292298, 292397, 292398, 292405, 292406, 292428, 292429, 292430, 292432, 292434, 292456, 292457, 292460, 292461, 292495, 292496, 292497, 292500, 292521, 292523, 292524, 292526, 292553, 292554, 292557, 292559, 292560, 292563, 292584, 292586, 292693, 292695, 292696, 292698, 292701, 292704, 292737, 292739, 292747, 292748, 292750, 292809, 292810, 292811, 292831, 292832, 292836

PCM-EMCal:

290323, 290324, 290327, 290350, 290374, 290375, 290376, 290399, 290401, 290411, 290412, 290425, 290426, 290427, 290428, 290456, 290458, 290459, 290469, 290499, 290500, 290538, 290539, 290540, 290544, 290549, 290550, 290553, 290588, 290590, 290612, 290613, 290614, 290615, 290627, 290632, 290645, 290658, 290660, 290665, 290687, 290689, 290692, 290696, 290699, 290721, 290764, 290766, 290769, 290774, 290787, 290790, 290841, 290843, 290846, 290848, 290860, 290862, 290886, 290887, 290892, 290894, 290895, 290932, 290935, 290941, 290943, 290944, 290948, 290974, 290975, 290976, 290979, 290980, 291002, 291003, 291004, 291005, 291035, 291037, 291041, 291065, 291066, 291069, 291093, 291100, 291110, 291111, 291116, 291143, 291188, 291209, 291240, 291257, 291262, 291263, 291265, 291266, 291282, 291283, 291284, 291285, 291286, 291360, 291361, 291362, 291373, 291375, 291377, 291397, 291399, 291402, 291417, 291419, 291420, 291424, 291446, 291447, 291453, 291456, 291457, 291481, 291482, 291484, 291485, 291614, 291615, 291618, 291622, 291624, 291626, 291657, 291661, 291665, 291690, 291692, 291694, 291698, 291706, 291729, 291755, 291756, 291760, 291768, 291795, 291796, 291803, 291942, 291943, 291944, 291945, 291946, 291948, 291953, 291976, 291977, 291982, 292012, 292040, 292060, 292061, 292062, 292067, 292075, 292080, 292081, 292106, 292107, 292108, 292109, 292114, 292115, 292140, 292160, 292161, 292162, 292163, 292164, 292166, 292167, 292168, 292192, 292218, 292240, 292242, 292265, 292270, 292273, 292274, 292298, 292397, 292398, 292405, 292406, 292428, 292429, 292430, 292432, 292434, 292456, 292457, 292460, 292461, 292495, 292496, 292497, 292500, 292521, 292523, 292524, 292526, 292553, 292554, 292557, 292559, 292560, 292563, 292584, 292586, 292693, 292695, 292696, 292698, 292701, 292704, 292737, 292739, 292747, 292748, 292750, 292809, 292810, 292811, 292831, 292832, 292836

PHOS:

292839, 292836, 292834, 292832, 292831, 292811, 292810, 292809, 292804, 292803, 292758, 292754, 292752, 292750, 292748, 292747, 292744, 292739, 292737, 292704, 292701, 292698, 292696, 292695, 292693, 292586, 292584, 292563, 292560, 292559, 292557, 292554, 292553, 292526, 292524, 292523, 292521, 292500, 292497, 292496, 292495, 292461, 292460, 292457, 292456, 292434, 292432, 292430, 292429, 292428, 292406, 292405, 292398, 292397, 292298, 292274, 292273, 292270, 292269, 292265, 292242, 292241, 292240, 292218, 292192, 292168, 292167, 292166, 292164, 292163, 292162, 292161, 292160, 292140, 292115, 292114, 292109, 292108, 292107, 292106, 292081, 292080, 292077, 292075, 292067, 292062, 292061, 292060, 292040, 292012, 291982, 291977, 291976, 291953, 291948, 291946, 291945, 291944, 291943, 291942, 291803, 291796, 291795, 291769, 291768, 291766, 291762, 291760, 291756, 291755, 291729, 291706, 291702, 291698, 291697, 291694, 291692, 291690, 291665, 291661, 291657, 291626, 291624, 291622, 291618, 291615, 291614, 291590, 291485, 291484, 291482, 291481, 291457, 291456, 291453, 291451, 291447, 291446, 291424, 291420, 291419, 291417, 291416, 291402, 291400, 291399, 291397, 291377, 291375, 291363, 291362, 291361, 291360, 291286, 291285, 291284, 291283, 291282, 291266, 291265, 291263, 291262, 291257, 291240, 291209, 291188, 291143, 291116, 291111, 291110, 291101, 291100, 291093, 291069, 291066, 291065, 291041, 291037, 291035, 291006, 291005, 291004, 291003, 291002, 290980, 290979, 290976, 290975, 290974, 290948, 290944, 290943, 290941, 290935, 290932, 290895, 290894, 290892, 290888, 290887, 290886, 290862, 290860, 290853, 290848, 290846, 290843, 290841, 290790, 290787, 290776, 290774, 290769, 290766, 290764, 290721, 290699, 290696, 290692, 290689, 290687, 290665, 290660, 290658,

290645, 290632, 290627, 290615, 290614, 290613, 290612, 290590, 290588, 290553, 290550, 290549, 290544, 290540, 290539, 290538, 290501, 290500, 290499, 290469, 290467, 290459, 290458, 290456, 290428, 290427, 290426, 290425, 290423, 290412, 290411, 290404, 290401, 290399, 290376, 290375, 290374, 290350, 290327, 290324, 290323

PHOS Trigger:

292839, 292836, 292834, 292832, 292831, 292811, 292810, 292809, 292804, 292803, 292758, 292754, 292752, 292750, 292748, 292747, 292744, 292739, 292737, 292704, 292701, 292698, 292696, 292695, 292693, 292586, 292584, 292563, 292560, 292559, 292554, 292553, 292526, 292524, 292523, 292521, 292500, 292497, 292496, 292495, 292461, 292460, 292457, 292456, 292434, 292432, 292430, 292429, 292428, 292406, 292405, 292398, 292397, 292298, 292274, 292273, 292270, 292269, 292265, 292242, 292241, 292240, 292218, 292192, 292168, 292167, 292166, 292164, 292163, 292162, 292161, 292160, 292140, 292115, 292108, 292107, 292106, 292081, 292080, 292077, 292075, 292067, 292062, 292061, 292060, 292040, 292012, 291982, 291977, 291976, 291953, 291948, 291946, 291945, 291944, 291943, 291942, 291803, 291796, 291795, 291769, 291768, 291766, 291762, 291760, 291756, 291755, 291729, 291706, 291702, 291698, 291697, 291694, 291692, 291690, 291665, 291661, 291657, 291626, 291624, 291622, 291618, 291615, 291614, 291590, 291485, 291484, 291482, 291481, 291457, 291456, 291453, 291451, 291447, 291446, 291424, 291420, 291419, 291417, 291416, 291402, 291400, 291399, 291397, 291377, 291375, 291363, 291362, 291361, 291360, 291286, 291285, 291284, 291283, 291282, 291266, 291265, 291263, 291262, 291257, 291240, 291209, 291188, 291143, 291116, 291111, 291110, 291101, 291100, 291093, 291069, 291066, 291065, 291041, 291037, 291035, 291006, 291005, 291004, 291003, 291002, 290980, 290979, 290976, 290975, 290974, 290948, 290944, 290943, 290941, 290932, 290895, 290894, 290892, 290888, 290887, 290886, 290862, 290860, 290853, 290848, 290846, 290843, 290841, 290790, 290787, 290776, 290774, 290769, 290766, 290764, 290721, 290699, 290696, 290692, 290689, 290687, 290665, 290660, 290658, 290645, 290632, 290627, 290615, 290614, 290613, 290612, 290590, 290588, 290553, 290550, 290549, 290544, 290540, 290539, 290538, 290501, 290500, 290499, 290469, 290467, 290459, 290458, 290456, 290428, 290427, 290426, 290425, 290423, 290412, 290411, 290404, 290401, 290399, 290376, 290375, 290374, 290350, 290324, 290323

LHC18n anchored to: LHC18k1

PCM:

293357, 293359

EMCal Trigger:

293357, 293359

EMCal:

293357, 293359

PCM-EMCal:

293357, 293359

PHOS:

293357, 293359

PHOS Trigger:

293357, 293359

LHC18o anchored to: LHC18k2

PCM:

293898, 293896, 293893, 293891, 293886, 293856, 293831, 293830, 293829, 293809, 293807, 293806, 293805, 293802, 293799, 293776, 293774, 293773, 293770, 293741, 293740, 293698, 293696, 293695, 293692, 293691, 293690, 293689, 293686, 293588, 293587, 293583, 293582, 293579, 293578, 293573, 293571, 293570, 293475

EMCal Trigger:

293368, 293386, 293392, 293413, 293424, 293474, 293475, 293494, 293496, 293497, 293570, 293571, 293582, 293587, 293588, 293686, 293690, 293691, 293695, 293696, 293740, 293741, 293770, 293773, 293774, 293776, 293799, 293805, 293806, 293809, 293829, 293830, 293831, 293856, 293886, 293891, 293893, 293896, 293898

EMCal:

293368, 293386, 293392, 293413, 293424, 293474, 293475, 293494, 293496, 293497, 293570, 293571, 293582, 293587, 293588, 293686, 293690, 293691, 293695, 293696, 293740, 293741, 293770, 293773, 293774, 293776, 293799, 293805, 293806, 293809, 293829, 293830, 293831, 293856, 293886, 293891, 293893, 293896, 293898

PCM-EMCal:

293368, 293386, 293392, 293413, 293424, 293474, 293475, 293494, 293496, 293497, 293570, 293571, 293582, 293587, 293588, 293686, 293690, 293691, 293695, 293696, 293740, 293741, 293770, 293773, 293774, 293776, 293799, 293805, 293806, 293809, 293829, 293830, 293831, 293856, 293886, 293891, 293893, 293896, 293898

PHOS:

293368, 293386, 293392, 293413, 293424, 293474, 293475, 293494, 293496, 293497, 293571, 293573, 293578, 293579, 293582, 293583, 293587, 293588, 293686, 293690, 293691, 293692, 293695, 293696, 293698, 293740, 293741, 293770, 293774, 293776, 293799, 293802, 293805, 293806, 293807, 293809, 293829, 293830, 293831, 293856, 293886, 293891, 293893, 293896, 293898

PHOS Trigger:

293898, 293896, 293893, 293891, 293886, 293856, 293831, 293830, 293829, 293809, 293807, 293806, 293805, 293802, 293799, 293776, 293774, 293770, 293741, 293740, 293698, 293696, 293695, 293692, 293691, 293690, 293686, 293588, 293587, 293583, 293582, 293579, 293578, 293573, 293571, 293475

LHC18p anchored to: LHC18k3

PCM:

294925, 294916, 294884, 294883, 294880, 294877, 294875, 294852, 294818, 294817, 294816, 294815, 294813, 294809, 294805, 294775, 294774, 294772, 294769, 294749, 294747, 294746, 294745, 294744, 294743, 294742, 294741, 294722, 294721, 294718, 294716, 294715, 294710, 294703, 294653, 294636, 294634, 294633, 294632, 294593, 294591, 294590, 294588, 294587, 294586, 294563, 294562, 294558, 294556, 294553, 294531, 294530, 294529, 294527, 294526, 294525, 294524, 294310, 294308, 294307, 294242, 294241, 294212, 294210, 294208, 294205, 294201, 294200, 294199, 294156, 294155, 294154, 294152, 294131, 294013, 294012, 294011, 294010, 294009

EMCal Trigger:

294009, 294010, 294011, 294012, 294013, 294131, 294152, 294154, 294155, 294156, 294199, 294200, 294208, 294210, 294212, 294241, 294242, 294305, 294307, 294310, 294524, 294525, 294526, 294529, 294530, 294531, 294553, 294556, 294558, 294562, 294563, 294586, 294587, 294588, 294590, 294591, 294593, 294632, 294633, 294634, 294636, 294653, 294715, 294716, 294721, 294722, 294741, 294742, 294743, 294744, 294745, 294746, 294747, 294769, 294774, 294775, 294805, 294815, 294816, 294817, 294818, 294852, 294875, 294877, 294883, 294884, 294925

EMCal:

294009, 294010, 294011, 294012, 294013, 294131, 294152, 294154, 294155, 294156, 294199, 294200, 294208, 294210, 294212, 294241, 294242, 294305, 294307, 294310, 294524, 294525, 294526, 294529, 294530, 294531, 294553, 294556, 294558, 294562, 294563, 294586, 294587, 294588, 294590, 294591, 294593, 294632, 294633, 294634, 294636, 294653, 294715, 294716, 294721, 294722, 294741, 294742, 294743, 294744, 294745, 294746, 294747, 294769, 294774, 294775, 294805, 294815, 294816, 294817, 294818, 294852, 294875, 294877, 294883, 294884, 294925

PCM-EMCal:

294009, 294010, 294011, 294012, 294013, 294131, 294152, 294154, 294155, 294156, 294199, 294200, 294208, 294210, 294212, 294241, 294242, 294305, 294307, 294310, 294524, 294525, 294526, 294529, 294530, 294531, 294553, 294556, 294558, 294562, 294563, 294586, 294587, 294588, 294590, 294591, 294593, 294632, 294633, 294634, 294636, 294653, 294715, 294716, 294721, 294722, 294741, 294742, 294743, 294744, 294745, 294746, 294747, 294769, 294774, 294775, 294805, 294815, 294816, 294817, 294818, 294852, 294875, 294877, 294883, 294884, 294925

PHOS:

294925, 294916, 294884, 294883, 294880, 294877, 294875, 294852, 294818, 294817, 294816, 294813, 294809, 294805, 294775, 294774, 294772, 294769, 294749, 294747, 294746, 294745, 294744, 294743, 294742, 294741, 294722, 294721, 294718, 294716, 294715, 294710, 294703, 294653, 294636, 294634, 294633, 294632, 294593, 294591, 294590, 294588, 294587, 294586, 294563, 294562, 294558, 294556, 294553, 294531, 294530, 294529, 294527, 294526, 294525, 294524, 294310, 294308, 294307, 294305, 294242, 294241, 294212, 294210, 294208, 294205, 294201, 294200, 294199, 294156, 294155, 294154, 294152, 294131, 294013, 294012, 294011, 294010, 294009

PHOS Trigger:

294925, 294916, 294884, 294883, 294880, 294877, 294875, 294852, 294818, 294817, 294816, 294815, 294813, 294809, 294805, 294775, 294774, 294772, 294769, 294749, 294747, 294746, 294745, 294744, 294743, 294742, 294741, 294722, 294721, 294718, 294716, 294715, 294710, 294703, 294653, 294636, 294634, 294633, 294632, 294593, 294591, 294590, 294588, 294587, 294586, 294563, 294562, 294558, 294556, 294553, 294531, 294530, 294529, 294527, 294526, 294525, 294524, 294310, 294308, 294307, 294242, 294241, 294212, 294210,

294208, 294205, 294201, 294200, 294199, 294156, 294155, 294154, 294152, 294131, 294013, 294012, 294011, 294010, 294009

Bibliography

[1] *CERN Experiments Observe Particle Consistent with Long-Sought Higgs Boson*. CERN. URL: https://home.web.cern.ch/news/press-release/cern/cern-experiments-observe-particle-consistent-long-sought-higgs-boson (visited on 01/11/2023).

[2] Rajeev S. Bhalerao. "Relativistic heavy-ion collisions". In: *1st Asia-Europe-Pacific School of High-Energy Physics*. 2014, pp. 219–239. DOI: 10.5170/CERN-2014-001.219. arXiv: 1404.3294 [nucl-th]. URL: https://arxiv.org/abs/1404.3294 (visited on 02/01/2023).

[3] "The ALICE experiment – A journey through QCD". In: (Nov. 2022). arXiv: 2211.04384 [nucl-ex]. URL: https://arxiv.org/abs/2211.04384 (visited on 02/01/2023).

[4] H. Saveetha, D. Indumathi, and Subhadip Mitra. "Vector meson fragmentation using a model with broken SU(3) at the Next-to-Leading Order". In: *Int. J. Mod. Phys. A* 29.07 (2014), p. 1450049. DOI: 10.1142/S0217751X14500493. arXiv: 1309.2134 [hep-ph]. URL: http://arxiv.org/abs/1309.2134 (visited on 01/11/2023).

[5] Bogdan Povh, Klaus Rith, Christoph Scholz, Frank Zetsche, and Werner Rodejohann. *Teilchen und Kerne*. de. 9th ed. Springer-Lehrbuch. Wiesbaden, Germany: Springer, Nov. 2013. ISBN: 978-3-642-37822-5.

[6] Mark Thomson. *Modern Particle Physics*. Cambridge: Cambridge University Press, 2013. ISBN: 978-1-107-29254-3.

[7] Nobel Media AB. *The Nobel Prize in Physics 1979*. URL: http://www.nobelprize.org/nobel_prizes/physics/laureates/1979/ (visited on 02/01/2023).

[8] S. Schael et al. "Precision electroweak measurements on the Z resonance". In: *Phys. Rept.* 427 (2006), pp. 257–454. DOI: 10.1016/j.physrep.2005.12.006. arXiv: hep-ex/0509008. URL: http://arxiv.org/abs/hep-ex/0509008 (visited on 02/01/2023).

[9] BIPM. *SI Brochure*. URL: https://www.bipm.org/en/publications/si-brochure (visited on 10/31/2022).

[10] Particle Data Group et al. "Review of Particle Physics". In: *Progress of Theoretical and Experimental Physics* 2020.8 (Aug. 2020). 083C01. ISSN: 2050-3911. DOI: 10.1093/ptep/ptaa104. eprint: https://academic.oup.com/ptep/article-pdf/2020/8/083C01/34673722/ptaa104.pdf. URL: https://doi.org/10.1093/ptep/ptaa104 (visited on 02/01/2023).

[11] Alexandre Deur, Stanley J. Brodsky, and Guy F. de Teramond. "The QCD Running Coupling". In: *Nucl. Phys.* 90 (2016), p. 1. DOI: 10.1016/j.ppnp.2016.04.003. arXiv: 1604.08082 [hep-ph]. URL: https://arxiv.org/abs/1604.08082 (visited on 02/01/2023).

[12] Roel Aaij et al. "Observation of $J/\psi p$ Resonances Consistent with Pentaquark States in $\Lambda_b^0 \to J/\psi K^- p$ Decays". In: *Phys. Rev. Lett.* 115 (2015), p. 072001. DOI: 10.1103/PhysRevLett.115.072001. arXiv: 1507.03414 [hep-ex]. URL: https://arxiv.org/abs/1507.03414 (visited on 02/01/2023).

[13] C. Grupen. *Physics of Particle Detection*. June 30, 1999. DOI: 10.1063/1.1361756. arXiv: physics/9906063. URL: http://arxiv.org/abs/physics/9906063 (visited on 08/22/2022).

[14] Claus Grupen. *Teilchendetektoren*. Mannheim, Germany: B.I.-Wissenschaftsverlag, 1993. ISBN: 3-411-16571-5.

[15] Peter Skands. "Introduction to QCD". In: *Theoretical Advanced Study Institute in Elementary Particle Physics: Searching for New Physics at Small and Large Scales*. 2013, pp. 341–420. DOI: 10.1142/9789814525220_0008. arXiv: 1207.2389 [hep-ph]. URL: https://arxiv.org/abs/1207.2389 (visited on 02/01/2023).

[16] John C. Collins and Davison E. Soper. "Parton Distribution and Decay Functions". In: *Nuclear Physics B* 194.3 (Jan. 25, 1982), pp. 445–492. ISSN: 0550-3213. DOI: 10.1016/0550-3213(82)90021-9. URL: https://www.sciencedirect.com/science/article/pii/0550321382900219 (visited on 09/13/2022).

[17] Andreas Metz and Anselm Vossen. "Parton Fragmentation Functions". In: *Prog. Part. Nucl. Phys.* 91 (2016), pp. 136–202. DOI: 10.1016/j.ppnp.2016.08.003. arXiv: 1607.02521 [hep-ex]. URL: http://arxiv.org/abs/1607.02521 (visited on 09/13/2022).

[18] Guang-You Qin and Xin-Nian Wang. "Jet quenching in high-energy heavy-ion collisions". In: *Int. J. Mod. Phys. E* 24.11 (2015). Ed. by Xin-Nian Wang, p. 1530014. DOI: 10.1142/S0218301315300143. arXiv: 1511.00790 [hep-ph]. URL: http://arxiv.org/abs/1511.00790 (visited on 01/21/2023).

[19] H. Zheng and Lilin Zhu. "Can Tsallis Distribution Fit All the Particle Spectra Produced at RHIC and LHC?" In: *Adv. High Energy Phys.* 2015 (2015), p. 180491. DOI: 10.1155/2015/180491. arXiv: 1510.05449 [nucl-th]. URL: http://arxiv.org/abs/1510.05449 (visited on 09/02/2022).

[20] Alexander Bylinkin, Nadezda S. Chernyavskaya, and Andrei A. Rostovtsev. "Predictions on the transverse momentum spectra for charged particle production at LHC-energies from a two component model". In: *Eur. Phys. J. C* 75.4 (2015), p. 166. DOI:

10.1140/epjc/s10052-015-3392-y. arXiv: 1501.05235 [hep-ph]. URL: http://arxiv.org/abs/1501.05235 (visited on 09/02/2022).

[21] Torbjörn Sjöstrand, Stefan Ask, Jesper R. Christiansen, Richard Corke, Nishita Desai, Philip Ilten, Stephen Mrenna, Stefan Prestel, Christine O. Rasmussen, and Peter Z. Skands. "An introduction to PYTHIA 8.2". In: *Comput. Phys. Commun.* 191 (2015), pp. 159–177. DOI: 10.1016/j.cpc.2015.01.024. arXiv: 1410.3012 [hep-ph]. URL: http://arxiv.org/abs/1410.3012 (visited on 09/13/2022).

[22] Peter Skands, Stefano Carrazza, and Juan Rojo. "Tuning PYTHIA 8.1: the Monash 2013 Tune". In: *Eur. Phys. J. C* 74.8 (2014), p. 3024. DOI: 10.1140/epjc/s10052-014-3024-y. arXiv: 1404.5630 [hep-ph]. URL: http://arxiv.org/abs/1404.5630 (visited on 12/20/2022).

[23] B. Andersson, G. Gustafson, G. Ingelman, and T. Sjöstrand. "Parton fragmentation and string dynamics". In: *Physics Reports* 97.2 (1983), pp. 31–145. ISSN: 0370-1573. DOI: https://doi.org/10.1016/0370-1573(83)90080-7. URL: https://www.sciencedirect.com/science/article/pii/0370157383900807 (visited on 02/01/2023).

[24] Bo Andersson. *The Lund Model*. Cambridge Monographs on Particle Physics, Nuclear Physics and Cosmology. Cambridge University Press, 1998. DOI: 10.1017/CBO9780511524363. URL: https://www.cambridge.org/core/books/lund-model/F9442FBA5696D5DE0D0E8D46F70C34C7 (visited on 09/13/2022).

[25] Peter Braun-Munzinger, Krzysztof Redlich, and Johanna Stachel. "Particle production in heavy ion collisions". In: (Apr. 2003). Ed. by Rudolph C. Hwa and Xin-Nian Wang, pp. 491–599. DOI: 10.1142/9789812795533_0008. arXiv: nucl-th/0304013. URL: http://arxiv.org/abs/nucl-th/0304013 (visited on 08/16/2022).

[26] Frithjof Karsch. "Lattice results on QCD thermodynamics". In: *Nucl. Phys. A* 698 (2002). Ed. by T. J. Hallman, D. E. Kharzeev, J. T. Mitchell, and T. S. Ullrich, pp. 199–208. DOI: 10.1016/S0375-9474(01)01365-3. arXiv: hep-ph/0103314. URL: http://arxiv.org/abs/hep-ph/0103314 (visited on 08/16/2022).

[27] M. Cheng et al. "The Transition temperature in QCD". In: *Phys. Rev. D* 74 (2006), p. 054507. DOI: 10.1103/PhysRevD.74.054507. arXiv: hep-lat/0608013. URL: http://arxiv.org/abs/hep-lat/0608013 (visited on 08/16/2022).

[28] Szabolcs Borsanyi, Gergely Endrodi, Zoltan Fodor, Antal Jakovac, Sandor D. Katz, Stefan Krieg, Claudia Ratti, and Kalman K. Szabo. "The QCD equation of state with dynamical quarks". In: *JHEP* 11 (2010), p. 077. DOI: 10.1007/JHEP11(2010)077. arXiv: 1007.2580 [hep-lat]. URL: http://arxiv.org/abs/1007.2580 (visited on 08/16/2022).

[29] Ulrich W. Heinz. "The Little bang: Searching for quark gluon matter in relativistic heavy ion collisions". In: *Nucl. Phys. A* 685 (2001). Ed. by W. Norenberg, D. Guerreau, and V. Metag, pp. 414–431. DOI: 10.1016/S0375-9474(01)00558-9. arXiv: hep-ph/0009170. URL: https://arxiv.org/abs/hep-ph/0009170 (visited on 02/01/2023).

[30] Zi-Wei Lin. "Extension of the Bjorken energy density formula of the initial state for relativistic heavy ion collisions". In: *Phys. Rev. C* 98.3 (2018), p. 034908. DOI: 10.1103/PhysRevC.98.034908. arXiv: 1704.08418 [nucl-th]. URL: https://arxiv.org/abs/1704.08418 (visited on 02/01/2023).

[31] Peter Braun-Munzinger and Johanna Stachel. "The Quest for the Quark–Gluon Plasma". In: *Nature* 448.7151 (7151 July 2007), pp. 302–309. ISSN: 1476-4687. DOI: 10.1038/nature06080. URL: https://www.nature.com/articles/nature06080 (visited on 08/16/2022).

[32] Jaroslav Adam et al. "Measurement of transverse energy at midrapidity in Pb-Pb collisions at $\sqrt{s_{NN}} = 2.76$ TeV". In: *Phys. Rev. C* 94.3 (2016), p. 034903. DOI: 10.1103/PhysRevC.94.034903. arXiv: 1603.04775 [nucl-ex]. URL: https://arxiv.org/abs/1603.04775 (visited on 02/01/2023).

[33] Betty Abelev et al. "Centrality determination of Pb-Pb collisions at $\sqrt{s_{NN}} = 2.76$ TeV with ALICE". In: *Phys. Rev. C* 88.4 (2013), p. 044909. DOI: 10.1103/PhysRevC.88.044909. arXiv: 1301.4361 [nucl-ex]. URL: http://arxiv.org/abs/1301.4361 (visited on 09/15/2022).

[34] Betty Bezverkhny Abelev et al. "Neutral pion production at midrapidity in pp and Pb-Pb collisions at $\sqrt{s_{\mathrm{NN}}} = 2.76\,\mathrm{TeV}$". In: *Eur. Phys. J. C* 74.10 (2014), p. 3108. DOI: 10.1140/epjc/s10052-014-3108-8. arXiv: 1405.3794 [nucl-ex]. URL: https://arxiv.org/abs/1405.3794 (visited on 02/01/2023).

[35] Jaroslav Adam et al. "Direct photon production in Pb-Pb collisions at $\sqrt{s_{NN}} = 2.76$ TeV". In: *Phys. Lett. B* 754 (2016), pp. 235–248. DOI: 10.1016/j.physletb.2016.01.020. arXiv: 1509.07324 [nucl-ex]. URL: http://arxiv.org/abs/1509.07324 (visited on 09/15/2022).

[36] Thomas Peitzmann and Markus H. Thoma. "Direct photons from relativistic heavy ion collisions". In: *Phys. Rept.* 364 (2002), pp. 175–246. DOI: 10.1016/S0370-1573(02)00012-1. arXiv: hep-ph/0111114. URL: http://arxiv.org/abs/hep-ph/0111114 (visited on 09/15/2022).

[37] Shreyasi Acharya et al. "Direct photon production at low transverse momentum in proton-proton collisions at $\sqrt{\mathbf{s}} = \mathbf{2.76}$ and 8 TeV". In: *Phys. Rev. C* 99.2 (2019), p. 024912. DOI: 10.1103/PhysRevC.99.024912. arXiv: 1803.09857 [nucl-ex]. URL: http://arxiv.org/abs/1803.09857 (visited on 09/16/2022).

[38] Lyndon Evans and Philip Bryant. "LHC Machine". In: *Journal of Instrumentation* 3.08 (2008), S08001. DOI: 10.1088/1748-0221/3/08/S08001. URL: https://dx.doi.org/10.1088/1748-0221/3/08/S08001 (visited on 02/01/2023).

[39] The ALICE Collaboration et al. "The ALICE experiment at the CERN LHC". In: *Journal of Instrumentation* 3.08 (2008), S08002. DOI: 10.1088/1748-0221/3/08/S08002. URL: https://dx.doi.org/10.1088/1748-0221/3/08/S08002 (visited on 02/01/2023).

[40] Cinzia De Melis. "The CERN accelerator complex. Complexe des accélérateurs du CERN". In: (2016). General Photo. URL: https://cds.cern.ch/record/2119882 (visited on 02/01/2023).

[41] The CMS Collaboration et al. "The CMS experiment at the CERN LHC". In: *Journal of Instrumentation* 3.08 (2008), S08004. DOI: 10.1088/1748-0221/3/08/S08004. URL: https://dx.doi.org/10.1088/1748-0221/3/08/S08004 (visited on 05/12/2022).

[42] The ATLAS Collaboration et al. "The ATLAS Experiment at the CERN Large Hadron Collider". In: *Journal of Instrumentation* 3.08 (2008), S08003. DOI: 10.1088/1748-0221/3/08/S08003. URL: https://dx.doi.org/10.1088/1748-0221/3/08/S08003 (visited on 02/01/2023).

[43] The LHCb Collaboration et al. "The LHCb Detector at the LHC". In: *Journal of Instrumentation* 3.08 (2008), S08005. DOI: 10.1088/1748-0221/3/08/S08005. URL: https://dx.doi.org/10.1088/1748-0221/3/08/S08005 (visited on 02/01/2023).

[44] ALICE Collaboration. *ALICE Figure Repository*. URL: https://alice-figure.web.cern.ch.

[45] "Performance of the ALICE experiment at the CERN LHC". In: *International Journal of Modern Physics A* 29.24 (2014), p. 1430044. DOI: 10.1142/S0217751X14300440. eprint: https://doi.org/10.1142/S0217751X14300440. URL: https://doi.org/10.1142/S0217751X1430044 (visited on 02/02/2023).

[46] "Pseudorapidity densities of charged particles with transverse momentum thresholds in pp collisions at $\sqrt{s} = 5.02$ and 13 TeV". In: (Nov. 2022). arXiv: 2211.15364 [nucl-ex]. URL: https://arxiv.org/abs/2211.15364 (visited on 02/02/2023).

[47] S. Acharya et al. "Calibration of the photon spectrometer PHOS of the ALICE experiment". In: *Journal of Instrumentation* 14.05 (2019), P05025. DOI: 10.1088/1748-0221/14/05/P05025. URL: https://dx.doi.org/10.1088/1748-0221/14/05/P05025 (visited on 02/02/2023).

[48] "Performance of the ALICE Electromagnetic Calorimeter". In: (Sept. 2022). arXiv: 2209.04216 [physics.ins-det]. URL: https://arxiv.org/abs/2209.04216 (visited on 02/02/2023).

[49] K Aamodt et al. “Alignment of the ALICE Inner Tracking System with cosmic-ray tracks”. In: *JINST* 5 (2010), P03003. DOI: 10.1088/1748-0221/5/03/P03003. arXiv: 1001.0502 [physics.ins-det]. URL: http://arxiv.org/abs/1001.0502 (visited on 05/19/2022).

[50] P. Kuijer. “The inner tracking system of the Alice experiment”. In: *Nuclear Instruments and Methods in Physics Research Section A: Accelerators, Spectrometers, Detectors and Associated Equipment* 530.1 (2004). Proceedings of the 6th International Conference on Large Scale Applications and Radiation Hardness of Semiconductor Detectors, pp. 28–32. ISSN: 0168-9002. DOI: https://doi.org/10.1016/j.nima.2004.05.042. URL: https://www.sciencedirect.com/science/article/pii/S0168900204010289 (visited on 02/02/2023).

[51] J. Alme et al. “The ALICE TPC, a large 3-dimensional tracking device with fast readout for ultra-high multiplicity events”. In: *Nuclear Instruments and Methods in Physics Research Section A: Accelerators, Spectrometers, Detectors and Associated Equipment* 622.1 (2010), pp. 316–367. ISSN: 0168-9002. DOI: https://doi.org/10.1016/j.nima.2010.04.042. URL: https://www.sciencedirect.com/science/article/pii/S0168900210008910 (visited on 02/02/2023).

[52] Shreyasi Acharya et al. “The ALICE Transition Radiation Detector: construction, operation, and performance”. In: *Nucl. Instrum. Meth. A* 881 (2018), pp. 88–127. DOI: 10.1016/j.nima.2017.09.028. arXiv: 1709.02743 [physics.ins-det]. URL: https://arxiv.org/abs/1709.02743 (visited on 02/02/2023).

[53] Dariusz Czerwinski, Andrzej Deloff, Krzysztof Karpio, S. Kozak, L. Lukaszek, Hubert Malinowski, Teodor Siemiarczuk, G. Stefanek, L. Tykarski, and G. Wilk. “Alice Technical Design Report of the Photon Spectrometer PHOS”. In: Mar. 1999. ISBN: ISBN 92-9083-138-3. URL: https://www.researchgate.net/publication/247768400_Alice_Technical_Design_Report_of_the_Photon_Spectrometer_PHOS (visited on 02/02/2023).

[54] Christian W. Fabjan and Fabiola Gianotti. “Calorimetry for particle physics”. In: *Rev. Mod. Phys.* 75 (4 2003), pp. 1243–1286. DOI: 10.1103/RevModPhys.75.1243. URL: https://link.aps.org/doi/10.1103/RevModPhys.75.1243 (visited on 02/02/2023).

[55] J Allen et al. *ALICE DCal: An Addendum to the EMCal Technical Design Report Di-Jet and Hadron-Jet correlation measurements in ALICE*. Tech. rep. 2010. URL: https://cds.cern.ch/record/1272952 (visited on 05/20/2022).

[56] P. Cortese et al. *ALICE Electromagnetic Calorimeter Technical Design Report*. 2008. URL: https://cds.cern.ch/record/1121574 (visited on 01/02/2023).

[57] **ALICE** Collaboration. *AliRoot Documentation*. URL: https://alice-offline.web.cern.ch/AliRoot/Manual.html (visited on 09/20/2022).

[58] **ALICE** Collaboration. *ALICE Analysis Repository*. URL: https://github.com/alisw/AliPhysics (visited on 09/21/2022).

[59] Rene Brun and Fons Rademakers. "ROOT — An object oriented data analysis framework". In: *Nuclear Instruments and Methods in Physics Research Section A: Accelerators, Spectrometers, Detectors and Associated Equipment* 389.1 (1997). New Computing Techniques in Physics Research V, pp. 81–86. ISSN: 0168-9002. DOI: https://doi.org/10.1016/S0168-9002(97)00048-X. URL: https://www.sciencedirect.com/science/article/pii/S016890029700048X (visited on 01/02/2023).

[60] Bjarne Stroustrup. *The C++ Programming Language*. Addison-Wesley Series in Computer Science. Reading, Mass: Addison-Wesley, 1986. 327 pp. ISBN: 978-0-201-12078-3.

[61] C. Hohne et al. "Results from NA49". In: *Nucl. Phys. A* 774 (2006). Ed. by T. Csorgo, P. Levai, G. David, and G. Papp, pp. 35–42. DOI: 10.1016/j.nuclphysa.2006.06.011. arXiv: nucl-ex/0510049. URL: https://arxiv.org/abs/nucl-ex/0510049 (visited on 01/02/2023).

[62] Miklos Gyulassy and Xin-Nian Wang. "HIJING 1.0: A Monte Carlo program for parton and particle production in high-energy hadronic and nuclear collisions". In: *Comput. Phys. Commun.* 83 (1994), p. 307. DOI: 10.1016/0010-4655(94)90057-4. arXiv: nucl-th/9502021. URL: https://arxiv.org/abs/nucl-th/9502021 (visited on 01/02/2023).

[63] R Brun, F Bruyant, M Maire, A C McPherson, and P Zanarini. *GEANT 3: user's guide Geant 3.10, Geant 3.11; rev. version*. Geneva: CERN, 1987. URL: https://cds.cern.ch/record/1119728 (visited on 01/02/2023).

[64] S. Agostinelli et al. "Geant4—a simulation toolkit". In: *Nuclear Instruments and Methods in Physics Research Section A: Accelerators, Spectrometers, Detectors and Associated Equipment* 506.3 (2003), pp. 250–303. ISSN: 0168-9002. DOI: https://doi.org/10.1016/S0168-9002(03)01368-8. URL: https://www.sciencedirect.com/science/article/pii/S0168900203013688 (visited on 01/02/2023).

[65] A Ferrari, Paola R Sala, A Fassò, and Johannes Ranft. *FLUKA: A multi-particle transport code (program version 2005)*. CERN Yellow Reports: Monographs. Geneva: CERN, 2005. DOI: 10.5170/CERN-2005-010. URL: https://cds.cern.ch/record/898301 (visited on 01/02/2023).

[66] K. Bos et al. *LHC computing Grid: Technical Design Report. Version 1.06 (20 Jun 2005)*. Technical design report. LCG. Geneva: CERN, 2005. URL: https://cds.cern.ch/record/840543 (visited on 01/02/2023).

[67] **ALICE** Photon Conversion Group. *Afterburner Framework - AnalysisSoftware*. GitLab. URL: https://gitlab.cern.ch/alice-pcg/AnalysisSoftware (visited on 09/21/2022).

[68] MartaVerweij. *Introduction: Hybrid Tracks*. [CERN TWiki]. URL: https://twiki.cern.ch/twiki/bin/viewauth/ALICE/HybridTracks (visited on 09/22/2022).

[69] Daniel Lohner. "Anisotropic Flow of Direct Photons". PhD thesis. University of Heidelberg, 2013, p. 215. URL: https://www.physi.uni-heidelberg.de/Publications/lohner_doktorarbeit.pdf (visited on 02/01/2023).

[70] Betty Bezverkhny Abelev et al. "Performance of the ALICE Experiment at the CERN LHC". In: *Int. J. Mod. Phys.* A29 (2014), p. 1430044. DOI: 10.1142/S0217751X14300440. arXiv: 1402.4476 [nucl-ex]. URL: https://arxiv.org/abs/1402.4476 (visited on 02/01/2023).

[71] Betty Abelev et al. "Measurement of inelastic, single- and double-diffraction cross sections in proton–proton collisions at the LHC with ALICE". In: *Eur. Phys. J.* C73 (2013), p. 2456. DOI: 10.1140/epjc/s10052-013-2456-0. arXiv: 1208.4968 [hep-ex]. URL: https://arxiv.org/abs/1208.4968 (visited on 02/01/2023).

[72] "ALICE luminosity determination for pp collisions at $\sqrt{s} = 13$ TeV". In: (2016). URL: https://cds.cern.ch/record/2160174 (visited on 02/01/2023).

[73] "Performance of the ALICE Electromagnetic Calorimeter". In: (Sept. 2022). arXiv: 2209.04216 [physics.ins-det]. URL: http://arxiv.org/abs/2209.04216 (visited on 09/12/2022).

[74] **ALICE** Collaboration. *AliPhysics: AliEmcalTriggerMaker Class Reference*. URL: http://alidoc.cern.ch/AliPhysics/master/class_ali_emcal_trigger_maker.html (visited on 10/19/2022).

[75] F. Bock. "ALICE Capabilities for Studying Photon Physics with the Conversion Method at LHC Energies". Bachelor thesis. University of Heidelberg, 2010. URL: http://www.physi.uni-heidelberg.de//Publications/Bock-Bachelorthesis.pdf (visited on 02/01/2023).

[76] F. Bock. "Neutral Pion and Eta Meson Production in pp and Pb-Pb Collisions at the LHC with the ALICE Detector". Master thesis. University of Heidelberg, 2012. URL: http://www.physi.uni-heidelberg.de//Publications/Bock-Masterthesis.pdf (visited on 02/01/2023).

[77] Kathrin Koch. "Measurement of Pi0 and Eta Mesons with Photon Conversions in ALICE in Proton-Proton Collisions at Sqrt(s) = 0.9, 2.76, 7 TeV". Dissertation. 2011. DOI: 10.11588/heidok.00013113. URL: https://archiv.ub.uni-heidelberg.de/volltextserver/13113/1/Thesis_Dec2011.pdf (visited on 02/01/2023).

[78] ALICE Collaboration. *Correction of the ALICE Material Budget via Weighting Procedure — Public & Analysis Notes*. URL: https://alice-notes.web.cern.ch/node/860 (visited on 11/09/2022).

[79] ALICE Collaboration. *[PWGGA-226] Recalib TPC-dEdx pp13TeV LHC16, 17, 18*. [JIRA Ticket]. URL: https://alice.its.cern.ch/jira/browse/PWGGA-226 (visited on 10/17/2022).

[80] S. Gorbunov and I. Kisel. "Reconstruction of decayed particles based on the Kalman filter". In: *CBM-SOFT-note* 003 (2007), pp. 1–16. URL: https://www.star.bnl.gov/~bouchet/KFParticle/DOC-2007-May-14-1.pdf (visited on 02/02/2023).

[81] R. Frühwirth. "Application of Kalman filtering to track and vertex fitting". In: *Nuclear Instruments and Methods in Physics Research Section A: Accelerators, Spectrometers, Detectors and Associated Equipment* 262.2 (1987), pp. 444–450. ISSN: 0168-9002. DOI: https://doi.org/10.1016/0168-9002(87)90887-4. URL: https://www.sciencedirect.com/science/article/pii/0168900287908874 (visited on 02/02/2023).

[82] Louis Lyons, Duncan Gibaut, and Peter Clifford. "How to Combine Correlated Estimates of a Single Physical Quantity". In: *Nucl. Instrum. Meth.* A270 (1988), p. 110. DOI: 10.1016/0168-9002(88)90018-6.

[83] A. Valassi. "Combining correlated measurements of several different physical quantities". In: *Nucl. Instrum. Meth.* A500 (2003), pp. 391–405. DOI: 10.1016/S0168-9002(03)00329-2.

[84] Andrea Valassi and Roberto Chierici. "Information and treatment of unknown correlations in the combination of measurements using the BLUE method". In: *Eur. Phys. J. C* 74 (2014), p. 2717. DOI: 10.1140/epjc/s10052-014-2717-6. arXiv: 1307.4003 [physics.data-an]. URL: https://arxiv.org/abs/1307.4003 (visited on 02/02/2023).

[85] Tie-Jiun Hou et al. "New CTEQ Global Analysis with High Precision Data from the LHC". In: (Aug. 2019). arXiv: 1908.11238 [hep-ph]. URL: https://arxiv.org/abs/1908.11238 (visited on 02/02/2023).

[86] Sayipjamal Dulat, Tie-Jiun Hou, Jun Gao, Marco Guzzi, Joey Huston, Pavel Nadolsky, Jon Pumplin, Carl Schmidt, Daniel Stump, and C. P. Yuan. "New parton distribution functions from a global analysis of quantum chromodynamics". In: *Phys. Rev. D* 93.3 (2016), p. 033006. DOI: 10.1103/PhysRevD.93.033006. arXiv: 1506.07443 [hep-ph]. URL: https://arxiv.org/abs/1506.07443 (visited on 02/02/2023).

[87] Valerio Bertone, Stefano Carrazza, Nathan P. Hartland, Emanuele R. Nocera, and Juan Rojo. "A determination of the fragmentation functions of pions, kaons, and

protons with faithful uncertainties". In: *Eur. Phys. J. C* 77.8 (2017), p. 516. DOI: 10.1140/epjc/s10052-017-5088-y. arXiv: 1706.07049 [hep-ph]. URL: https://arxiv.org/abs/1706.07049 (visited on 02/02/2023).

[88] Daniel de Florian, R. Sassot, Manuel Epele, Roger J. Hernández-Pinto, and Marco Stratmann. "Parton-to-Pion Fragmentation Reloaded". In: *Phys. Rev. D* 91.1 (2015), p. 014035. DOI: 10.1103/PhysRevD.91.014035. arXiv: 1410.6027 [hep-ph]. URL: https://arxiv.org/abs/1410.6027 (visited on 02/09/2023).

[89] Shreyasi Acharya et al. "Production of light-flavor hadrons in pp collisions at $\sqrt{s} = 7$ and $\sqrt{s} = 13$ TeV" In: *Eur. Phys. J. C* 81.3 (2021), p. 256. DOI: 10.1140/epjc/s10052-020-08690-5. arXiv: 2005.11120 [nucl-ex]. URL: http://arxiv.org/abs/2005.11120 (visited on 11/30/2022).

[90] Shreyasi Acharya et al. "Nuclear modification factor of light neutral-meson spectra up to high transverse momentum in p–Pb collisions at sNN=8.16 TeV". In: *Phys. Lett. B* 827 (2022), p. 136943. DOI: 10.1016/j.physletb.2022.136943. arXiv: 2104.03116 [nucl-ex]. URL: https://arxiv.org/abs/2104.03116 (visited on 02/08/2023).

[91] R. Albrecht et al. "Production of eta mesons in 200-A/GeV S + S and S + Au reactions". In: *Phys. Lett. B* 361 (1995), pp. 14–20. DOI: 10.1016/0370-2693(95)01166-N. arXiv: hep-ex/9507009. URL: https://arxiv.org/abs/hep-ex/9507009 (visited on 02/02/2023).

[92] P. K. Khandai, P. Shukla, and V. Singh. "Meson spectra and m_T scaling in $p + p$, d+Au, and Au + Au collisions at $\sqrt{s_{NN}} = 200$ GeV". In: *Phys. Rev. C* 84 (2011), p. 054904. DOI: 10.1103/PhysRevC.84.054904. arXiv: 1110.3929 [hep-ph]. URL: https://arxiv.org/abs/1110.3929 (visited on 02/02/2023).

[93] G. Agakichiev et al. "Neutral meson production in p Be and p Au collisions at 450-GeV beam energy". In: *Eur. Phys. J. C* 4 (1998), pp. 249–257. DOI: 10.1007/s100529800804. URL: https://link.springer.com/article/10.1007/s100529800804 (visited on 02/09/2023).

[94] Shreyasi Acharya et al. "π^0 and η meson production in proton-proton collisions at $\sqrt{s} = 8$ TeV". In: *Eur. Phys. J. C* 78.3 (2018), p. 263. DOI: 10.1140/epjc/s10052-018-5612-8. arXiv: 1708.08745 [hep-ex]. URL: https://arxiv.org/abs/1708.08745 (visited on 02/09/2023).

[95] Shreyasi Acharya et al. "Neutral pion and η meson production in p-Pb collisions at $\sqrt{s_{\mathrm{NN}}} = 5.02$ TeV". In: *Eur. Phys. J. C* 78.8 (2018), p. 624. DOI: 10.1140/epjc/s10052-018-6013-8. arXiv: 1801.07051 [nucl-ex]. URL: https://arxiv.org/abs/1801.07051 (visited on 02/09/2023).

[96] Lucas Altenkämper, Friederike Bock, Constantin Loizides, and Nicolas Schmidt. "Applicability of transverse mass scaling in hadronic collisions at energies available at the CERN Large Hadron Collider". In: *Phys. Rev. C* 96.6 (2017), p. 064907. DOI: 10.1103/PhysRevC.96.064907. arXiv: 1710.01933 [hep-ph]. URL: https://arxiv.org/abs/1710.01933 (visited on 02/05/2023).

[97] Shreyasi Acharya et al. "Production of ω mesons in pp collisions at $\sqrt{\mathbf{s}} = \mathbf{7}$ TeV". In: *Eur. Phys. J. C* 80.12 (2020), p. 1130. DOI: 10.1140/epjc/s10052-020-08651-y. arXiv: 2007.02208 [nucl-ex]. URL: http://arxiv.org/abs/2007.02208 (visited on 08/29/2022).

[98] Roger Barlow. "Systematic errors: Facts and fictions". In: *Conference on Advanced Statistical Techniques in Particle Physics*. July 2002, pp. 134–144. arXiv: hep-ex/0207026. URL: https://arxiv.org/abs/hep-ex/0207026 (visited on 02/02/2023).

[99] Shreyasi Acharya et al. "π^0 and η meson production in proton-proton collisions at $\sqrt{s} = 8$ TeV". In: *Eur. Phys. J. C* 78.3 (2018), p. 263. DOI: 10.1140/epjc/s10052-018-5612-8. arXiv: 1708.08745 [hep-ex]. URL: https://arxiv.org/abs/1708.08745 (visited on 02/02/2023).

[100] ALICE Collaboration. *Measurement of Neutral Mesons in Pp and PbPb Collisions at Sqrt(sNN) = 5.02 TeV with the PHOS Detector — Public & Analysis Notes*. URL: https://alice-notes.web.cern.ch/node/712 (visited on 12/20/2022).

[101] Shreyasi Acharya et al. "Multiplicity dependence of π, K, and p production in pp collisions at $\sqrt{s} = 13$ TeV". In: *Eur. Phys. J. C* 80.8 (2020), p. 693. DOI: 10.1140/epjc/s10052-020-8125-1. arXiv: 2003.02394 [nucl-ex]. URL: http://arxiv.org/abs/2003.02394 (visited on 12/19/2022).

[102] "Performance of the ALICE Electromagnetic Calorimeter". In: (Sept. 2022). arXiv: 2209.04216 [physics.ins-det]. URL: http://arxiv.org/abs/2209.04216 (visited on 10/19/2022).

[103] Guo-Yang Ma, Wei Dai, Ben-Wei Zhang, and En-Ke Wang. "NLO Productions of ω and K^0_S with a global extraction of the jet transport parameter in heavy-ion collisions". In: *Eur. Phys. J. C* 79.6 (2019), p. 518. DOI: 10.1140/epjc/s10052-019-7005-z. arXiv: 1812.02033 [nucl-th]. URL: http://arxiv.org/abs/1812.02033 (visited on 12/16/2022).

[104] M. Diakonou et al. "Inclusive high-pT ω^0 and η' production at the ISR". In: *Physics Letters B* 89.3 (1980), pp. 432–436. ISSN: 0370-2693. DOI: https://doi.org/10.1016/0370-2693(80)90159-8. URL: https://www.sciencedirect.com/science/article/pii/0370269380901598 (visited on 02/02/2023).

[105] A. Adare et al. "Measurement of neutral mesons in $p+p$ collisions at $\sqrt{s} = 200$ GeV and scaling properties of hadron production". In: *Phys. Rev. D* 83 (5 2011), p. 052004. DOI: 10.1103/PhysRevD.83.052004. URL: https://link.aps.org/doi/10.1103/PhysRevD.83.052004 (visited on 12/20/2022).

[106] A. Adare et al. "Production of ω mesons in $p+p$, d+Au, Cu+Cu, and Au+Au collisions at $\sqrt{s_N N} = 200$ GeV". In: *Phys. Rev. C* 84 (2011), p. 044902. DOI: 10.1103/PhysRevC.84.044902. arXiv: 1105.3467 [nucl-ex]. URL: http://arxiv.org/abs/1105.3467 (visited on 02/02/2023).

[107] S. S. Adler et al. "Production of omega mesons at Large Transverse Momenta in p + p and d + Au Collisions at s**(1/2)(NN) = 200-GeV". In: *Phys. Rev. C* 75 (2007), p. 051902. DOI: 10.1103/PhysRevC.75.051902. arXiv: nucl-ex/0611031. URL: https://arxiv.org/abs/nucl-ex/0611031 (visited on 02/02/2023).

[108] B.A. Kniehl, G. Kramer, and B. Pötter. "Fragmentation functions for pions, kaons, and protons at next-to-leading order". In: *Nuclear Physics B* 582.1 (2000), pp. 514–536. ISSN: 0550-3213. DOI: https://doi.org/10.1016/S0550-3213(00)00303-5. URL: https://www.sciencedirect.com/science/article/pii/S0550321300003035 (visited on 02/02/2023).

[109] S. Albino, B. A. Kniehl, and G. Kramer. "AKK Update: Improvements from New Theoretical Input and Experimental Data". In: *Nucl. Phys. B* 803 (2008), pp. 42–104. DOI: 10.1016/j.nuclphysb.2008.05.017. arXiv: 0803.2768 [hep-ph]. URL: https://arxiv.org/abs/0803.2768 (visited on 02/02/2023).

[110] S. Kretzer. "Fragmentation functions from flavor-inclusive and flavor-tagged e^+e^- annihilations". In: *Phys. Rev. D* 62 (5 2000), p. 054001. DOI: 10.1103/PhysRevD.62.054001. URL: https://link.aps.org/doi/10.1103/PhysRevD.62.054001 (visited on 02/02/2023).